Study of strongly interacting matter using dimuons produced in Pb+Pb collisions at $\sqrt{s_{\mathrm{NN}}} = 2.76$ TeV

By

Vineet Kumar

PHYS01201104006

Bhabha Atomic Research Centre, Mumbai

A thesis submitted to the

Board of Studies in Physical Sciences

In partial fulfillment of requirements

for the Degree of

DOCTOR OF PHILOSOPHY

of

HOMI BHABHA NATIONAL INSTITUTE

August 2014

Homi Bhabha National Institute

Recommendations of the Viva Voce Board

As members of the Viva Voce Board, we certify that we have read the dissertation prepared by Vineet Kumar entitled "Study of strongly interacting matter using dimuons produced in Pb+Pb collisions at $\sqrt{s_{\rm NN}} = 2.76$ TeV" and recommend that it maybe accepted as fulfilling the dissertation requirement for the Degree of Doctor of Philosophy.

____ Date:

Chairman: Dr. V. M. Datar

____ Date:

Guide/Convener: Dr. Prashant Shukla

____ Date:

Member 1: Dr. A. K. Mohanty

____ Date:

Member 2: Dr. Subhasis Chattopadhyaya

Final approval and acceptance of this dissertation is contingent upon the candidate's submission of the final copies of the dissertation to HBNI.

I hereby certify that I have read this dissertation prepared under my direction and recommend that it may be accepted as fulfilling the dissertation requirement.

Date:

Place: Dr. Prashant Shukla

STATEMENT BY AUTHOR

This dissertation has been submitted in partial fulfillment of requirements for an advanced degree at Homi Bhabha National Institute (HBNI) and is deposited in the Library to be made available to borrowers under rules of the HBNI.

Brief quotations from this dissertation are allowable without special permission, provided that accurate acknowledgement of source is made. Requests for permission for extended quotation from or reproduction of this manuscript in whole or in part may be granted by the Competent Authority of HBNI when in his or her judgement the proposed use of the material is in the interests of scholarship. In all other instances, however, permission must be obtained from the author.

Vineet Kumar

DECLARATION

I, hereby declare that the investigation presented in the thesis has been carried out by me. The work is original and has not been submitted earlier as a whole or in part for a degree / diploma at this or any other Institution / University.

Vineet Kumar

LIST OF PUBLICATION

Journal

1. **"Event activity dependence of Υ(nS) production in $\sqrt{s_{\mathrm{NN}}} = 5.02$ TeV pPb and $\sqrt{s} = 2.76$ TeV pp collisions"**, S. Chatrchyan..,V. Kumar *et al.* [CMS Collaboration], JHEP **1404**, 103 (2014), [arXiv:1312.6300– [nucl-ex]], CMS HIN-13-003, CMS AN-13-025.

2. **"Observation of sequential Υ suppression in PbPb collisions"**, S. Chatrchyan..,V. Kumar *et al.* [CMS Collaboration], Phys. Rev. Lett. **109**, 222301 (2012), [arXiv:1208.2826 [nucl-ex]], CMS HIN-11-011, CMS AN-11-455.

3. **"Indications of suppression of excited Υ states in PbPb collisions at $\sqrt{S_{NN}} = 2.76$ TeV"**, S. Chatrchyan..,V. Kumar *et al.* [CMS Collaboration], Phys. Rev. Lett. **107**, 052302 (2011), [arXiv:1105.4894 [nucl-ex]], CMS-HIN-11-007, CMS AN-10-386.

4. **"Components of the dilepton continuum in Pb+Pb collisions at $\sqrt{s_{NN}} = 2.76$ TeV"**, V. Kumar, P. Shukla and R. Vogt, Phys. Rev. C **86**, 054907 (2012), [arXiv:1205.3860 [hep-ph]].

5. **"Quarkonia suppression in PbPb collisions at $\sqrt{s}_{\mathrm{NN}} = 2.76$ TeV"**, V. Kumar and P. Shukla [arXiv:1410.3299 [hep-ph]].

6. **"Suppression of non-prompt J/ψ, prompt J/ψ, and Υ(1S) in PbPb collisions at $\sqrt{s_{NN}} = 2.76$ TeV"**, S. Chatrchyan..,V. Kumar *et al.* [CMS Collaboration], JHEP **1205**, 063 (2012), [arXiv:1201.5069 [nucl-ex]], CMS HIN-10-006, CMS AN-11-062.

7. **“Study of Z boson production in PbPb collisions at nucleon-nucleon centre of mass energy = 2.76 TeV”**, S. Chatrchyan..,V. Kumar *et al.* [CMS Collaboration], Phys. Rev. Lett. **106**, 212301 (2011), [arXiv:1102.5435 [nucl-ex]], CMS HIN-10-003, CMS AN-10-386.

Conferences

8. **“Measurement of Υ production in PbPb collisions at 2.76 TeV with CMS”**, V. Kumar for CMS collaboration, CMS CR-2013/008, Proc. QGP Meet Narosa Publications.

9. **“Quarkonia production in PbPb collisions at $\sqrt{s_{\mathrm{NN}}} = 2.76$ TeV”**, Vineet Kumar, Abdulla Abdulsalam and P. Shukla, Proc. DAE Symp. Nucl. Phys. **58**, 710 (2013).

10. **“Bottomonium production in pp, pPb, and PbPb collisions with CMS”**, Vineet Kumar, Abdulla Abdulsalam, P. Shukla and CMS collaboration, Proc. DAE Symp. Nucl. Phys. **58**, 722 (2013).

11. **“Υ Production in PbPb collisions at 2.76 TeV”**, Vineet Kumar, Abdulla Abdulsalam, P. Shukla and CMS collaboration, Proc. DAE Symp. Nucl. Phys. **57**, 762 (2012).

12. **“Υ production in p+p and Pb+Pb collisions at $\sqrt{s_{\mathrm{NN}}} = 2.76$ TeV”**, Vineet Kumar, Abdulla Abdulsalam, P Shukla and CMS collaboration, Proc. DAE Symp. Nucl. Phys **56**, 900 (2011).

13. **“Continuum components in dilepton mass spectrum in Pb+Pb collisions at $\sqrt{s_{\mathbf{NN}}}$ = 2.76 TeV”**, Vineet Kumar, P Shukla, R Vogt, Proc. DAE Symp. Nucl. Phys. **56**, 934 (2011).

This thesis is based on publications 1-5.

Vineet Kumar

DEDICATIONS

To my parents and family

ACKNOWLEDGMENTS

I would like to express my sincere gratitude to my adviser, Dr. Prashant Shukla. I appreciate his continued support and understanding. I would like to thank all members of Doctoral committee for their valuable suggestions during my Ph.D. The present and past members are Dr. V. M. Datar (Chairman), Dr. Prashant Shukla (Guide & Convener), Dr. A. K. Mohanty, Dr. Subhasis Chattopadhyay and Dr. Ambar Chatterjee (former chairman,retired).

I want to thank all of my colleagues in Nuclear Physics Division. Specially all of my colleagues in High Energy Physics Section, Raman Sehgal, Dr. Pawan Kumar and Dr. Dipak Mishra require special mention. It was a wonderful time I spent with my friends Prakhar, Khandai, Kapil, Ruchi and Priyanka.

I utilize this opportunity to thank the entire CMS Heavy-ion collaboration. Specially all my CMS dilepton colleagues. Dr. Raphael Granier de Cassagnac, Catherine Silvestre and Torsten Dahms who helped a lot and provided fruitful advice. Also I am grateful to my special friends, Dongho Moon, Jorge A. Robles, Mihee, and Hyunchul. Again, I am very happy to give a special and sincere thanks to Abdulla. We both shared many late night discussions at HBNI. Those were difficult times specially if things are not going in right direction. I find him always enthusiastic to do more to understand the things.

Finally, to my family. My words are not enough to express my deepest gratitude to my family members for their support. To my wife Anamika, warm thanks for being with me in all my ups and downs of life, who endured all my shortcomings with smiling face. To my daughter Sanvi, thanks for being a nice sweet angel and not distrubing me much during writing of thesis.

Contents

List of Figures

List of Tables

SYNOPSIS

Quantum chromodynamics (QCD) predicts that strongly interacting matter undergoes a phase transition to a deconfined state, often referred to as the quark-gluon plasma (QGP), in which quarks and gluons are no longer bound within hadrons. Aim of Heavy Ion Collisions at high energies is to create, characterize and quantify the properties of Quark Gluon Plasma (QGP). Calculations in lattice QCD [1] indicate that the transition should occur at a critical temperature $T_c \simeq$ 150-175 MeV, corresponding to an energy density $\epsilon_c \simeq 1$ GeV/fm^3. Relativistic Heavy Ion Collider (RHIC) at BNL is colliding Au+Au ions at $\sqrt{s_{NN}}$ 200 GeV since 2001. Large Hadron Collider (LHC) at CERN becomes operational in 2010 and have first Pb+Pb run at $\sqrt{s_{NN}}$ 2.76 TeV, 14 times more than previously available at RHIC. The matter created at LHC is closer to the conditions of early universe. In addition many QGP probes can be measured with better accuracy and large statistics. If the QGP is formed in heavy-ion collisions, it is expected to screen the confining potential of heavy quark-antiquark pairs [2], leading to the melting of charmonia (J/$\psi, \psi^{'}, \chi_c$....) and bottomonia (Υ(1S), Υ(2S) and Υ(3S), $\chi_{\rm b}$....) The melting temperature depends on the binding energy of the quarkonium state. The ground states J/ψ and $\Upsilon(1S)$ are expected to dissolve at significantly higher temperatures than the more loosely bound excited states. Quenched lattice QCD calculations [3] predict that the $\Upsilon(n\mathrm{S})$ states melt at 1.2 T_c (3S), 1.6 Tc (2S), and above 4 Tc (1S), while modern spectral-function approaches with complex potentials [4] favor somewhat lower dissolution temperatures. This sequential melting pattern is generally considered a smoking-gun signature of the QCD deconfinement transition. Production yields of quarkonium states can also be modified, from pp to Pb-Pb collisions, in the absence of QGP formation, by cold nuclear matter effects [5]. However, such effects should have a similar impact on all three Υ states due to their small mass difference and identical quantum number. Understanding the production of bottomonia in elementary pp collisions is equally important for interpreting any additional effects in collisions involving heavy ions. At RHIC, bottomonia production becomes measurable, though limited integrated luminosities combined with available resolution of detectors does not allow separate measurement of all three Υ states. PHENIX observed, with limited statistics that the dimuon yield in the Υ mass region for minimum bias Au-Au collisions is less than 64%, at the 90% confidence level, of the value expected by extrapolating the proton-proton yields [6].

This work concentrate on production and suppression of $b\overline{b}$ bound states, namely Υ(1S), Υ(2S) and Υ(3S) which are measured in pp, pPb and PbPb collisions at LHC. This is the first time we are able to measure all three Υ states separately with good statistics thanks to the large integrated luminosity and high-tech detectors available at LHC. In addition, theoretical calculations are performed to estimate the background in dimuon spectra and to calculate the suppression of quarkonia states using different models.

Quarkonia measurement using CMS detector at LHC

The Compact Muon Solenoid (CMS) experiment is one of two large general-purpose particle physics detectors built on the Large Hadron Collider (LHC) at CERN. With excellent muon detection capabilities CMS is ideal for measuring quarkonia, specially upsilon states. It consists of silicon pixel and strip tracker, the crystal electromagnetic calorimeter, and the brass/scintillator hadron calorimeter housed inside a magnetic field of 3.8 Teslla. The silicon pixel and strip tracker measures charged-particle trajectories in the range pseudorapidity $|\eta| \leq 2.5$. Muons are detected in the range $|\eta| \leq 2.4$, with detection planes based on three technologies: drift tubes, cathode strip chambers, and resistive plate chambers. The muon p_T measurement based on information from the tracker alone has a resolution between 1 to 2 % for a typical muon coming from quarkonia decay. The CMS apparatus also has two steel/quartz-fiber Cerenkov hadron forward calorimeters (HF), which cover the range $2.9 \leq |\eta| \leq 5.2$. These detectors are used for event selection and impact parameter-like characterization of the events in heavy ion collisions.

Υ measurement in PbPb collisions

The quarkonium states are identified through their dimuon decay. Muons are reconstructed by matching tracks in the muon detectors and silicon tracker. The measurement presented here use the data recorded by the Compact Muon Solenoid (CMS) experiment during the first lead-lead (Pb-Pb) LHC run, at the end of 2010, and during the proton-proton (pp) run of March 2011, both at $\sqrt{s_{NN}}$ 2.76 TeV. The integrated luminosity used in this measurement corresponds to 7.28 μb^{-1} for Pb-Pb and 225 nb^{-1} for pp collisions. The momentum resolution of the CMS detector results in well-resolved peaks in the dimuon mass spectrum. Only muons with a transverse momentum ($\mathrm{p_T}$) higher than 4 GeV/c and $|\eta| \leq 2.4$ are considered. The ratio of the (Υ(2S) + Υ(3S)/Υ(1S)) in Pb-Pb and pp, also known as double ratio, benefits from an almost complete cancellation of possible acceptance and/or efficiency differences among the reconstructed resonances. A simultaneous fit to the pp and Pb-Pb mass spectra gives the double ratio $0.31^{+0.19}_{-0.15}(\mathrm{stat}) \pm 0.03(\mathrm{syst})$. The probability to obtain the measured value, or lower, if the true double ratio is unity, has been calculated to be less than 1%.

An update of these measurements is performed, utilizing a PbPb data sample corresponding to an integrated luminosity of 150 μb^{-1} collected in 2011 by CMS, at $\sqrt{s_{NN}}$ 2.76 TeV as in the previous study. This larger PbPb data set enables the measurement of the centrality dependence of all three Υ states yields. The event centrality observable corresponds to the fraction of the total inelastic cross section, starting at 0% for the most central collisions and evaluated as percentiles of the distribution of the energy deposited in the HF [7]. The signal candidates generated by PYTHIA [8] are embedded in the underlying PbPb events from HYDJET [9]. The detector response is simulated with GEANT4 [10].

Absolute suppressions of the individual Υ states and their dependence on the collision centrality are studied using the nuclear modification factor, R_{AA}, defined as the yield per nucleon-nucleon collision in PbPb relative to that in pp. The R_{AA} observable,

$$R_{\mathrm{AA}} = \frac{L_{\mathrm{pp}}}{T_{\mathrm{AA}} N_{\mathrm{MB}}} \frac{\Upsilon(n\mathrm{S})|_{\mathrm{PbPb}}}{\Upsilon(n\mathrm{S})|_{\mathrm{pp}}} \frac{\epsilon_{\mathrm{pp}}}{\epsilon_{\mathrm{PbPb}}}$$

is evaluated from the ratio of total $\Upsilon(n\mathrm{S})$ yields in PbPb and pp collisions corrected for the difference in efficiencies $\epsilon_{\mathrm{pp}}/\epsilon_{\mathrm{PbPb}}$, with the average nuclear overlap function T_{AA}, number of minimum-bias (MB) events sampled by the event selection N_{MB}, and integrated luminosity of the pp data set L_{pp} accounting for the normalization. The results indicate a significant suppression of the $\Upsilon(n\mathrm{S})$ states in heavy-ion collisions compared to pp collisions at the same per-nucleon-pair energy. The data support the hypothesis of increased suppression of less strongly bound states. The Υ(1S) is the least suppressed and the Υ(3S) is the most suppressed of the three states. The Υ(1S) and Υ(2S) suppressions are observed to increase with collision centrality. T he suppression of Υ(2S) is stronger than that of Υ(1S) in all centrality ranges, including the most peripheral bin.

Υ measurement in pPb and pp collisions

The production of Υ(1S), Υ(2S), Υ(3S) is investigated in pPb and pp collisions at center-of-mass energies per nucleon pair of 5.02 TeV and 2.76 TeV respectively. The datasets correspond to recorded integrated luminosities of about 31 nb^{-1} (pPb) and 5.4 pb^{-1} (pp), collected in 2013 by the CMS experiment at the LHC. Upsilons, which decay into muons of transverse momentum above 4 GeV/c and pseudorapidity in the nucleon-nucleon center-of-mass frame of $|\eta_{\mathrm{CM}}| \leq 1.93$, are studied as a function of two measures of event activity, namely the charged-particle multiplicity measured in pseudorapidity interval $\eta \leq$ 2.4, and the transverse energy deposited at large pseudorapidity, 4.0 $\leq |\eta| \leq$ 5.2. The Υ yields normalized by their event average, $\Upsilon(n\mathrm{S})/\langle\Upsilon(n\mathrm{S})\rangle$, rise with both measures of the event activity in pp and pPb. In both datasets, the ratios of the excited to the ground state, $\Upsilon(\mathrm{nS})/\Upsilon(1\mathrm{S})$, decrease with the charged-particle multiplicity. The ratios of excited to ground state production show a smaller variation when measured as a function of the transverse energy. The event-activity integrated double ratios, $[\Upsilon(n\mathrm{S})/\Upsilon(1\mathrm{S})]_{\mathrm{pPb}}/[\Upsilon(n\mathrm{S})/\Upsilon(1\mathrm{S})]_{\mathrm{pp}}$, are also measured and found to be $0.83 \pm 0.05(\mathrm{stat.}) \pm 0.05(\mathrm{syst.})$ and $0.71 \pm 0.08(\mathrm{stat.}) \pm 0.09(\mathrm{syst.})$ for $\Upsilon(2\mathrm{S})$ and $\Upsilon(3\mathrm{S})$, respectively. These double ratios although less than one, are yet well above the ratios measured in PbPb collisions indicating presence of additional final state effects in PbPb collisions. Single ratios ($\Upsilon(n\mathrm{S})/\Upsilon(1\mathrm{S})$) seems to be constantly decreasing with increasing mid rapidity multiplicity in all three collision systems. A global understanding of effects at play in pp, pPb and PbPb collisions calls for more activity related study of Υ yields.

Estimating dimuon continuum at LHC

The dilepton invariant mass spectrum measured in heavy-ion collisions includes contributions from important quark-gluon plasma (QGP) probes such as thermal radiation and the quarkonium (J/ψ, ψ',Υ) states. Dileptons coming from hard quark anti-quark scattering, the Drell-Yan process, contribute in all mass regions. In heavy-ion colliders, such as the Large Hadron Collider (LHC), semi-leptonic decays of heavy flavor hadrons provide a substantial contribution to the dilepton continuum. In the present study, cross sections for heavy quark pairs are calculated to NLO in pQCD using the CTEQ6M parton densities [11]. The central EPS09 parameter set [12] is used to calculate the modifications of the parton densities in Pb+Pb collisions. We use the same set of parameters as that of Ref. [13] with the NLO calculation of Ref. [14] to obtain the exclusive $\mathrm{Q}\overline{Q}$ pair rates as well as their decays to dileptons. Their contributions to the dilepton continuum in

Pb + Pb collisions at $\sqrt{s_{NN}}$ 2.76 TeV with and without including heavy quark energy loss is determined. These rates are then compared with Drell-Yan and thermal dilepton production. The contributions of all these sources are obtained in kinematic regions relevant for the LHC detectors. Thermal leptons have very small transeverse momentum components and since most detectors accept only high-$\mathrm{p_T}$ leptons, thermal dileptons mostly escape detection in the experiments. Heavy flavors are the dominant source of dileptons in most kinematic regimes, even after energy loss. In most of the kinematic regions considered, the $\mathrm{b\overline{b}}$ decay contributions become larger than those of $c\bar{c}$ for lepton pair masses greater than 7 GeV/c^2.

Study of quarkonia suppression by gluon dissociation

Quarkonia suppression is studied using different scenarios. There are several models of quarkonia suppression which include hot matter effect like color screening[2] and/or cold nuclear matter effect like shadowing and comovar dissociation [5]. We study quarkonia suppression via thermal gluon dissociation. Using gluon dissociation cross section (σ_{D}) we calculate temperature dependent dissociation rates, $\lambda_{\mathrm{D}} = \langle v_{\mathrm{rel}} \sigma_{\mathrm{D}}(k \cdot u) \rangle_k$ as a function of quarkonia transverse momentum. We assume QGP formation with initial temperature calculated using measured mid rapidity track density at LHC. Assuming isentropic cylindrical expansion of QGP fireball we get temperature evolution in QGP and mixed phase. The survival probability $S(p_T)$ of quarkonia from gluon dissociation can be obtained by integrating from initial time τ_0 to freeze out time τ_f

$$S(p_T) = \exp\left(- \int_{\tau_0}^{\tau_f} f(\tau) \lambda_{\mathrm{D}}(T)\, \rho_g(T)\, d\tau \right), \tag{1}$$

where $\rho_g(T)$ is the gluon density of QGP at temperature T and $f(\tau)$ is fraction of QGP in mixed phase. Other modifications such as Cold Nuclear Matter effect and regeneration have been considered. Our model gives good description of data measured at LHC.

Chapter 1.

Relativistic heavy ion collisions and quark gluon plasma

Relativistic heavy ion collisions are means to create and study strongly interacting matter at very high temperature/density. The interest in this field arises from the prediction of Quantum Chromodynamics (QCD) that hadronic matter at energy density above 1 GeV/fm^3 undergoes a phase transition to Quark Gluon Plasma (QGP), a new state of matter where quarks and gluons roam in a volume much larger than the size of a hadron. When the temperature of the universe was very high (within few μs after big bang) it could be in the form of QGP. When the universe expanded and cooled below a temperature ($\sim$ 200 MeV), the quarks and gluons were permanently confined inside hadrons. The heavy ion collisions create a large enough system with the conditions similar to those existing in the early universe. Creating and characterizing the properties of QGP has become an interesting field of research in last couple of decades. This chapter provides an introduction and the present status of the field of heavy ion collisions and QGP.

1.1. Standard model

The Standard Model (SM) of particle physics is a theory of particle properties and particle interactions [15]. It describes the strong, weak, and electromagnetic forces between the fundamental particles of matter. Special relativity and quantum mechanics form the basis for quantum field theory and the Standard Model. The SM includes 12 elementary particles of spin $\frac{1}{2}$ known as fermions. The fermions of the SM are classified according to how they interact (or equivalently, by what charges they carry). There are six quarks (up, down, charm, strange, top, bottom), and six leptons (electron, electron neutrino, muon, muon neutrino, tau, tau neutrino) their properties are summarized in Table 1.1. The quarks and leptons are grouped in three generations. The first generation contains the most stable particles which make most of the observed matter in the universe, while the second and the third generations contain particles which decay to the lower generation of particles. The interactions among quarks and leptons occur via exchange of another type of particles named Gauge Bosons. Gauge Bosons and their properties are shown in Table 1.2. The quarks and leptons have spin-1/2 while bosons are spin-1 particles. There are four fundamental interactions: Strong, Weak, Electromagnetic and Gravitational. Each of the interactions has different strength and range of influence. Leptons participate in gravitational, electromagnetic and weak interactions. Quarks on the other hand can participate in all four interactions. The theory which describes the strong interaction between quarks and gluons is known as Quantum Chromodynamics or QCD. Basic properties of this theory are discussed in Section 1.2.

Table 1.1.: Quarks and leptons properties. Every particle in the table has a corresponding antiparticle with opposite charge. According to the Standard Model, the neutrino masses are equal to zero. Observed neutrino oscillation suggests that the neutrinos have mass and their experimental values are reported in the table

Generation	Name	Symbol	Electric charge	Mass[MeV/c^2]
I	Electron	e^-	-1	0.511
	Electron neutrino	ν_e	0	$\leq$0.000225
II	Muon	μ^-	-1	105.658
	Muon neutrino	ν_μ	0	$\leq$ 0.19
III	Tau	τ^-	-1	1776.82
	Tau neutrino	ν_τ	0	$\leq$ 18.2
		Quarks		
I	Up	u	$+\frac{2}{3}$	1.8−3.0
	Down	d	$-\frac{1}{3}$	4.5−5.5
II	Charm	c	$+\frac{2}{3}$	1250−1300
	Strange	s	$-\frac{1}{3}$	90−100
III	Top	t	$+\frac{2}{3}$	172100−174900
	Bottom	b	$-\frac{1}{3}$	4150−4210

Table 1.2.: Boson properties

Name Symbol	Force Range(m)	Electric Charge Spin	Mass [GeV/c^2] Strength
Photon γ	Electromagnetic ∞	0 1	0 $\alpha = \frac{1}{137}$
Gluon g	Strong 10^{-15}	0 1	0 $\alpha_s = 1$, at high energy $\alpha_s \to 0$
Z Boson Z^0	Weak 10^{-18}	0 1	91.187 $\alpha_z = 10^{-6}$
W Boson $W^\pm$	Weak 10^{-18}	± 1 1	80.399 $\alpha_W = 10^{-6}$
Higgs Boson H		0 0	~ 126

1.2. Quantum chromodynamics

Quantum chromodynamics (QCD) [16–19] is the field theory describing the strong interactions of colored quarks and gluons. Color charge comes in three versions (red, green and blue) that form a fundamental representation of the SU(3) group, and is carried by both the quarks and gluons. Analogous to electric charge in quantum electrodynamics (QED) [20, 21], color charge is conserved in QCD, but since the gluons carry color charge, they can interact with other gluons. This is not possible in QED, as photons do not carry electric charge. The existence of self-coupling in QCD (Fig. 1.1) has important implications for the scale dependence of the strong coupling. In quantum field theory, the coupling constant describing the interaction between two particles is an effective constant, which is dependent on the energy−scale (Q^2) of the interaction. In QED this dependence is very weak; in QCD, however, it is very strong. The reason is the self-coupling of the gluons. The dependence of the strong coupling constant $\alpha_s(Q^2)$ on Q^2 is known as a running coupling constant. In perturbative QCD (pQCD), a first-order approximation yields:

$$\alpha_s(Q^2) = \frac{1}{\beta_0 \, ln(\frac{Q^2}{\Lambda^2_{QCD}})}, \text{ where } \beta_0 = \frac{33 - n_f}{12\pi} \tag{1.1}$$

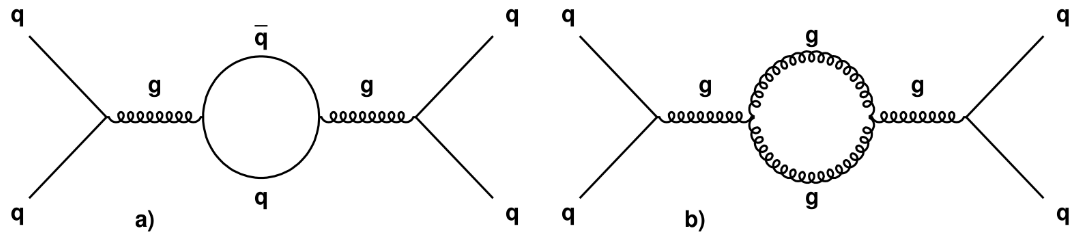

Figure 1.1.: Feynman diagrams at first order, of the vacuum polarization in QCD a) screening and b) anti-screening. In the case of QED, anti-screening does not exist since photons are not charged particles.

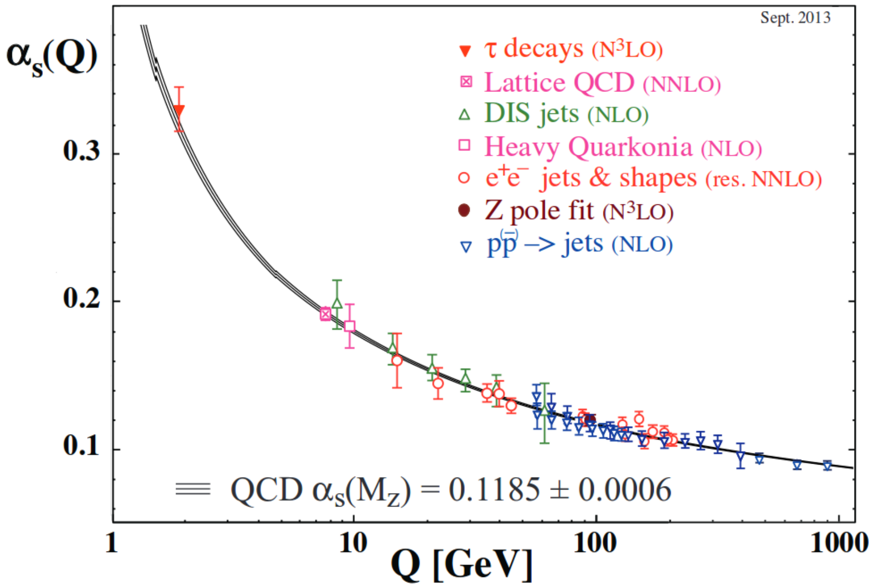

Figure 1.2.: Figure shows a compilation of the values for α_s, derived from many different experiments, and for different momenta Q of the exchanged gluons. Gluon momentum is measured in GeV/c, and a logarithmic scale has been used to allow to show a bigger range of values.

Here, n_f denotes the number of quark types with mass below Q, and Λ_{QCD} represents the characteristic scale of confinement. Λ_{QCD} is determined by comparing predictions with experimental data and is found to be on the order of 250 MeV [22].

The Q^2- dependence of the coupling strength corresponds to a dependence on quark separation. For very small distances, i.e. high values of Q^2, the strong coupling decreases, vanishing asymptotically as $Q^2 \rightarrow \infty$. In the limit $Q^2 \rightarrow \infty$, quarks can be considered to be "free"; this phenomenon is known as **Asymptotic Freedom**. Figure 1.2 shows a compilation of the values for α_s, derived from different experiments at various energy scales. It is clear that Asymptotic Freedom is a fundamental property of Quantum Chromo Dynamics which is confirmed by the experiments.

In contrast, at large distances, the strong coupling increases substantially so that it is not possible to detach individual quarks from hadrons. This leads to another important property of strong interaction known as **Confinement**. It remains to be shown, however, that quark confinement is indeed a property of QCD and can be derived from first principle calculations. This is one of the basic open problems of modern science. It is because of confinement that quarks and gluons are never seen free in experiments. Instead, they turn into hadrons, which are observed in the detectors. This process is called *hadronization*. Hadronization of quarks happens at a later time (t $\sim \frac{1}{\Lambda_{QCD}}$) than the production process (t $\sim \frac{1}{Q}$). This is why the calculations of hadronic cross sections can be factorized into perturbative and non-perturbative parts. The perturbative QCD has been very successful in predicting phenomena involving large momentum transfer. In this regime the coupling constant is small and perturbation theory becomes a reliable tool. On the other hand, at the scale of the hadronic world (t $\sim \frac{1}{\Lambda_{QCD}}$) the coupling constant is of order unity and perturbative methods fail. In this domain *lattice QCD* provides a non-perturbative tool for calculating the hadronic spectrum. Lattice QCD is QCD formulated on a discrete Euclidean space time grid. Since no new parameters are introduced in this discretization, LQCD retains the fundamental character of QCD.

1.2.1. High temperature QCD matter

The interest in analyzing the behavior of QCD at high temperatures or densities is two fold. On the one hand it is the goal to reach a quantitative description of the behavior of matter at high temperature and density. On the other hand the analysis of a complicated quantum field theory like QCD at non-zero temperature can also help to improve our understanding of its non-perturbative properties at zero temperature. QCD at high temperatures does provide important inputs for a quantitative description of experimental signatures for the occurrence of a phase transition in heavy ion collisions and eventually it should help to understand better the phase transitions that occurred during the early times of the evolution of the universe. For this reason one would like to reach a quantitative understanding of the QCD equation of state, determine critical parameters such as the critical temperature and the critical energy density and predict the modification of basic hadron properties (masses, decay widths) with temperature.

At vanishing baryon number density (or zero chemical potential) the properties of the QCD phase transition depend on the number of quark flavors and their masses. While it is a detailed quantitative question at which temperature the transition to the high

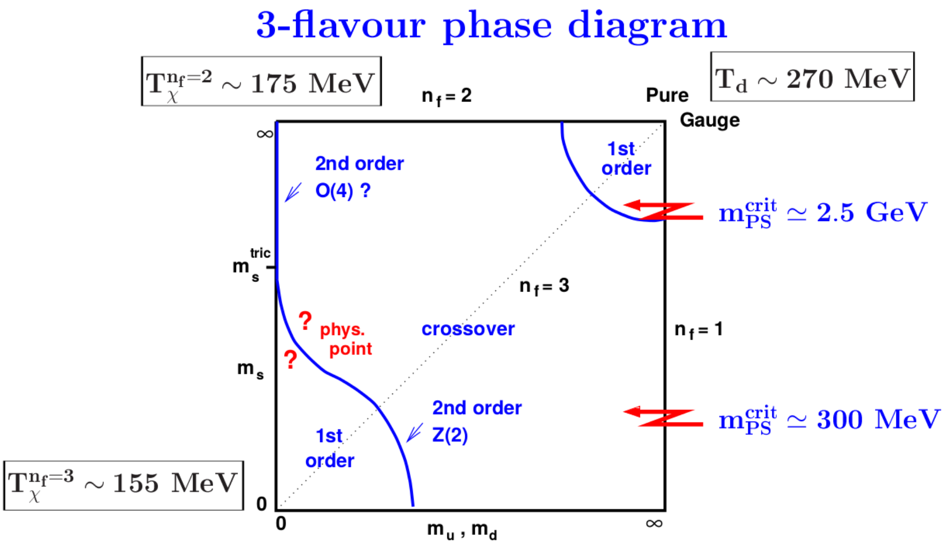

Figure 1.3.: The QCD phase diagram of 3-flavor QCD with degenerate (u,d)-quark masses and a strange quark mass m_s. Figure is taken from Ref.[1].

temperature plasma phase occurs, we do expect that the nature of the transition, e.g. its order and details of the critical behavior, are controlled by global symmetries of the QCD Lagrangian. Such symmetries only exist in the limits of either infinite or vanishing quark masses. For any non-zero, finite value of quark masses the global symmetries are explicitly broken.

The anticipated phase diagram of 3-flavor QCD at vanishing baryon number density is shown in Fig. 1.3. The transition is first order in case of three light degenrate quark flavors and most likely is second order in case of 2 flavored QCD. An interesting aspect of the phase diagram is the occurrence of a second order transition line in the light quark mass regime, the boundary of the region of first order phase transitions. Whether a true phase transition exists in QCD with the physically realized spectrum of quark masses or whether in this case the transition is just a (rapid) crossover, is a quantitative question which we have to answer through direct numerical calculations.

When talking about phase transition in QCD we should have in mind that a large number of new degrees of freedom gets liberated at a (phase) transition temperature; quarks and gluons which at low temperature are confined in colorless hadrons and thus do not contribute to the thermodynamics, suddenly become liberated and start contributing to bulk thermodynamic observables like the energy density or pressure. Due to asymptotic freedom the QCD pressure approaches the ideal gas value at large temperatures. In this limit the number of degrees of freedom (quarks+gluons) is much larger than the three

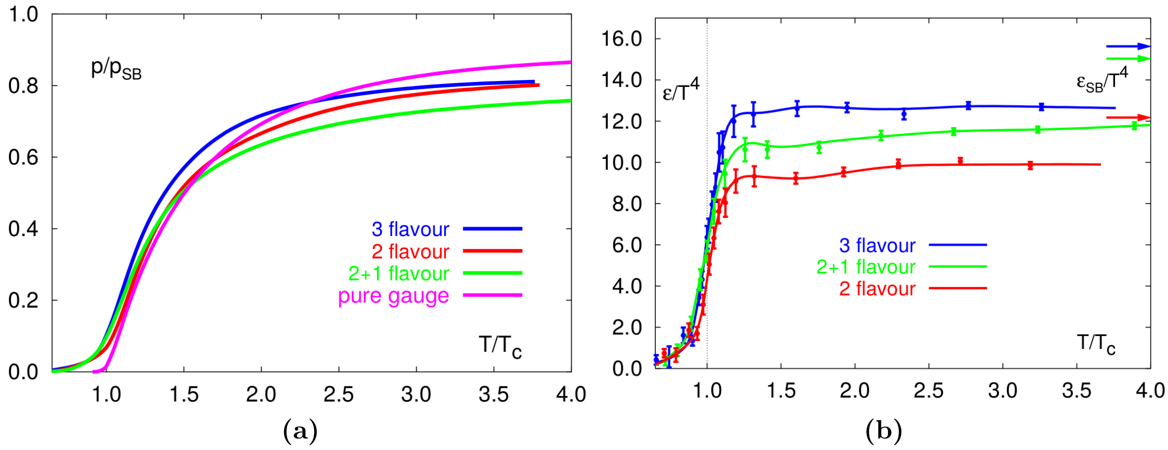

Figure 1.4.: (a)The pressure in units of the ideal gas pressure for the SU(3) gauge theory and QCD with various number of flavors. The latter calculations have been performed on lattices. (b) Energy density in units of T^4 as calculated in lattice QCD. The sharp rise at $T \sim T_c$ corresponds to the phase transition to the QGP. Figures are taken from Ref.[1]

light pions which dominate the thermodynamics at low temperature. This change of active degrees of freedom is clearly visible in calculations of e.g. the pressure in the pure gauge sector and for QCD with different numbers of flavors. Figure 1.4 (a) shows that the pressure strongly reacts to changes in the number of degrees of freedom. It is this drastic change in the behavior of the pressure or the energy density (Fig. 1.4 (b)), which indicates that the QCD transition to the plasma phase indeed is deconfining.

As discussed earlier the transition to the high temperature phase, with physical quark masses, is a continuous and non-singular phase transition. Nonetheless, this transition proceeds rather rapidly in a small temperature interval. A definite transition point thus can be identified, known as **Critical Temperature ($\mathbf{T_C}$)**. T_C can be calculated using lattice QCD but there are some uncertainties involved based on different methods. We note however, that the results obtained so far suggest that the transition temperature in (2+1)-flavor QCD is close to that of 2-flavor QCD. The 3-flavor theory, on the other hand, leads to consistently smaller values of the critical temperature. *The extrapolation of the transition temperatures to the chiral limit gave $T_C \sim$ 170 MeV for 2-flavor QCD, while this value is $\sim$ 150 MeV for 3-flavor QCD [23–25].*

1.3. Quark gluon plasma in high energy heavy ion collisions

With the advent of the high-energy colliders RHIC (the Relativistic Heavy Ion Collider operating at BNL since 2000) and the LHC (the Large Hadron Collider which started operating at CERN in 2009), the physics of relativistic heavy ion collisions has entered a new era: the energies available for the collisions are high enough — up to 200 GeV per interacting nucleon pair at RHIC and potentially up to 5.5 TeV at the LHC (although so far one has reached 'only' 2.76 TeV) — to ensure that *new forms of QCD matter*, characterized by high temperature and parton densities, are being explored by the collisions. The asymptotic freedom property of QCD implies that these high–density forms of matter are *weakly coupled* (at least in so far as their bulk properties are concerned) and hence can be studied via controlled calculations within perturbative QCD. But there are also phenomena (first revealed by the experiments at RHIC) which seem to elude a weak–coupling description and call for non–perturbative techniques [26, 27]. The ongoing experimental programs at RHIC and the LHC provide a unique and timely opportunity to test many new ideas, constrain or reject models, and orient the theoretical developments. Over the last decade, the experimental and theoretical efforts have gone hand in hand, leading to a continuously improving physical picture, which is by now well rooted in QCD.

1.3.1. Various stages of a heavy ion collision

1. Prior to the collision, and in the center-of-mass frame (which at the RHIC and at the LHC is the same as the laboratory frame), the two incoming nuclei look as two Lorentz–contracted disks, with a longitudinal extent smaller by a factor $\gamma \sim 100$ (the Lorentz boost factor) than the radial extent in the transverse plane. As we shall see, these 'disks' are mostly composed with *gluons* which carry only tiny fractions $x \ll 1$ of the longitudinal momenta of their parent nucleons, but whose density is rapidly increasing with $1/x$. This dense and weakly coupled, gluonic form of matter is known as the *Color Glass Condensate* or CGC.

2. At time $\tau = 0$, the two nuclei hit each other and the interactions start developing. The 'hard' processes, i.e. those involving relatively large transferred momenta $Q \sim 10$ GeV, are those which occur faster (within a time $\tau \sim 1/Q$). These processes

are responsible for the production of 'hard particles', i.e. particles carrying transverse energies and momenta of the order of Q. Such particles, like (hadronic) jets, direct photons, dilepton pairs, heavy quarks, or vector bosons, are generally the most important ingredients of the final state and are often used to characterize the topology of the latter.

3. At a time $\tau \sim 0.2$ fm/c, corresponding to a 'semi-hard' transverse momentum scale $Q \sim 1$ GeV, the bulk of the partonic constituents of the colliding nuclei (gluons) are liberated by the collision. This is when most of the 'multiplicity' in the final state is generated.

4. If the produced partons did not interact with each other, or if these interactions were negligible, then they would rapidly separate from each other and independently evolve (via fragmentation and hadronization) towards the final–state hadrons. This is, roughly speaking, the situation in proton–proton collisions. But the data for heavy ion collisions at both RHIC and the LHC exhibit collective phenomena (like the 'elliptic flow' to be discussed later) which clearly show that the partons liberated by the collision *do* actually interact with each other, and quite strongly. A striking consequence of these interactions is the fact that this partonic matter rapidly approaches towards *thermal equilibrium* : the data are consistent with a relatively short thermalization time, of order $\tau \sim 1$ fm/c.

5. The outcome of this thermalization process is the high–temperature phase of QCD known as the *Quark Gluon Plasma*. The abundant production and detailed study of this phase is the main aim of the heavy ion programs at RHIC and the LHC. The partonic matter keeps expanding and cooling down and it eventually hadronizes — the 'colored' quark and gluons get trapped within colorless hadrons. Hadronization occurs when the temperature becomes of the order of the critical temperature T_c. In Pb+Pb collisions at the LHC, this is estimated to happen around a time $\tau \sim 10$ fm/c.

6. For larger times $10 \leq \tau \leq 20$ fm/c, this hadronic system is still relatively dense, so it preserves local thermal equilibrium while expanding. One then speaks of a *hot hadron gas*, whose temperature and density are however decreasing with time.

7. Around a time $\tau \sim 20$ fm/c, the density becomes so low that the hadrons stop interacting with each other. That is, the collision rate becomes smaller than the expansion rate. This transition between a fluid state (where the hadrons undergo

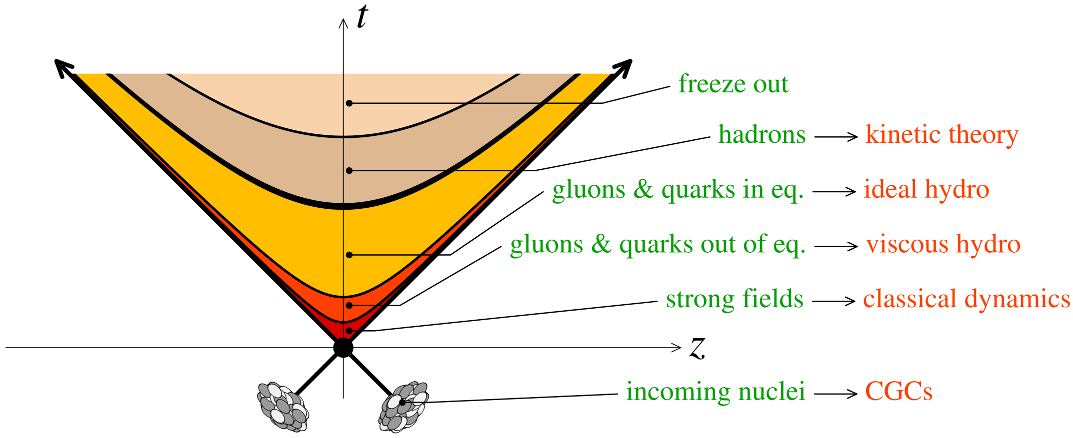

Figure 1.5.: Schematic representation of the various stages of a HIC as a function of time t and the longitudinal coordinate z (the collision axis). The 'time' variable which is used in the discussion in the text is the *proper time* $\tau \equiv \sqrt{t^2 - z^2}$, which has a Lorentz–invariant meaning and is constant along the hyperbolic curves separating various stages in this figure.

many collisions) and a system of free particles is referred to as the *freeze–out*. From that moment on, the hadrons undergo free streaming until they reach the detector.

Although extremely schematic, this simple picture of the various stages of a heavy ion collision already illustrates the variety and complexity of the forms of matter traversed by the QCD matter liberated by the collision on its way to the detectors. After years of work a Standard Model of ultra relativistic heavy ion collisions has emerged. The initial state is constructed using either the Glauber model [28] or one of the models implementing ideas originating from CGC [29]; The intermediate evolution is considered using some version of the Müller-Israel-Stewart-like theory [30, 31] of causal relativistic imperfect fluid dynamics, together with a QCD equation of state spanning partonic and hadronic phases [32]. The end evolution of the hadron-rich medium leading to a freezeout uses the Boltzmann equation in the relativistic transport theory [33]. A schematic representation of various stages of heavy ion collision is shown in Fig. 1.5.

1.4. Experimental signatures of quark gluon plasma

Experimental signatures of matter produced in relativistic heavy ion collisions can be broadly categorized in three categories.

1. **Global observables** observables like total charge particle multiplicity, Hanbury-Brown-Twiss (HBT) interferometry etc. comes under this categories.

2. **Soft Probes** probes which develop at a latter stage of collision comes under this category. These probes gives very good measurement of collectivity created in the medium. This include elliptical flow (v_2), fluctuation etc.

3. **Hard Probes** particles with high transverse momentum, which are produced very early in the collision are studied under this category. This include Jet Suppression, Nuclear modification factor of high p_T particles and Quarkonia suppression.

We will review these signatures here. Elliptic flow, jet quenching and quarkonia suppression are arguably three most important observables of quark gluon plasma. Observation of an elliptic flow almost as large as that predicted by ideal hydrodynamics led to the claim of formation of an almost perfect fluid at RHIC [34]. A natural explanation of the observed jet quenching is in terms of a dense and colored (hence partonic, not hadronic) medium that is rather opaque to high-momentum hadrons.

1.4.1. Global observables

Charge particle multiplicity distributions

The most basic quantity, and indeed the one measured within days of the first ion collision, is the number of charged particles produced per unit of (pseudo)rapidity, dN/dy ($dN_{\rm ch}/d\eta$), in a central, "head-on" collision. The value measured at LHC is $dN_{\rm ch}/d\eta \approx 1600$ [35]. From the measured multiplicity one can derive a rough estimate of the energy density with the help of a formula first proposed by Bjorken [36]. The value measured at the LHC implies that the initial energy density (at $\tau_0 = 1$ fm/c) is about 15 GeV/fm^3 [37], approximately a factor three higher than in Au+Au collisions at the top energy of RHIC (200 GeV per nucleon pair) [26, 27, 38]. The corresponding initial temperature increases by at least 30% to $T \approx 300$ MeV, even with the conservative assumption that the formation time τ_0, when thermal equilibrium is first established, remains the same as at RHIC.

The charged particle multiplicity per participant pair [39–41], $dN_{\rm ch}/d\eta/(0.5\ N_{\rm part})$, is shown in Fig. 1.6 (a) together with lower energy data [42–44] for central A+A collisions (typically 0-5% or 0-6% centrality). Particle production is no longer compatible with a logarithmic dependence with centre of mass energy per nucleon pair ($\sqrt{s_{NN}}$), as it was

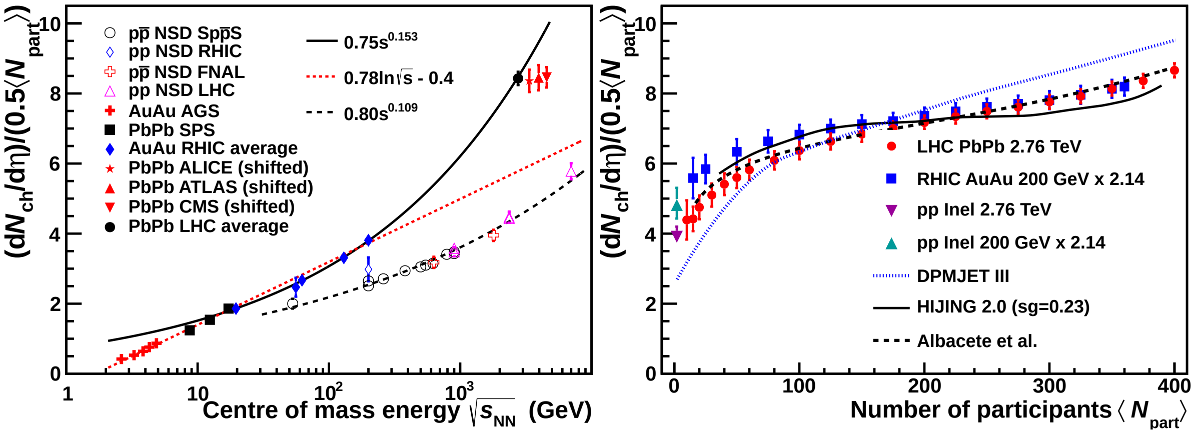

(a) (b)

Figure 1.6.: (a) Charged particle pseudorapidity density $\mathrm{d}N_{\mathrm{ch}}/\mathrm{d}\eta$ per colliding nucleon pair ($0.5N_{\mathrm{part}}$) versus center of mass energy for *pp* and A+A collisions. (b) $\mathrm{d}N_{\mathrm{ch}}/\mathrm{d}\eta$ per colliding nucleon pair versus the number of participating nucleons together with model predictions for Pb+Pb at 2.67 TeV

true for the data up to top RHIC energy [44], but follows a power law $\approx s^{0.15}$. Also the *pp* data are well described by a power law, however with a less steep dependence on energy ($\approx s^{0.11}$).

The centrality dependence of particle production is compared in Fig. 1.6 (b) with the one measured at RHIC, which is normalized to the LHC result at $N_{\mathrm{part}} = 350$ by scaling it with a factor 2.14. The results from the three LHC detectors [39–41] are in excellent agreement with each other (within 1-2%) and have been averaged in this figure. Comparison to the averaged and scaled 200 GeV Au+Au data (from [42], updated using more recent STAR [43] and PHOBOS [44] data) shows a remarkable similarity in the shape of both distributions. For peripheral collisions, however, both distributions extrapolate towards respective values measured in pp inelastic collisions ($N_{\mathrm{part}} = 2$) at 200 GeV and 2.76 TeV and therefore start to separate because of the different energy dependence seen for pp and A+A in Fig. 1.6 (a).

The fact that the shape of the normalized multiplicity distribution varies little with energy had already been noticed at RHIC [44]. It was still a surprise that it stays almost constant up to TeV energies, because hard processes, which scale with the number of binary collisions N_{coll}, could be expected to contribute significantly to particle production at LHC and lead to a steeper centrality dependence, as predicted by the two component (soft + hard) Dual Parton Model DPMJET [45] (dotted line in Fig. 1.6 (b)). However, a strong impact parameter dependent shadowing of the nuclear parton distribution function can limit this rise with centrality and is responsible for the flatter shape seen in the two component model HIJING [46], which agrees better with the data (full line). Saturation physics based on the "Color Glass Condensate" (CGC) description [47], an example of which is shown by the dashed line in Fig. 1.6 (b), predicts such a strong nuclear modification, as well as the strong rise of particle production as a function of $\sqrt{s}$ seen in Fig. 1.6 (a).

Identical particle (HBT) correlations

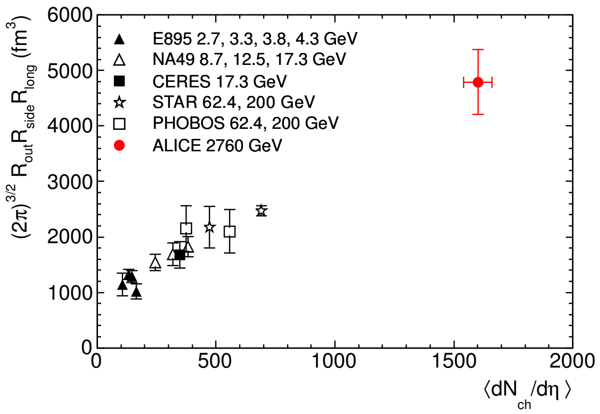

(a)

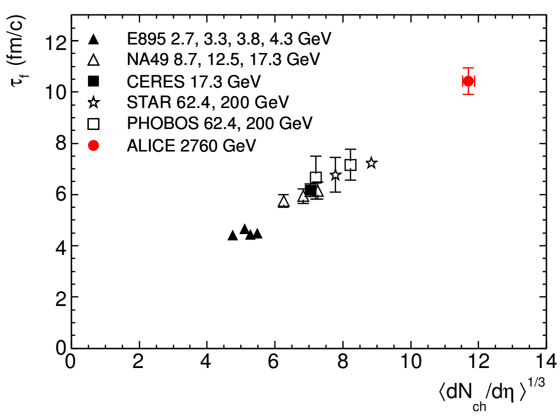

(b)

Figure 1.7.: (a) Local freeze-out volume as measured by identical pion interferometry at LHC compared to central gold and lead collisions at lower energies. (b) The system lifetime (decoupling time) τ_f compared to results from lower energies.

The freeze-out volume (the size of the matter at the time when strong interactions cease) and the total lifetime of the created system (the time between collision and freeze-out) can be measured by identical particle interferometry (also called Hanbury-Brown–Twiss or HBT correlations) [48]. For identical bosons (fermions), quantum statistics leads to an enhancement (depletion) for particles emitted close-by in phase space. This modifies the two-particle correlation function, measured in energy and momentum variables, and can be related via a Fourier transformation to the space and time distribution of the emitting source, i.e. the space-time hyper surface of last rescattering. Results from HBT correlation measurements are shown in Fig. 1.7 for central collisions from very low energies up to LHC as a function of the charged particle density $dN_{ch}/d\eta$ [49]. The total freeze-out volume is given as the product of a geometrical factor and the radii measured in three orthogonal directions (called R_{long}, R_{side}, and R_{out}), whereas the lifetime was estimated from the pair-momentum dependence of R_{long}. The locally comoving freeze-out volume is directly proportional to the particle multiplicity (Fig. 1.7 (a)) and therefore increases by a factor two compared to top RHIC energy to about 5000 fm^3. The system lifetime is proportional to the cube root of the particle density (Fig. 1.7 (b)) and increases by about 30% to 10 fm/c.

Ratio of shear viscosity and entropy density (η_s/s)

η_s/s ratio is a very important parameter to know the nature of matter produced in URHIC. This ratio is being used in hydro-dynamic calculations to explain the transport properties of Quark Gluon Plasma. This ratio is found to be very small for the matter created at RHIC. That was the reason this matter is described as almost perfect fluid. We should first understand what is meant by an almost perfect fluid. Air and water are the two most common fluids we encounter. Which of them is more viscous? Water has a higher coefficient of shear viscosity (η_s) than air, and appears more viscous. But that is misleading. To compare different fluids, one should consider their kinematic viscosities defined as η_s/ρ where ρ is the density. Air has a higher kinematic viscosity and hence is actually more viscous than water! Relativistic analogue of η_s/ρ is the dimensionless ratio η_s/s where s is the entropy density. Scaling by s is appropriate because number density is ill-defined in the relativistic case. Figure 1.8 shows constant-pressure (P_{critical}) curves for η_s/s as a function of temperature for various fluids, namely water, nitrogen, helium, and the fluid formed at RHIC. All fluids show a minimum at the critical temperature, and among them the RHIC fluid has the lowest η_s/s, even lower than that of helium. Hence it is the most perfect fluid observed so far. Although more recently, trapped ultra cold atomic systems are also shown to have η_s/s much smaller than that for helium [50]. For water, nitrogen, and helium, points to the left (right) of the minimum refer to the liquid (gaseous) phase. As T rises, η_s/s for these liquids drops, attains a minimum at the critical temperature T_C, and then in the gaseous phase it rises. This is because liquids and gases transport momentum differently [51]. RHIC fluid is an example of a strongly coupled quantum fluid and has been called sQGP to distinguish it from weakly coupled QGP (wQGP) expected at extremely high temperatures. Interestingly, the liquid formed at RHIC and LHC cools into a (hadron resonance) gas!

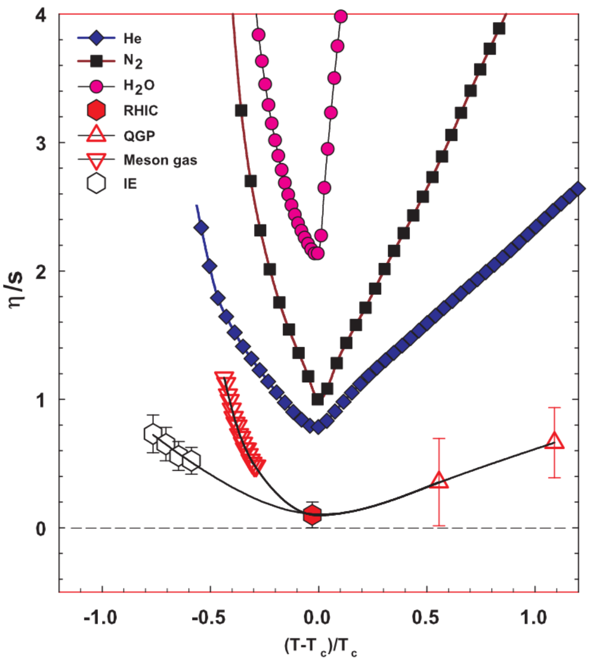

Figure 1.8.: Constant pressure (P_{critical}) curves for (shear viscosity/entropy density) vs temperature. T_0 is the critical temperature of the liquid-gas phase transition. Points labelled Meson Gas are based on chiral perturbation theory and have 50% errors (not shown). Points labelled QGP are based on lattice QCD simulations. Figure is taken from Ref. [52].

1.4.2. Soft probes

Elliptic flow

Elliptic flow is one of the most important and well studied signature of Quark Gluon Plasma. Consider a non-central (i.e. non-zero impact parameter) collision of two identical spherical nuclei traveling in opposite directions. In a non-central collision, the initial state is characterized by a *spatial anisotropy* in the azimuthal plane (Fig. 1.9). Consider particles in the almond-shaped overlap zone. Their initial momenta are predominantly longitudinal. Transverse momenta, if any, are distributed isotropically. If these particles do not interact with each other, the final (azimuthal) distribution will be isotropic. On the other hand, if they do interact with each other frequently and with adequate strength (or cross section), then the (local) thermal equilibrium is likely to be reached. The spatial anisotropy of the overlap zone ensures anisotropic pressure gradients in the transverse plane. This leads to a final state characterized by *momentum anisotropy*, an anisotropic azimuthal distribution of particles. The triple differential invariant distribution of particles emitted in the final state can be Fourier-decomposed as follows

$$E\frac{d^3N}{d^3p} = \frac{d^3N}{p_T dp_T dy d\phi} = \frac{d^2N}{p_T dp_T dy}\frac{1}{2\pi}\left[1 + \sum_{n=1}^{\infty} 2v_n \cos n(\phi - \Phi_R)\right], \tag{1.2}$$

where p_T is the transverse momentum, y the rapidity, ϕ the azimuthal angle of the outgoing particle momentum, and Φ_R the reaction-plane angle. The plane made by impact parameter and beam axis is known as reaction plane. The angle of reaction plane is not fixed in a real experiment. It is estimated using the transverse distribution of particles in the final state. The estimated reaction plane is known as event plane. The leading term in the square brackets in Eq. (1.2) represents the azimuthally symmetric radial flow. The first two harmonic coefficients v_1 and v_2 are called directed and elliptic flows, respectively. Thus v_n is a measure of the degree of thermalization of the quark-gluon matter produced in a non-central heavy-ion collision — a central issue in this field.

Figure 1.10 (a) shows the integrated elliptic flow, v_2, measured in PbPb collisions at 2.76 TeV/nucleon. The immediate conclusion to be drawn from the comparison of v_2 results measured at LHC by the ALICE, ATLAS, and CMS Collaborations to that at lower RHIC energies is that the integrated v_2 increases by 30% [53]. Figure 1.10 (b) shows the p_T differential elliptic flow, as a function of charged particles transverse momentum,

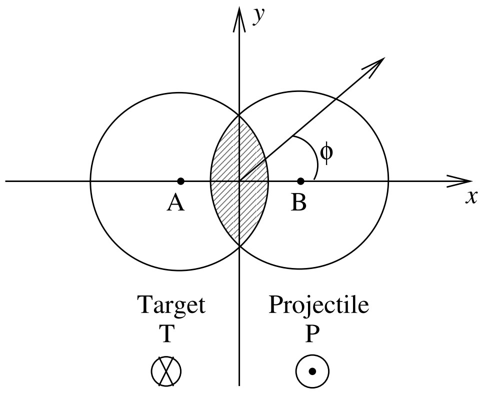

Figure 1.9.: Non-central collision of two nuclei. Collision or beam axis is perpendicular to the plane of the figure. Impact parameter b = length AB. z is the longitudinal direction, xy is the transverse or azimuthal plane, xz is the reaction plane, and ϕ is the azimuthal angle of one of the outgoing particles. The shaded area indicates the overlap zone.

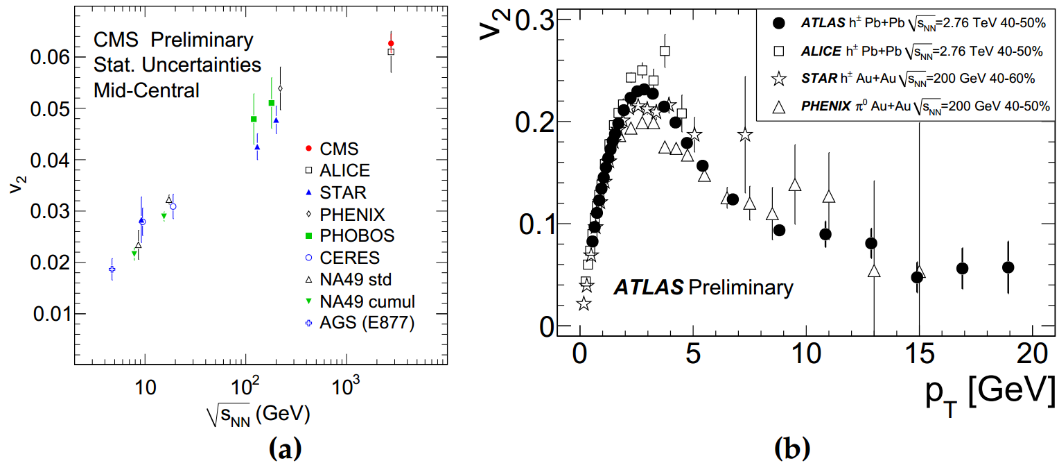

Figure 1.10.: (a)Integrated elliptic flow v_2 as a function of the collisions energy (b) v_2 as a function of transverse momentum for the 40-50% centrality range measured in heavy-ion collisions at RHIC and LHC.

p_T [54]. The results from RHIC and the LHC are similar in both magnitude and the shape of p_T dependence. This behavior is a consequence of a stronger radial flow at the LHC. The strong particle collectivity reflected by large v_2 at LHC shows that the system created in heavy-ion collision at TeV energy scale behaves as a strongly interacting, close to be a perfect fluid - similar to the properties of the QGP observed at RHIC.

Constituent quark number scaling

In the high-p_T regime, hadronization occurs by fragmentation, whereas in the medium-p_T regime, it is modelled by quark recombination or coalescence. The phenomenon of constituent quark number scaling provides experimental support to this model. Figure 1.11 explains the meaning of constituent quark number (n_q) scaling. In the left panel one sees two distinct branches, one for baryons ($n_q = 3$) and the other for mesons ($n_q = 2$). When scaled by n_q (right panel), the two curves merge into one universal curve, suggesting that the flow is developed at the quark level, and hadrons form by the merging of constituent quarks. This observation provides the most direct evidence for deconfinement so far. ALICE (LHC) has also reported results for the elliptic flow $v_2(p_T)$ of identified particles produced in PbPb collisions at 2.76 TeV. The constituent quark number scaling was found to be not as good as at RHIC[55].

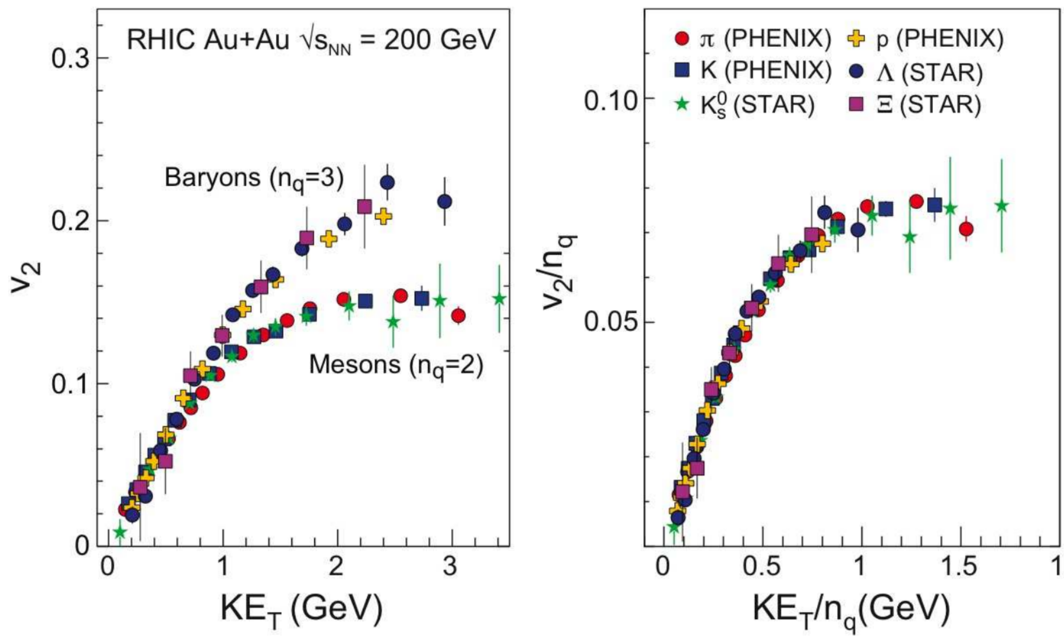

Figure 1.11.: (Left) Elliptic flow v_2 vs transverse kinetic energy KE_T for various baryons and mesons. (Right) Both v_2 and KE_T are scaled by the number of constituent quarks n_q. Figure is taken from Ref. [56].

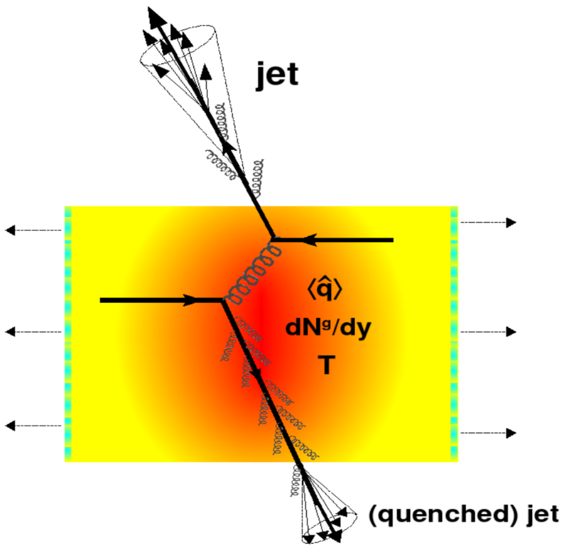

Figure 1.12.: "Jet quenching" in a head-on nucleus-nucleus collision. Two quarks suffer a hard scattering: one goes out directly to the vacuum, radiates a few gluons and hadronises, the other goes through the dense plasma created (characterised by transport coefficient $\langle \hat{q} \rangle$, gluon density $\frac{dN^g}{dy}$ and temperature T), suffers energy loss due to medium-induced gluonstrahlung and finally fragments outside into a (quenched) jet.

1.4.3. Hard probes

Jet quenching

High transverse momentum partonic interactions in perturbative quantum chromodynamics (pQCD) leads to a production of two highly virtual back-to-back partons which subsequently evolve as parton showers, hadronize, and are experimentally observed as back-to-back di-jet events in the detector. If the partons traverse on their path a dense colored medium they will loose energy (Fig. 1.12). The result of the energy loss can be detected as modifications of jet yields and jet properties. This phenomenon is commonly referred to as the jet quenching.

Jet quenching at RHIC is measured by dihadron angular correlations. Figure 1.13 (a) and 1.13 (b) shows dihadron angular correlations measured by STAR experiment at RHIC as a function of the opening angle between the trigger and associated particles. The only difference between these figures is the definition of the associated particles. Figure 1.13 (a) shows the suppression of the away-side jet in AuAu central, but not in pp and dAu central collisions. This is expected because unlike AuAu collisions, no hot and dense medium is likely to be formed in pp and dAu collisions, and so there is no quenching of the away-side jet. Energy of the away-side parton in a AuAu collision is dissipated in the medium thereby producing low-p_T or soft particles. When even the soft particles are included, the away-side jet reappears in the AuAu data as shown in the Figure 1.13 (b) . Its shape is broadened due to interactions with the medium.

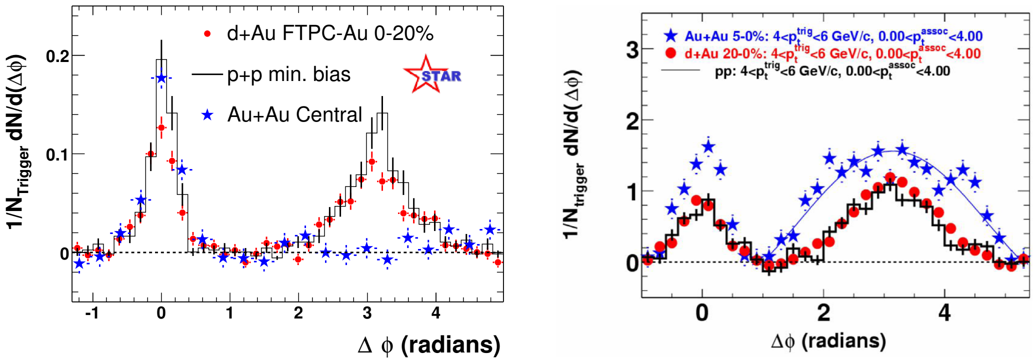

(a) (b)

Figure 1.13.: (a) STAR data on dihadron angular correlations. $\Delta\phi$ is the opening angle between the trigger ($4 < p_T^{trig} < 6$ GeV/c) and associated particles ($2 < p_T^{assoc} < p_T^{trig}$ GeV/c). Figure from Ref.[57]. (b)Similar to the panel (a), except that $0 < p_T^{assoc} < 4$ GeV/c. Figure from the data presented in Ref.[58].

The first experimental evidence of the jet quenching at LHC has been observed in the measurement of the di-jet asymmetry [7, 59]. The di-jet asymmetry has been defined as

$$A_J = \frac{E_{T,1} - E_{T,2}}{E_{T,1} + E_{T,2}} \tag{1.3}$$

where $E_{T,1}$ and $E_{T,2}$ is the transverse energy of the leading and sub leading jet in the event. Energy loss of parent partons in the created matter may reduce or "suppress" the rate for producing jets at a given E_T. This suppression is expected to increase with medium temperature and with increasing path length of the parton in the medium. As a result, there should be more suppression in central Pb+Pb collisions which have nearly complete overlap between incident nuclei, and little or no suppression in peripheral events where the nuclei barely overlap. This was indeed observed in the measurement of di-jet asymmetry where the jet suppression exhibits itself by an increase of the number of events with larger jet asymmetry compared to Monte-Carlo (MC) reference and pp collisions. Figure 1.14 shows the di-jet asymmetry A_J measured by CMS experiment at LHC [7]. In central heavy ion collisions an excess of events with large di-jet asymmetry has been observed when compared to pp or Pb+Pb MC reference. Pythia events embedded in real heavy ion data are used as Pb+Pb MC. This asymmetry has been accompanied by a balance in azimuth, that is jets in the di-jet system remain "back-to-back despite to a sizable modification of their energy. The original [7,59] and updated [60,61] experimental observation was followed by theoretical work [9,62,63] suggesting that the suppression can be explained in terms of radiative and collisional energy loss of partons propagating through the QCD medium.

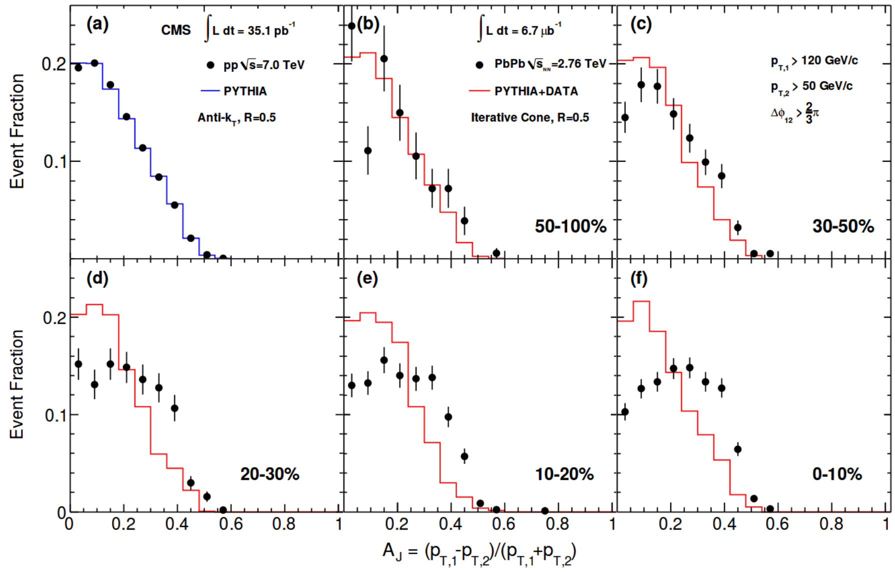

Figure 1.14.: Dijet asymmetry ratio,A$_J$, for leading jets of p$_{T,1}$ > 120 GeV/c, subleading jets of p$_{T,2}$ > 50 GeV/c and $\Delta\phi_{12} > 2\pi/3$ for 7 TeV pp collisions (a) and 2.76 TeV PbPb collisions in several centrality bins: (b) 50–100%, (c) 30–0%, (d) 20–30%, (e) 10–20% and (f) 0–10%. Data are shown as black points, while the histograms show (a) PYTHIA events and (b)-(f)PYTHIA events embedded into PbPb data. The error bars show the statistical uncertainties. Figure is take from Ref.[7].

Single particle nuclear modification factor

The suppression effects of a given particle are typically expressed in terms of the nuclear modification ratio:

$$R_{AA}(p_T) = \frac{d^2N_{AA}/dp_Td\eta}{\langle T_{AA}\rangle d^2\sigma_{NN}/dp_Td\eta}, \tag{1.4}$$

where N_{AA} and σ_{NN} represent the particle yield in nucleus-nucleus collisions and the cross section in nucleon-nucleon collisions, respectively. The nuclear overlap function $\langle T_{AA}\rangle$ is the ratio of the number of binary nucleon-nucleon collisions, $\langle N_{\text{coll}}\rangle$, calculated from the Glauber model, and the inelastic nucleon-nucleon cross section. In the absence of nuclear effects the nuclear modification factor (R_{AA}) is unity by construction. Figure 1.15 (a) shows nuclear modification ratio (R_{AA}) as a function of p_T for π^0, η meson and direct photon measured by PHENIX experiment at RHIC [64]. As evident from the Fig. 1.15 (a) the single particle production rates at RHIC have shown a large suppression of hadrons in nuclear collisions relative to pp, whereas particles that do not interact strongly, e. g. photons, are not modified. The LHC has significantly extend the accessible p_T range and allow the measurement of additional particles, such as the Z^0 and W.

A summary of R_{AA} measurements for different particle species measured at LHC is shown in Fig. 1.15 (b) and Fig. 1.15 (c). The inclusive charged particle R_{AA} follows, up to about $10-15$ GeV/c, the characteristic shape discovered at RHIC (Fig. 1.15 (b) , full circles). The pronounced maximum at a few GeV/c, which is sometimes attributed to initial or final state interactions in nuclei ("Cronin effect"), is at very high energies more likely to be yet another manifestation of collective flow. It is qualitatively described by the dashed line, which shows the R_{AA} obtained by dividing the inclusive charged particle distribution calculated by viscous hydrodynamics [65] for central Pb+Pb by the experimentally measured pp spectrum. This interpretation is also supported by the fact that the apparent "suppression" factor is slightly larger for kaons and significantly larger for the Λ, as expected from flow. The peak region is followed by a steep decline and a minimum, around $5-7$ GeV/c, where the suppression reaches a factor of about seven, very similar to but slightly larger than the one measured at RHIC.

Heavy quarks, as shown by the R_{AA} of prompt D mesons (open squares) and non-prompt J/ψ (from the decay of bottom quarks, closed diamond) in Fig. 1.15 (b), are almost as strongly suppressed as inclusive charged particles. A similar conclusion can be drawn from the measurement of leptons from heavy flavor decays [66]. This seems contrary to the expectation that gluons, which are the dominant source of inclusive charged particles at LHC, should suffer twice as much energy loss as light quarks and that, in addition, the energy loss of heavy quarks should be even less than that of light quarks because of the mass dependence of radiation ("dead-cone" effect [67]). The strong suppression found for hadrons containing c- and b-quarks confirms observations made at RHIC and may indicate that the energy loss rate depends less strongly on the parton mass than expected for radiative energy loss.

Above $p_T \approx 8$ GeV/c, the suppression becomes universal for all particle species (with the possible exception of the non-prompt J/ψ originating from B-meson decays shown in the Fig. 1.15 (b)). With increasing p_T, R_{AA} rises gradually towards a value of 0.5 (Fig. 1.15 (c)), a feature which was not readily apparent in the RHIC data. Isolated photons and the Z^0 boson are not suppressed, within the currently still large statistical errors[68, 69]. This finding is consistent with the hypothesis that the suppression observed for hadrons is due to final-state interactions with the hot medium.

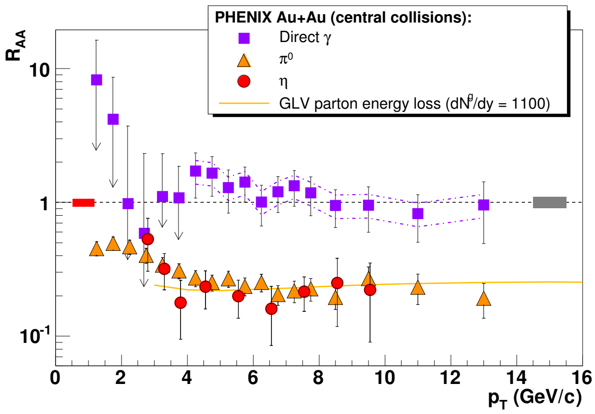

(a)

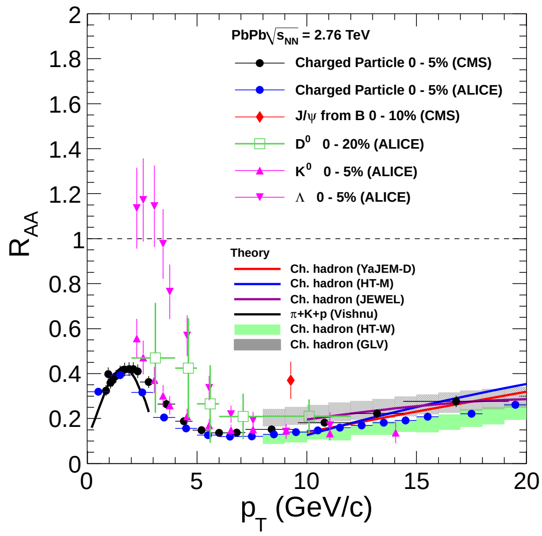

(b)

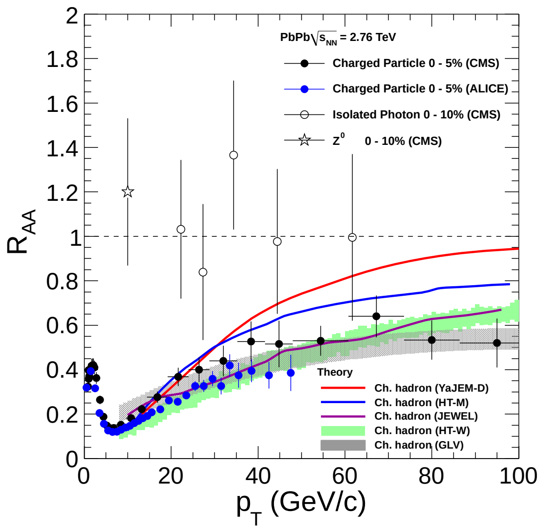

(c)

Figure 1.15.: Nuclear modification factor R_{AA} as a function of p_T for a variety of particle species together with theoretical predictions at RHIC and LHC. (a) AuAu central collision data on nuclear modification factor R_{AA} as a function of p_T, at the center-of-mass energy $\sqrt{s_{NN}} = 200$ GeV. Dash-dotted lines: theoretical uncertainties in the direct photon R_{AA}. Solid yellow line: jet-quenching calculation of [70, 71] for leading pions in a medium with initial effective gluon density $dN^g/dy = 1100$. Error bands at $R_{AA} = 1$ indicate the absolute normalization errors. Figure from [64] (b) Low momentum region $p_T < 20$ GeV; (c) Entire momentum range measured at LHC. The curves show the results of various QCD-based models of parton energy loss. For details, see text and Ref.[72].

The observed trend is semi-quantitatively described by several models implementing the perturbative QCD (pQCD) formalism for energy loss [73–77]. The qualitative success of several models in correctly reproducing the rise and saturation of R_{AA} with p_T suggests that the energy loss of the leading parton in a jet shower may be described by perturbative QCD radiation in a strongly coupled medium.

Quarkonia suppression

Typical hard probe particles have only one "hard" scale characterized by their high energy, therefore they are not particularly sensitive to physics at the energy scale of medium temperature, T. However there exists one special hard probe particle which has an additional (softer) energy scale (on the order of T) making it very sensitive to physics at the medium temperature. This probe is the measurement of quarkonium. Quarkonia are important probes of the quark gluon plasma since they are produced early in the collision and their survival is affected by the surrounding medium. The bound states of charm and bottom quarks are predicted to be suppressed in heavy ion collisions in comparison with pp, primarily as a consequence of deconfinement (melting) in the QGP. Thus measurement of a suppressed quarkonium yield may provide direct experimental sensitivity to the temperature of the medium created in high energy heavy ion collisions. Measurement of Υ suppression is main subject of the thesis. Status of quarkonia production and suppression in pp, pPb and PbPb collisions is reviewed in Chapter 2.

1.4.4. RHIC-LHC comparison

Table 1.3 compares some basic results obtained at LHC, with similar results obtained earlier at RHIC. Here $dN_{ch}/d\eta$ is the charged particle pseudorapidity density, at mid-rapidity, normalized by $\langle N_{part}\rangle/2$ where $\langle N_{part}\rangle$ is the mean number of participating nucleons in a nucleus-nucleus collision, estimated using the Glauber model [28]. ϵ_{Bj} is the initial energy density estimated using the well-known Bjorken formula [36]. τ_i is the initial or formation time of QGP. Assuming conservatively the same $\tau_i \simeq 0.5$ fm at LHC as at RHIC, one gets an estimate of ϵ_{Bj} at LHC. T_i is the initial temperature fitted to reproduce the observed multiplicity of charged particles in a hydrodynamical model. Note that the $\sim 30\%$ increase in T_i is consistent with the factor of ~ 3 rise in ϵ_{Bj}. $V_{f.o.}$ is the volume of the system at the freezeout, measured with two-pion Bose-Einstein

Table 1.3.: RHIC-LHC comparison

	RHIC (AuAu)	LHC (PbPb)	Increase by factor or %
$\sqrt{s_{NN}}$ (GeV)	200	2760	14
$dN_{ch}/d\eta/\left(\frac{<N_{part}>}{2}\right)$	3.76	8.4	2.2 [39–41]
$\epsilon_{Bj}\tau_i$ (GeV/fm^2)	16/3	16	3
ϵ_{Bj} (GeV/fm^3)	10	30	3
T_i (MeV)	360	470	30%
$V_{f.o.}$ (fm^3)	2500	5000	2
Lifetime (fm/c)	8.4	10.6	26%
v_{flow}	0.6	0.66	10%
$< p_T >_\pi$ (GeV)	0.36	0.45	25%
Differential $v_2(p_T)$			unchanged
p_T-integrated v_2			30% [53]

correlations. v_{flow} is the radial velocity of the collective flow of matter. v_2 is the elliptic flow. It is clear from Table 1.3 that the QGP fireball produced at LHC is hotter, larger, and longer-lasting, as compared with that at RHIC.

1.4.5. Status of quark gluon plasma

(1) Quark-gluon plasma has been discovered, and we are in the midst of trying to determine its thermodynamic and transport properties accurately.

(2) Data on the collective flow at RHIC/LHC have provided a strong support to hydrodynamics as the appropriate effective theory for relativistic heavy-ion collisions. The most complete event-to-event hydrodynamic calculations to date [78, 79] have yielded $\eta/s = 0.12$ and 0.20 at RHIC (AuAu, 200 GeV) and LHC (PbPb, 2.76 TeV), respectively, with at least 50% systematic uncertainties. These are the average values over the temperature histories of the collisions. Uncertainties associated with (mainly) the initial conditions have so far prevented a more precise determination of η/s.

(3) Surprisingly, even the *pp* collision data at 7 TeV are consistent with the hydrodynamic picture, if the final multiplicity is sufficiently large!

(4) An important open question is at what kinematic scale partons lose their quasi particle nature (evident in jet quenching) and become fluid like (as seen in the collective flow)?

(5) QCD phase diagram still remains largely unknown.

(6) RHIC remains operational. ALICE, ATLAS, and CMS at LHC all have come up with many new results on heavy-ion collisions. Further updates of these facilities are planned or being proposed. Compressed baryonic matter experiments at FAIR [80] and NICA [81], which will probe the QCD phase diagram in a high baryon density but relatively low temperature region, are a few years in the future. Electron-ion collider (EIC) has been proposed to understand the glue that binds us all [82]. So this exciting field is going to remain very active for a decade at least.

1.5. Outline of thesis

The thesis is organized as follows. In Chapter 2 we review quarkonium production and properies. Experimental status of quarkonia measurements at SPS, RHIC and LHC is reviewed. Chapter 3 gives an overview of the CMS detector and its main components. Chapter 4 and Chapter 5 describes the measurement of Υ production and suppression in PbPb collisions using the data collected by CMS experiment during first and second heavy ion runs. Relative suppression of excited Upsilon states (Υ(2S) and Υ(3S)) as well as absolute suppression of all three Υ states (Υ(1S), Υ(2S) and Υ(3S)) is discussed in detail. Υ suppression in pPb collisions is described in Chapter 6. Cross section ratios of Υ states and their dependence on event activity variables is discussed. This thesis consist of measurements as well as theoretical calculations. Chapter 7 outline calculations of different components of dilepton continuum in PbPb collisions at $\sqrt{s_{NN}} = 2.76$ TeV. Calculations for quarkonia suppression due to gluon dissociation in PbPb collisions at $\sqrt{s_{NN}} = 2.76$ TeV are described in Chapter 8. Effect of both hot and cold nuclear matter are taken in to account. Calculations are compared with the measurements at LHC. Chapter 9 gives summary and outlook.

Chapter 2.

Quarkonia : production and properties

This chapter describes quarkonia production and properties in hot and cold nuclear matter. Experimental status of quarkonia production and suppression in pp, pA and AA collisions is reviewed at SPS (Super Proton Synchrotron), RHIC and LHC energies.

2.1. The discovery of quarkonia

The J/ψ meson was discovered virtually simultaneously at Brookhaven National Laboratory and at the Stanford Linear Accelerator Center in 1974 [83, 84]. The BNL group used the reaction

$$p + Be \rightarrow J/\psi + X \rightarrow e^{+} + e^{-} + X$$

while the SLAC group used

$$e^{+} + e^{-} \rightarrow J/\psi \rightarrow \text{hadrons},\ e^{+}e^{-},\ \mu^{+}\mu^{-}.$$

At that time, the world was expected to consist of up, down and strange quarks plus electrons and muons. In addition a fourth quark was predicted by the Glashow-Iliopoulos-Maiani (GIM) mechanism [85]. Soon after the first observation it became clear that the newly discovered particle consisted of the predicted quark species, the charm quarks. This event is known as November revolution in particle physics. This discovery added a new particle to the fundamental building blocks of nature. In addition, the description

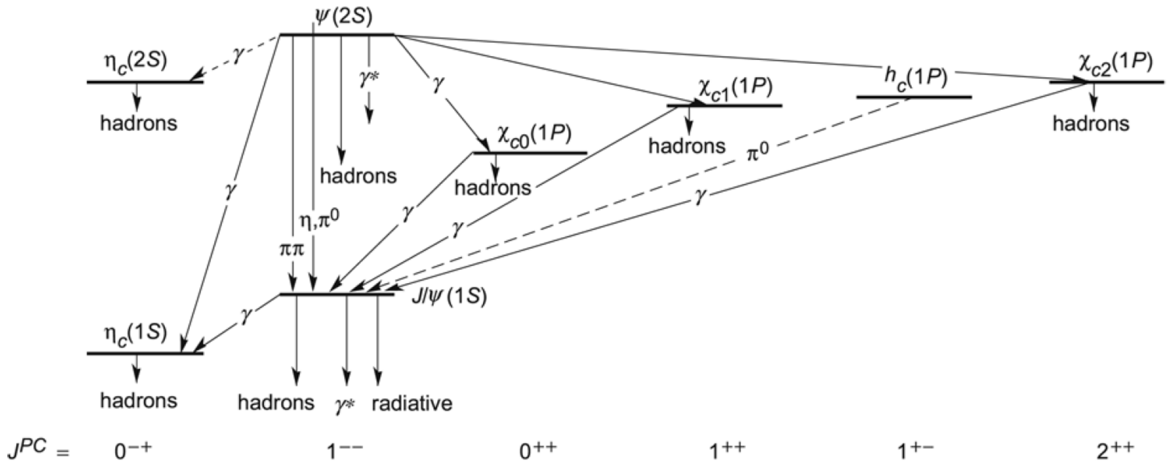

Figure 2.1.: Charmonium mass levels and spin states. Common feed down channels are indicated by arrow.

of the small width of the observed peak, 93.4 ± 1.2 keV [86], was one of the first big successes of QCD, a theory still relatively new at that time.

Three years later another sharp resonance in the dimuon spectrum was discovered in proton-nucleus collisions [87], the Upsilon (Υ). This time the surprise in the physics community was not as large since the third lepton, the τ, was discovered in the mean-time and for symmetry reasons one expected a third quark family. The heaviest quark, the top quark, was discovered in 1995 [88]. This discovery completed the three quark families. Up, down and strange quarks are commonly called light quarks, while the charm, bottom and top are referred to as heavy quarks. The bound state of these heavy quarks with their corresponding anti-particle is known as *quarkonia*. A heavy quark-anti-quark pair is able to form more then one bound state. Apart from the J/ψ and the Υ higher excited states exist, forming the so-called J/ψ and the Υ families. Figure 2.1 and 2.2 shows all bound states of $c\bar{c}$ and $b\bar{b}$ below the heavy flavor threshold [89].

2.2. Quarkonia production

In general one can subdivide the quarkonia production process into two major parts

1. Production of a heavy quark pair in hard collisions.
2. Formation of quarkonia out of the two heavy quarks.

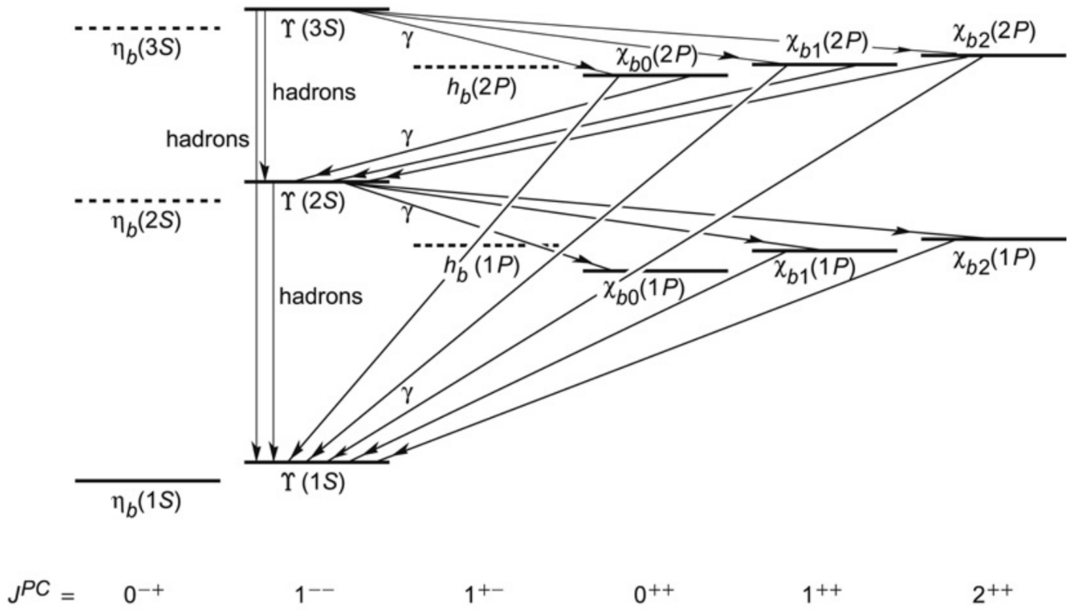

Figure 2.2.: Bottomonium mass levels and spin states. The common feed down channels are indicated by arrow.

First process can be calculated by the perturbative QCD calculations while the formation of quarkonia out of the two heavy quarks is a non purterbative process and require some effective theories for modeling. These processes will be explained in detail in next sections.

2.2.1. Production of a heavy quark pair in hard collisions

Due to the high mass of the heavy quarks ($\mathrm{m_c} \sim 1.3\ \mathrm{GeV/c^2}$, $\mathrm{m_b} \sim 4.7\ \mathrm{GeV/c^2}$), they can be produced only during the first phase of a collision. Only at that time the elementary collisions with sufficiently high momentum transfers (to create such high masses) takes place. For this reason the heavy quark production is a hard process that can be treated perturbatively. The hadronic cross section in *pp* collisions can be written as

$$\sigma_{pp}(s, m^2) \;\; = \sum_{i,j=q,\overline{q},g} \int dx_1\, dx_2\, f_i^p(x_1, \mu_F^2)\, f_j^p(x_2, \mu_F^2)\, \widehat{\sigma}_{ij}(s, m^2, \mu_F^2, \mu_R^2) \qquad (2.1)$$

where x_1 and x_2 are the fractional momenta carried by the colliding partons and f_i^p are the proton parton densities. The total partonic cross section has been completely calculated up to NLO [90, 91]. The partonic cross section is given by

$$\begin{aligned}\widehat{\sigma}_{ij}(s, m, \mu_F^2, \mu_R^2) &= \frac{\alpha_s^2(\mu_R^2)}{m^2}\Big\{f_{ij}^{(0,0)}(\rho) \\ &+ 4\pi\alpha_s(\mu_R^2)\left[f_{ij}^{(1,0)}(\rho) + f_{ij}^{(1,1)}(\rho)\ln\left(\frac{\mu_F^2}{m^2}\right)\right] + \mathcal{O}(\alpha_s^2)\Big\} \qquad (2.2)\end{aligned}$$

where $\rho = 4m^2/s$ and $f_{ij}^{(k,l)}$ are the scaling functions to NLO [90, 91]. At small ρ, the $\mathcal{O}(\alpha_s^2)$ and $\mathcal{O}(\alpha_s^3)$ $q\overline{q}$ and the $\mathcal{O}(\alpha_s^2)$ gg scaling functions become small while the $\mathcal{O}(\alpha_s^3)$ gg and qg scaling functions plateau at finite values. Thus, at collider energies, the total cross sections are primarily dependent on the small x parton densities and phase space. The total cross section does not depend on any kinematic variables, only on the quark mass, m, and the renormalization and factorization scales with central value $\mu_{R,F} = \mu_0 = m$. The energy dependence of the charm and bottom total cross sections is shown in Figs. 2.3 and 2.4 respectively. The theoretical uncertainty bands for the two distributions is obtained by summing the mass and scale uncertainties in quadrature. The central value of the band is indicated by the solid curve while the upper and lower edges of the band are given by the dashed curves.

The dotted curves in Fig. 2.3 are calculated with $\mu_F = \mu_R = 2m$ and $m = 1.2$ GeV, used in Ref. [92, 93]. Note that the charm uncertainty band broadens as the energy increases. The lower edge of the charm band grows more slowly with $\sqrt{s}$ above RHIC energies while the upper edge is compatible with the reported total cross sections at RHIC [94, 95]. The total charm production cross section measured by PHENIX experiment at RHIC is $\sigma^{c\overline{c}} = 567 \pm 57^{\text{stat.}} \pm 224^{\text{syst.}}$ [95].

Figure 2.4 shows the NLO total $b\bar{b}$ cross sections as a function of $\sqrt{s}$ calculated with the CTEQ6M parton densities. The solid red curve is the central value (μ_F/m, μ_R/m) = (1, 1) with $\mathrm{m_b}$ = 4.75 GeV. The green and blue solid curves are $\mathrm{m_b}$ = 4.5 and 5 GeV with (1,1) respectively. The red, blue and green dashed curves correspond to (0.5,0.5), (1,0.5) and (0.5,1) respectively while the red, blue and green dotted curves are for (2,2), (1,2) and (2,1) respectively, all for $\mathrm{m_b}$ = 4.75 GeV.

2.2.2. Formation of quarkonia out of the two heavy quarks

The nonperturbative evolution of the $Q\bar{Q}$ pair into a quarkonium has been discussed extensively in terms of models and in terms of the language of effective theories of QCD [96, 97]. Different treatments of this evolution have led to various theoretical models

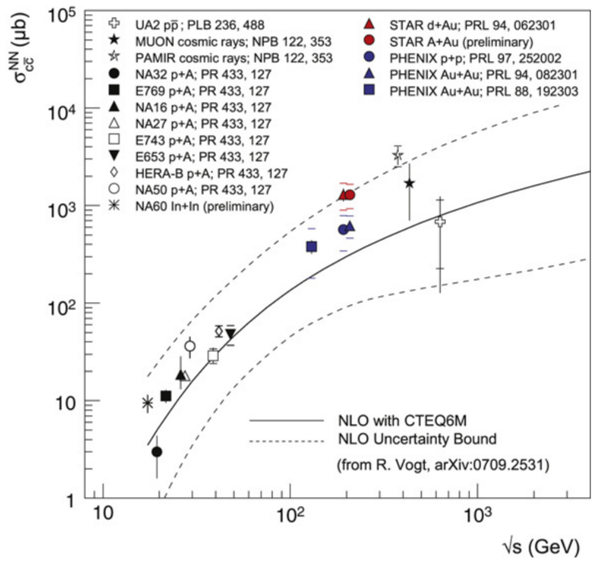

Figure 2.3.: Comparison of total cross section measurements. The STAR and PHENIX results are given as cross section per binary collisions. Vertical lines reflect the statistical errors, horizontal bars indicate the systematic uncertainties (where available). The NLO calculations and the depicted uncertainty bands are described in text.

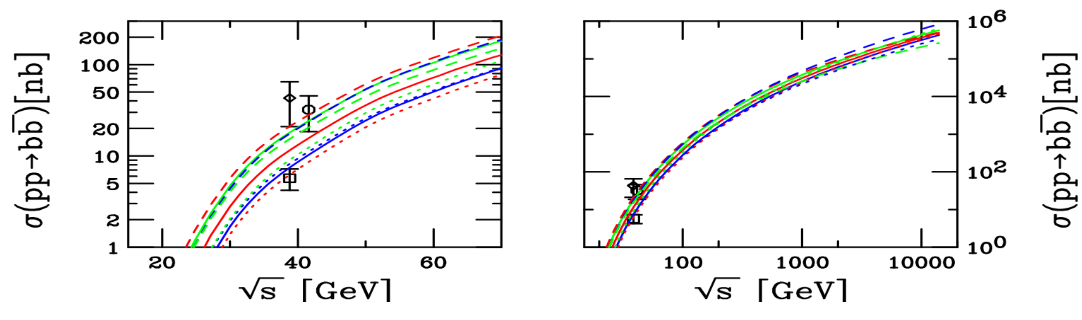

Figure 2.4.: The NLO total $b\bar{b}$ cross sections as a function of $\sqrt{s}$ for $\sqrt{s} \leq 70$ GeV (left-hand side) and up to 14 TeV (right-hand side) calculated with the CTEQ6M parton densities. The solid red curve is the central value other curves indicates theoretical uncertainties as explained in text.

for inclusive quarkonium production. Most notable among these are the color-singlet model (CSM), the color-evaporation model (CEM), the non-relativistic QCD (NRQCD) factorization approach, and the fragmentation-function approach.

The color singlet model

The CSM was first proposed shortly after the discovery of the J/ψ [98–101]. In this model, it is assumed that the $Q\bar{Q}$ pair that evolves into the quarkonium is in a color-singlet state and that it has the same spin and angular-momentum quantum numbers as the quarkonium. In the CSM, the production rate for each quarkonium state is related to the absolute values of the color-singlet $Q\bar{Q}$ wave function and its derivatives, evaluated at zero $Q\bar{Q}$ separation. These quantities can be extracted by comparing theoretical expressions for quarkonium decay rates in the CSM with experimental measurements. Once this extraction has been carried out, the CSM has no free parameters. The CSM was successful in predicting quarkonium production rates at relatively low energy [102]. Recently, it has been found that, at high energies, very large corrections to the CSM appear at next-to-leading order (NLO) and next-to-next-to-leading order (NNLO) in α_s [103–105]. Consequently, the possibility that the CSM might embody an important production mechanism at high energies has re-emerged. However, given the very large corrections at NLO and NNLO, it is not clear that the perturbative expansion in α_s is convergent. As we will describe below, the NRQCD factorization approach encompasses the color-singlet model, but goes beyond it.

The color evaporation model

The CEM [106–108] is motivated by the principle of quark-hadron duality. In the CEM, it is assumed that every produced $Q\overline{Q}$ pair evolves into a quarkonium if it has an invariant mass that is less than the threshold for producing a pair of open-flavor heavy mesons. It is further assumed that the nonperturbative probability for the $Q\overline{Q}$ pair to evolve into a quarkonium state H is given by a constant F_H that is energy-momentum and process independent. Once F_H has been fixed by comparison with the measured total cross section for the production of the quarkonium H, the CEM can predict, with no additional free parameters, the momentum distribution of the quarkonium production rate. The CEM predictions provide good descriptions of the CDF data for J/ψ, $\psi(2S)$, and χ_c production at $\sqrt{s} = 1.8$ TeV [108].

The NRQCD factorization approach

The NRQCD factorization approach expresses the probability for a $Q\overline{Q}$ pair to evolve into a quarkonium in terms of matrix elements of NRQCD operators. These matrix elements can be characterized in terms of their scaling with the heavy-quark velocity v [96]. In the NRQCD factorization approach, the inclusive cross section for the direct production of a quarkonium state H is written as a sum of products of these NRQCD matrix elements with the corresponding $Q\overline{Q}$ production cross sections:

$$\sigma(H) = \sum_n \sigma_n(\Lambda)\langle \mathcal{O}_n^H(\Lambda)\rangle \,. \tag{2.3}$$

Here Λ is the ultraviolet cutoff of the effective theory. The σ_n are, expansions in powers of v, of the cross sections to produce a $Q\overline{Q}$ pair in the color, spin, and orbital-angular momentum state n. The σ_n are convolutions of parton-level cross sections at the scale p with parton distribution functions. The matrix elements $\langle \mathcal{O}_n^H(\Lambda)\rangle$ are vacuum-expectation values of four-fermion operators in NRQCD. We emphasize that Eq. (2.3) represents both processes in which the $Q\bar{Q}$ pair is produced in a color-singlet state and processes in which the $Q\bar{Q}$ pair is produced in a color-octet state. Unlike the CSM and the CEM expressions for the production cross section, the NRQCD factorization formula for heavy-quarkonium production depends on an infinite number of unknown matrix elements. However, the sum in Eq. (2.3) can be organized as an expansion in powers of v. Hence, the NRQCD factorization formula is a double expansion in powers of v and powers of α_s. In phenomenological applications, the sum in Eq. (2.3) is truncated at a fixed order in v, and only a few matrix elements typically enter into the phenomenology. The predictive power of the NRQCD factorization approach is based on the validity of such a truncation, as well as on perturbative calculability of the $Q\overline{Q}$ cross sections and the universality of the long-distance matrix elements. Although the application of NRQCD factorization to heavy-quarkonium production processes has had many successes, there remain a number of discrepancies between its predictions and experimental measurements.

The fragmentation function approach

In the fragmentation-function approach the inclusive quarkonium production cross sections is written in terms of convolutions of parton production cross sections with light-cone fragmentation functions [109, 110]. This procedure provides a convenient way to organize the contributions to the cross section in terms of powers of m_Q/p. The contribution to the cross section at the leading power in m_Q/p_T is given by the production of a single parton (*e.g.*, a gluon), at a distance scale of order $1/p_T$, which subsequently fragments into a heavy quarkonium [111]. The contribution to the cross section at the first sub-leading power in m_Q/p_T is given by the production of a $Q\bar{Q}$ pair in a vector- or axial-vector state, at a distance scale of order $1/p_T$, which then fragments into a heavy quarkonium. It was shown in the perturbative-QCD factorization approach [109] that the production cross section can be factorized as

$$\begin{aligned} d\sigma_{A+B\to H+X}(p_T) = & \\ & \sum_i d\hat{\sigma}_{A+B\to i+X}(p_T/z,\mu)\otimes D_{i\to H}(z,m_Q,\mu) \\ & + \sum_{[Q\bar{Q}(\kappa)]} d\hat{\sigma}_{A+B\to [Q\bar{Q}(\kappa)]+X}(P_{[Q\bar{Q}(\kappa)]}=p_T/z,\mu) \\ & \qquad \otimes D_{[Q\bar{Q}(\kappa)]\to H}(z,m_Q,\mu) \\ & + \mathcal{O}(m_Q^4/p_T^4)\,, \end{aligned} \tag{2.4}$$

where the first term in Eq. (2.4) gives the contribution of leading power in m_Q/p, and the second term gives the first contribution of sub-leading power in m_Q/p. A and B are the initial particles in the hard-scattering process and $\otimes$ represents a convolution in the momentum fraction z. In the first term in Eq. (2.4), the cross section for the inclusive production of a single particle i, $d\hat{\sigma}_{A+B\to i+X}$, contains all of the information about the incoming state and includes convolutions with parton distributions in the cases in which A or B is a hadron. The quantity $D_{i\to H}$ is the fragmentation function for an off-shell parton of flavor i to fragment into a quarkonium state H [112]. The argument m_Q indicates explicitly the dependence of $D_{i\to H}$ on the heavy-quark mass. The predictive power of the factorization formula in Eq. (2.4) relies on the perturbative calculability of the single-particle inclusive and $Q\bar{Q}$ inclusive cross sections and the universality of the fragmentation functions.

In summary we can say that one of the crucial theoretical issues in quarkonium physics is the validity of models in predicting quarkonia production cross-section and its kinematic dependence.

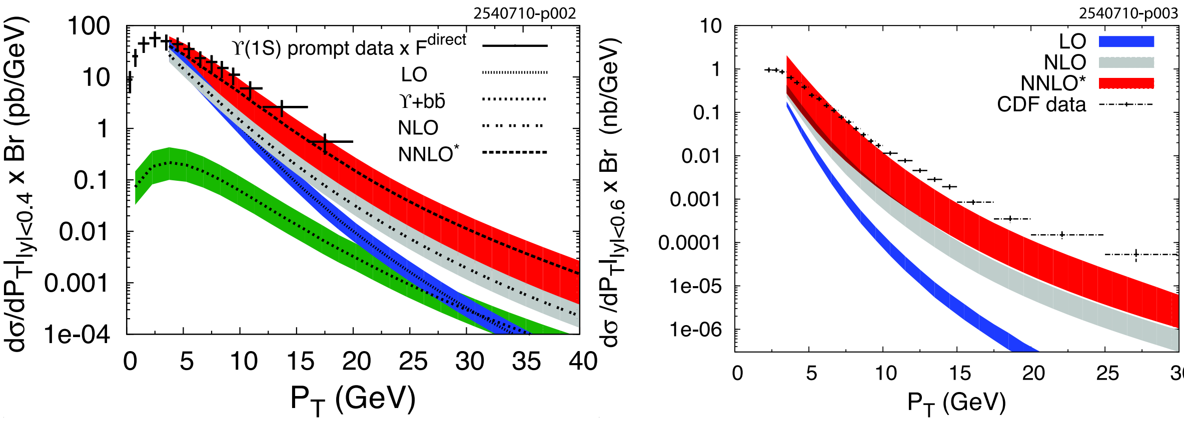

(a) (b)

Figure 2.5.: (a) Comparison between the CSM predictions at NLO and NNLO* accuracy for the Υ cross section as a function of the transverse momentum measured by CDF experiment at the Tevatron. The crosses are the CDF data for prompt $\Upsilon(1S)$ production, multiplied by F^{direct}, the fraction of direct $\Upsilon(1S)$'s in prompt $\Upsilon(1S)$ events. The *lines* show the central values of the theoretical predictions, and the *bands* depict the theoretical uncertainties [105]. (b) Comparison between the CSM predictions for the $\psi(2S)$ cross sections at LO, NLO, and NNLO* accuracy as a function of the $\psi(2S)$ p_T [113]. The data is prompt $\psi(2S)$ production measured by CDF experiment at the Tevatron.

2.2.3. Production at the Tevatron, RHIC and the LHC

The first measurements by the CDF collaboration of the *direct* production[1] of the J/ψ and the $\psi(2S)$ at $\sqrt{s} = 1.8$ TeV revealed a striking discrepancy with the existing theoretical calculations [114, 115]. The observed rates were more than an order of magnitude greater than the calculated rates at leading order (LO) in the CSM. This discrepancy has triggered many theoretical studies of quarkonium hadroproduction, especially in the framework of NRQCD factorization. Despite recent theoretical advances, which we discuss in section 2.2 we are still lacking a clear picture of the mechanisms at work in quarkonium hadroproduction. These mechanisms would have to explain, in a consistent way, both the cross section measurements and the polarization measurements for quarkonia production at the Tevatron [114–118], RHIC [6, 119–123] and LHC [124–126].

Figure 2.5 (a) shows $\Upsilon(1S)$ differential cross-section as function of transverse momentum measured by CDF experiment at Tevatron [118]. The measured data is for prompt

[1] "Prompt production" excludes quarkonium production from more massive states, such as the B meson. "Direct production" further excludes quarkonium production from feed-down from more massive states, such as higher-mass quarkonium states.

$\Upsilon(1S)$ production. It is multiplied by the fraction of direct $\Upsilon(1S)$'s in prompt $\Upsilon(1S)$ events, as measured by the same experiment using an older event sample [127]. This is done to compare with theoretical calculations directly which can only calculate direct production. In the case of Υ production, the contributions of the NLO corrections to the color-singlet channels reduce the discrepancy between the color-singlet contribution to the inclusive cross section. However, the predicted NLO rate drops too rapidly at large p_T, indicating that another production mechanism is at work in that phase-space region. A recent study [105] has shown that contributions from channels that open at NNLO (order α_s^5) may fill the remaining gap between the color-singlet contribution at NLO and the data. The estimate of the NNLO contribution from this study, called the "NNLO* contribution", is shown in the (red) band labeled NNLO* in Fig. 2.5 (a) [105].

The impact of the QCD corrections on the color-singlet contribution has also been studied in the case of ψ hadroproduction [113]. The comparison with the data is simpler in the case of the $\psi(2S)$ than in the case of the J/ψ, owing to the absence of significant feed-down from excited charmonium states to the $\psi(2S)$. Figure 2.5 (b) shows the reconstructed differential cross section for the prompt $\psi(2S)$ as a function of p_T [128]. The cross section is compared to the prediction for the color-singlet rate at LO, NLO and NNLO* accuracy. At medium values of p_T, the upper limit of the NNLO* rate is compatible with the CDF results. At larger values of p_T, a gap appears between the color-singlet rate and the data [113]. The J/ψ differential production cross section has the same qualitative features as the $\psi(2S)$ differential production rate [129]. It is worth emphasizing that the current discrepancy between the color-singlet rate and the Tevatron data has been dramatically reduced by the inclusion of higher-order QCD corrections.

Figure 2.6 (a) shows prompt J/ψ production cross section as a function of p_T measured by STAR experiment at RHIC [121]. The measured production rate is compared with predictions based on NRQCD factorization at LO [130] and the CSM up to NNLO* accuracy [105]. The calculations do not include feed-down from the $\psi(2S)$ and the χ_c states. The data clearly favor the NRQCD factorization prediction over the CSM prediction. However, no definite conclusions can be drawn because the effects of feed-down have not been taken into account. A calculation of prompt J/ψ production at RHIC, including feed-down from the $\psi(2S)$ and χ_c states, has been carried out in Ref. [131]. These calculations are compared with the prompt J/ψ production cross section as a function of p_T measured by PHENIX collaboration at RHIC [122, 123] in Fig. 2.6 (b). The calculations are done in the CSM and the NRQCD factorization formalism up to LO. The theoretical uncertainty bands were obtained by combining the uncertainties

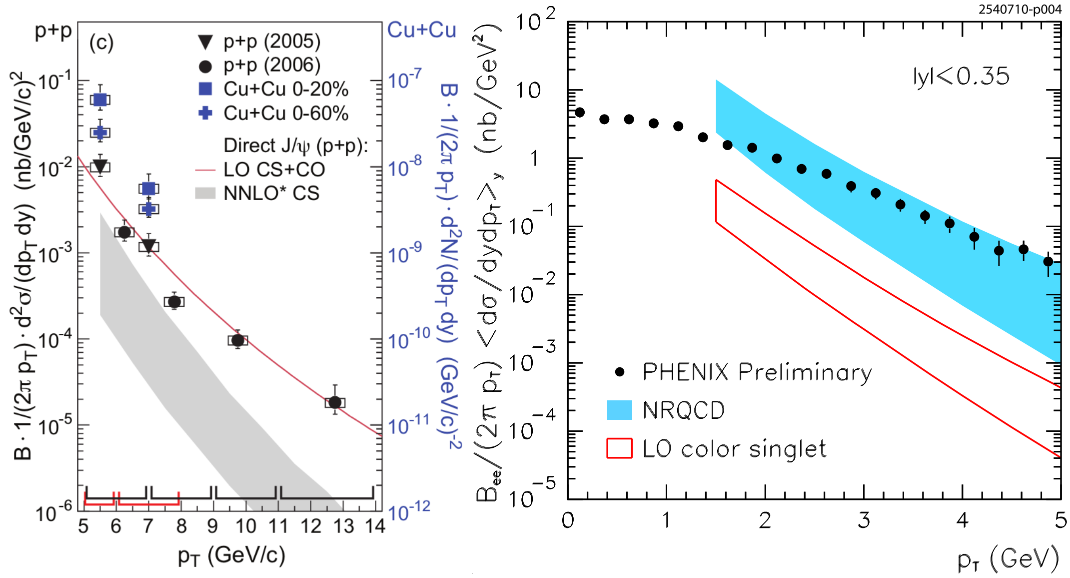

(a) (b)

Figure 2.6.: (a) The measured production rate of J/ψ as a function of p_T is compared with predictions based on NRQCD factorization at LO and the CSM up to NNLO* accuracy. In these calculations feed down effects are not included. (b) Comparison of the LO NRQCD and the LO CSM predictions for the J/ψ cross section as a function of J/ψ p_T with the data from the PHENIX collaboration.

from m_c and the NRQCD long-distance matrix elements with the uncertainties that are obtained by varying the renormalization scale μ_r and the factorization scale μ_f between $2m_T$ and $m_T/2$. Here $m_T = \sqrt{4m_c^2 + p_T^2}$. Again, the NRQCD predictions are favored over the CSM predictions. However, in this case, the small values of p_T involved may call into question the validity of perturbation theory, and the omission of higher-order corrections to the CSM, which are known to be large, also undermines the comparison.

With the advent of the LHC, the study of Υ production has become more accessible than ever. First results [124–126], in pp and PbPb collisions, have already been obtained and the Υ production pattern at the LHC differs from that of the lighter ψ's. Υ's are thus complementary probes of the QCD dynamics in pp and PbPb collisions besides the charmonia. Figure 2.7 nicely illustrate the situation at LHC. Figure 2.7 (a) shows the p_T integrated $\Upsilon(1S)$ production cross section as a function of rapidity, measured by CMS and LHCb experiments at LHC [124, 125]. The data is multiplied by the $F^{\text{direct}}_{\Upsilon(1S)}$ factor measured by CDF experiment [127] to remove the feed down contribution. The data is in good agreement with the band of CSM at LO. The theory uncertainty at LO is unfortunately large due to the presence of three powers of α_S in the LO cross-

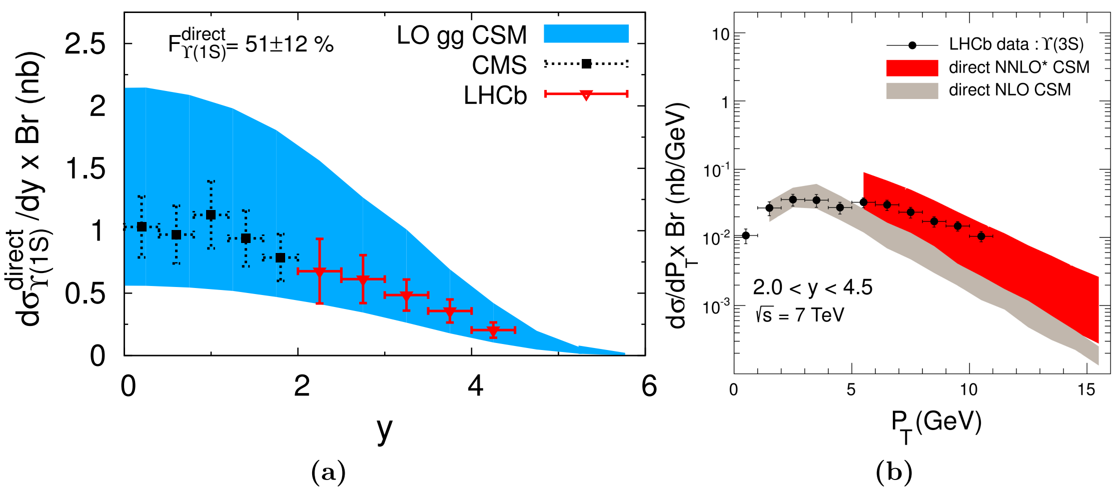

(a) (b)

Figure 2.7.: (a) comparison between the CSM predictions for the direct $\Upsilon(1S)$ yield and various experimental data from CMS and LHCb. Data points are prompt $\Upsilon(1S)$ yield multiplied by $F^{\rm direct}_{\Upsilon(1S)}$ to remove contribution from feed down. (b) Comparison between the $\Upsilon(3S)$ LHCb data and the NLO and NNLO* CSM predictions for the direct yield.

section, hence one finds a significant renormalisation-scale dependence. The experimental measurements at the Tevatron and the LHC are in fact more precise than the theory. Yet, it has to be noted that, at the LHC (Fig. 2.7 (a)), the experimental points tend to lie in the lower part of the theory band.

The situation is nevertheless more complicated when the p_T dependence of the yield is concerned. Figure 2.7 (b) shows the $\Upsilon(3S)$ data measured by LHCb experiment at LHC [125]. $\Upsilon(3S)$ is a very good candidate for constraining quarkonia production models because it do not have significant feed down contributions. The data is compared with the calculations of CSM at NLO and NNLO* [113]. The main reason for discrepancy with LO calculations is that the leading-p_T contributions to Υ hadroproduction only appear at NNLO in the CSM. For the time being, only the NLO cross section [104] is fully known along with a partial evaluation of the NNLO yield, dubbed NNLO* [105]. As expected from the discussion of the p_T integrated yields, the cross section at low p_T is well reproduced by the NLO yield; it only differs from the LO yield by a harder p_T spectrum. The partial NNLO yield is even harder and it matches the data at higher p_T. Yet, a full NNLO computation is needed before drawing final conclusions. The full NLO evaluation without any adjustable parameter perfectly matches the LHCb data up to 5 GeV. The comparison is equally good with the $\Upsilon(1S)$ and $\Upsilon(2S)$ states provided that one subtracts the part of the yield from feed downs [125] . At larger p_T, the leading-p_T contributions of the NNLO seem to be required to describe the data.

2.3. Quarkonia as a probe of hot and dense matter

The deconfinement transition and the properties of hot, strongly-interacting matter can be studied experimentally in heavy-ion collisions [38, 132]. A significant part of the extensive experimental heavy-ion program is dedicated to measuring quarkonium yields since Matsui and Satz suggested that quarkonium suppression could be a signature of deconfinement [2]. However, not all of the observed quarkonium suppression in nucleus-nucleus (AB) collisions relative to scaled proton-proton (pp) collisions is due to quark-gluon plasma formation. In fact, quarkonium suppression was also observed in proton-nucleus (pA) collisions, so that part of the nucleus-nucleus suppression is due to cold-nuclear-matter effects. Therefore it is necessary to disentangle hot and cold-medium effects. We first discuss cold-nuclear-matter effects at different center-of-mass energies. Then we discuss what is known about the properties of heavy $Q\overline{Q}$ states in hot, deconfined media. Finally, we review recent experimental results on quarkonium production from pp, pA and AA collisions at the SPS, RHIC and LHC.

2.3.1. Cold nuclear matter effects

The baseline for quarkonium production and suppression in heavy-ion collisions should be determined from studies of cold-nuclear-matter (CNM) effects. The name cold matter arises because these effects are observed in hadron-nucleus interactions where no hot, dense matter effects are expected. There are several CNM effects. Modifications of the parton distribution functions in the nucleus, relative to the nucleon, (i.e. *shadowing*) and energy loss of the parton traversing the nucleus before the hard scattering are both assumed to be initial-state effects, intrinsic to the nuclear target. Another CNM effect is absorption (i. e. destruction) of the quarkonium state as it passes through the nucleus. Since the latter occurs after the $Q\overline{Q}$ pair has been produced and while it is traversing the nuclear medium, this absorption is typically referred to as a final-state effect.

Even though the contributions to CNM effects may seem rather straightforward, there are a number of associated uncertainties. First, while nuclear modifications of the quark densities are relatively well-measured in nuclear deep-inelastic scattering (nDIS), the

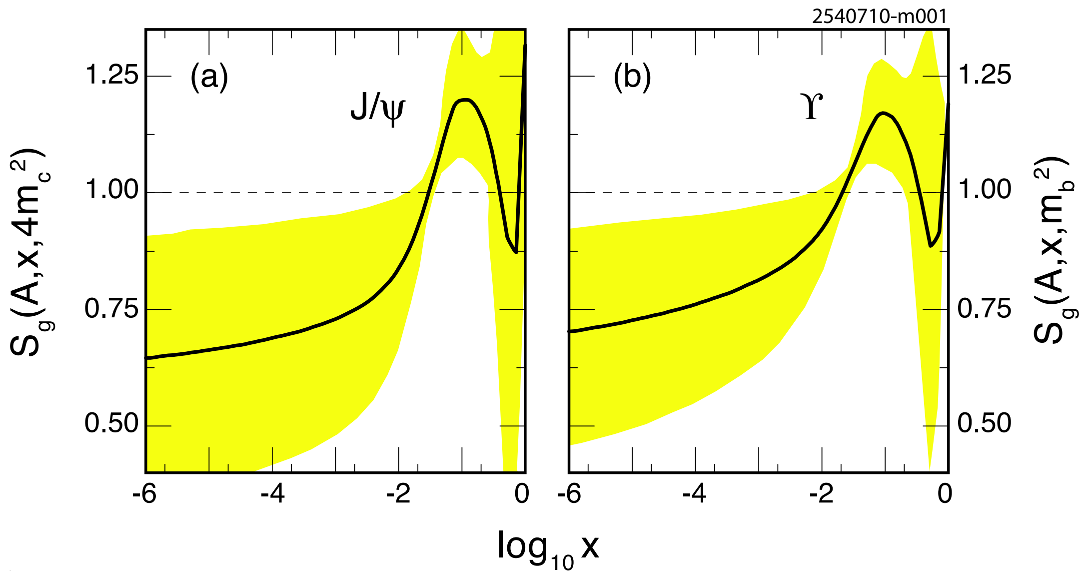

Figure 2.8.: The EPS09 gluon-shadowing parametrization [12] at $Q = 2m_c$ and m_b. The central value (solid curves) and the associated uncertainty (shaded band) are shown

modifications of the gluon density are not directly measured. The nDIS measurements probe only the quark and antiquark distributions directly. The scaling violations in nDIS can be used to constrain the nuclear gluon density. Overall momentum conservation provides another constraint. However, more direct probes of the gluon density are needed. Current shadowing parametrizations are derived from global fits to the nuclear parton densities and give wide variations in the nuclear gluon density, from almost no effect to very large shadowing at low-x, compensated by strong antishadowing around $x \sim 0.1$. The range of the possible shadowing effects is illustrated in Fig. 2.8 by the new EPS09 [12] parametrization and its associated uncertainties, employing the scale values used to fix the J/ψ and Υ cross sections below the open-heavy-flavor threshold [89].

The nuclear absorption survival probability depends on the quarkonium absorption cross section. There are more inherent uncertainties in absorption than in the shadowing parametrization. It is obtained from data on other processes and is independent of the final state. Typically an absorption cross section is fit to the A dependence of J/ψ and/or ψ' production in pA collision at a given energy. This is rather simplistic since it is unknown whether the object traversing the nucleus is a precursor color-octet state or a fully-formed color-singlet quarkonium state. The J/ψ absorption cross section at $y \sim 0$ is seen to decrease with energy, regardless of the chosen shadowing parametrization [133], as shown in Fig. 2.9.

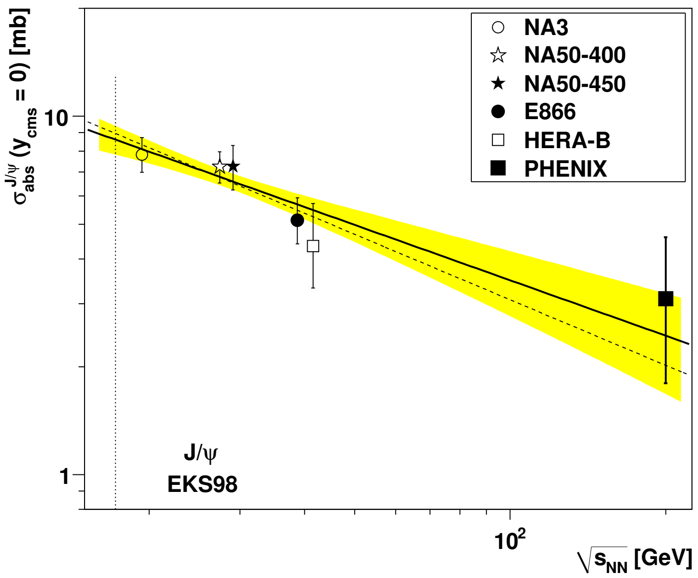

Figure 2.9.: The extracted energy dependence of $\sigma_{\text{abs}}^{J/\psi}$ at midrapidity. The *solid line* is a power law approximation to $\sigma_{\text{abs}}^{J/\psi}(y = 0, \sqrt{s_{\text{NN}}})$ using the EKS98 [134, 135] shadowing parametrization with the CTEQ61L parton densities [11, 136]. The *band* indicates the uncertainty in the extracted cross sections. The *dashed curve* shows an exponential fit for comparison. The data at $y_{\text{cms}} \sim 0$ from NA3 [137], NA50 at 400 GeV[138] and 450 GeV[139], E866 [140], HERA-B [141], and PHENIX [122] are also shown. The *vertical dotted line* indicates the energy of the Pb+Pb and In+In collisions at the CERN SPS. Figure is take from Ref. [133]

Recent analyses of J/ψ production in fixed-target interactions [133] show that the effective absorption cross section depends on the energy of the initial beam and the rapidity or x_F of the observed J/ψ. One possible interpretation is that low-momentum color-singlet states can hadronize in the target, resulting in larger effective absorption cross sections at lower center-of-mass energies and backward x_F (or center-of-mass rapidity). At higher energies, the states traverse the target more rapidly so that the x_F values at which they can hadronize in the target move back from midrapidity toward more negative x_F. Finally, at sufficiently high energies, the quarkonium states pass through the target before hadronizing, resulting in negligible absorption effects. Thus the *effective* absorption cross section decreases with increasing center-of-mass energy because faster states are less likely to hadronize inside the target.

This is a very simplistic picture in practice cold-nuclear-matter effects (initial-state energy loss, shadowing, final-state breakup, *etc.*) depend differently on the quarkonium kinematic variables and the collision energy. It is clearly unsatisfactory to combine all these mechanisms into an *effective* absorption cross section, as employed in the Glauber formalism, that only evaluates final-state absorption. Simply taking the $\sigma_{\rm abs}$ obtained from the analysis of the pA data and using it to define the Pb+Pb baseline is not be sufficient. A better understanding of absorption requires more detailed knowledge of the production mechanisms which it self are largely unknown.

2.3.2. Quarkonium in hot medium

There has been considerable interest in studying quarkonia in hot media. It has been argued that color screening in a deconfined QCD medium will destroy all $Q\overline{Q}$ bound states at sufficiently high temperatures. Although this idea was proposed long ago, first principle QCD calculations, which go beyond qualitative arguments, have been performed only recently. Such calculations include lattice QCD determinations of quarkonium correlators [142–146], potential model calculations of the quarkonium spectral functions with potentials based on lattice QCD [4, 147–153], as well as effective field theory approaches that justify potential models and reveal new medium effects [154–157]. Furthermore, better modeling of quarkonium production in the medium created by heavy-ion collisions has been achieved. These advancements make it possible to disentangle the cold and hot-medium effects on the quarkonium states, crucial for the interpretation of heavy-ion data.

Color screening and deconfinement

At high temperatures, strongly-interacting matter undergoes a deconfining phase transition to a quark-gluon plasma. This transition is triggered by a rapid increase of the energy and entropy densities as well as the disappearance of hadronic states. The special property of QGP is color screening: the range of interaction between heavy quarks becomes inversely proportional to the temperature. Thus at sufficiently high temperatures, it is impossible to produce a bound state between a heavy quark and its antiquark.

Color screening is studied on the lattice by calculating the spatial correlation function of a static quark and antiquark in a color-singlet state which propagates in Euclidean time from $\tau = 0$ to $\tau = 1/T$, where T is the temperature. Lattice calculations of this quantity with dynamical quarks have been reported [158–160]. The logarithm of the singlet correlation function, also called the singlet free energy, is shown in Fig. 2.10 As expected, in the zero-temperature limit the singlet free energy coincides with the zero-temperature potential. Figure 2.10 also illustrates that, at sufficiently short distances, the singlet free energy is temperature independent and equal to the zero-temperature potential. The range of interaction decreases with increasing temperature. For temperatures above the transition temperature, T_c, the heavy-quark interaction range becomes comparable to the charmonium radius. Based on this general observation, one would expect that the charmonium states, as well as the excited bottomonium states, do not remain bound at temperatures just above the deconfinement transition, often referred to as *dissociation* or *melting*.

Quarkonium spectral functions and quarkonium potential

In-medium quarkonium properties are encoded in the corresponding spectral functions, as is quarkonium dissociation at high temperatures. Spectral functions are defined as the imaginary part of the retarded correlation function of quarkonium operators. Bound states appear as peaks in the spectral functions. The peaks broaden and eventually disappear with increasing temperature. The disappearance of a peak signals the melting of the given quarkonium state. The quarkonium spectral functions can be calculated in potential models using the singlet free energy from Fig. 2.10 or with different lattice-based potentials obtained using the singlet free energy as an input [4, 153]. The results for quenched QCD calculations are shown in Fig. 2.11 for S-wave charmonium (a) and bottomonium (b) spectral functions [153]. All charmonium states are dissolved in the deconfined phase while the bottomonium 1S state may persist up to $T \sim 2T_c$. An upper

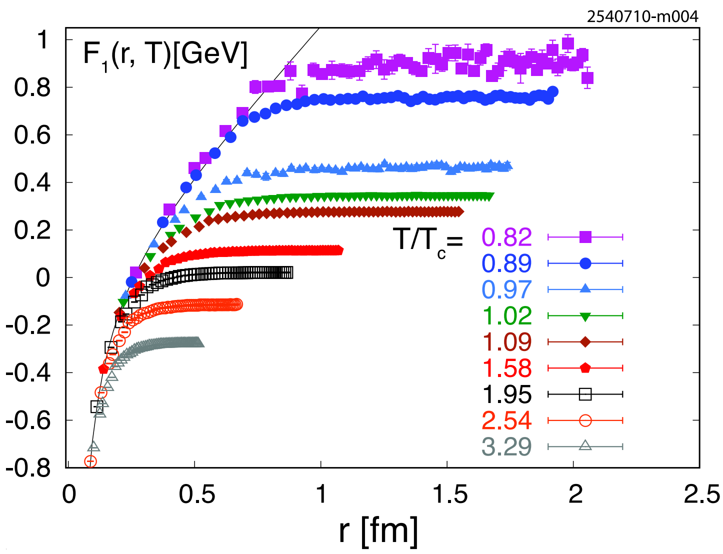

Figure 2.10.: Heavy-quark-singlet free energy versus quark separation calculated in 2+1 flavor QCD on $16^3 \times 4$ lattices at different temperatures [159, 160]

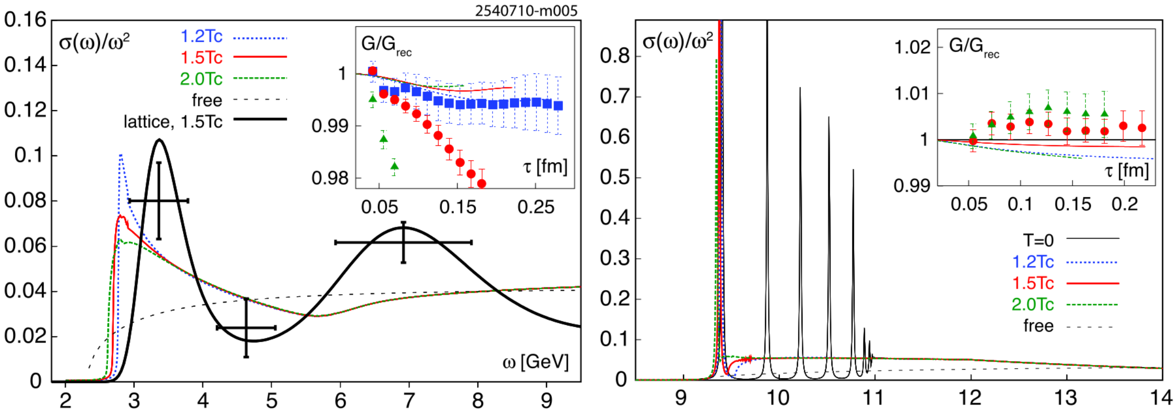

(a) **(b)**

Figure 2.11.: The S-wave charmonium (a) and bottomonium (b) spectral functions calculated in potential models. Insets: correlators compared to lattice data. The *dotted curves* are the free spectral functions.Figure is taken from Ref. [153].

Table 2.1.: Upper bounds on the dissociation temperatures [4].

State	$\chi_{cJ}(1P)$	ψ'	J/ψ	$\Upsilon(2S)$	$\chi_{bJ}(1P)$	$\Upsilon(1S)$
T_{diss}	$\leq T_c$	$\leq T_c$	$1.2T_c$	$1.2T_c$	$1.3T_c$	$2T_c$

bound on the dissociation temperature (the temperatures above which no bound states peaks can be seen in the spectral function and bound state formation is suppressed) can be obtained from the analysis of the spectral functions. Conservative upper limits on the dissociation temperatures for the different quarkonium states obtained from a full QCD calculation [4] are given in Tab. 2.1.

Summary of hot medium effects

Potential model calculations based on lattice QCD, as well as resummed perturbative QCD calculations, indicate that all charmonium states and the excited bottomonium states dissolve in the deconfined medium. This leads to the reduction of the quarkonium yields in heavy-ion collisions compared to the binary scaling of pp collisions. Recombination and edge effects, however, guarantee a nonzero yield. One of the great opportunities of the LHC heavy-ion program is the ability to study bottomonium yields. From a theoretical perspective, bottomonium is an important and clean probe for at least two reasons. First, the effective field theory approach, which provides a link to first principles

QCD, is more applicable for bottomonium due to better separation of scales and higher dissociation temperatures. Second, the heavier bottom quark mass reduces the importance of statistical recombination effects. Experimentally it has less background contribution and is easy to reconstruct. All these properties make bottomonium a good probe of QGP formation in heavy ion collisions.

2.4. Experimental status of quarkonia suppression at SPS, RHIC and LHC

2.4.1. Recent results at SPS energies

One of the main results of the SPS heavy-ion program was the observation of anomalous J/ψ suppression. Results obtained in Pb+Pb collisions at 158 GeV/nucleon by the NA50 collaboration showed that the J/ψ yield was suppressed with respect to estimates that include only cold-nuclear-matter effects [161]. The magnitude of the cold-nuclear-matter effects has typically been extracted by extrapolating the J/ψ production data obtained in pA collisions. Until recently the reference SPS pA data were based on samples collected at 400/450 GeV by the NA50 collaboration, at higher energy than the nuclear collisions and in a slightly different rapidity domain [138, 139]. The need for reference pA data taken under the same conditions as the AA data was a major motivation for the NA60 run with an SPS primary proton beam at 158 GeV in 2004.

Nuclear effects have usually been parametrized by fitting the A dependence of the J/ψ production cross section using the expression

$$\sigma_{pA}^{J/\psi} = \sigma_{pp}^{J/\psi} A^{\alpha} \ . \tag{2.5}$$

Both α and $\sigma_{\rm abs}^{J/\psi}$ are effective quantities since they represent the strength of the cold-nuclear-matter effects that reduce the J/ψ yield. However, they cannot distinguish among the different effects, *e.g.* shadowing and nuclear absorption, contributing to this reduction. The results in Fig. 2.12 (a) were used to extract

$$\begin{aligned} \sigma_{\rm abs}^{J/\psi} &= 7.6 \pm 0.7\,(\text{stat.}) \pm 0.6\,(\text{syst.})\ \text{mb}\,; \\ \alpha &= 0.882 \pm 0.009 \pm 0.008 \end{aligned} \tag{2.6}$$

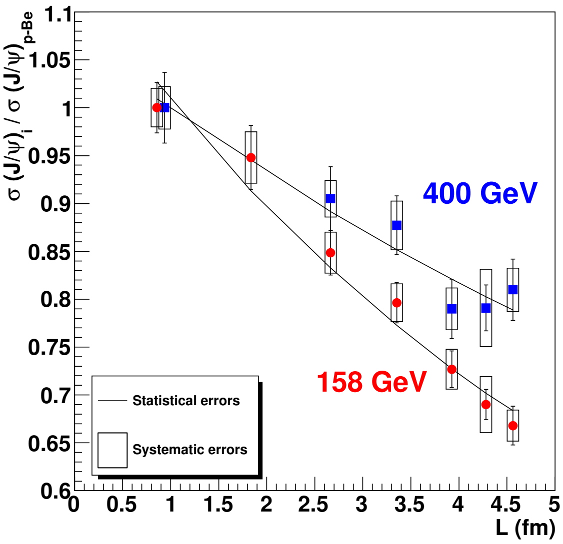

(a)

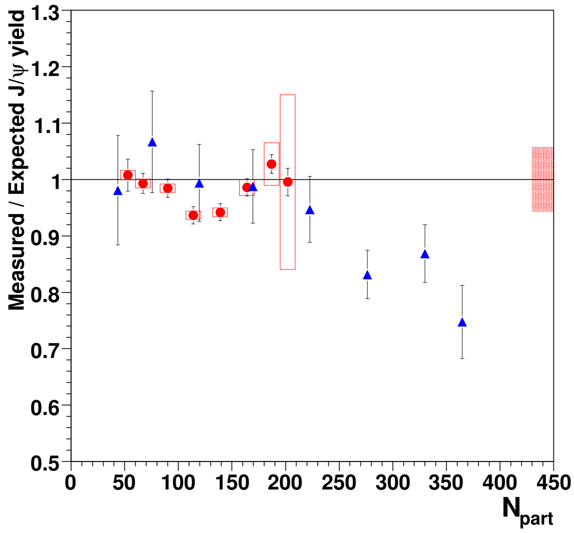

(b)

Figure 2.12.: (a) The J/ψ cross section ratios for pA collisions at 158 GeV *(circles)* and 400 GeV *(squares)*, as a function of L, the mean thickness of nuclear matter traversed by the J/ψ. (b)Anomalous J/ψ suppression in In+In *(circles)* and Pb+Pb collisions *(triangles)* as a function of N_{part}. The *boxes* around the In+In *points* represent correlated systematic errors. The *filled box* on the right corresponds to the uncertainty in the absolute normalization of the In+In *points*. A 12% global error, due to the uncertainty on $\sigma_{\text{abs}}^{J/\psi}$ at 158 GeV is not shown. Figure is taken from [162].

at 158 GeV and

$$\begin{aligned} \sigma_{\text{abs}}^{J/\psi} &= 4.3 \pm 0.8\,(\text{stat.}) \pm 0.6\,(\text{syst.})\text{ mb}\,; \\ \alpha &= 0.927 \pm 0.013 \pm 0.009 \end{aligned} \tag{2.7}$$

at 400 GeV. Thus $\sigma_{\text{abs}}^{J/\psi}$ is larger at 158 GeV than at 400 GeV by three standard deviations. The 400 GeV result is, on the other hand, in excellent agreement with the previous NA50 result obtained at the same energy [138].

The pA results at 158 GeV shown in Fig. 2.12 (a) have been collected at the same energy and in the same rapidity range as the SPS AA data. These results are then used to calculate the expected magnitude of cold-nuclear-matter effects on J/ψ production in nuclear collisions. Figure 2.12 (b) presents the results for the anomalous J/ψ suppression in In+In and Pb+Pb collisions [162, 163] as a function of N_{part}, the number of participant nucleons. Up to $N_{\text{part}} \sim 200$ the J/ψ yield is, within errors, compatible with the extrapolation of cold-nuclear-matter effects. When $N_{\text{part}} > 200$, there is an anomalous suppression of up to $\sim 20-30\%$ in the most central Pb+Pb collisions.

2.4.2. J/ψ suppression at RHIC and LHC

The strategy of the RHIC J/ψ program has been to measure production cross sections in $\sqrt{s_{NN}} = 200$ GeV collisions for pp, d+Au, Au+Au and Cu+Cu collisions. The pp collisions are studied both to learn about the J/ψ production mechanism and to provide baseline production cross sections needed for understanding the d+Au and AA data. Similarly, the d+Au measurements are inherently interesting because they study the physical processes that modify J/ψ production cross sections in nuclear targets and also provide the crucial cold-nuclear-matter baseline for understanding J/ψ production in AA collisions. The last few years of the RHIC program have produced J/ψ data from PHENIX and STAR for pp, d+Au and Au+Au collisions with sufficient statistical precision to establish the centrality dependence of both hot and cold-nuclear-matter effects at $\sqrt{s_{\text{NN}}}$ = 200 GeV. The nuclear suppression factor, R_{AB}, for dA, and AA collisions is defined as the ratio

$$R_{AB}(N_{\text{part}}; b) = \frac{d\sigma_{AB}/dy}{T_{AB}(b)\, d\sigma_{pp}/dy} \tag{2.8}$$

where $d\sigma_{AB}/dy$ and $d\sigma_{pp}/dy$ are the quarkonium rapidity distributions in AB and pp collisions and T_{AB} is the nuclear overlap function. In AA collisions, R_{AA} is sometimes shown relative to the extracted cold-nuclear-matter baseline, R_{AA}^{CNM}.

As discussed previously, modification of the J/ψ production cross section due to the presence of a nuclear target is expected to be caused by shadowing, breakup of the precursor J/ψ state by collisions with nucleons, initial-state energy loss, and other possible effects. Parametrizing these effects by employing a Glauber model with a fitted effective J/ψ-absorption cross section, $\sigma_{\text{abs}}^{J}/\psi$, results in an effective cross section with strong rapidity and $\sqrt{s_{NN}}$ dependencies [133] that are not well understood. The extraction of hot-matter effects in the AuAu J/ψ data at RHIC has been seriously hampered by the poor understanding of J/ψ production in nuclear targets, including the underlying production mechanism. Thus the cold-nuclear-matter baseline has to be obtained experimentally.

PHENIX [164] has published the centrality dependence of R_{AA} for AuAu collisions. The data are shown in Fig. 2.13 (a). The suppression is considerably stronger at forward rapidity than at midrapidity. The significance of this difference with respect to hot-matter effects will not be clear, however, until the suppression due to cold-nuclear-matter effects is more accurately known. To estimate the cold-nuclear-matter contribution to the AuAu J/ψ R_{AA} the d+Au J/ψ $\mathrm{R_{CP}}$ data is analyzed using the EKS98 and nDSg [165] shadowing parametrization. The cold-nuclear-matter R_{AA} for Au+Au collisions was then estimated in a Glauber calculation using the fitted absorption cross sections and the centrality-dependent $\mathrm{R_{pAu}}$ values calculated using EKS98 and nDSg shadowing parametrizations [5]. The J/ψ suppression beyond CNM effects in AuAu collisions can be estimated by dividing the measured R_{AA} by the estimates of the CNM R_{AA}. The result for EKS98 is shown in Fig. 2.13 (b). The systematic uncertainty of the baseline cold-nuclear-matter R_{AA} is depicted by the *wide box* around each *point*. The *narrow box* is the systematic uncertainty in the AuAu R_{AA}. The result for nDSg is nearly identical. Assuming that the PHENIX $\mathrm{R_{dAu}}$ confirms the strong suppression at forward rapidity seen in $\mathrm{R_{CP}}$, it would suggest that the stronger suppression seen at forward/backward rapidity in the PHENIX AuAu R_{AA} data is primarily due to cold-nuclear-matter effects. The suppression due to hot-matter effects seems to be comparable at midrapidity and at forward/backward rapidity. Figure 2.13 (c) shows comparison of J/ψ nuclear modification factor at SPS and RHIC energies. PHENIX mid rapidity data is compared with SPS measurements in different collision systems. It is evident from the figure that magnitude of suppression is similar at RHIC and SPS, despite the large differences in center of mass energies.

After the LHC started PbPb collisions at $\sqrt{s_{NN}}$ = 2.76 TeV, a wealth of results have become available on quarkonia production and suppression. The CMS experiment carries out J/ψ measurements at high transverse momentum (p_T > 6.5 GeV/c) and in the rapidity range $|y| \leq 2.4$. Figure 2.14 (a) shows the nuclear modification factor (R_{AA}) of J/ψ in PbPb collisions at $\sqrt{s_{NN}}$ = 2.76 TeV as a function of number of participants measured by CMS [166, 167]. The R_{AA} of these high p_T prompt J/ψ decreases with increasing centrality showing moderate suppression even in the most peripheral collisions. On comparing with the STAR results [168] at RHIC, it follows that the suppression of (high p_T) J/ψ has increased with collision energy. The ALICE results on J/ψ correspond to a low p_T range which have little or no centrality dependence except for the most peripheral collisions as shown in Fig. 2.14 (b). The suppression of low p_T J/ψ measured by ALICE experiment at 2.76 TeV is smaller than that measured by PHENIX experiment at 200 GeV. This gives a hint of significant regeneration of J/ψ from uncorrelated charm pairs.

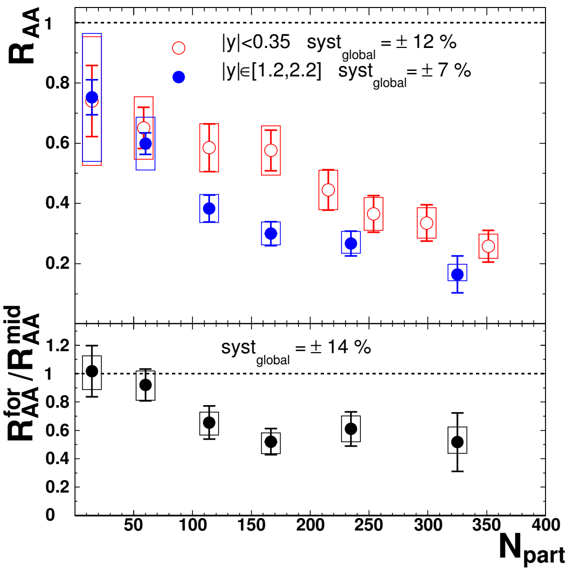

(a)

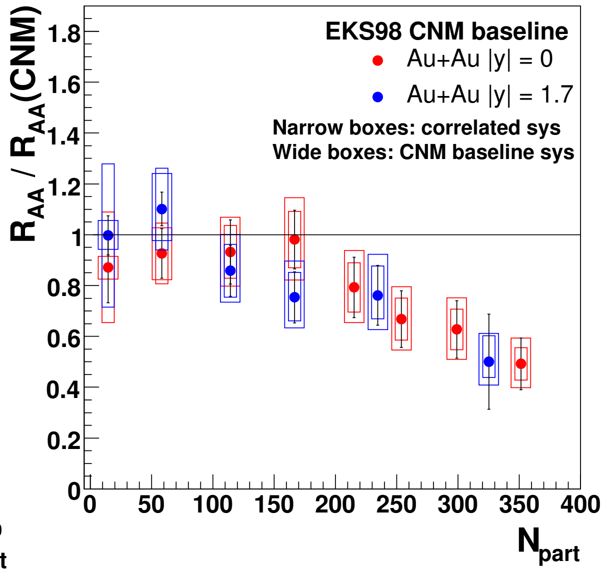

(b)

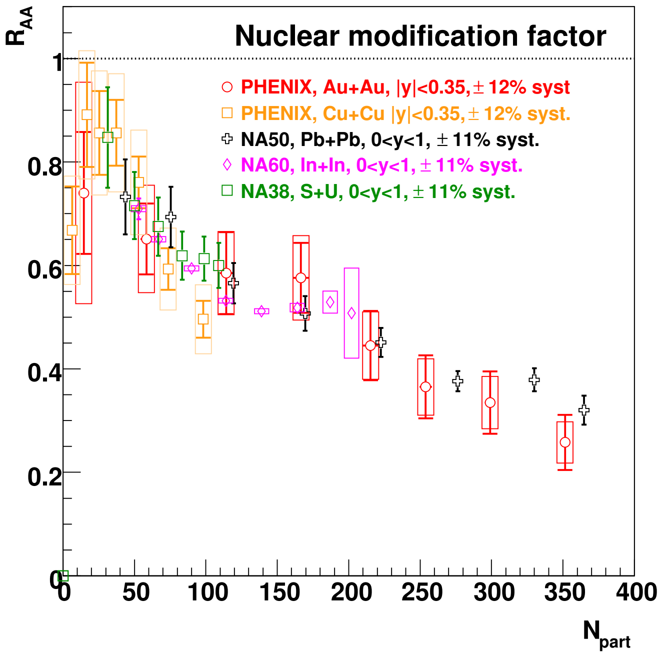

(c)

Figure 2.13.: (a) The PHENIX AuA R_{AA} as a function of centrality for $|y| < 0.35$ and $1.2 < |y| < 2.2$. (b) The estimated AuAu suppression relative to the cold-nuclear-matter R_{AA} as a function of centrality for $|y| < 0.35$ and $1.2 < |y| < 2.2$. (c) Comparison of J/ψ nuclear modification factor at RHIC and SPS energies. PHENIX mid rapidity data is compared with SPS measurements in different collision systems.

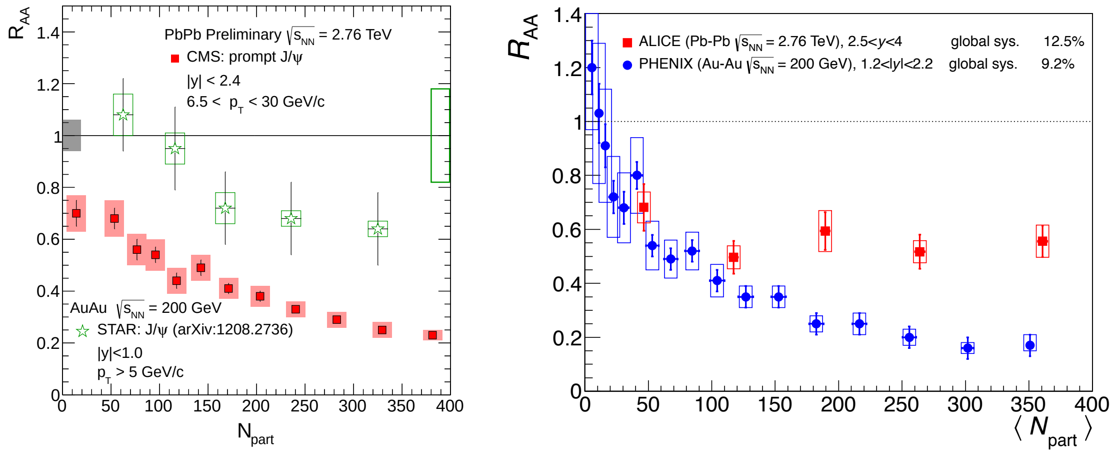

Figure 2.14.: (a) The nuclear modification factor (R_{AA}) of J/ψ in PbPb collisions at $\sqrt{s_{NN}} =$ 2.76 TeV as a function of number of participants measured by CMS experiment [166, 167]. RHIC measurements are shown for comparison [168]. (b) Nuclear modification factor (R_{AA}) of J/ψ as a function of number of participants measured by ALICE and PHENIX experiment at forward rapidity. Figure is based on data presented in Ref. [169] and Ref.[170].

Figure 2.15 shows R_{AA} of J/ψ in PbPb collisions at $\sqrt{s_{NN}} = 2.76$ TeV as a function of p_T measured by CMS, ALICE and PHENIX experiments. The R_{AA} is found to be nearly independent of p_T (above 6.5 GeV/c) showing that J/ψ remains suppressed even at very high p_T ($\sim$ 16 GeV/c) [166, 167]. The ALICE J/ψ data [169] shows that R_{AA} increases with decreasing p_T below 4 GeV/c. On comparing with the PHENIX forward rapidity measurement [170], it can be said that low p_T J/ψ at LHC are enhanced in comparison to RHIC. These observations again suggest regeneration of J/ψ at low p_T by recombination of independently produced charm pairs.

2.4.3. Υ(nS) suppression at RHIC

Υ states are measured at RHIC by STAR [171] and PHENIX [172] experiments. Due to small production cross-section of b quark at $\sqrt{s_{NN}} = 200$ GeV, total yield of Υ is very small at RHIC, also poor resolution of detectors does not allow separation of different Υ states. STAR measured Υ production in pp, dAu, and AuAu collisions at $\sqrt{s_{NN}} = 200$ GeV via the e^+e^- decay channel. Figure 2.16 (a) shows the invariant mass distributions of electron pairs for most central (0-10%) AuAu collisions. The data is collected in the kinematic region $|y_\Upsilon| < 1.0$. Unlike-sign pairs are shown as red filled circles and like-sign pairs as hollow blue circles. The data are fitted with a parameterization consisting of the sum of various contributions to the electron-pair invariant-mass spectrum. The fit is

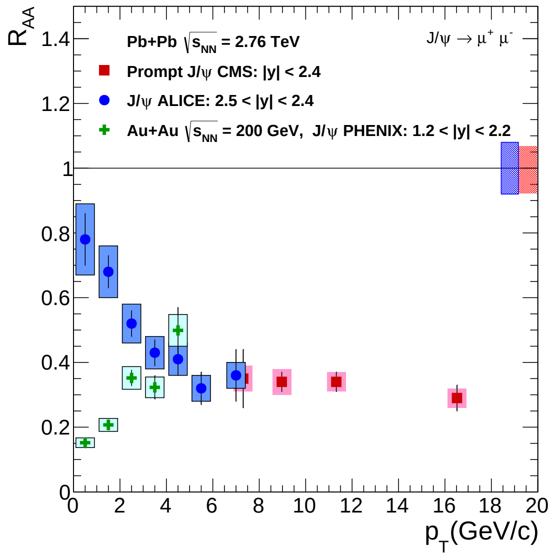

Figure 2.15.: Nuclear modification factor (R_{AA}) of J/ψ as a function of p_T measured by CMS [166, 167], ALICE [169] and PHENIX [170] experiments.

performed simultaneously with the like-sign and unlike-sign spectra using a maximum-likelihood method. The lines in Fig. 2.16 (a) show the yield from the combinatorial background (dashed blue line), the result of adding the physics background from Drell-Yan and $b\bar{b}$ pairs (dot-dashed green line), and finally the inclusion of the Υ contribution (solid red line). Each of the Υ states is modeled with a Crystal Ball function, which incorporates detector resolution and losses from bremsstrahlung in the detector material. The gray bands in figure illustrate the expected signal from the pp data scaled by the number of binary collisions. There is a clear suppression of the expected yield in AuAu collisions. This suppression is quantified in Fig. 2.16 (b), which displays the nuclear modification factor, R_{AA}, plotted as a function of N_{Part} with the 0-10% most-central collisions corresponding to $\langle N_{\text{Part}} \rangle = 326 \pm 4$. Figure 2.16 (b) shows the data for all three states in the rapidity range $|y| < 1$. The data confirm that bottomonia are indeed suppressed in dAu and in AuAu collisions.

PHENIX experiment also reports the measurement of the inclusive Υ (1S+2S+3S) yield at $|y| < 0.35$ in Au+Au collisions at $\sqrt{s_{NN}} = 200$ GeV [172]. The PHENIX experiment measures quarkonia at midrapidity through their dielectron decays. Figure 2.17 (a) shows the invariant mass spectrum in the Υ mass region for Au+Au data in 0-30% centrality region. The number of Υ counts was determined from a direct count of unlike-sign and like-sign dielectrons in the Υ mass region and the fraction of correlated

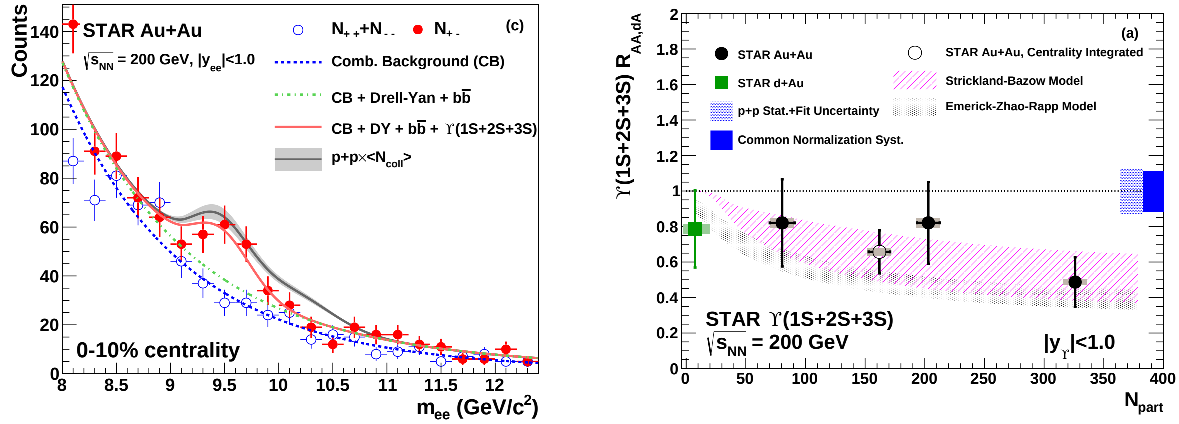

(a) (b)

Figure 2.16.: (a) Invariant mass distributions of electron pairs in the region $|y_{ee}| \leq 1$ for the most central collisions (0-10%).Unlike-sign pairs are shown as filled red circles and like-sign pairs as hollow blue circles. The gray band shows the expected signal assuming scaling of the pp yield with the number of binary collisions including resolution effects. (b) Nuclear modification factor for Υ (1S+2S+3S), in $|y| < 1.0$ in d+Au (green square) and AuAu (black circles) collisions as a function of N_{part}. The boxes around unity show the statistical (shaded) and systematic (filled) uncertainty from the pp measurement. The gray bands around the data points are the systematic uncertainties. The data are compared with calculations using a combination of lattice-based QCD and hydrodynamical expansion and cooling. Figures are taken from Ref. [171].

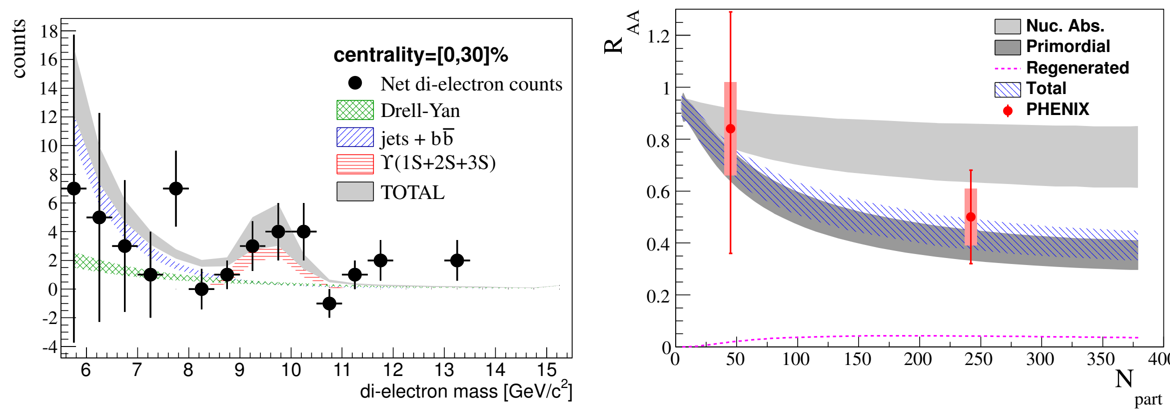

(a) (b)

Figure 2.17.: (a) Fits to correlated dielectron mass distribution around the Υ region obtained in Au+Au collisions in most central bin (0-30%) by PHENIX detector at RHIC. The bands correspond to fitting and theoretical uncertainties for the Drell-Yan estimation. (b) Nuclear modification factor for for Υ (1S+2S+3S) plotted as a function of N_{part}. A comparison of PHENIX data to the model from [173] for the strong binding scenario. Figures are taken from Ref. [172].

background f_{cont} in the same mass range

$$N_{\Upsilon} = (N_{\text{unlike}} - N_{\text{like}})\,(1 - f_{\text{cont}}). \tag{2.9}$$

The correlated background underneath the Υ region is determined from fits of the expected mass dependence of Drell-Yan, correlated electrons from B meson decays and possible contamination of hadrons within jets. The nuclear modification factors for the binned centrality data set R_{AA} is calculated as:

$$R_{AA} = \frac{dN/dy_{\text{AuAu}}}{< N_{\text{coll}} > dN/dy_{\text{pp}}} \tag{2.10}$$

A global uncertainty of 38% is calculated from the quadratic sum of the relative uncertainty from pp data (statistical+systematic) and the Glauber estimate of the number of collisions. Figure 2.17 (b) shows the R_{AA} as a function of the number of participants for the two centrality-split classes. The inclusive Υ states are suppressed in central 200 GeV Au+Au collisions, corresponding to large N_{Part}. However, the degree of suppression in semi-peripheral collisions is unclear, due to limited statistics. PHENIX data is also compared with model predictions by Rapp et. al [173], albeit with large statistical uncertainties, data is found consistent with model.

Due to small production cross section and poor detector resolutions, Υ measurement is not conclusive at RHIC. All three Υ states are reconstructed with large statistics and good resolution at LHC. Υ measurement in pp, pPb and PbPb collisions is main topic of this thesis and explained in detail further.

Chapter 3.

The Compact Muon Solenoid experiment at the Large Hadron Collider

3.1. The LHC

The Large Hadron Collider (LHC) at CERN near Geneva is the world's newest and most powerful tool for Particle Physics research. It is designed to collide proton beams with a center-of-mass energy of 14 TeV and an unprecedented luminosity of 10^{34} cm^{-2}s^{-1} . It can also collide heavy (Pb) ions with a center-of-mass energy of 5.5 TeV per nucleon and a peak luminosity of 10^{27} cm^{-2}s^{-1}. Center of mass energies achieved so far are 8 TeV for pp collisions and 2.76 TeV for Pb+Pb collisions. LHC also had a p+Pb run at 5 TeV center of mass energy. All the systems, center of mass energies delivered at LHC and collected integrated luminosities are shown in Table 3.2.

LHC has circumference of 27 kms and is placed in a tunnel, 175 meters under the ground near Geneva. The tunnel was originally built for the Large Electron-Positron collider [174]. For the LHC operation, they have been upgraded to provide beams of protons for collisions at unprecedented energies. Technical limitations in the production and storage of antiprotons led to the decision to build a proton-proton collider. Accelerated light particles, e.g. electrons and positrons, suffer large energy loss due to the synchrotron radiation, which is proportional to $\frac{E^4}{(Rm^4)}$, where E is the electron energy, m is the particle's mass and R is the accelerator radius. Therefore, only massive charged particles

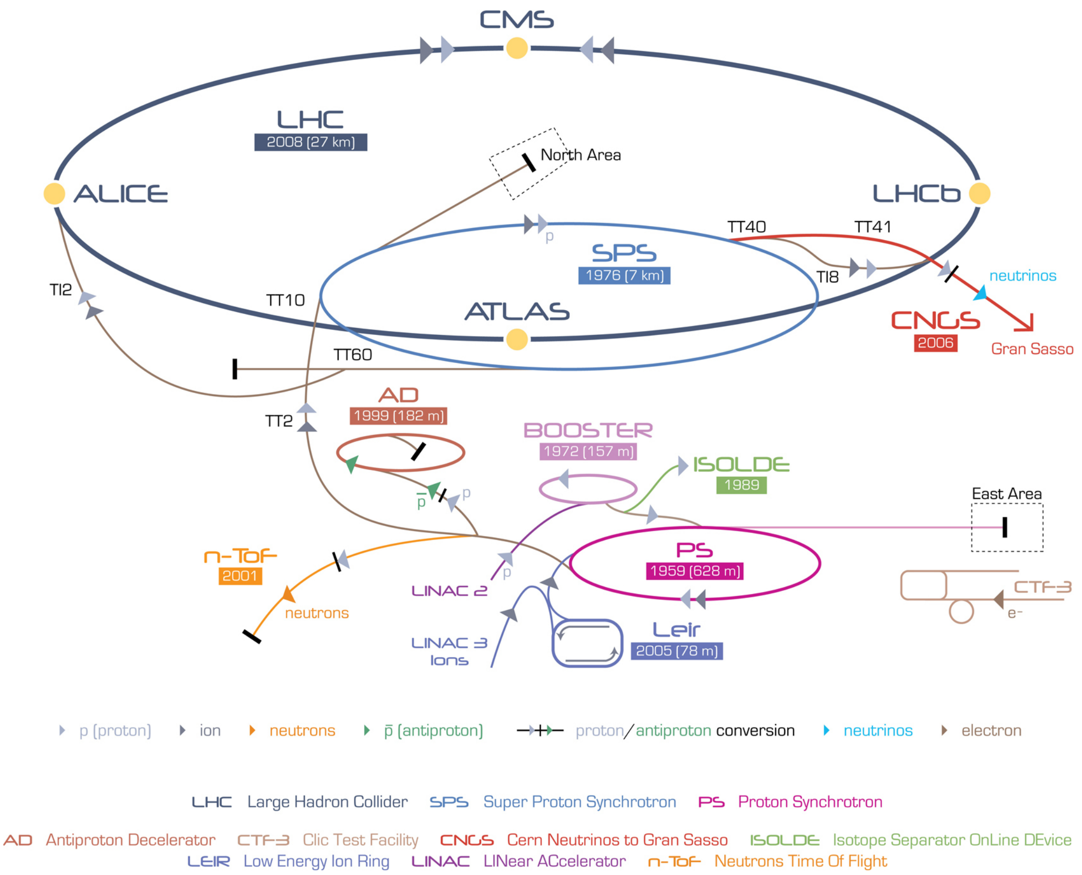

Figure 3.1.: CERN accelerator complex with all detectors. LHC have four running experiments named as ALICE, ATLAS, CMS and LHCb

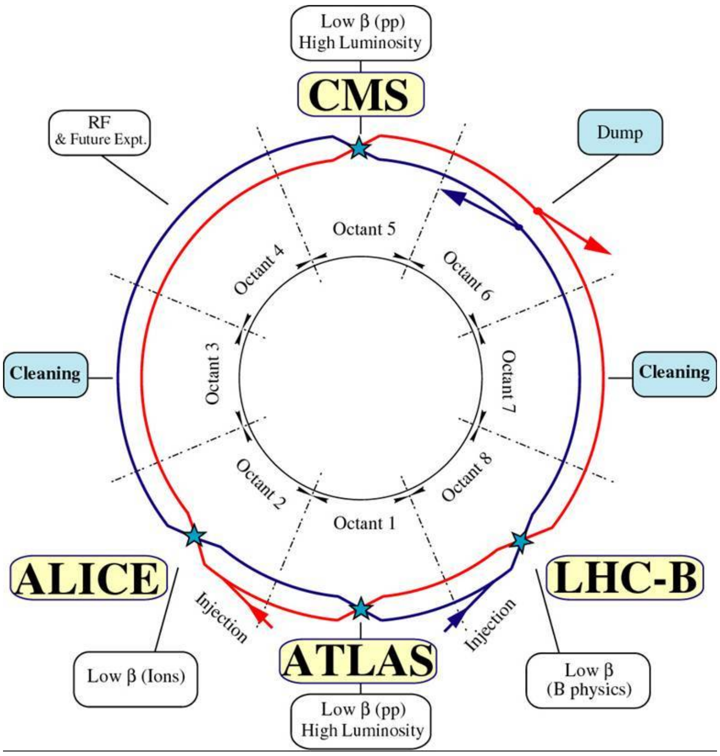

Figure 3.2.: LHC ring

can be used, e.g. protons and heavy nuclei, in order to obtain energies of the order of TeV at the fixed accelerator radius.

3.1.1. The accelerator complex

The LHC is constituted by 1232 super-conducting dipole magnets each 15 m long, delivering a 8.3 T magnetic field to let the beams circulate inside their trajectories along the 27 km circumference. Two vacuum pipes are utilized to let beams circulate in opposite directions. More than 8000 other magnets are utilized for the beam injection, their collimation, trajectory correction, crossing. All the magnets are kept cool by superfluid helium at 1.9 K temperature. The beams are accelerated from 450 GeV (the injection energy from the SPS) to 7 TeV with 16 Radio Frequency cavities (8 per beam) which raise the beam energy by 16 MeV each round with an electric field of 5 MV/m oscillating at 400 MHz frequency. Before the injection into the LHC, the beams are produced and accelerated by different 26 components of the CERN accelerator complex. Being produced from ionized hydrogen atoms, protons are accelerated by the linear accelerator LINAC, Booster and the Proton Synchrotron (PS) up to 26 GeV energy, the bunches being separated by 25 ns each. The beams are then injected into the Super Proton Synchrotron (SPS) where they are accelerated up to 450 GeV. They are then finally transferred to the LHC and accelerated up to 7 TeV energy per beam. The full CERN accelerator complex is shown in Fig. 3.2. In addition to pp operation, the LHC had heavy nuclei (PbPb) collisions in 2009 and 2011 with an energy of 2.76 TeV per nucleon. The availability of high energy heavy-ion beams at energies over 30 times higher than at the present other accelerators will allow us to further extend the range of the heavy-ion physics program to include studies of hot nuclear matter. The two LHC symmetrical rings are divided into eight octants and arcs and eight straight sections approximately 528 m long. The two high luminosity experimental insertions are located at diametrically opposite straight sections: the A Toroidal LHC ApparatuS (ATLAS) experiment is located at Point 1 and the Compact Muon Solenoid (CMS) experiment at Point 5. The other two large experiments, A Large Ion Collider Experiment (ALICE) and Large Hadron Collider beauty (LHCb), are located at Point 2 and at Point 8, respectively, where the machine reaches a lower design luminosity of $L = 5 \times 10^{32} cm^{-2} s^{-1}$. The remaining four straight sections do not have beam crossings. The two beams are injected into the LHC in two different octants, octant 2 and octant 8 respectively for clockwise and anticlockwise beam. The octants 3 and 7, instead, contain two collimation systems for the beam cleaning.

3.2. Luminosity

The number of events per second generated in the LHC collisions is given by

$$N = L \cdot \sigma \tag{3.1}$$

where σ is the cross section for the collisions process under study and L the machine luminosity. The machine luminosity depends only on the beam parameters and can be written, for a Gaussian beam distribution, as:

$$L = \frac{f \cdot N_1 \cdot N_2}{4\pi\sigma_1\sigma_2} \tag{3.2}$$

Here f is the bunch crossing frequency, N_1 and N_2 are the number of protons in each bunch. If we assume the gaussian beam profile σ_1 and σ_2 gives bunch radius at the

Table 3.1.: typical values of beam perameters for pp and PbPb collisions at LHC

	pp	PbPb
Bunch crossing	25 ns	25 ns
f	40 MHz	40 MHz
Number of bunches	2808	2808
Bunch radius	16 μm	16 μm
Particles per beam	10^{11}	10^{7}
Bunch spacing	7.65 m	7.65 m
Luminosity	7×10^{33}	5×10^{26}

Table 3.2.: LHC runs of heavy ion intrest.

year	system	$\sqrt{s_{\rm NN}}$(TeV)	$L_{\rm int}$
2010	Pb−Pb	2.76	$\sim 10\mu$b^{-1}
2011	pp	2.76	~ 250 nb^{-1}
2011	Pb−Pb	2.76	~ 150 μb^{-1}
2013	p−Pb	5.02	~ 30 nb^{-1}
2013	pp	2.76	$\sim$ 5 pb^{-1}

interaction point. Table 3.1 gives typical values of beam perameters for pp and PbPb collisions at LHC.

With respect to other high energy colliders, the design luminosity of LHC is several orders of magnitudes larger. This is needed because LHC is designed to discover new particles at TeV scale. The production cross section for these particles is extremely small. Therefore more data needs to be collected which can only be achieved by having large luminosity. The LHC luminosity is not constant over physics a run, but decays due to the degradation of intensities and emittance of circulating beams. The main cause of the luminosity decay during normal LHC operation is the beam loss from collisions. The integral of the delivered luminosity over time is called integrated luminosity. It is a measurement of the collected data size, and it is an important value to characterize the performance of an accelerator. Usually, it is expressed in inverse of cross section (i.e. 1/nb or nb^{-1}).

3.3. The Compact Muon Solenoid (CMS) experiment

The CMS experiment is a general purpose proton-proton detector designed to run at the highest luminosity of LHC. Figure 3.3 gives a 3D structure view of the CMS detector. The over all length of CMS detector is 28.7 meter. It has a cylindrical geometry with a radius of 7.5 meter. The detector is extremely heavy with total weight exceeding 14000 tonnes. The design of the CMS detector is based on a compact superconducting solenoid coupled with a muon detector system for optimized muon detection.

The coordinate system of CMS has its origin inside the detector at the primary interaction point. The x-axis points radially towards the center of the LHC, whereas the y-axis points vertically upward. Thus, the z-axis shares the same direction with the beam line. The azimuthal angle ϕ is measured from the x-axis in the x-y plane whereas the polar angle θ is measured from the z-axis.

Particle physicists often use a quantity called rapidity y instead of θ. It is defined as:

$$y = \frac{1}{2} \ln \frac{E + p_z}{E - p_z} = tanh^{-1} \frac{p_z}{E} \tag{3.3}$$

and equals, in case of massless particles, the pseudorapidity η given by

$$\eta = -\ln[\tan(\theta/2)] \tag{3.4}$$

The use of rapidity instead of the polar angle is motivated by the fact that the difference in rapidity between two particles is invariant under Lorentz boosts along the beam axis. The angular distance between two particles observed from the origin of the coordinate system is

$$\Delta R = \sqrt{\Delta\phi^2 + \Delta\eta^2} \tag{3.5}$$

Measurable quantities like momentum and energy transverse to the beam line are denoted by p_T and E_T , respectively, and can be derived from its x and y components.

The CMS detector is located north of the LHC center. The origin of the CMS coordinate system is the CMS collision point. Neglecting the small tilt of the LEP/LHC plane.

The Superconducting solenoid of CMS detector provides a strong magnetic field of 3.8 T. Inside it, the inner tracking comprises a Pixel detector surrounded by the Silicon Strip detector. Its high granularity (70 millions pixels, 10 millions strip) and precision ensures good track reconstruction efficiency. The tracking system of CMS detector covers a range of $|\eta| \leq 2.4$. It is surrounded by Electromagnetic calorimeter (ECAL) made of 76000 lead tungstate crystals grouped in 36 barrel and 4 endcap supermodules. The brass-scintillator sampling hadron calorimeter (HCAL) completes the in-coil detectors. Both ECAL and HCAL have a psudo rapidity coverage of $|\eta| \leq 3.0$. To ensure hermeticity the in-coil calorimetric system is extended, away from the central dector, by the hadron outer detector (HO) and a quartz fiber very forward calorimeter (HF) to cover $|\eta| \leq 5.0$.

Outside the solenoid a muon system is built in the magnet steel return yoke. It's formed by four stations of muon chambers: Drift Tube (DT) in the barrel region, Cathode Strip Chambers (CSC) in the endcap, Resistive Plate Chamber (RPC) in both parts, providing muon detection redundancy. The muon system can reconstruct muons with very good momentum resolution up to $|\eta| \leq 2.4$.

Two trigger levels are employed in CMS. The Level-1 Trigger (L1) is implemented using custom hardware processors and is designed to reduce the event rate to 100 kHz during LHC operation using information from the calorimeters and the muon detectors. It operates nearly dead time-free and synchronously with the LHC bunch crossing frequency of 40 MHz. The High Level Trigger (HLT) is implemented across a large cluster of commodity computers referred to as the event filter farm, and provides further rate reduction to $\mathcal{O}(100)$ Hz using filtering software applied to data from all detectors at full granularity. The overall dimension of CMS are a length of 21.6 m, a diameter of 14.6 m and a total weight of 12500 tons.

A slice of the transverse view of the CMS detector is shown in Figure 3.4. The principle of detection of charged and neutral particles in the various sub-detectors is shown. All charged particles leave signals in the inner tracking system. Electrons and photons deposit their energy in the electromagnetic calorimeter. Charged Hadrons ($K^{\pm}$, $\pi^{\pm}$ ...) and neutrons deposit their energy in the hadronic calorimeter. Muon is a particle which passes through calorimeters without interacting much, but which leaves a track of its passage in the muon chambers. Neutrinos, barely interacting, will escape from all direct detections. While adding the transverse momenta of all the particles detected by

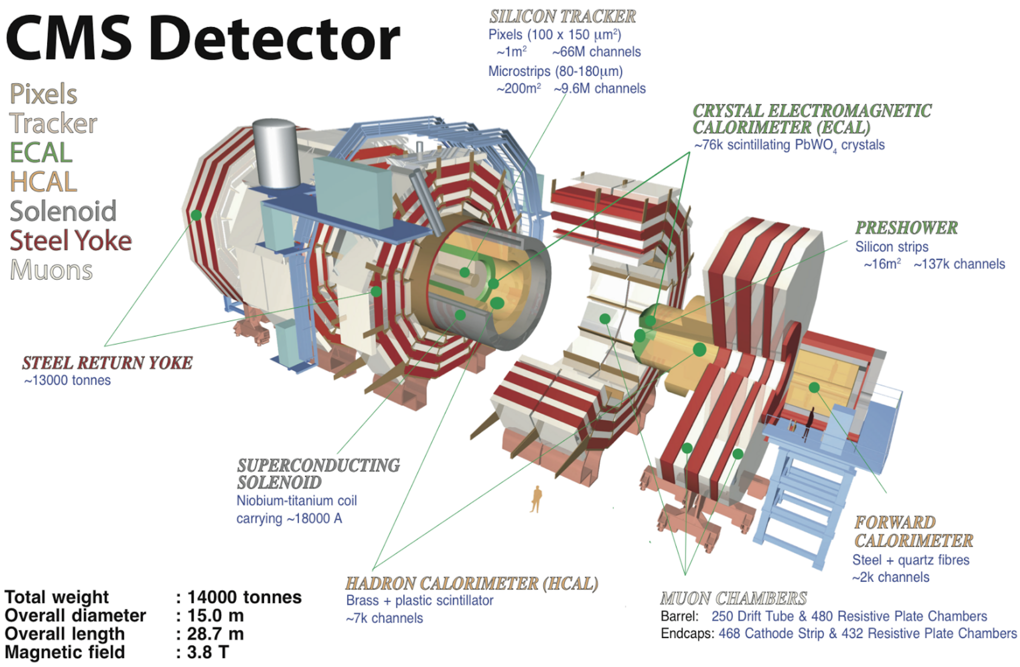

Figure 3.3.: CMS detector figure

the detector, one can determine the imbalance of energy in the transverse plane, so called the missing transverse energy.

3.3.1. Magnet

The superconducting solenoid magnet reaches a maximum magnetic field of 3.8 T in the positive z direction in the inner detectors. A high magnetic field provides a large bending power in the transverse plane for charged particles, which makes possible to reach precise measurement of muon momenta. The magnet is 12.5 m long and with an inner radius of 6 m and is made of four-layers of NbTi. It is the largest superconducting magnet ever built, with the capacity to store an energy of 2.6 GJ at full current. The magnetic flux is returned via a 1.5 m thick iron yoke instrumented with four stations of muon chambers. In this part of the detector the magnetic field is saturated at 2 T. More detailed information can be found in reference [175] Figure 3.5 shows artistic view of CMS magnet, a huminoid is also persent on figure to highlight the huge size of magnet.

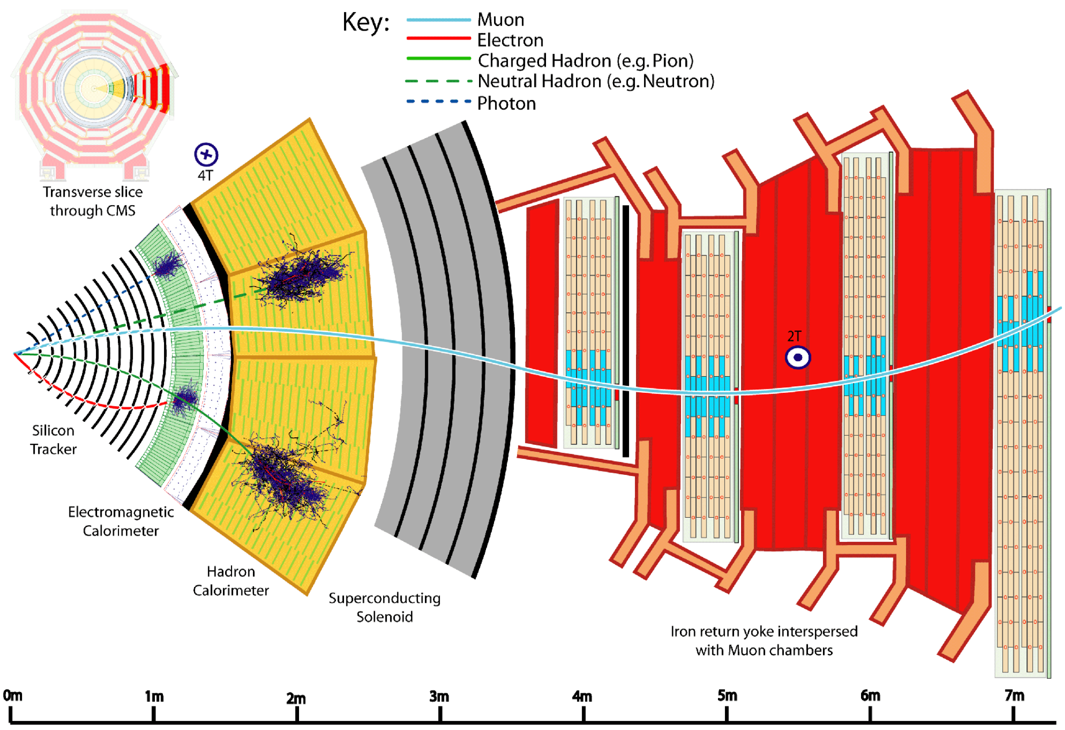

Figure 3.4.: CMS detector figure slice

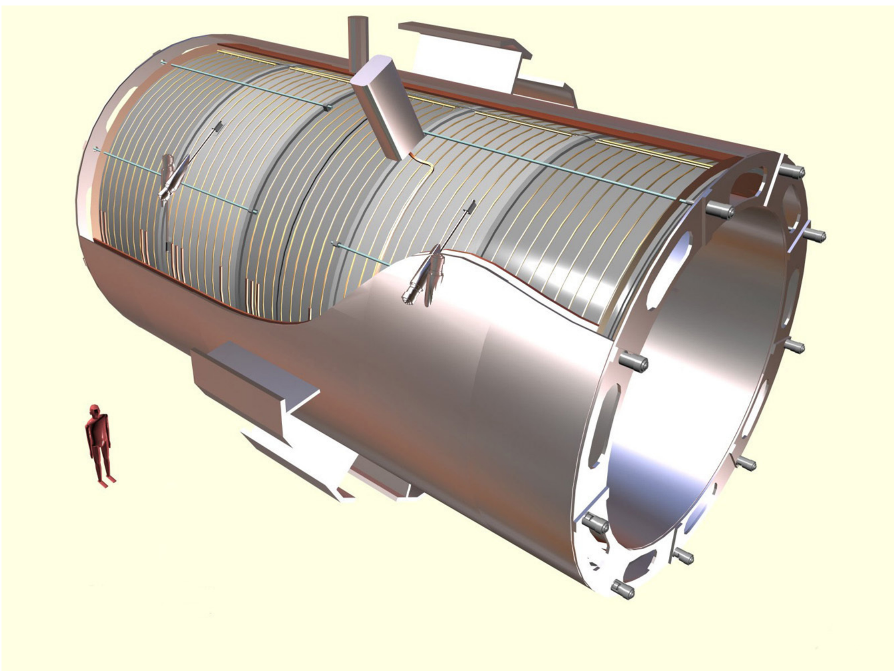

Figure 3.5.: CMS Magnet

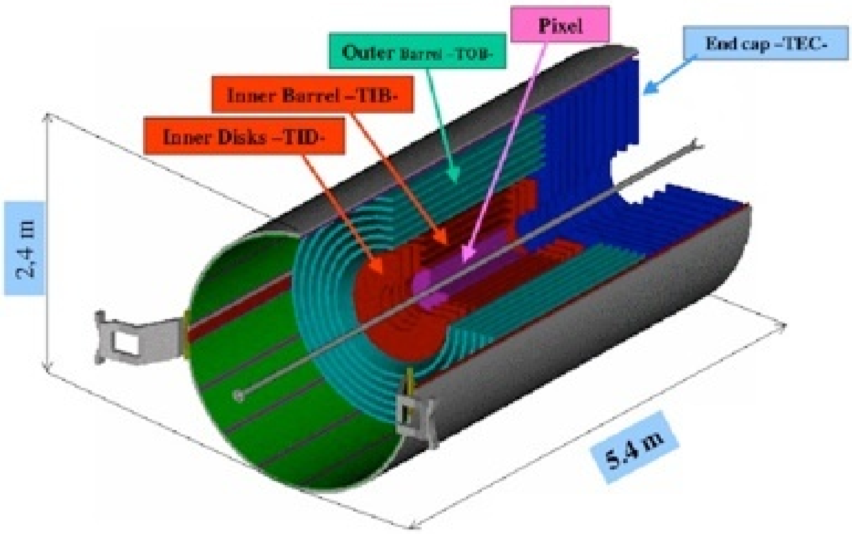

Figure 3.6.: CMS Tracker drawing

3.3.2. Tracker

The Tracker is the subdetector system which is closest to the interaction point, a general layout is presented in Figure 3.6 It is designed to provide an efficient mea- surement of the trajectories of charged particles emerging from the LHC collisions, as well as a precise reconstruction of secondary vertices. The CMS Tracking System is composed of q silicon pixel detector close to the interaction region and a strip detector covering radii from 0.2 m to 1.1 m. The Pixel Detector consists of 1440 pixel modules arranged in three barrel layers and two disks in each end-cap. The barrel layers are located at radii of 4.4, 7.3 and 10.2 cm around the interaction point with a length of 53 cm. On each side of the barrel, two discs are placed at $|z| = 32.5$ cm and 46.5 cm.

3.3.3. Calorimetry

ECAL

The electromagnetic calorimeter (ECAL) is used to measure the energy of photons and electrons. The ECAL is a high precision scintillating crystal calorimeter. The structure of the ECAL can be seen in Figure 3.7. It is composed of 61,200 lead tungstate ($PbWO_4$) crystals in the barrel region and 7,324 crystals in the endcaps. The choice of that material is motivated by its fast response and high radiation resistance and its very good resolution.

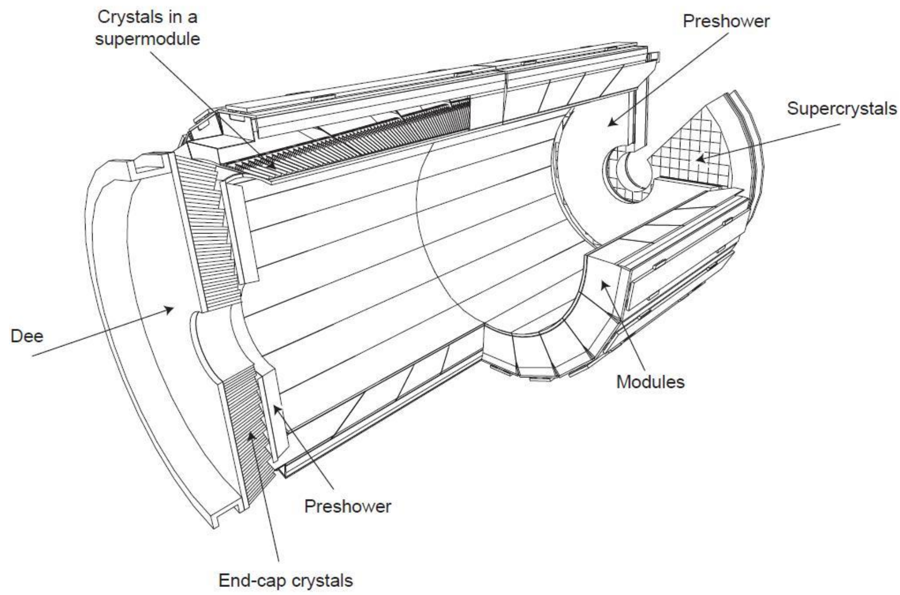

Figure 3.7.: CMS ECAL detector

The ECAL barrel coverage is up to $|\eta| \leq 1.48$; the endcaps extend the coverage to $|\eta| \leq 3.0$. In front of each ECAL Endcap is a preshower detector (ES), from $1.65 \leq |\eta| \leq 2.6$ made from silicon strip detectors in order to identify neutral pions (π^0). The nominal energy resolution, measured with electron beams having momenta between 20 and 250 GeV, is:

$$\frac{\sigma_E}{E} = (\frac{S}{\sqrt{E}})^2 + (\frac{N}{E})^2 + C^2. \tag{3.6}$$

where S is the stochastic term, which includes fluctuations in the shower containment as well as a contribution from photostatistics, N is the noise term, which accounts for the electronic, digitization, and pileup noise, and C is the constant term, which comes from the light collection non-uniformity, errors on the inter-calibration among the modules, and the energy leakage from the back of the crystal.

HCAL

The hadronic calorimeter (HCAL) is designed to measure the energy of hadrons. The HCAL is comprised of four subsystems: the HCAL Barrel (HB), the outer calorimeter (HO), the HCAL Endcap (HE), and the forward calorimeter (HF). Figure 3.8 gives a

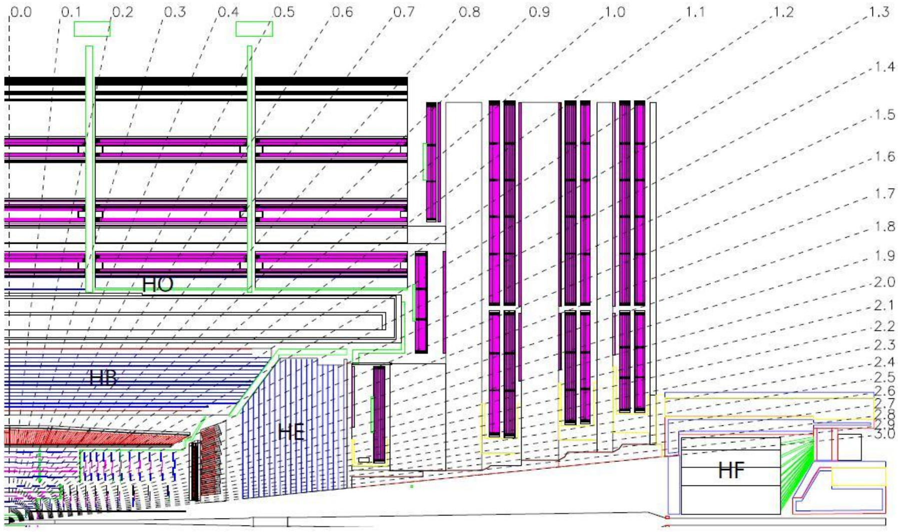

Figure 3.8.: CMS HCAL detector

schematic overview on the HCAL sub-detector. The HB is a sampling calorimeter that covers the range $|\eta| \leq 1.3$. It consists of 36 identical azimuthal wedges aligned parallel to the beamline. It is located between the ECAL and the solenoid coil and is supplemented by the HO located between the solenoid and the muon chambers. The HO is designed to absorb the remnant of the hadronic shower which has not been fully absorbed in the HB. The HE covers a large portion of the solid angle, $1.3 < |\eta| < 3$. Beyond that region, the HF placed at 11.2 m from the interaction point extends the pseudorapidity coverage up to $|\eta| \leq 5.2$. The HE must have high radiation tolerance, with 10 Mrad expected after 10 years of operation. The reason for the absorber material to be non-magnetic is that it must not affect the magnetic field. The HF experiences the harshest radiation environment and therefore requires an extremely radiation tolerant material. The active material chosen is quartz fibers. The fibers are mounted in grooves in the steel absorber plates. The inner part of the HF will be exposed to close to 100 Mrad/year. As the absorber will become radioactive the entire HF can be moved into a garage to limit exposure of personnel during maintenance periods.

3.3.4. CMS muon system

One of the main design objectives of the CMS detector was to obtain a high precision muon momentum measurement, for its key role both in new physics searches and in Standard Model measurements. The CMS muon system uses three diffrent types of gaseous detectors to detect muons. In the barrel region, Drift Tubes (DTs) and Resistive

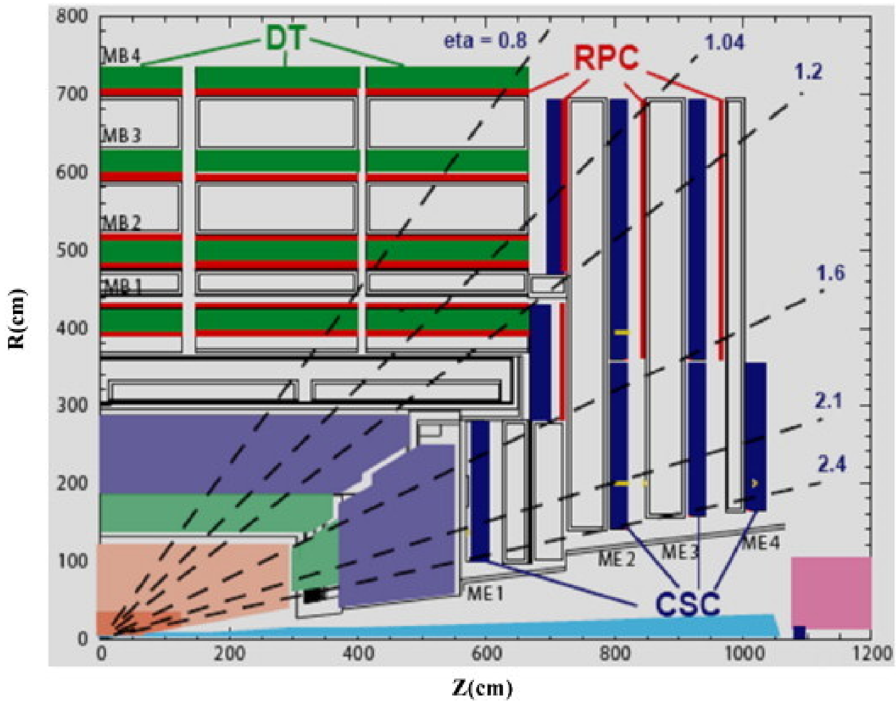

Figure 3.9.: CMS Muon system

Plate Chambers (RPCs) are used, while in the endcap there are Cathode Strip Chambers (CSCs) and also RPCs. The layout of the CMS muon system is shown in Figure 3.9.

Drift tubes

In the central region of CMS, $|\eta| < 1.2$, the muon system consists of four concentric cylinders containing 250 gas drift chambers. Each Drift Tube is filled will a mix of 85% Argon and 15% CO_2 with active wires for charge collection. As muons pass through the gas they leave an ionization trail. The charge drifts to the wires, which detect the charge. The size of the drift cell was chosen so the maximum drift time is 380 ns. There are 172000 active wires in the entire system. The use of DTs is only possible in this region due its low magnetic field.

Cathode strip chambers

In the endcap, the muon system is comprised of Cathode Strip Chambers (CSC). The CSC's cover the 0.9$< |\eta| <$2.4 pseudorapidity range. Each CSC is trapezoidal in shape and consists of 6 gas gaps, each gap having a plane of radial cathode strips and a plane of anode wires running almost perpendicularly to the strips. The CSC is a fast detector (response time of 4.5 ns), but with rather coarse position resolution; a precise position measurement is made by determining the center-of-gravity of the charge distribution induced on the cathode strips (spatial resolution 200 μm, angular resolution 10 mrad).

Resistive plate chamber

In order to improve muon trigger system and for a good measurement of the bunch crossing time, resistive plate chambers (RPC) are mounted in the barrel and endcap region ($|\eta|$ <1.6). The RPCs are able to provide independent and fast trigger with high segmentation and sharp pT threshold over a large portion of the pseudorapidity range. However, the RPCs have coarser position resolution making them more useful for the trigger

3.3.5. Trigger and data acquisition

The CMS trigger system is designed to cope with an unprecedented high luminosity and interactions rates. The LHC will collide proton bunches at a rate of 40 MHz which leads to 10^9 interactions per second at design luminosity. Since it is not possible to record events at this rate, a two-part trigger system, consisting of a hardware-based trigger (Level 1) and a software-based trigger (High Level Trigger) is used [176, 177]. The rate is then reduced by a factor of 10^6.

Level 1 trigger

The Level 1 (L1) trigger is designed to achieve a maximum output rate of 100 kHz and consists of custom-designed, programmable electronics. The front-end (FE) electronics can store information from up to 128 consecutive events, which equates to 3 μs. To cope with the time limitation, the L1 trigger system uses only coarsely segmented data from the muon system and the calorimeters while the full granularity data are stored in the FE electronics waiting for the L1 decision. The L1 muon trigger is organized into subsystems representing the three different muon detectors: the DT trigger in the barrel, the CSC trigger in the endcap and the RPC trigger covering both barrel and endcap. The Level-1 muon trigger also has the Global Muon Trigger (GMT) that combines the trigger information from the DT, CSC, and RPC muon subsystems, as well as from the

Table 3.3.: Typical values of event rates in pp and PbPb collisions at LHC

	pp	PbPb
Luminosity	7×10^{33}	5×10^{26}
σ_{inel}	60 mb	7.65 b
Event rate	4.2×10^{8}Hz	$\approx$4KHz
Pile up (@25 ns)	$\approx$11	no
MB HLT rate	3 KHz	2 KHz
Dimuon HLT rate	30 Hz	15 Hz

calorimeter subsystem, and sends it to the Level-1 Global Trigger. Table 3.3 gives typical values for event rates and trigger rates for pp and PbPb collisions.

High level trigger

The High Level Trigger (HLT) exploits the full amount of collected data for each bunch crossing accepted by Level 1 Trigger and is capable of complex calculations such as the offine ones. It is structured in two levels, Level 2 (L2) and Level 3 (L3) implemented in software. The L2 uses information from the muon spectrometer (parameters from the L1 muon candidates converted into seeds) to perform a standalone reconstruction, providing a muon pT measurement with a precision of about 15 %. The L2 reconstruction follows closely the offine standalone reconstruction using Kalman-filter techniques. The L3 takes L2 candidates as seeds and adds information from the inner tracker by performing track reconstruction in the silicon tracker. This reconstruction is regional, it performs pattern recognition and track fitting only in a small $\eta - \phi$ slice of the tracker, to keep execution time low. Trajectories are then reconstructed using Kalman-filter techniques. Level 3 provides a much more precise p_T measurement (1% - 2% in the barrel region) than Level 2, as well as the ability to select on the basis of the track impact parameter with respect to the beam spot. After the HLT decisions, the event rate decreases down to 100Hz for mass storage which corresponds to a data rate of 150 Mbyte/s.

3.3.6. CMS data flow

Raw data that passed HLT and CMS Online Data Acquisition system (system which collects data from different detectors and builds events) is stored at a storage facility at CERN, known as Tier-0. The raw data contains information for every single proton-proton collision which passed HLT and it is called an event. There are about 10^9 events per year stored at Tier-0. Standard CMS algorithms perform calibration and alignment of the detector using raw data and do prompt (first) reconstruction of physics objects like muons, electrons, jets etc. Later, their momenta, energies and trajectories are measured and this is done by using all detectors of CMS experiment. The output data from prompt reconstruction is saved in different primary datasets based on trigger information. The data from Tier-0 is transferred to Tier-1 storage facilities worldwide where further calibration and re-reconstruction is performed centrally to be used by all CMS analyzes. The Tier-2 centers are more numerous and they are based at different universities in the world. They have limited disk space and are used for running individual analysis and Monte Carlo simulations. Data is stored in three types of root files which contain information about raw, reconstructed and analysis object data, respectively RAW, RECO and AOD root files. The RAW root files contain information about the recorded event in raw format as hits, energy deposits in the detector etc. The RECO root files contain detailed information of reconstructed physics objects and the AOD root files are simplified version of the RECO files which are mostly used in the analyses. Tier-0, Tier-1 and Tier-2 centers form a GRID [178] based computer infrastructure in 35 countries.

Chapter 4.

Measurement of Υ production and suppression in PbPb collisions at $\sqrt{s_{NN}} = 2.76$ TeV

The LHC allows for the first detailed studies of the bottomonium family of states in ultra-relativistic heavy-ion collisions. Given the momentum resolution attained, and the capability of the trigger system, CMS is well positioned to lead these studies. In this chapter, the measurements of the production and suppression of the Υ states are presented. The production of Υ states is studied by comparing their production rates in PbPb and pp collision data, collected by CMS experiment during first LHC heavy ion run. Both data are taken at the same collision energy of $\sqrt{s_{NN}} = 2.76$ TeV.

4.1. Data selection

4.1.1. Event selection

Inelastic hadronic PbPb collisions are selected using information from the Beam Scintillation Counter (BSC) and HF calorimeters, in coincidence with a bunch crossing identified by the Beam Pick-up Timing for Experiments (BPTX) detector (one on each side of the interaction point) [179]. Events are further filtered offline by requiring a reconstructed primary vertex based on at least two tracks, and at least 3 towers on each HF with an energy deposit of more than 3 GeV per tower. These criteria reduce contributions from single-beam interactions with the environment (e.g. beam-gas collisions and collisions of the beam halo with the beam pipe), ultra-peripheral electromagnetic interactions, and cosmic-ray muons. A small fraction of the most peripheral PbPb collisions are not selected by these *minimum-bias* requirements, which accept $(97 \pm 3)\%$ of the inelastic hadronic cross section [7]. A sample corresponding to 55.7 M minimum-bias events passes all these filters. Assuming an inelastic hadronic cross section $\sigma_{\mathrm{PbPb}} = 7.65$ b [7], this sample corresponds to an integrated luminosity of $\int \mathcal{L} = 7.28\,\mu\mathrm{b}^{-1}$. This value is only mentioned for illustration purposes; the final results are normalized to the number of minimum-bias events. The measurements explained here are based on dimuon events triggered by the L1 trigger, a hardware-based trigger that uses information from the muon detectors. The CMS detector is also equipped with a software-based high-level trigger (HLT). However, no further requirements at the HLT level have been applied to the L1 muon objects used for this analysis.

Event Centrality is a key parameter in the study of the properties of QCD matter at extreme temperature and energy density because it is related directly to the initial overlap region of the colliding nuclei. Geometrically, it is defined by the impact parameter, b the distance between the centres of the two colliding nuclei in a plane transverse to the collision axis. Centrality is thus related to the fraction of the geometrical cross-section that overlaps. The event centrality distribution of minimum-bias events is compared to events selected by the double-muon trigger in Figure 4.1. The centrality variable is defined as the fraction of the total cross section, starting at 0% for the most central collisions. This fraction is determined from the distribution of total energy measured in both HF calorimeters [41]. Using a Glauber-model calculation, one can estimate variables related to the centrality, such as the number of nucleons participating in the collisions (N_{part}) and the nuclear overlap function (T_{AA}), which is equal to the number of elementary nucleon-nucleon (NN) binary collisions divided by the elementary NN cross section and can be interpreted as the NN equivalent integrated luminosity per heavy ion collision, at a given centrality [28]. The values of these variables are presented in Tab. 4.1 for the centrality bins used in this analysis. The double-muon-triggered events are more frequent in central collisions since the main physics processes that generate high-p_T muon pairs scale with the number of inelastic nucleon-nucleon collisions. In the following, N_{part} will be the variable used to show the centrality dependence of the measurements.

Simulated MC events for $\Upsilon(1S)$ are used to tune the muon selection criteria, and to compute the acceptance and efficiency corrections. $\Upsilon(1S)$ are produced using PYTHIA 6.424 [8] at $\sqrt{s} = 2.76$TeV, which generates events based on the leading-order color-

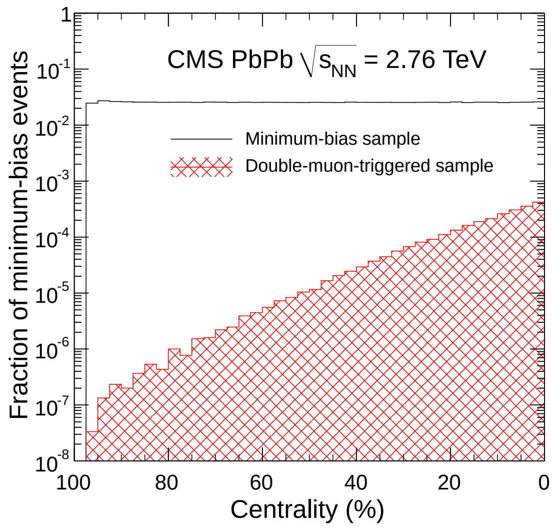

Figure 4.1.: Centrality distribution of the minimum-bias sample (solid black line) overlaid with the double-muon triggered sample (hashed red) in bins of 2.5%.

Table 4.1.: Average and root-mean-square (RMS) values of the number of participating nucleons (N_{part}) and of the nuclear overlap function (T_{AA}) for the centrality bins used in this analysis [7].

	N_{part}		T_{AA} (mb^{-1})	
Centrality (%)	Mean	RMS	Mean	RMS
0–10	355.4	33.3	23.19	3.77
10–20	261.4	30.4	14.48	2.86
20–100	64.2	63.0	2.37	3.05
0–100	113.1	115.6	5.66	7.54

singlet and color-octet mechanisms, with non-relativistic quantum chromodynamics (QCD) matrix elements tuned [180] by comparison with CDF data [117]. Υ(1S) decay is simulated using the EVTGEN [181] package. Υ(1S) are simulated assuming unpolarized production. Final-state bremsstrahlung is implemented using PHOTOS [182]. For some MC simulation studies, in particular the efficiency corrections described in Section 4.3.2, the detector response to each PYTHIA signal event is simulated with GEANT-4 [10] and then embedded in a realistic heavy-ion background event. The background events are produced with the HYDJET event generator [183] and then simulated with GEANT-4 as well. The HYDJET parameters were tuned to reproduce the particle multiplicities at all centralities seen in data. The embedding is done at the level of detector hits and requires that the signal and background production vertices match. Collision data are used to validate the efficiencies evaluated using MC simulations, as discussed in Section 4.3.2.

4.1.2. Muon selection

The muon offline reconstruction algorithm starts by reconstructing tracks in the muon detectors, called *standalone muons*. These tracks are then matched to tracks reconstructed in the silicon tracker by means of an algorithm optimized for the heavy-ion environment [184, 185]. The final muon objects, called *global muons*, result from a global fit of the standalone muon and tracker tracks. These are used to obtain the results presented in this Chapter. In Fig. 4.2, the single-muon reconstruction efficiency from MC simulations is presented as a function of the muon p_T^{μ} and η^{μ}. The reconstruction efficiency is defined as the number of all reconstructed global muons divided by the number of generated muons in a given (η^{μ}, p_T^{μ}) bin. It takes into account detector resolution effects, i.e. reconstructed p_T and η values are used in the numerator and generated p_T and η values in the denominator. To obtain a clear separation between acceptance and efficiency corrections, a *detectable* single-muon acceptance is defined in the (η^{μ}, p_T^{μ}) space. Figure 4.2, shows reconstruction efficiency of global muons in the (η^{μ}, p_T^{μ}) space, the superimposed contour indicated by the white lines matches a global muon reconstruction efficiency of $\sim$ 10%. For the Υ(1S) analysis, all muons with $p_T^{\mu} > 4$ GeV/c are used independent of η^{μ}. Muons failing this conditions are accounted for in the acceptance corrections discussed in Section 4.3.1. Muons that pass this acceptance requirement can still fail to pass the trigger, track reconstruction, or muon selection requirements. These losses are accounted for by the efficiency corrections discussed in Section 4.3.2.

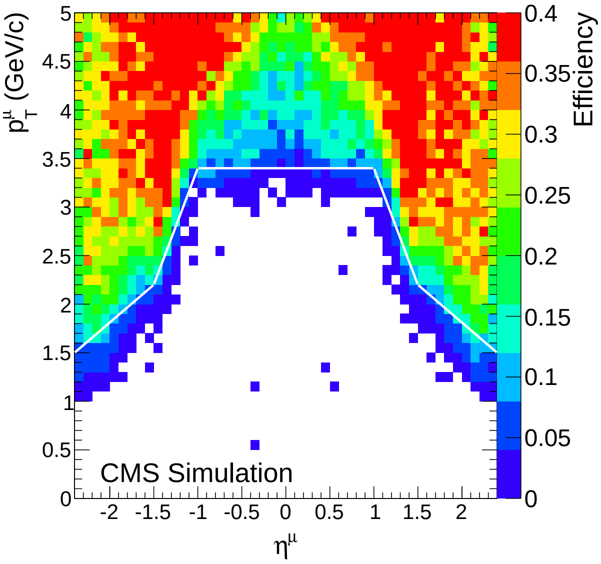

Figure 4.2.: Reconstruction efficiency of global muons in the (η^{μ}, p_T^{μ}) space, illustrating the lower limits (white lines) of what is considered a detectable single muon for the analysis.

Various additional global muon selection criteria are studied in MC simulations. The transverse (longitudinal) distance of closest approach to the measured vertex is required to be less than 3 (15) cm. Tracks are only kept if they have 11 or more hits in the silicon tracker, and the χ^2 per degree of freedom of the global (inner) track fit is less than 20 (4). The χ^2 probability of the two tracks originating from a common vertex is required to be larger than 1%. From MC simulations we find that these criteria result in a 3.9% loss of Υ(1S) events.

4.2. Signal extraction

To extract the Υ(1S) yield, an extended unbinned maximum-likelihood fit to the $\mu^+\mu^-$ invariant mass spectrum between 7 and 14 GeV/c^2 is performed, integrated over p_T, rapidity, and centrality, as shown in the left panel of Fig. 4.3. The measured mass line shape of each Υ state is parametrised by a Crystal Ball function. Since the three Υ resonances partially overlap in the measured dimuon mass spectrum, they are fitted simultaneously. Therefore, the probability distribution function describing the signal consists of three Crystal Ball functions. In addition to the three Υ(nS) yields, the Υ(1S) mass is the only parameter left free, to accommodate a possible bias in the momentum scale calibration. The mass ratios between the states are fixed to their world average values [186], and the mass resolution is forced to scale linearly with the resonance mass. The $\Upsilon(1S)$ resolution is fixed to the value found in the simulation, 92 MeV/c^2. This value is consistent with what is measured when leaving this parameter free in a fit to the data, (122 ± 30) MeV/c^2. The low-side tail parameters in the Crystal Ball function are also fixed to the values obtained from simulation. Finally, a second-order polynomial is chosen to describe the background in the mass range 7–14 GeV/c^2. From this fit, before accounting for acceptance and efficiencies, the measured $\Upsilon(1S)$ raw yield is 86 ± 12. The observed suppression of the excited states will be discussed in Section 4.4.1. The fitted mean value is $m_0 = (9.441 \pm 0.016)$ GeV/c^2, which is, slightly below the PDG value $m_{\Upsilon(1S)} = 9.460$ GeV/c^2 [186] because of slight momentum scale biases in the data reconstruction.

A pp run at $\sqrt{s} = 2.76$TeVwas taken in March 2011. The integrated luminosity was 231 nb^{-1}, with an associated uncertainty of 6%. For hard-scattering processes, the integrated luminosity of the pp sample is comparable to that of the PbPb sample ($7.28\mu\, b^{-1} \cdot 208^2 \approx 315nb^{-1}$). Given the higher instantaneous luminosity, the trigger required slightly higher quality muons in the pp run than in the PbPb run. The offline event selection is the same as in the PbPb analysis, only slightly relaxed for the HF coincidence requirement: instead of three towers, only one tower with at least 3 GeV deposited is required in the pp case. The same reconstruction algorithm, i.e. the one optimized for the heavy-ion environment, is used for both pp and PbPb data. The quarkonium signals in pp collisions are extracted following the same methods as in PbPb collisions. The invariant-mass spectrum of $\mu^+\mu^-$ pairs in the Υ region from pp collisions is shown in 4.3(b).

The data are binned in p_T and rapidity of the $\mu^+\mu^-$ pairs, as well as in bins of the event centrality (0–10%, 10–20%, and 20–100%). The bins in rapidity are $|y| < 1.2$ and $1.2 < |y| < 2.4$. The p_T bins in this analysis are $0 < p_T < 6.5$ GeV/c , $6.5 < p_T <$ 10 GeV/c , and $10 < p_T < 20$ GeV/c . The raw yields of $\Upsilon(1S)$ are tabulated in Table 4.2.

The systematic uncertainties are computed by varying the line shape in the following ways: (i) the Crystal Ball function tail parameters are varied randomly according to their covariance matrix and within conservative values covering imperfect knowledge of the amount of detector material and final-state radiation in the underlying process; (ii) the width is varied by ± 5 MeV/c^2, a value motivated by the current understanding of the detector performance (eg., the dimuon mass resolution, accurately measured at the J/ψ mass, is identical in pp and PbPb collisions); (iii) the background shape is changed from quadratic to linear, and the mass range of the fit is varied from 6–15 to 8–12 GeV/c^2 ;

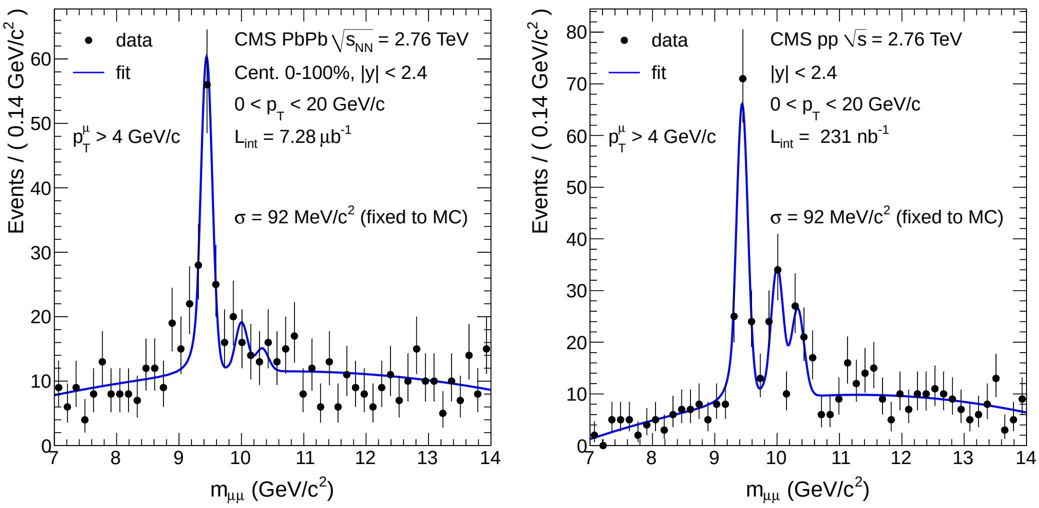

(a) **(b)**

Figure 4.3.: (a) Invariant-mass spectrum of $\mu^+\mu^-$ pairs (black circles) with $p_T < 20$ GeV/c and $|y| < 2.4$, for muons above 4 GeV/c , integrated over centrality. (b)The pp dimuon invariant-mass distribution in the range $p_T < 20$ GeV/c for $|y| < 2.4$ and the result of the fit to the Υ resonances

Table 4.2.: Raw yield of Υ(1S) as a function of Υ(1S) rapidity and p_T in PbPb and pp collisions. For PbPb, the raw yield is also included as a function of collision centrality. All quoted uncertainties are statistical.

$\|y\|$	p_T [GeV/c]	centrality	Raw yield PbPb	Raw yield pp
0.0–2.4	0–6.5	0–100%	44 ± 9	75 ± 10
	6.5–10		18 ± 5	15 ± 5
	10–20		24 ± 6	10 ± 4
	0–20		86 ± 12	101 ± 12
0.0–1.2	0–20	0–100%	48 ± 9	66 ± 9
1.2–2.4			40 ± 8	34 ± 7
0.0–2.4	0–20	0–10%	24 ± 7	
		10–20%	30 ± 7	
		20–100%	32 ± 6	
		0–20%	54 ± 9	

the observed RMS of the results in each category is taken as the systematic uncertainty. The quadratic sum of these three systematic uncertainties is dominated by the variation of the resolution of the mass fit, and is of the order of 10%, reaching 13% for the 0–10% centrality bin. A simple counting of the yield in the signal region after the subtraction of the same-sign spectrum leads to consistent results for yields.

4.3. Acceptance and efficiency

4.3.1. Acceptance

The dimuon acceptance, A, is defined as the fraction of $\mu^+\mu^-$ pairs for which both muons are declared detectable in the CMS detector with respect to all muon pairs produced in $|y| < 2.4$,

$$A(p_T, y; \lambda_\theta) = \frac{N^{\mu\mu}_{\text{detectable}}(p_T, y; \lambda_\theta)}{N^{\mu\mu}_{\text{generated}}(p_T, y; \lambda_\theta)}, \tag{4.1}$$

where:

- $\mathrm{N}^{\mu\mu}_{\text{detectable}}$ is the number of generated events in a given quarkonium (p_T, y) bin in the MC simulation, for which both muons are detectable according to the selections defined in Section 4.1.2.
- $\mathrm{N}^{\mu\mu}_{\text{generated}}$ is the number of all $\mu^+\mu^-$ pairs generated within the considered (p_T, y) bin.

The acceptance depends on the p_T and y of the $\mu^+\mu^-$ pair, and the polarization parameter λ_θ. Different polarizations of the Υ(1S) will cause different single-muon angular distributions in the laboratory frame and, hence, different probabilities for the muons to fall inside the CMS detector acceptance. Since the quarkonium polarization has not been measured in heavy-ion or pp collisions at $\sqrt{s_{NN}} = 2.76$TeV, Υ(1S) results are quoted for the unpolarized scenario only. The acceptance is calculated using the MC sample described in Section 4.1.1. The p_T and rapidity dependencies of the Υ(1S) acceptance are shown in Figure 4.4. J/ψ acceptance is also shown for comparison purpose.

Since the acceptance is a function of both p_T and y, uncertainties in the predicted distributions for these variables can lead to a systematic uncertainty in the average acceptance over a p_T or y bin. To estimate these uncertainties, the shapes of the

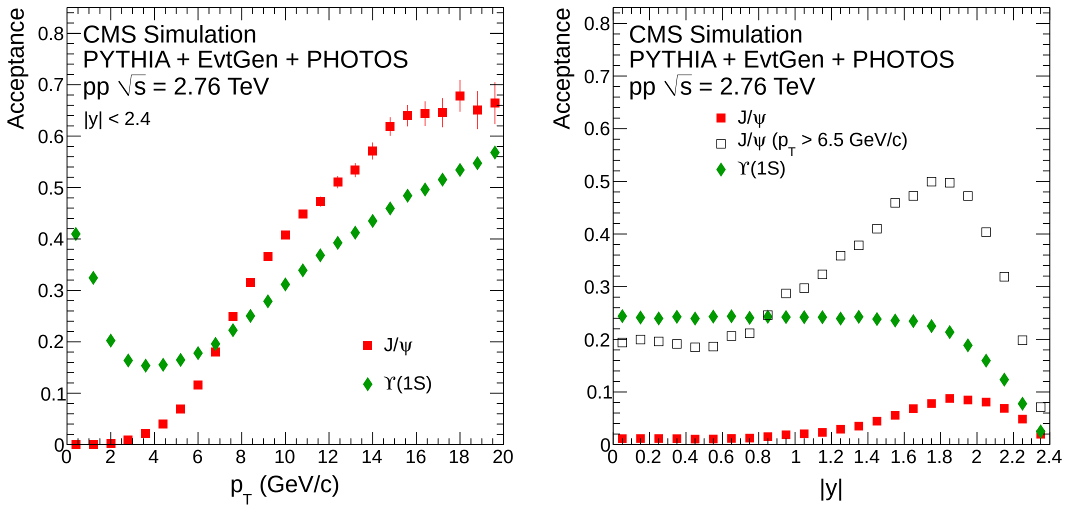

Figure 4.4.: Dimuon acceptance as a function of p_T (left) and $|y|$ (right) for J/ψ (red squares) and Υ(1S) (green diamonds). Also shown in the right panel is the acceptance for J/ψ with $p_T > 6.5$ GeV/c (open black squares). The error bars represent the statistical uncertainties only.

generated MC p_T and $|y|$ distributions are varied by applying a weight that increases linearly from 0.7 to 1.3 over the range $0 < |y| < 2.4$ and $0 < p_T < 20$ GeV/c. The RMS of the resulting changes in the acceptance for each p_T and y bin are summed in quadrature to compute the overall systematic uncertainty from this source. The largest relative systematic uncertainties obtained is 2.8% for the Υ(1S) acceptance.

4.3.2. Efficiency

The trigger, reconstruction, and selection efficiencies of $\mu^+\mu^-$ pairs are evaluated using simulated MC signal events embedded in simulated PbPb events, as described in Section 4.1.1. The overall efficiency is calculated, in each analysis bin, as the fraction of generated events (passing the single muon phase space cuts) where both muons are reconstructed, fulfil the quality selection criteria and pass the trigger requirements. In the embedded sample, the signal over background ratio is by construction higher than in data, so the background contribution underneath the resonance peak is negligible and the signal is extracted by simply counting the $\mu^+\mu^-$ pairs in the quarkonium mass region. The counting method is crosschecked by using exactly the same fitting procedure as if the MC events were collision data. Only muons in the kinematic region ($|\eta^\mu| \leq 2.4, p_T^\mu > 4.0$ GeV/c) are considered. In Figure 4.5, the efficiencies are shown as a function of the $\mu^+\mu^-$ pair p_T, y, and the event centrality, for all signals: red squares for prompt J/ψ, orange stars for non-prompt J/ψ, and green diamonds for $\Upsilon(1S)$. The $\Upsilon(1S)$ efficiency is $\sim$55%, independent of p_T. The efficiencies decrease slowly as a function of centrality because of the increasing occupancy in the silicon tracker; the relative difference between peripheral and central collisions is $\sim$ 10% for $\Upsilon(1S)$. The systematic

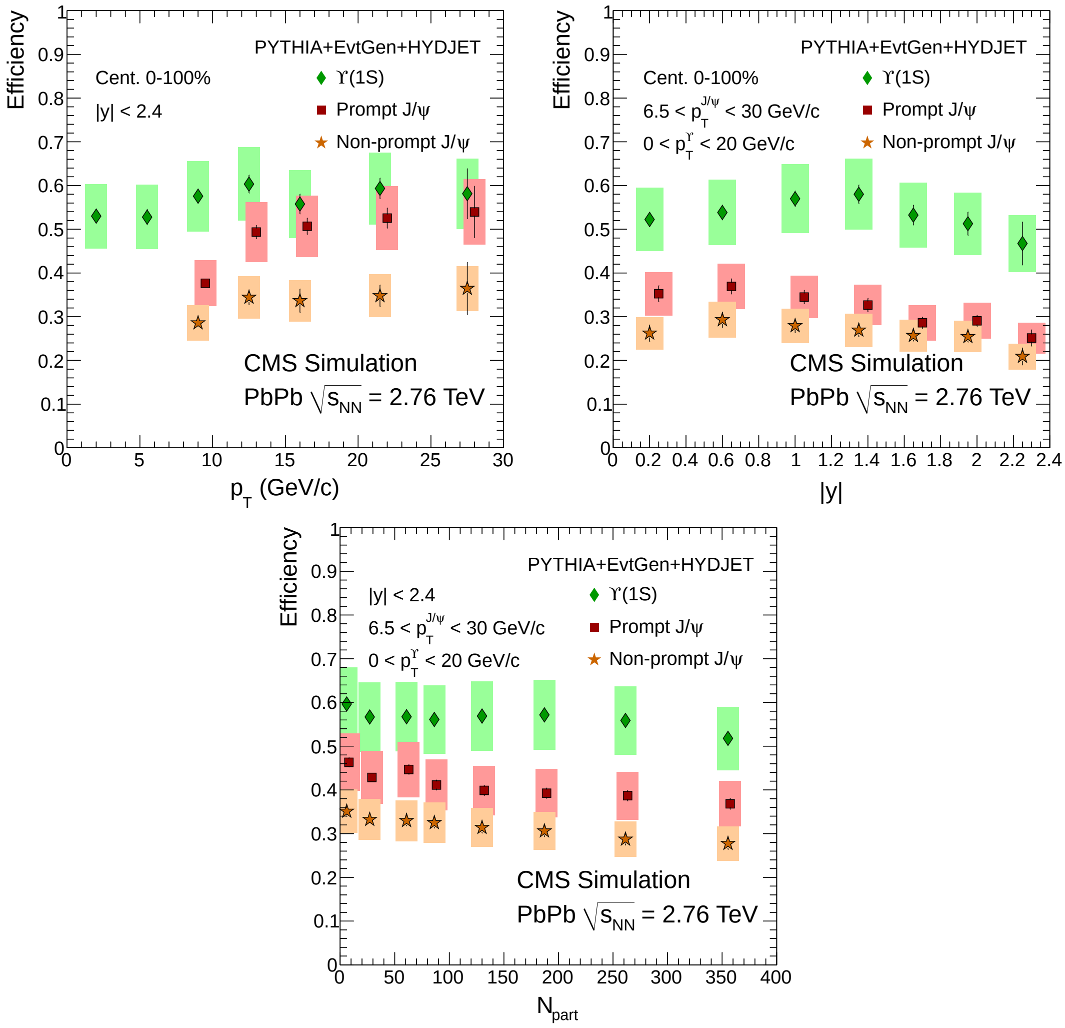

Figure 4.5.: Combined trigger, reconstruction, and selection efficiencies as a function of quarkonium p_T and $|y|$, and event centrality, for each signal: red squares and orange stars for prompt and non-prompt J/ψ, respectively, and green diamonds for $\Upsilon(1S)$. For better visibility, the prompt J/ψ points are shifted by $\Delta p_T = 0.5$ GeV/c , $\Delta y = 0.05$, and $\Delta N_{\text{part}} = 2$. Statistical (systematic) uncertainties are shown as bars (boxes). The systematic uncertainties are the quadratic sum of the uncertainty on the kinematic distributions and the MC validation uncertainty.

uncertainty on the final corrections due to the kinematic distributions is estimated by a $\pm$30% variation of the slopes of the generated p_T and rapidity shapes, similar to the acceptance variation described in the previous section. The systematic uncertainties are in the range of 1.4–2.7% for $\Upsilon(1\mathrm{S})$, including the statistical precision of the MC samples. The individual components of the MC efficiency are crosschecked using muons from J/ψ decays in simulated and collision data with a technique called *tag-and-probe*, similar to the one used for the corresponding pp measurement [187].

4.4. Results

The double-differential quarkonium cross sections in PbPb collisions are reported in the form

$$\frac{1}{T_{AA}} \cdot \frac{\mathrm{d}^2 N}{\mathrm{d}y\,\mathrm{d}p_T} = \frac{1}{T_{AA}\,N_{\mathrm{MB}}} \cdot \frac{1}{\Delta y\,\Delta p_T} \cdot \frac{N_{Q\overline{Q}}}{A\,\varepsilon}, \tag{4.2}$$

while in pp collisions they are calculated as

$$\frac{d^2\sigma}{\mathrm{d}y\,\mathrm{d}p_T} = \frac{1}{L_{\mathrm{pp}}} \cdot \frac{1}{\Delta y\,\Delta p_T} \cdot \frac{N_{Q\overline{Q}}}{A\,\varepsilon}, \tag{4.3}$$

where:

- $N_{Q\overline{Q}}$ is the number of measured $\Upsilon(1\mathrm{S})$ in the $\mu^+\mu^-$ decay channel;
- N_{MB} is the number of minimum-bias events sampled by the event selection; when binned in centrality, only the fraction of minimum-bias events in that centrality bin is considered;
- A is the geometric acceptance, which depends on the p_T and y of the quarkonium state;
- ε is the combined trigger and reconstruction efficiency, which depends on the p_T and y of the quarkonium state and on the centrality of the collision;
- Δy and Δp_T are the bin widths in rapidity and p_T, respectively;
- T_{AA} is the nuclear overlap function, which depends on the collision centrality;
- $L_{\mathrm{pp}} = (231 \pm 14)\mathrm{nb}^{-1}$ is the integrated luminosity of the pp data set.

Following Eq. (4.2), the uncorrected yields of $\Upsilon(1\mathrm{S})$, measured in PbPb collisions are corrected for acceptance and efficiency (reported in Figs. 4.4 and 4.5), and converted into yields divided by the nuclear overlap function T_{AA}. These quantities can be directly compared to cross sections in pp collisions measured from the raw yields according to Eq. (4.3). The rapidity and centrality-dependent results are presented integrated over p_T. All results are presented for the unpolarized scenario and are tabulated in Table A.1 and Table A.2. The systematic uncertainties detailed in the previous sections are summarized in Table 4.3. The relative uncertainties for all terms appearing in Eqs. (4.2) and (4.3) are added in quadrature, leading to a total of 15–21% on the corrected yields. For results plotted as a function of p_T or rapidity, the systematic uncertainty on T_{AA} enters as a global uncertainty on the scale and is not included in the systematic uncertainties of the yields. As a function of centrality, the uncertainty on T_{AA} varies point-to-point and is included in the systematic uncertainties of the yields.

Table 4.3.: Point-to-point systematic uncertainties on Υ(1S) yields measured in pp and PbPb collisions.

	pp (%)	PbPb (%)
Yield extraction	10.0	8.7–13.4
Efficiency	0.4–0.9	1.4–2.7
Acceptance	1.5–2.8	1.5–2.8
MC Validation	13.7	13.7
Stand-alone μ reco.	1.0	1.0
T_{AA}	–	4.3–8.6
Total	17–18	18–20

The nuclear modification factor,

$$R_{AA} = \frac{L_{\text{pp}}}{T_{AA} N_{\text{MB}}} \frac{N_{\text{PbPb}}(Q\overline{Q})}{N_{\text{pp}}(Q\overline{Q})} \cdot \frac{\varepsilon_{\text{pp}}}{\varepsilon_{\text{PbPb}}}\,, \tag{4.4}$$

is calculated from the raw yields $N_{\text{PbPb}}(Q\overline{Q})$ and $N_{\text{pp}}(Q\overline{Q})$, correcting only for the multiplicity-dependent fraction of the efficiency ($\frac{\varepsilon_{\text{pp}}}{\varepsilon_{\text{PbPb}}}$ ~1.16 for the most central bin); the p_T and rapidity dependencies of the efficiency cancel in the ratio. These results are tabulated in Table A.1 and Table A.2. It should be noted that the R_{AA} would be sensitive to changes of the Υ(1S) polarization between pp and PbPb collisions, an interesting physics effect on its own [188]. In all figures showing results, statistical uncertainties are represented by error bars and systematic uncertainties by boxes. Results as a function of rapidity are averaged over the positive and negative rapidity regions.

In Fig. 4.6, the $\Upsilon(1S)$ yield divided by T_{AA} in PbPb collisions and its cross section in pp collisions are shown as a function of p_T; the R_{AA} of $\Upsilon(1S)$ is displayed in the right panel of Fig. 4.6. The p_T dependence shows a significant suppression, by a factor of ∼2.3 at low p_T, that disappears for $p_T > 6.5$ GeV/c . The rapidity dependence indicates a slightly smaller suppression at forward rapidity, as shown in Fig. 4.7. However, the statistical uncertainties are too large to draw strong conclusions on any p_T or rapidity dependence. The $\Upsilon(1S)$ yield in PbPb collisions divided by T_{AA} and the $\Upsilon(1S)$ R_{AA} are presented as a function of N_{part} in the left and right panels of Fig. 4.8, respectively. Within uncertainties, no centrality dependence of the $\Upsilon(1S)$ suppression is observed.

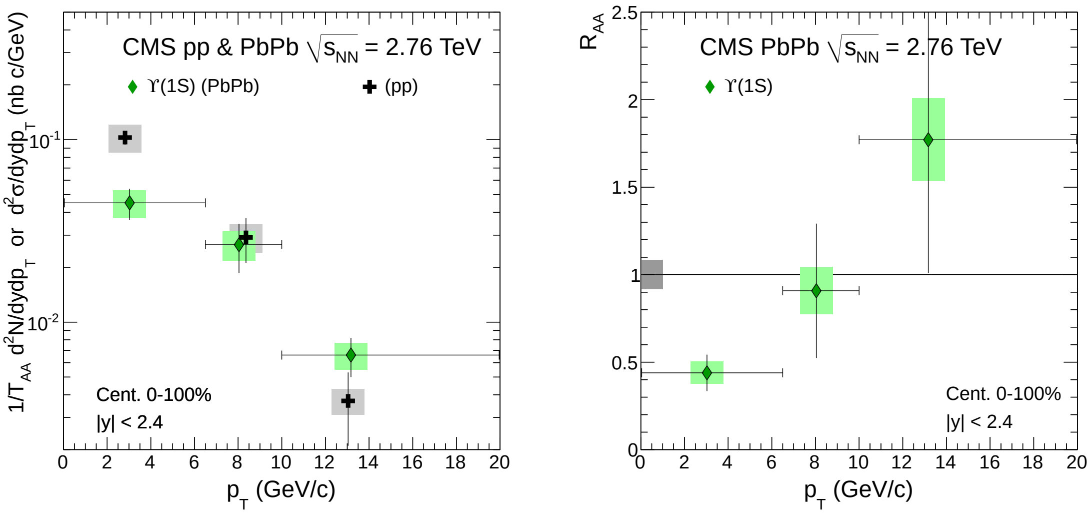

Figure 4.6.: Left: $\Upsilon(1S)$ yield divided by T_{AA} in PbPb collisions (green diamonds) as a function of p_T. The result is compared to the cross section measured in pp collisions (black crosses). The global scale uncertainties on the PbPb data due to T_{AA} (5.7%) and the pp integrated luminosity (6.0%) are not shown. Right: nuclear modification factor R_{AA} of $\Upsilon(1S)$ as a function of p_T. A global uncertainty of 8.3%, from T_{AA} and the integrated luminosity of the pp data sample, is shown as a gray box at $R_{AA} = 1$. Points are plotted at their measured average p_T. Statistical (systematic) uncertainties are shown as bars (boxes). Horizontal bars indicate the bin width.

4.4.1. Indication of suppression of excited Υ states in PbPb collisions at $\sqrt{s_{NN}} = 2.76$ TeV

In this section we will describe the measurement of suppression of excited Υ states in PbPb collisions. A comparison of the relative yields of Υ resonances in the $\mu^+\mu^-$ decay channel in PbPb and pp collisions at a center-of-mass energy per nucleon pair of 2.76 TeV,

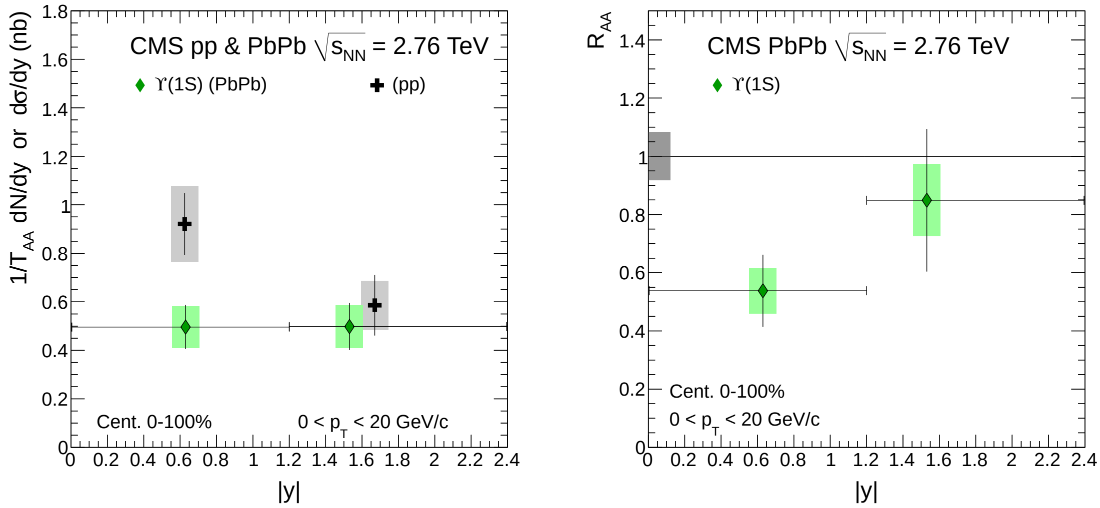

Figure 4.7.: Left: $\Upsilon(1S)$ yield divided by T_{AA} in PbPb collisions (green diamonds) as a function of rapidity. The result is compared to the cross section measured in pp collisions (black crosses). The global scale uncertainties on the PbPb data due to T_{AA} (5.7%) and the pp integrated luminosity (6.0%) are not shown. Right: nuclear modification factor R_{AA} of $\Upsilon(1S)$ as a function of rapidity. A global uncertainty of 8.3%, from T_{AA} and the integrated luminosity of the pp data sample, is shown as a grey box at $R_{AA} = 1$. Points are plotted at their measured average $|y|$. Statistical (systematic) uncertainties are shown as bars (boxes). Horizontal bars indicate the bin width.

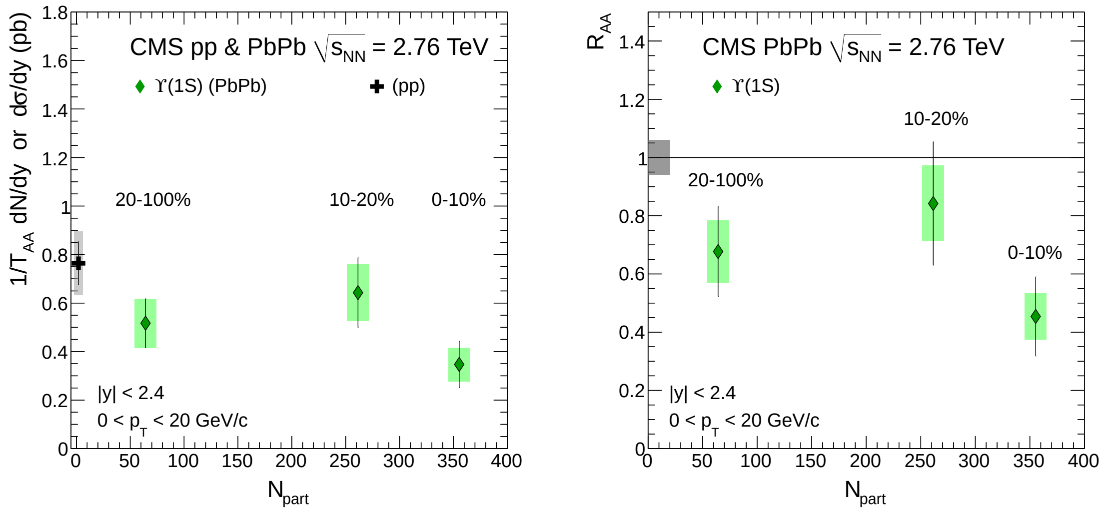

Figure 4.8.: Left: $\Upsilon(1S)$ yield divided by T_{AA} (green diamonds) as a function of N_{part} compared to the $\Upsilon(1S)$ cross section measured in pp (black cross). Right: nuclear modification factor R_{AA} of $\Upsilon(1S)$ as a function of N_{part}. A global uncertainty of 6%, from the integrated luminosity of the pp data sample, is shown as a gray box at $R_{AA} = 1$. Statistical (systematic) uncertainties are shown as bars (boxes).

is performed and the double ratio of the $\Upsilon(2S)$ and $\Upsilon(3S)$ excited states to the $\Upsilon(1S)$ ground state in PbPb and pp collisions, $[\Upsilon(2S+3S)/\Upsilon(1S)]_{PbPb}/[\Upsilon(2S+3S)/\Upsilon(1S))]_{pp}$, is calculated. The dimuon invariant mass spectra with the selection criteria applied, as described in section 4.1 are shown in Figure 4.9 for the pp and PbPb data sets. Within the 7–14 GeV/c^2 mass range, there are 561 (628) opposite-sign muon pairs in the pp (PbPb) data set. The three Υ peaks are clearly observed in the pp case, but the $\Upsilon(2S)$ and $\Upsilon(3S)$ are barely visible over the residual background in PbPb collisions.

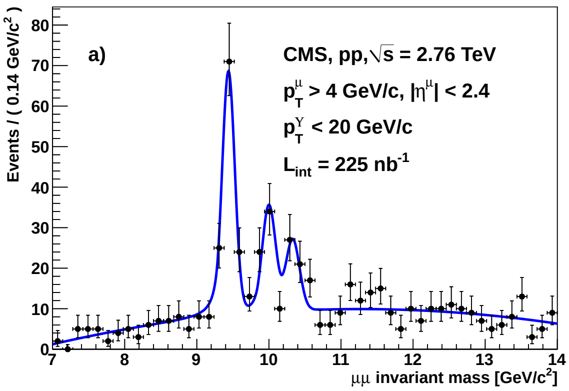

(a)

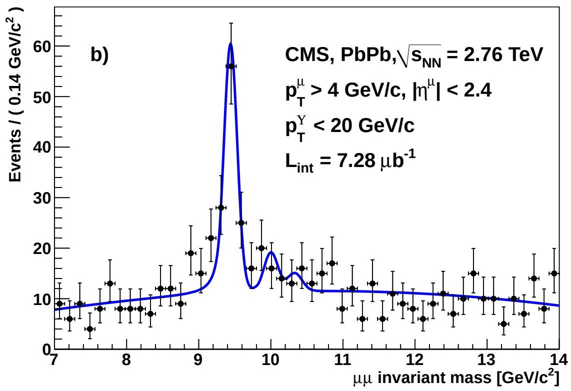

(b)

Figure 4.9.: Dimuon invariant-mass distributions from the pp (a) and PbPb (b) data at $\sqrt{s_{\mathrm{NN}}} = 2.76$ TeV. The same reconstruction algorithm and analysis criteria are applied to both data sets, including a transverse momentum requirement on single muons of $p_T^\mu > 4$ GeV/c. The solid lines show the result of the fit described in the text.

An extended unbinned maximum likelihood fit to the two invariant mass distributions of Figure 4.9 is performed to extract the yields, following the method described in section 4.2. The ratios of the observed yields of the $\Upsilon(2S)$ and $\Upsilon(3S)$ excited states to the $\Upsilon(1S)$ ground state in the pp and PbPb data are:

$$\Upsilon(2S+3S)/\Upsilon(1S)|_{pp} = 0.78^{+0.16}_{-0.14} \pm 0.02, \quad (4.5)$$

$$\Upsilon(2S+3S)/\Upsilon(1S)|_{PbPb} = 0.24^{+0.13}_{-0.12} \pm 0.02, \quad (4.6)$$

where the first uncertainty is statistical and the second is systematic. The systematic uncertainties are computed by varying the lineshape as explained in section 4.2. The quadrature sum of systematic uncertainties gives a relative uncertainty on the ratio of 10% (3%) on the PbPb (pp) data. The ratio of the $\Upsilon(2S+3S)/\Upsilon(1S)$ ratios in PbPb and pp benefits from an almost complete cancellation of possible acceptance and/or efficiency differences among the reconstructed resonances. A simultaneous fit to the pp and PbPb mass spectra gives the double ratio

$$\frac{\Upsilon(2\mathrm{S}+3\mathrm{S})/\Upsilon(1\mathrm{S})|_{\mathrm{PbPb}}}{\Upsilon(2\mathrm{S}+3\mathrm{S})/\Upsilon(1\mathrm{S})|_{\mathrm{pp}}} = 0.31^{+0.19}_{-0.15}\,(\mathrm{stat.}) \pm 0.03\,(\mathrm{syst.}), \tag{4.7}$$

where the systematic uncertainty (9%) arises from varying the lineshape as described above. The difference in reconstruction and selection efficiencies between the Υ states is less than 5% and the variation with charged particle multiplicity is less than 10% from pp to central PbPb collisions, producing a maximum change of 0.5% on the double ratio. The magnitudes of the statistical and systematic uncertainties on the double ratio, respectively 55% and 9%, are significantly larger than the systematic uncertainties associated with possible imperfect cancellation of acceptance and efficiency effects. Therefore no additional uncertainty from these sources is applied. Finally, using an ensemble of one million pseudo-experiments, generated with the signal lineshape obtained from the pp data (Fig. 4.9a), the background lineshapes from both data sets, and a double ratio (Eq. 6.6) equal to unity within uncertainties, the probability of finding the measured value of 0.31 or below is estimated to be 0.9%. In other words, in the absence of a suppression due to physics mechanisms, the probability of a downward departure of the ratio from unity of this significance or greater is 0.9%, i.e. that corresponding to 2.4 sigma in a one-tailed integral of a Gaussian distribution.

4.5. Discussion

The $\Upsilon(1\mathrm{S})$ yield divided by T_{AA} as a function of p_T, rapidity, and centrality has been measured in PbPb collisions. No strong centrality dependence is observed within the uncertainties. The nuclear modification factor integrated over centrality is $R_{AA} = 0.63 \pm 0.11\,(\mathrm{stat.}) \pm 0.09\,(\mathrm{syst.})$. This suppression is observed predominantly at low p_T. Using $p\overline{p}$ collisions at $\sqrt{s} = 1.8$ TeV, CDF measured the fraction of directly produced $\Upsilon(1\mathrm{S})$ as $(50.9 \pm 8.2\,(\mathrm{stat.}) \pm 9.0\,(\mathrm{syst.}))\%$ for $\Upsilon(1\mathrm{S})$ with $p_T > 8$ GeV/c [127]. Therefore, the $\Upsilon(1\mathrm{S})$ suppression presented in this chapter could be indirectly caused by the suppression of excited Υ states. Comparison of the relative yields of Υ resonances has been performed in PbPb and pp collisions at the same center-of-mass energy per nucleon pair of 2.76 TeV. The double ratio of the $\Upsilon(2\mathrm{S})$ and $\Upsilon(3\mathrm{S})$ excited states to the $\Upsilon(1\mathrm{S})$ ground state in PbPb and pp collisions, $[\Upsilon(2\mathrm{S}+3\mathrm{S})/\Upsilon(1\mathrm{S})]_{\mathrm{PbPb}}/[\Upsilon(2\mathrm{S}+3\mathrm{S})/\Upsilon(1\mathrm{S})]_{\mathrm{pp}}$, is found to be $0.31\ ^{+0.19}_{-0.15}$ (stat.) $\pm$ 0.03 (syst.), for muons of $p_{\mathrm{T}} > 4$ GeV/c and $|\eta| < 2.4$.

The probability to obtain the measured value, or lower, if the true double ratio is unity, has been calculated to be less than 1%.

Chapter 5.

Detailed study of Υ suppression in PbPb collisions using 150 μb^{-1} data with CMS detector at the LHC.

First measurement on Υ production and suppression was carried out by us based on the dataset collected during the first LHC PbPb run, at $\sqrt{s_{NN}} = 2.76$ TeV, in 2010, and in the special pp run at the same energy in early 2011. The results included the first evidence for suppression of the excited Υ states relative to the ground state, at the $2.4\,\sigma$ level. These measurements are explained in detail in chapter 4. Main results from these measurements may be summarized as follows:

$$\begin{aligned}
\Upsilon(2\mathrm{S}+3\mathrm{S})/\Upsilon(1\mathrm{S})|_{\mathrm{PbPb}} &= 0.24^{+0.13}_{-0.12} \pm 0.02\,, \\
\Upsilon(2\mathrm{S}+3\mathrm{S})/\Upsilon(1\mathrm{S})|_{\mathrm{pp}} &= 0.78^{+0.16}_{-0.14} \pm 0.02\,, \\
(\chi \equiv)\frac{\Upsilon(2\mathrm{S}+3\mathrm{S})/\Upsilon(1\mathrm{S})|_{\mathrm{PbPb}}}{\Upsilon(2\mathrm{S}+3\mathrm{S})/\Upsilon(1\mathrm{S})|_{\mathrm{pp}}} &= 0.31^{+0.19}_{-0.15} \pm 0.03\,, \\
(R_{AA} \equiv)\frac{\Upsilon(1\mathrm{S})|_{\mathrm{PbPb;\,0-20\%}}}{\Upsilon(1\mathrm{S})|_{\mathrm{pp}}} &= 0.681 \pm 0.143 \pm 0.119\,.
\end{aligned}$$

In the 2011 PbPb run, CMS collected a dataset approximately 20 times larger than that gathered in 2010. These data are analyzed, in order to extract further novel and precision results. In particular, the yield of the higher-mass states is measured relative to the ground state. In this way, we explore the double ratios – Υ(2S,3S) vs Υ(1S) and PbPb vs pp–which allows a self-calibrating measurement. Double ratio is a measured as a function of centrality of collision. Absolute suppression of Υ(1S) and Υ(2S) are measured by calculating nuclear modification factor, R_{AA} as a function of centrality of collision.

5.1. Data selection

In this section selections to choose interesting MB events and further quality criteria applied on muons are explained.

5.1.1. Event selection

Inelastic hadronic PbPb collisions are selected using information from the BSC and HF calorimeters, in coincidence with a bunch crossing identified by the beam pick-up (one on each side of the interaction point) [179]. Events are further filtered offline by requiring a reconstructed primary vertex based on at least two tracks, and at least 3 towers on each HF with an energy deposit of more than 3 GeV per tower. These criteria reduce contributions from single-beam interactions with the environment (e.g. beam-gas collisions and collisions of the beam halo with the beam pipe), ultra-peripheral electromagnetic interactions, and cosmic-ray muons. A small fraction of the most peripheral PbPb collisions are not selected by these *minimum-bias* requirements, which accept $(97 \pm 3)\%$ of the inelastic hadronic cross section [7]. After correcting for this source of inefficiency, a sample corresponding to 1.16×10^9 minimum-bias events passes all these filters. Assuming a PbPb cross-section of 7.65 b [7], this corresponds to an integrated luminosity of $L_{\text{int}} \approx 150\ \mu\text{b}^{-1}$. A pp dataset recorded at $\sqrt{s} = 2.76\,\text{TeV}$ is also used in the analysis. The integrated luminosity is 231 nb^{-1}, with an associated uncertainty of 6%. The measurements explained here are based on dimuon events triggered by the L1 trigger, a hardware-based trigger that uses information from the muon detectors. The trigger used had no constraints on the momentum of the muons.

Simulated MC events are used to tune the muon selection criteria, and to compute the acceptance and efficiency corrections. $\Upsilon(1S)$ are produced using PYTHIA 6.424 [8] at $\sqrt{s} = 2.76\text{TeV}$, which generates events based on the leading-order color-singlet and color-octet mechanisms, with non-relativistic quantum chromodynamics (QCD) matrix elements tuned [180] by comparison with CDF data [117]. $\Upsilon(1S)$ decay is simulated using the EVTGEN [181] package. $\Upsilon(1S)$ are simulated assuming unpolarized production. Final-state bremsstrahlung is implemented using PHOTOS [182]. For some MC simulation studies, in particular the efficiency corrections described in Section 5.3, the detector response to each PYTHIA signal event is simulated with GEANT-4 [10] and then embedded in a realistic heavy-ion background event. The background events are produced with the HYDJET event generator [183] and then simulated with GEANT-4 as well. The HYDJET parameters were tuned to reproduce the particle multiplicities at all centralities seen in data. The embedding is done at the level of detector hits and requires that the signal and background production vertices match. Collision data are used to validate the efficiencies evaluated using MC simulations, as discussed in Section 5.3.

The centrality of heavy-ion collisions, i.e. the geometrical overlap of the incoming nuclei, is related to the energy released in the collisions. In CMS, centrality is defined as percentiles of the distribution of the energy deposited in the HFs. Using a Glauber-model calculation as described in Ref.[7], one can estimate variables related to the centrality, such as the mean number of nucleons participating in the collisions ($\mathrm{N_{part}}$), the mean number of binary nucleon-nucleon collisions ($\mathrm{N_{coll}}$) or the average nuclear overlap function (T_{AA}). The most central (highest HF energy deposit) and most peripheral (lowest HF energy deposit) centrality bins used in the analysis are 0–5% and 50–100%. In the following, $\mathrm{N_{part}}$ will be the variable used to show the centrality dependence of the measurements, and its value, computed for events with flat centrality distribution, ranges from 381 ± 2 in the 0–5% bin to 22 ± 3 in the 50–100% bin.

5.1.2. Muon selection

In order to select good quality muons, different variables were studied. This section describes how the cuts are defined and what is the final set of quality criteria that used in the analysis. Muon candidates are selected if reconstructed as both *global muons* and *tracker muons* (accessed via the standard methods `isGlobal()` and `isTracker()` in CMS software CMSSW). Muon arbitration requirements are applied which insure that one track is used only once when matches to muon detectors. Muon candidates are accepted if belonging to the kinematic region given by

$$|\eta^{\mu}| < 2.4 \quad \text{and} \quad p_T^{\mu} > 4.0\,\mathrm{GeV/c}. \tag{5.1}$$

where the single muon p_T cut was determined with the optimization procedure described below. This region is within acceptance for muon reconstruction.

5.1.3. Cut optimization procedure

The leading figure of merit employed in the optimization study is the Υ(1S) peak significance, $\mathcal{S}$, defined as

$$\mathcal{S} \equiv \frac{N_{\text{signal}}}{\sqrt{N_{\text{signal}} + N_{\text{background}}}}\,, \tag{5.2}$$

where N_{signal} and $N_{\text{background}}$ are the Υ(1S) signal and background yields, respectively, estimated in a $\pm$ 100 MeV/c^2 signal window around the Υ(1S) peak. Each variable will be studied for dimuons falling in the Υ mass range in [7, 14] GeV/c^2. The signal yields are obtained from the Monte Carlo sample by counting the dimuons in the [-0.1, 0.1] GeV/c^2 signal window around the Υ(1S) peak. The background yields are estimated from the data sidebands using two 1 GeV/c^2 wide intervals placed symmetrically around the Υ(1S) peak. The samples used for cut optimization includes:

1. **MC:** realistic Υ embedded in HYDJET PbPb background where the signal efficiency can be studied with the caveat that because one signal is embedded per minimum bias event, the signal over background ratio is greatly over-estimated;
2. **Data:** prompt reconstruction of the data where the background rejection can be studied

5.1.4. Track and muon quality cuts

The following quantities are studied:

- the number of valid hits within the pixels and the strips (inner tracker) a single muon track has, indicating how good the inner track part of the track is;
- the number of pixel layers, with valid hits, crossed by a single muon. There are 2-3% of muons with tracks with 0 pixel hit;
- the χ^2/ndf of the single muon inner track, which indicates the quality of the inner track fit;
- the χ^2/ndf of the single muon global track, which indicates the quality of the global fit;
- the number of muon valid hits;

- the distance between the event vertex and the muon track in the transverse plane, D_{xy}, and the longitudinal plane, D_z, which indicates if the muon comes from a decay in flight or is a prompt muon, and removes cosmics;
- the probability of two tracks to belong to the same decay vertex known as vProb.
- one track sagment is used to match only once with muon system standalone muons known as TrackerMuonArbitrated.

In addition to the significance $\mathcal{S}$, the following factors are also estimated:
(i) The efficiency of the signal using the MC sample, defined as the signal fraction measured after applying the cut, relative the number of signal events found before applying the cut;
(ii) The background rejection, defined as one minus the background fraction estimated after applying the cut, relative to the background yield estimated without the cut.

These estimators are evaluated for each variable, applying all other cuts, as a function of the cut threshold value. Table 5.1 shows the effect on the significance, as well as signal efficiency and background rejection, when applying all other cuts but the one studied. It further gives an indication of the correlation between the cuts. Once the nominal cut thresholds are applied, variations of a single cut have little impact on the significance.

Table 5.1.: Estimated $\Upsilon(1S)$ yield significance, signal efficiency (MC) and background rejection in % after applying all other cuts but the one listed.

Cut Variable	real data 1-ϵ_{Bkg}[%]	MC ϵ_{Bkg}[%]	Significance
InnerTrackHits > 10	51.0	85.0	14.5
PixeLayers > 0	54.1	84.6	14.6
InnerTrackχ^2/ndf <4.	53.2	84.7	14.5
Dxy < 3. cm	54.1	84.6	14.6
Dz < 15. cm	54.1	84.6	14.6
GlobalTrackχ^2/ndf <20	51.8	87.2	15.1
vProb > 0.05	20.2	89.5	13.7
TrackerMuonArbitrated =1	52.7	84.9	14.5
All cuts	54.1	84.6	14.6

5.1.5. Muon kinematic threshold

The single muon p_T cut was chosen according to the described optimization procedure. The results of the calculation are shown in Fig. 5.1 (a), for three different values of the signal mass window size. The points show a maximum at the single muon p_T >4.0 GeV/c, independent of the size of the signal window chosen. This optimization method indicates the best choice of the cut value to be 4.0 GeV/c. Alternative figures of merit were also investigated for single muon p_T cut, which aim at optimizing the precision of the ratio measurement (instead of the 1S peak significance). The alternative method attempts to minimize the uncertainty on the ratio $N(\Upsilon(2\mathrm{S}) + \Upsilon(3\mathrm{S}))/N(\Upsilon(1\mathrm{S}))$, where the ratio is approximately estimated as $2B/(S + B)$. S is the signal counted from the MC $\Upsilon(1\mathrm{S})$ peak and B is the background in the signal window determined from the data sidebands assuming a linear mass shape. The uncertainty on the ratio to be minimized is $\frac{2B}{S+B}\sqrt{\frac{1}{2B} + \frac{1}{S+B}}$, as calculated with standard error propagation and using $\sqrt{S}$ and $\sqrt{B}$ as estimates for the uncertainties on S and B. The results of the calculation are shown in Fig. 5.1 (b), for three different values of the signal mass window size. The points reach a minimum at single muon $p_T > 4$ GeV/c independent of the size of the signal window. This optimization method also favors a p_T cut value at 4 GeV/c.

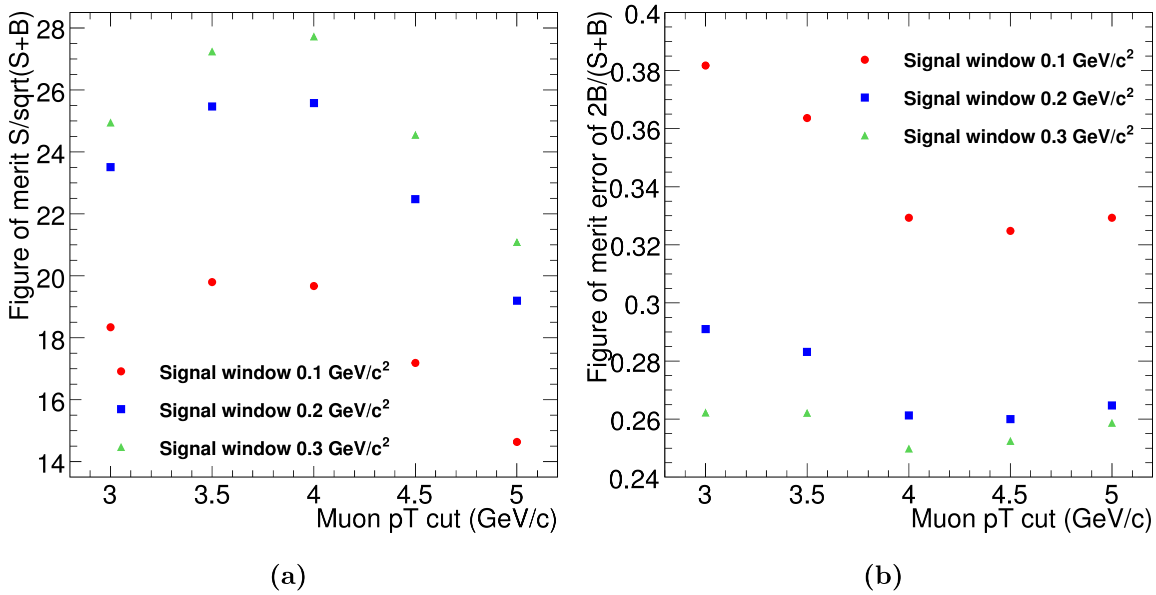

Figure 5.1.: (a) Significance of $\Upsilon(1S)$ peak as a function of the single muon p_T cut.(b) Uncertainty on the $2B/(S+B)$ quantity as a function of the single muon p_T cut.

5.2. Fitting the dimuon spectra

The parameters of interest are extracted from the data samples via an extended unbinned maximum likelihood fit to the dimuon invariant-mass spectra. Each of the Υ(nS) signals is modeled via a crystal-ball shape (CB), which consists of a Gaussian function with the low-side tail replaced by a power law describing final-state radiation (FSR) of muon. The crystal-ball function is given by:

$$f(x;\alpha,n,\bar{x},\sigma) = N \cdot \begin{cases} \exp(-\frac{(x-\bar{x})^2}{2\sigma^2}) & \text{for } \frac{x-\bar{x}}{\sigma} > -\alpha \\ A \cdot (B - \frac{x-\bar{x}}{\sigma})^{-n} & \text{for } \frac{x-\bar{x}}{\sigma} \leq -\alpha\,, \end{cases} \tag{5.3}$$

where

$$\begin{aligned} A &= \left(\frac{n}{|\alpha|}\right)^n \cdot \exp\left(-\frac{|\alpha|^2}{2}\right)\,, \\ B &= \frac{n}{|\alpha|} - |\alpha|\;. \end{aligned}$$

The CB function is parameterized by four parameters – the mass mean $\bar{x}$ and resolution σ, and the tail parameters α and n – which are constrained amongst the three signal peaks: the tail parameters are common for all peaks; the resolution is forced to scale with the resonance mass; the differences of the mass means between states are fixed to their PDG values ($\Delta_{12} = 563\,\mathrm{MeV/c^2}$, $\Delta_{13} = 332\,\mathrm{MeV/c^2}$). The p_T threshold applied for muon selection induces a sculpting of the mass background distribution. The background parameterization adopted corresponds to an exponential function (exp), multiplied by an error-function (erf), The background function is given by:

$$f(x;a;x_0,W) = N \cdot \exp\left(-\frac{x}{a}\right) \cdot (\mathrm{erf}\left(\frac{x-x_0}{W}\right) + 1). \tag{5.4}$$

The background model is thus described by three parameters: the exponential decay constant (a), and the turn-on mean (x_0) and width (W) . All background parameters are left free. The error-function (erf) which is used to describes the induced kinematic shoulder is defined as

$$\mathrm{erf}(x) = \frac{2}{\sqrt{\pi}} \int_0^x e^{-t^2}\,dt \tag{5.5}$$

The nominal fit results to the PbPb data are shown in Fig. 5.2 (a).

The pp dataset used in the analysis was collected by CMS experiment during the first pp run at 2.76 TeV. It corresponds to the integrated luminosity $L_{int} \sim 231\ nb^{-1}$. Same signal perameterization is used for pp data as for PbPb data. A second order polynomial is used as background function for pp dataset. The nominal fit results to the pp data are shown in Fig. 5.2 (b).

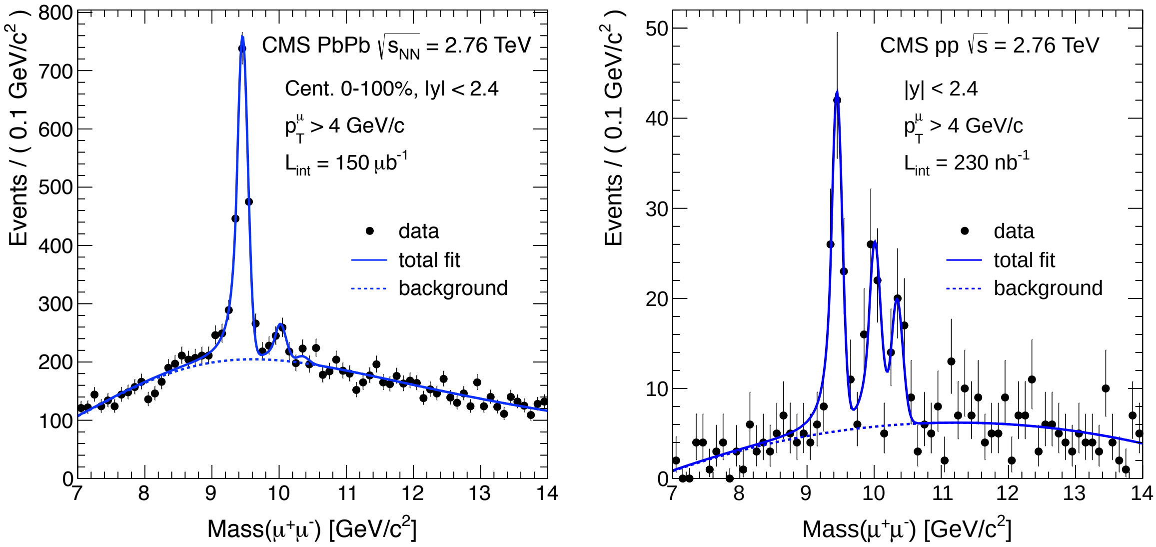

(a) PbPb nominal Fit **(b)** pp nominal Fit

Figure 5.2.: Fit to the dimuon invariant-mass distributions, for the PbPb and pp sample.

5.3. Efficiency correction

The signal reconstruction efficiencies may differ for the individual $\Upsilon(nS)$ states reconstructed in the pp and PbPb data. These are expected to cancel to first order in the double ratio. In this section, these efficiencies and their residual differences are estimated, based on Monte Carlo simulation as explained in section 5.1.1. In particular, in order to estimate the corresponding corrections required for the double ratio, the reconstruction efficiency is calculated as a function of centrality for the Υ(1S) and Υ(2S) states. We use

$$\varepsilon \quad = \quad \frac{N^{\text{dimuons reco,M}}_{|\eta^{\mu}|<2.4,\, p_T^{\mu}>4.0}(p_T, y)}{N^{\text{dimuons gen}}_{|\eta^{\mu}|<2.4,\, p_T^{\mu}>4.0}(p_T, y)} \tag{5.6}$$

where $N^{\text{dimuons gen}}$ is the number of events that fall within our acceptance conditions ($|\eta| < 2.4$, $p_T > 4$ for each of the muons), and $N^{\text{dimuons reco,M}}$ is the number of dimuons that are reconstructed, match the trigger, pass the muon quality cuts presented in Section 5.1.2, and fall within an invariant-mass window of $[9.0, 10.0]$ for $\Upsilon(1S)$ and $[9.5, 10.5]$ for $\Upsilon(2S)$. Yields were estimated by counting and, alternatively, fitting the MC mass spectrum to account for backgrounds. Tables 5.2 show the reconstruction efficiencies of $\Upsilon(1S)$ and $\Upsilon(2S)$ in various centrality bins.

Table 5.2.: Reconstruction efficiency for $\Upsilon(1S)$ and $\Upsilon(2S)$ embedded in MB HYDJET sample.

	Centrality	$\Upsilon(1S)$	$\Upsilon(2S)$
PbPb	$0-100\%$	$48.6 \pm 0.2\%$	$49.3 \pm 0.2\%$
	$0-5\%$	$46.6 \pm 0.6\%$	$47.3 \pm 0.8\%$
	$5-10\%$	$47.1 \pm 0.6\%$	$48.0 \pm 0.8\%$
	$10-20\%$	$49.2 \pm 0.5\%$	$49.0 \pm 0.5\%$
	$20-30\%$	$49.1 \pm 0.5\%$	$50.2 \pm 0.5\%$
	$30-40\%$	$51.0 \pm 0.4\%$	$51.1 \pm 0.5\%$
	$40-50\%$	$51.7 \pm 0.5\%$	$51.5 \pm 0.5\%$
	$50-100\%$	$51.6 \pm 0.3\%$	$53.0 \pm 0.3\%$
	$50-60\%$	$51.1 \pm 0.4\%$	$53.0 \pm 0.4\%$
	$60-100\%$	$52.1 \pm 0.3\%$	$53.0 \pm 0.3\%$
pp	–	$48.7 \pm 0.1\%$	$49.4 \pm 0.2\%$

Figure 5.3 (a) shows the centrality dependence of the $\Upsilon(1S)$ and $\Upsilon(2S)$ total efficiencies in PbPb, compared with the same in pp. The efficiency, for either $\Upsilon(1S)$ or $\Upsilon(2S)$ in PbPb, is shown to decrease slightly as a function of the event centrality (being smallest for the highest multiplicity events, or lowest centrality percentile). This is expected, as the effect of larger tracking reconstruction inefficiencies for the higher track multiplicities which characterize the more central collisions. Figure 5.3 (b) shows the centrality dependence of the $\Upsilon(1S)/\Upsilon(2S)$ ratio of total efficiencies in PbPb, compared with the same in pp. The slightly larger efficiency for $\Upsilon(2S)$ than $\Upsilon(1S)$ arises from the softer muon distribution from $\Upsilon(1S)$ decays.

In order to estimate possible efficiency corrections to the double ratio observable, we calculate the double ratio of efficiencies:

$$\chi_{\text{(efficiency correction)}} \equiv \frac{\varepsilon_{\Upsilon(1S)}/\varepsilon_{\Upsilon(2S)}\,|_{\text{PbPb}}}{\varepsilon_{\Upsilon(1S)}/\varepsilon_{\Upsilon(2S)}\,|_{\text{pp}}}$$

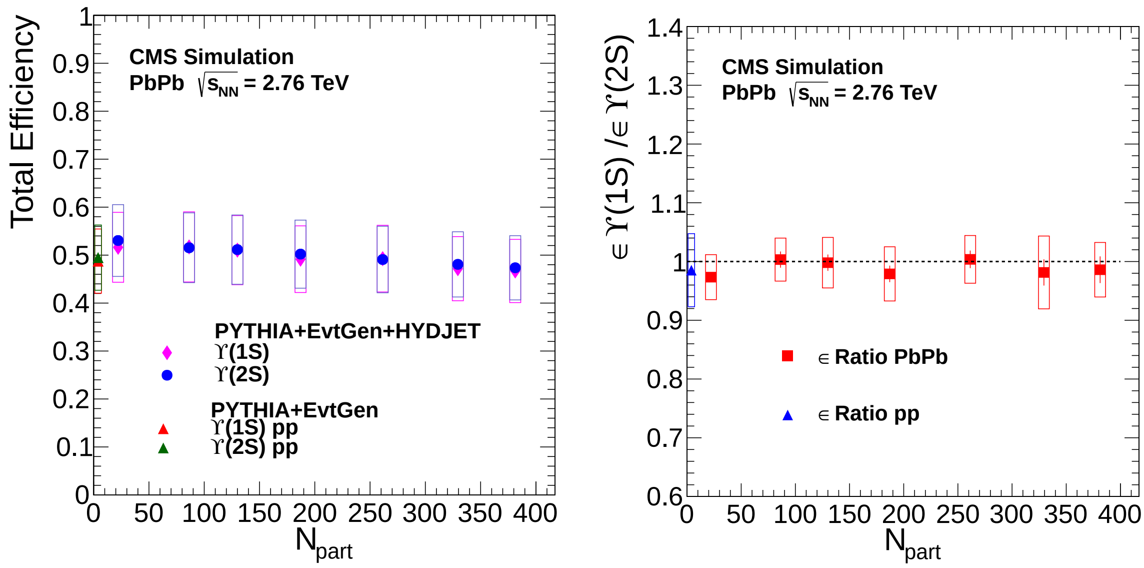

(a) Total Efficiency **(b)** Efficiency Ratio

Figure 5.3.: Total efficiency and their ratios, as a function of event centrality, in PbPb and pp MC.

The value of such a possible correction, evaluated for different centrality bins is found to lie in the range (0.98 to 1.03). This is found to be consistent and fluctuating about unit, the variations are small and negligible compared to the statistical uncertainty expected for the double ratio measurement.

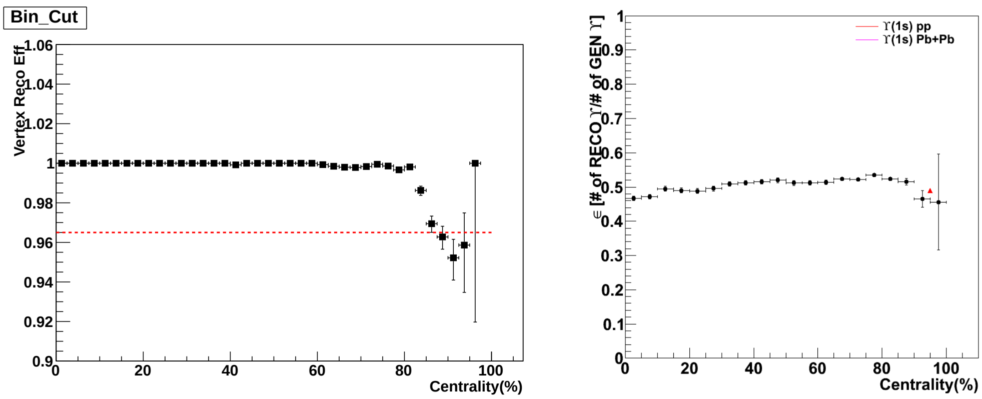

(a) **(b)**

Figure 5.4.: (a) Primary vertex selection efficiency. The horizontal dashed, red line indicates the pp efficiency. (b) Total Υ(1S) efficiency. The red triangle indicates the pp efficiency.

The comparison between pp and PbPb events, shown as the rightmost bins in Fig. 5.3 (a), indicates a larger efficiency for PbPb peripheral than pp, which is not readily expected. This is clarified in Fig. 5.4. It shows a decrease of efficiency for very peripheral ($> 80\%$) events, induced by the primary vertex selection requirement. As seen in Fig. 5.4 (a), the primary vertex selection efficiency is flat in PbPb for centralities up to about 80% and is larger than for pp: $99.7 \pm 0.4\%$ (PbPb) vs $96.5 \pm 0.1\%$ (pp). For peripheral PbPb as well as for pp collisions, which are characterized by small track multiplicities, the primary vertex selection induces inefficiencies. It is shown, finally in Fig. 5.4 (b), that the efficiencies for pp and most peripheral events coincide. In addition to these verifications in MC, the primary vertex selection efficiency was estimated directly in the pp minbias dataset as well: the fraction of events found to satisfy this selection requirement is $95.9 \pm 0.8\%$, in agreement with the pp value estimated in MC quoted above ($96.5 \pm 0.1\%$).

5.4. Relative suppression of excited Υ states

Bottomonium suppression in PbPb collisions is studied in this section by measuring the ratios of observed yields of excited Υ states relative to the ground Υ(1S) state, with the 150 μb^{-1} 2011 PbPb data. The suppression is inferred by performing a comparison of the ratios measured in PbPb against the pp reference. Dependencies on the centrality of the PbPb collision are explored.

5.4.1. Single ratio measurement

The data samples, reconstruction and selection criteria are described in Section 5.1. The parameters of interest are extracted from the data samples directly via an extended unbinned maximum likelihood fit to the dimuon invariant-mass spectra, described in Section 5.2. The following ratios of observed yields of Υ excited states relative to the ground state are studied:

$$R_{23} \equiv \frac{N\left(\Upsilon(2\mathrm{S}) + \Upsilon(3\mathrm{S})\right)}{N(\Upsilon(1\mathrm{S}))}, \tag{5.7}$$

$$R_{2} \equiv \frac{N\left(\Upsilon(2\mathrm{S})\right)}{N(\Upsilon(1\mathrm{S}))}, \tag{5.8}$$

$$R_{3} \equiv \frac{N\left(\Upsilon(3\mathrm{S})\right)}{N(\Upsilon(1\mathrm{S}))}. \tag{5.9}$$

In addition to the combined excited-to-ground ratio, R_{23}, the current statistics allow to extract the separate 2S and 3S ratios, R_2 and R_3. No evidence for the Υ(3S) state is found in the PbPb data, and the only upper limit is calculated for corresponding ratio. These ratios are measured from fits to the PbPb and pp datasets, separately performed. These fits are displayed in Fig. 5.5.

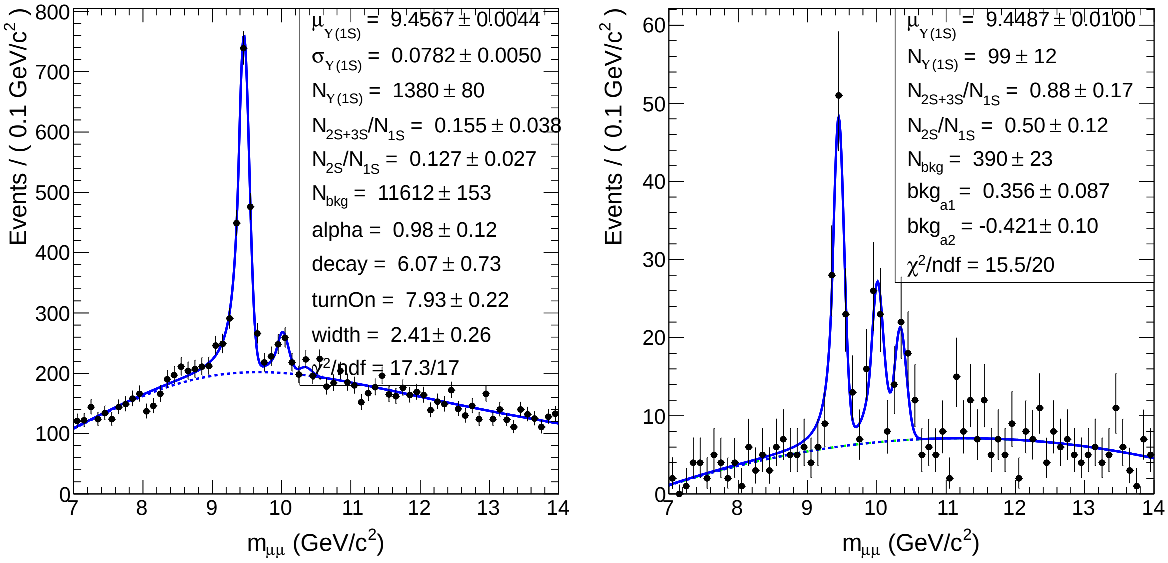

(a) Fit to the PbPb data **(b)** Fit to the pp data

Figure 5.5.: Nominal mass fits, performed separately to the PbPb ($\int \mathcal{L}$=150μb^{-1}) and pp ($\int \mathcal{L}$=231 nb^{-1}) full datasets.

The fit results are shown in Table B.1 for the PbPb data, and in Table B.2 for the pp (2.76 TeV) dataset.

Systemics from fitting procedure

PbPb Data set Various systematic variations of the fit model are performed, to further establish the stability of the results. For the fit to the PbPb data, the following variations are considered:

Signal model variations

- the CB signal tail parameters are fixed ($\alpha = 1.4$)(Fig 5.6a)
- the resolution is fixed ($\sigma_{1S} = 92\,\mathrm{MeV/c^2}$) (Fig 5.6b)

- the signal shape parameters are fixed ($\alpha = 1.4$, $n = 2.3$, $\sigma_{1S} = 92\,\mathrm{MeV/c^2}$) (Fig 5.6c)

Background model variations

- like-sign background modeling: the background model is formed of two components, given by the like-sign distribution and a second order polynomial (`pol2`); the PDF from the like-sign data is obtained from the `RooKeysPdf` smoothing method (Fig 5.6d)
- track-rotation background modeling: (In this method track of one muon is rotated by 180 degree in ϕ direction and then it is combined with the other muon to make dimuon pair) the background model is formed of two components, given by the track-rotation distribution and a second order polynomial (`pol2`); the PDF from the track-rotation data is obtained from the `RooKeysPdf` smoothing method (Fig 5.6e and 5.6f)
- like-sign background modeling: the background model is formed of two components, given by the like-sign distribution and a second order polynomial (`pol2`); the PDF from the like-sign data is obtained from a fit employing the `erf*exp` model (Fig 5.6g)
- track-rotation background modeling: the background model is formed of two components, given by the track-rotation distribution and a second order polynomial (`pol2`); the PDF from the track-rotation data is obtained from a fit employing the `erf*exp` model (Fig 5.6h and 5.6i)

pp Data set Different background systematic variations are used for pp and PbPb data. PbPb data have several additional background sources which are not important for pp data theraml muons are one such example. For the fit to the pp data, these variations are considered:

Signal model variations

- the CB signal tail parameters are fixed ($\alpha = 1.4$)
- the resolution is fixed ($\sigma_{1S} = 92\,\mathrm{MeV/c^2}$)
- the signal shape parameters are fixed ($\alpha = 1.4$, $n = 2.3$, $\sigma_{1S} = 92\,\mathrm{MeV/c^2}$)

Background model variations

- like-sign background modeling: the background model is formed of two components, given by the like-sign distribution and a second order polynomial (`pol2`); the PDF from the like-sign data is obtained from a fit employing the `erf*exp` model
- like-sign background modeling: the background model is formed of two components, given by the like-sign distribution and a second order polynomial (`pol2`); the PDF from the like-sign data is obtained from the `RooKeysPdf` smoothing method
- error function `erf` is used as background shape

The associated systematic uncertainties are summarized in Table B.1 for PbPb, and in Table B.2 for pp. From the several variations, two estimates of the systematic uncertainty are provided: (i) the quadratic-mean deviation relative to the nominal central value, RMS (schematically, $\sqrt{(\sum \text{variation - nominal})^2/(n-1)}$); and (ii) the largest deviation. The latter is used as the estimated systematic uncertainty.

The ratios of the observed yields, not corrected for differences in acceptance and efficiency, of the $\Upsilon(2S)$ and $\Upsilon(3S)$ states to the $\Upsilon(1S)$ state, in the PbPb and pp data, are

$$\begin{aligned}
\Upsilon(2S)/\Upsilon(1S)|_{\mathrm{pp}} &= 0.56 \pm 0.13\,(\text{stat.}) \pm 0.02\,(\text{syst.})\,, \\
\Upsilon(2S)/\Upsilon(1S)|_{\mathrm{PbPb}} &= 0.12 \pm 0.03\,(\text{stat.}) \pm 0.02\,(\text{syst.})\,, \\
\Upsilon(3S)/\Upsilon(1S)|_{\mathrm{pp}} &= 0.41 \pm 0.11\,(\text{stat.}) \pm 0.04\,(\text{syst.})\,, \\
\Upsilon(3S)/\Upsilon(1S)|_{\mathrm{PbPb}} &= < 0.07\ (95\%\ \text{confidence level})\,, \qquad (5.10)
\end{aligned}$$

where the systematic uncertainty arises from the fitting procedure, as described above. For the $\Upsilon(3S)$ to $\Upsilon(1S)$ ratio in PbPb, a 95% confidence level (CL) limit is set, based on the Feldman–Cousins statistical method [189].

5.4.2. Centrality dependence of double ratio

Effects induced by the medium are expected to display, in general, a dependence on the centrality of the collision – the effects are more prominent for the most central collision events, and approaching the most peripheral events tend asymptotically towards the

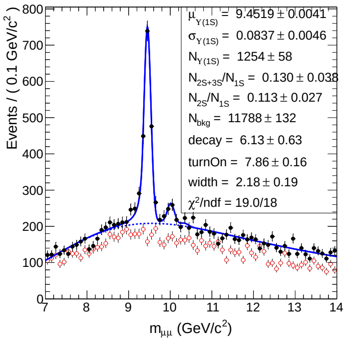

(a) fix CB to MC (alpha = 1.4)

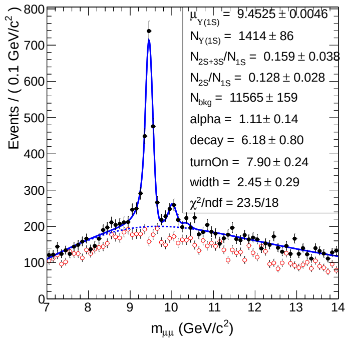

(b) fix resolution to MC

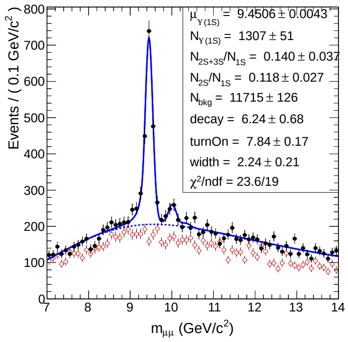

(c) fix CB and resolution to MC

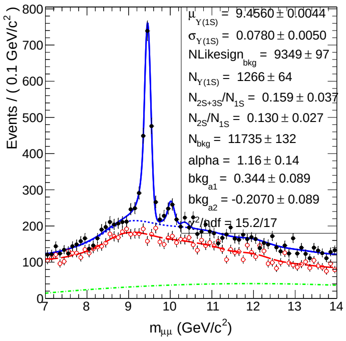

(d) LS keys + pol2

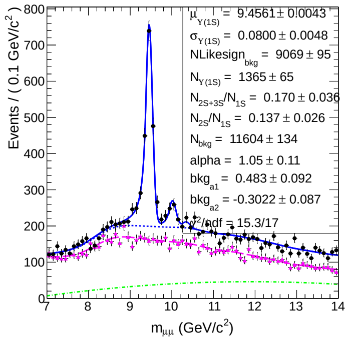

(e) LS TrkRot keys + pol2

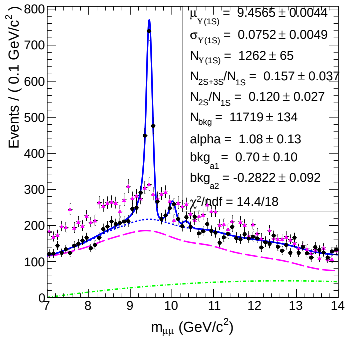

(f) OS TrkRot keys + pol2

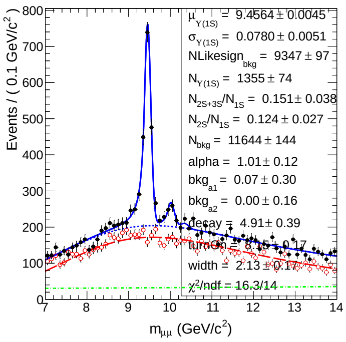

(g) LS erf*exp + pol2

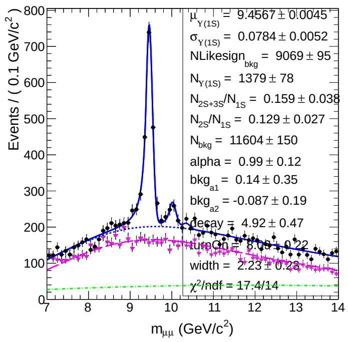

(h) LS TrkRot erf*exp + pol2

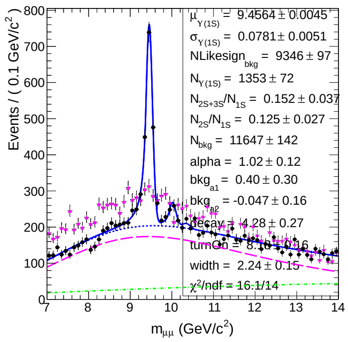

(i) OS TrkRot erf*exp + pol2

Figure 5.6.: PbPb fit model variations ($\int \mathcal{L}$=150μb^{-1}).

results expected in the absence of medium. The pp collision results are taken as reference for absence of nuclear effects. The double ratios are defined as follows:

$$\chi_{23} \equiv \frac{R_{23|\mathrm{PbPb}}}{R_{23|\mathrm{pp}}} = \frac{[N\left(\Upsilon(2\mathrm{S})+\Upsilon(3\mathrm{S})\right)/N(\Upsilon(1\mathrm{S}))]_{\mathrm{PbPb}}}{[N\left(\Upsilon(2\mathrm{S})+\Upsilon(3\mathrm{S})\right)/N(\Upsilon(1\mathrm{S}))]_{\mathrm{pp}}}, \tag{5.11}$$

$$\chi_{2} \equiv \frac{R_{2|\mathrm{PbPb}}}{R_{2|\mathrm{pp}}} = \frac{[N\left(\Upsilon(2\mathrm{S})\right)/N(\Upsilon(1\mathrm{S}))]_{\mathrm{PbPb}}}{[N\left(\Upsilon(2\mathrm{S})\right)/N(\Upsilon(1\mathrm{S}))]_{\mathrm{pp}}}. \tag{5.12}$$

We repeat the single ratio measurement, by splitting the PbPb dataset in ranges of the collision centrality. The mass fit results are shown in Figures B.1. The systematic uncertainties are evaluated for the nominal selection, and summarized in Table B.3. The corresponding differential results are displayed in Fig. 5.7. In these plots, the single ratio values are normalized by the central value of the measurement performed using the pp data. Uncertainties on the single-point pp measurement are not included, as such common uncertainty factor is not relevant for point-to-point comparison in this plot showing the double ratio trend with N_{part}.

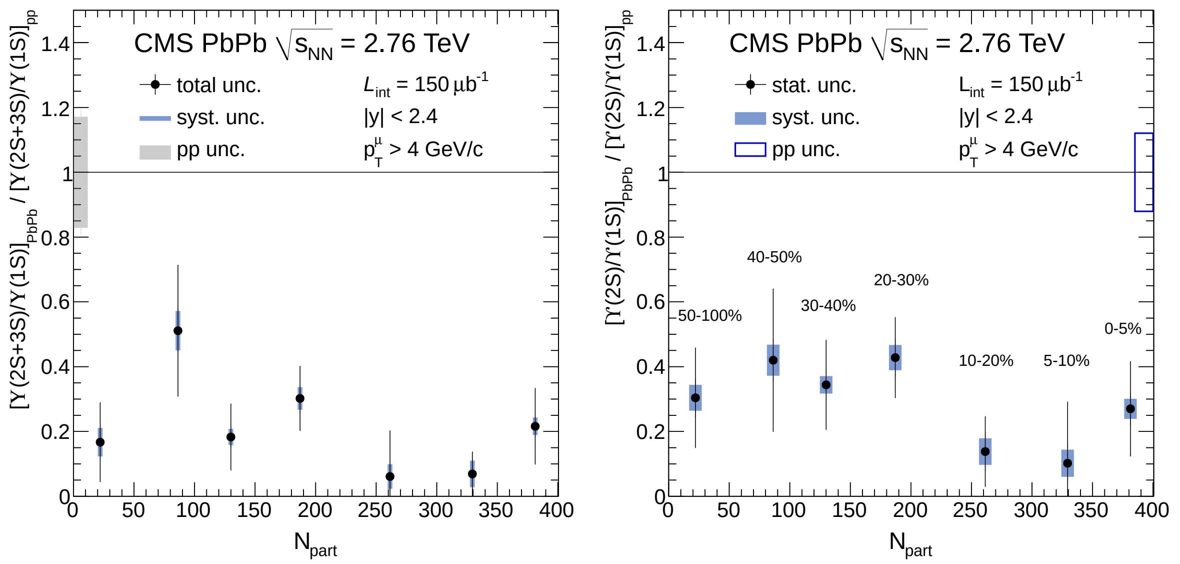

(a) χ_{23},$p_T^{\mu} > 4.0\mathrm{GeV/c}$ **(b)** χ_2, $p_T^{\mu} > 4.0\mathrm{GeV/c}$

Figure 5.7.: Centrality dependence of the double ratios χ_{23} and χ_2; the PbPb statistical and systematic uncertainties are included; the graphs are normalized by the corresponding pp single-ratio central values; pp uncertainties are represented by gray box at unity, and are excluded from the data points as they do not affect point-to-point trend comparison ($\int \mathcal{L}$=150μb^{-1}).

No clear dependence can be inferred within the statistical precision offered by the data. We also note that the most peripheral bin in PbPb and the pp reference do not necessarily match, both because a fully peripheral bin is not accessible given limited statistics in the data, and as a consequence of complexity of the underlying phenomena.

5.5. Absolute suppression of $\Upsilon(\mathrm{nS})$ states

In addition to the *relative* excited-to-ground-state suppression, explored in Sec. 5.4, a measurement of the *absolute* suppression of the individual $\Upsilon(nS)$ states is performed. Additional, relevant information about the suppression phenomena is this way extracted from the data. Such a ratio is estimated via the nuclear modification factor, R_{AA}, which can be calculated using the following defining equation:

$$R_{AA}(\Upsilon(nS)) = \frac{L_{\mathrm{pp}}}{T_{AA}N_{\mathrm{MB}}}\frac{N_{\mathrm{PbPb}}(\Upsilon(nS))}{N_{\mathrm{pp}}(\Upsilon(nS))} \cdot \frac{\varepsilon_{\mathrm{pp}}}{\varepsilon_{\mathrm{PbPb}}} \tag{5.13}$$

and based on raw yields, and correcting for the multiplicity-dependent fraction of the efficiency ($\frac{\varepsilon_{\mathrm{pp}}}{\varepsilon_{\mathrm{PbPb}}}$). The individual terms entering in Eq. 5.13 are:

- N_{pp} and N_{PbPb} are the number of measured $\Upsilon(nS)$ in the pp and PbPb data, respectively;
- L_{pp}, luminosity of the pp 2.76 TeV dataset, 231 ± 14 nb^{-1};
- $N_{\mathrm{MB}} = 1126653312$, is the number of minimum bias events sampled by the event selection. It is multiplied by the centrality bin width for distributions as a function of N_{part};
- T_{AA} is the nuclear overlap function which varies with the centrality of the collision, has units of mb^{-1}, being defined as $T_{AA} = N_{\mathrm{coll}}/\sigma_{\mathrm{pp}}$, with σ_{pp} the inelastic pp cross section.
- ε is the combined trigger and reconstruction efficiency which depends on the p_T and rapidity of the quarkonium state and the centrality of the collision;

5.5.1. Υ(1S) and Υ(2S) R_{AA} measurements

Measurements are provided for the Υ(1S) and Υ(2S) states, individually. The Υ(3S) state is not prominent in the PbPb dataset; an upper limit on the corresponding R_{AA} is presented. The observed Υ(1S) and Υ(2S) yields are summarized in Tables 5.3 and 5.4, for PbPb and pp. The efficiency corrections are those from Table 5.2. The R_{AA} values for the various centrality bins are listed in Table 5.7 and displayed in the graphs in Fig. 5.8 (a). The systematic uncertainties from the yields determination (Tables 5.3, 5.4, method discussed in Sec. 5.4.1), from the efficiency ratio determination from the tag-and-probe systematic and from T_{AA}, are represented as the smaller error bar in the data points of Fig. 5.8. The common systematic uncertainty in Fig. 5.8 contains the pp luminosity measurement systematic (6%) and the pp yield systematic (2.3% for Υ(1S) and 3.3% for Υ(2S)), which is represented in Fig. 5.8 as the gray square at unity. The uncertainty on the R_{AA} measured values is estimated from the uncertainties associated to each term in Eq. 5.13. The statistical uncertainty on the R_{AA} measurement corresponds to the statistical uncertainty on the yields.

Figure 5.8 shows the nuclear modification factor,R_{AA} for Υ(1S) and Υ(2S) as a function of centrality of the collisions. A strong centrality dependence can be observed for the R_{AA} of both Υ(1S) and Υ(2S). R_{AA} for Υ(1S) is almost one in most peripheral collisions (50-100%) but Υ(2S) is significantly suppressed even in most peripheral events. To check this effect the most peripheral bin is splitted in to two bins for Υ(1S). The result is shown in Fig. 5.8 (b). Limitted statistics does not allow the split for Υ(2S). We also studied the stability of R_{AA} results against different single muon p_T cut. Figure 5.9 shows the minimum bias (0-100%) R_{AA} for both Υ states with different single muon p_T cuts. It is clear that the results are compatible within errors for all p_T cuts.

5.5.2. R_{AA} comparisons

A comparison of the centrality-dependent results with Υ(1S) and Υ(2S) R_{AA} with prompt J/ψ R_{AA} and Υ(1S) R_{AA}, measured with 2010 data is shown in Fig. 5.10. Figure 5.10 (a) shows the comparison of Υ(1S) R_{AA} with earlier measurement with a small data sample collected by CMS in 2010. The pp statistical error is treated as bin-to-bin error in the

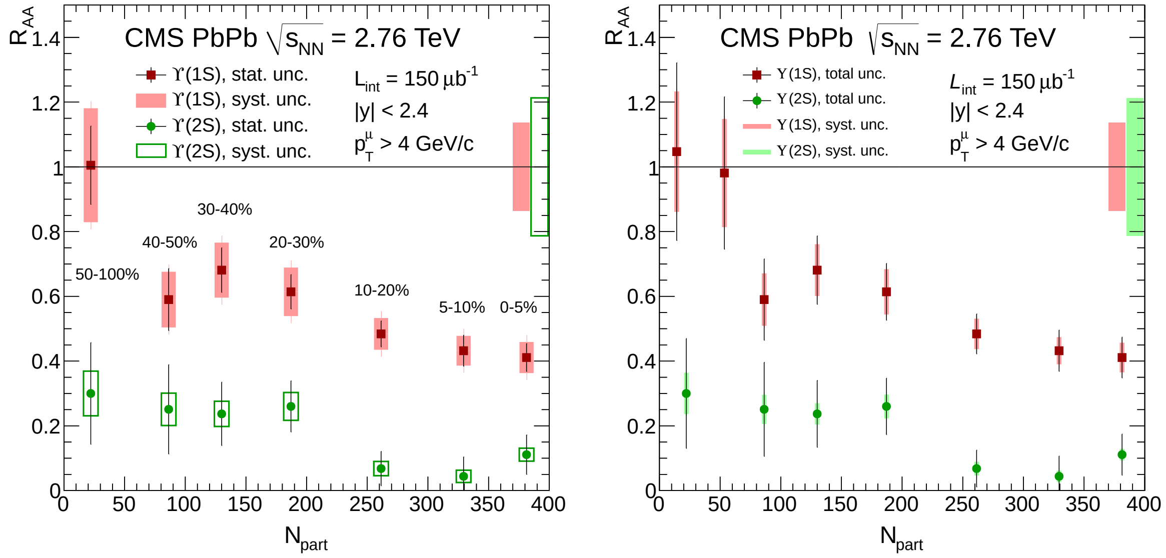

(a) R_{AA} of Υ(1S) and Υ(2S) as a function of centrality of collision.

(b) same as left figure only most peripheral bin is splitted in two bins.

Figure 5.8.: Υ(1S) and Υ(2S) nuclear modification factors, R_{AA}, and their dependence on centrality of collision.

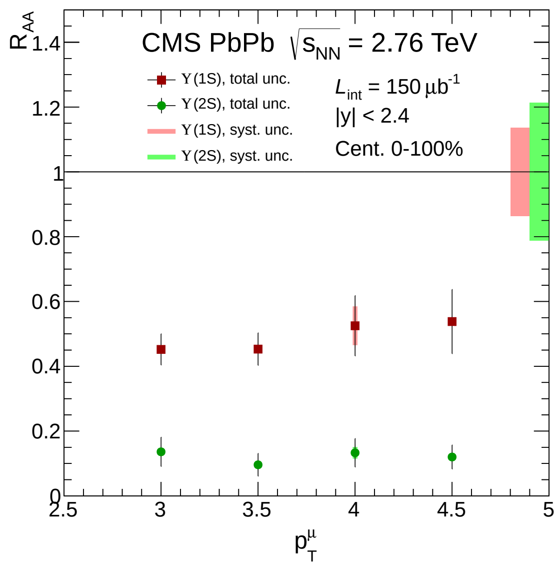

(a) Υ(1S) and Υ(2S) R_{AA} vs muon p_T cut

Figure 5.9.: Υ(1S) and Υ(2S) R_{AA} dependence on muon p_T cut.

Table 5.3.: $\Upsilon(1S)$, $\Upsilon(2S)$ and $\Upsilon(3S)$ raw yields for the PbPb dataset versus centrality.

centrality	$\Upsilon(1S) \pm$ stat. $\pm$ syst.	$\Upsilon(2S) \pm$ stat. $\pm$ syst.	$\Upsilon(3S) \pm$ stat. $\pm$ syst.
0-5%	$237 \pm 25 \pm 21$	$32.0 \pm 17.6 \pm 4.6$	
5-10%	$199 \pm 22 \pm 12$	$10.1 \pm 14.0 \pm 4.2$	
10-20%	$329 \pm 27 \pm 21$	$22.7 \pm 17.9 \pm 6.9$	
20-30%	$253 \pm 22 \pm 19$	$54.1 \pm 16.4 \pm 6.2$	
30-40%	$169 \pm 17 \pm 11$	$29.1 \pm 12.0 \pm 2.8$	
40-50%	$80 \pm 13 \pm 6$	$16.8 \pm 9.2 \pm 2.2$	
50-100%	$116 \pm 14 \pm 7.5$	$17.6 \pm 9.2 \pm 2.4$	
50-60%	$65 \pm 11 \pm 4$		
60-100%	$51.3 \pm 9.9 \pm 4$		
0-100%	$1317 \pm 73 \pm 85$	$156 \pm 38 \pm 14.5$	$31.5 \pm 33.5 \pm 4.3$

Table 5.4.: $\Upsilon(1S)$, $\Upsilon(2S)$ and $\Upsilon(3S)$ raw yields for the pp dataset versus centrality.

	$\Upsilon(1S) \pm$ stat. $\pm$ syst.	$\Upsilon(2S) \pm$ stat. $\pm$ syst.	$\Upsilon(3S) \pm$ stat. $\pm$ syst.
pp data	$88 \pm 11 \pm 2$	$49 \pm 10 \pm 2$	$36 \pm 9 \pm 2$

Table 5.5.: $\Upsilon(1S)$, $\Upsilon(2S)$ and $\Upsilon(3S)$ nuclear modification factors systematics from various sources (in percent).

	MC eff.	Tag and Probe	PbPb fit	T_{AA}	pp fit	pp lumi
$\Upsilon(1S)$	5.36	3	6.5	5.7	2.3	6
$\Upsilon(2S)$	5.45	3	9.3	5.7	3.3	6
$\Upsilon(3S)$	5.45	3	13.7	5.7	4.2	6

2010 data, while in this analysis it is assigned as the common error. Both measurements are compatible with each other within statistical and systematic errors. Figure 5.10 (b) shows the comparison of $\Upsilon(1S)$ and $\Upsilon(2S)$ R_{AA} with prompt J/ψ R_{AA}. It is clear that J/ψ is more suppressed than $\Upsilon(1S)$ and less suppressed than $\Upsilon(2S)$ as expected from sequential melting scenario of quarkonia. Figure 5.11 (a) shows the Comparisons of the $\Upsilon(1S)$ and $\Upsilon(2S)$ R_{AA} result with the $\Upsilon(1S)$ R_{AA} measured by STAR experiment at RHIC. STAR measured $\Upsilon(1S)$ R_{AA} in AuAu collisions at $\sqrt{s_{NN}} = 200$ GeV [171]. It is clear from the figure that $\Upsilon(1S)$ is more suppressed at LHC energies. Figure 5.11 (b) shows the Comparisons of the $\Upsilon(1S)$ and $\Upsilon(2S)$ R_{AA} result with the $\Upsilon(1S)$ R_{AA} measured by ALICE experiment at $\sqrt{s_{NN}} = 2.76$ TeV [190]. ALICE measured $\Upsilon(1S)$

Table 5.6.: Υ(1S) and Υ(2S) nuclear modification factors systematic for centrality bins (in percent).

	Υ(1S)				Υ(2S)			
N_{part} (centrality)	MC eff.	TnP	PbPb fit	T_{AA}	MC eff.	TnP	PbPb fit	T_{AA}
381 (0- 5%)	5.15	3	8.9	4.1	5.68	3	14.4	4.1
329 (5- 10%)	6.64	3	6.0	4.6	5.71	3	41.6	4.6
261 (10- 20%)	4.77	3	6.4	5.2	5.46	3	30.4	5.2
187 (20- 30%)	5.90	3	7.5	6.6	4.98	3	11.5	6.6
130 (30- 40%)	5.36	3	6.5	8.5	5.19	3	9.6	8.5
86 (40- 50%)	5.18	3	7.5	10.9	4.74	3	13.1	10.9
22 (50-100%)	5.26	3	6.5	15.0	4.86	3	14.2	15.0
54 (50- 60%)	5.00	3	6.2	15.0				
14 (60-100%)	5.39	3	7.8	15.0				

Table 5.7.: Υ(1S), Υ(2S) and Υ(3S) nuclear modification factors, R_{AA}, versus centrality.

N_{part} (centrality)	Υ(1S) $\pm$ syst. $\pm$ stat.	Υ(2S) $\pm$ syst. $\pm$ stat.	Υ(3S) $\pm$ syst. $\pm$ stat.
381 (0- 5%)	$0.41 \pm 0.05 \pm 0.04$	$0.11 \pm 0.02 \pm 0.06$	
329 (5- 10%)	$0.43 \pm 0.05 \pm 0.05$	$0.04 \pm 0.02 \pm 0.06$	
261 (10- 20%)	$0.48 \pm 0.05 \pm 0.04$	$0.07 \pm 0.02 \pm 0.05$	
187 (20- 30%)	$0.61 \pm 0.08 \pm 0.05$	$0.26 \pm 0.04 \pm 0.08$	
130 (30- 40%)	$0.68 \pm 0.09 \pm 0.07$	$0.24 \pm 0.04 \pm 0.10$	
86 (40- 50%)	$0.59 \pm 0.09 \pm 0.10$	$0.25 \pm 0.05 \pm 0.14$	
22 (50-100%)	$1.01 \pm 0.18 \pm 0.12$	$0.30 \pm 0.07 \pm 0.16$	
54 (50- 60%)	$0.98 \pm 0.17 \pm 0.17$		
14 (60-100%)	$1.05 \pm 0.19 \pm 0.20$		
114 (0-100%)	$0.56 \pm 0.07 \pm 0.08$	$0.12 \pm 0.02 \pm 0.04$	$0.03 \pm 0.01 \pm 0.04$

R_{AA} in forward rapidities ($2.5 < y^{\Upsilon} < 4.0$) while our measurement is in mid rapidity ($2.4 < |y^{\Upsilon}|$). ALICE measurement shows that Υ(1S) is more suppressed in forward rapidities. It indicate towards stronger cold matter effects at forward rapidities.

Figure 5.12 shows comparison of our measurement with some theory models. Figure 5.12 (a) shows comparison to a model by Strickland [191]. In this model p_T dependent survival probabilities are calculated using lattice based potentials. Anisotropic hydrodynamics is used for medium evolution. Model calculations are in good agreement with

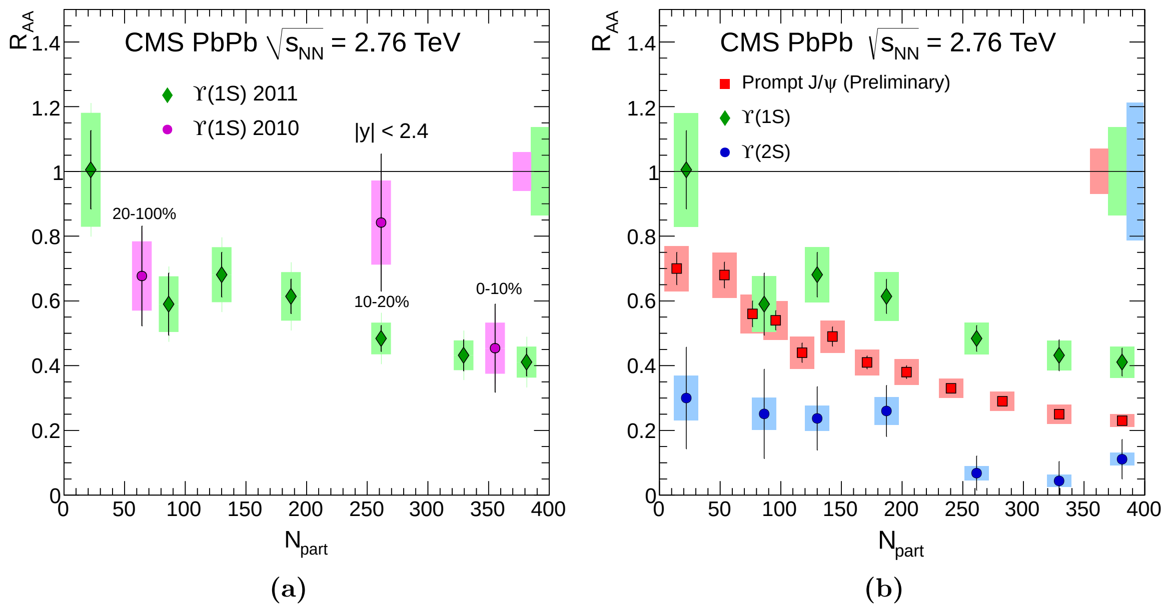

Figure 5.10.: (a) Compare Υ(1S) and Υ(2S) R_{AA} with previous Υ(1S) R_{AA} measurement and (b) comparison with prompt J/ψ R_{AA} measured by CMS.

the measurement. Figure 5.12 (b) shows comparison with a model which uses kinetic equation approach [173]. It uses strong binding scenario i.e. the potential between $b\bar{b}$ does not get modified in thermal medium. The significance of cold-nuclear-matter effects has been simulated by employing two nuclear absorption cross sections to estimate an upper and lower bound. For LHC 0.0 mb and 2.0 mb are used to produce the bands seen in the Fig. 5.12 (b). The regeneration component is calculated during plotting as "Total R_{AA}" - "Primordial R_{AA}". This model also gives good description of data.

5.6. Summary and interpretation

The relative suppression of the Υ excited states has been measured, based on the 150 μb^{-1} of the 2011 PbPb dataset. The larger luminosity of the PbPb dataset allows to carry out the measurement in ranges of centrality of the collision. The results indicate a significant suppression of the Υ(nS) states in heavy-ion collisions compared to pp collisions at the same per-nucleon-pair energy. The data support the hypothesis of increased suppression of less strongly bound states: the Υ(1S) is the least suppressed and the Υ(3S) is the most suppressed of the three states. The Υ(1S) and Υ(2S) suppression is observed to increase with collision centrality. The suppression of Υ(2S) is stronger

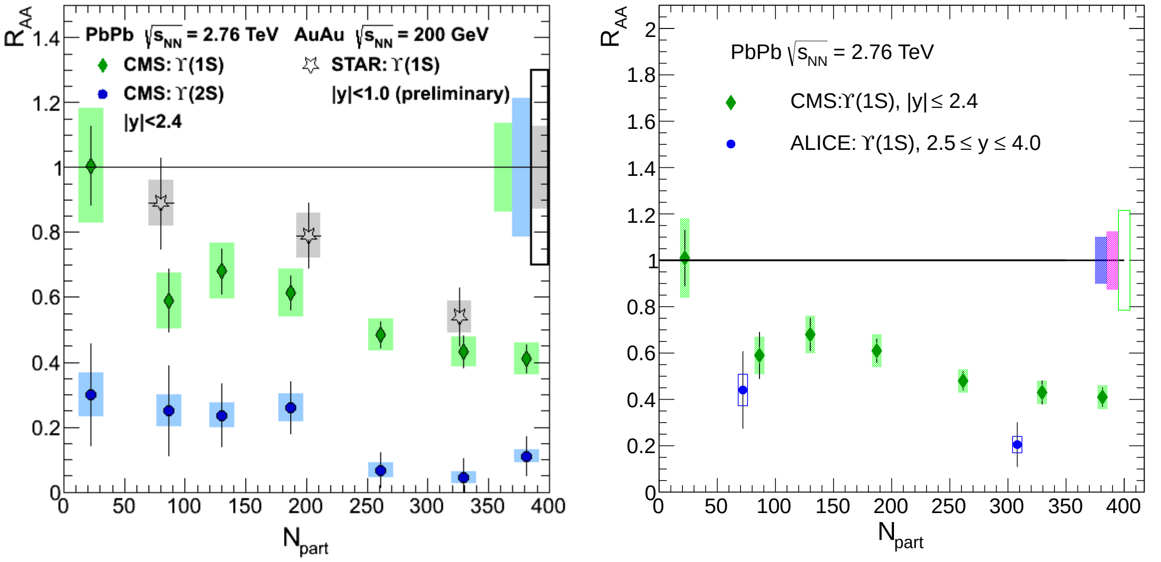

(a) (b)

Figure 5.11.: Comparison of the Υ(1S) R_{AA} results with the STAR experiment[171] and ALICE experiments[190].

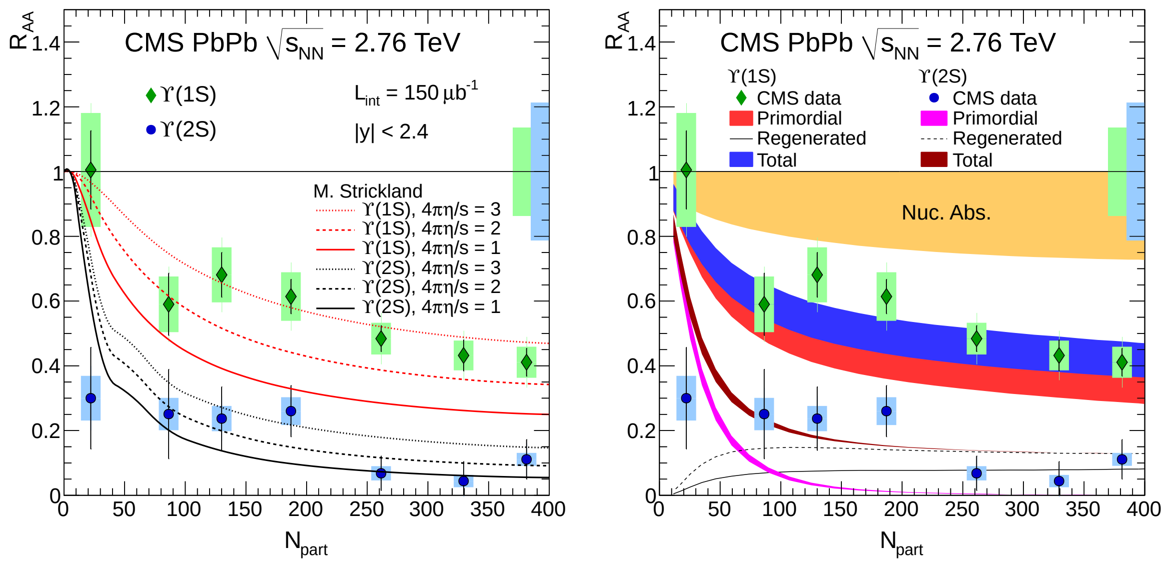

(a) (b)

Figure 5.12.: Comparison of the Υ(1S) R_{AA} results with the the model Calculations.

than that of Υ(1S) in all centrality ranges, including the most peripheral bin. It should be noted that this bin (50–100%) is rather wide and mostly populated by more central events (closer to 50%). For this most peripheral bin the Υ(1S) nuclear modification factor is $1.01 \pm 0.12\,(\text{stat.}) \pm 0.22\,(\text{syst.})$, while for the most central bin (0–5%) R_{AA} is $0.41 \pm 0.04\,(\text{stat.}) \pm 0.07\,(\text{syst.})$ indicating a significant suppression.

The observed Υ yields contain contributions from decays of heavier bottomonium states and, thus, the measured suppression is affected by the dissociation of these states. This feed-down contribution to the Υ(1S) state was measured to be of the order of 50% [127], albeit in different kinematic ranges than used here. These results indicate that the directly produced Υ(1S) state is not significantly suppressed, however quantitative conclusions will require precise estimations of the feed-down contribution matching the phase space of the suppression measurement.

In addition to QGP formation, differences between quarkonium production yields in PbPb and pp collisions can also arise from cold-nuclear-matter effects [5]. However, such effects should have a small impact on the double ratios reported here. Initial-state nuclear effects are expected to affect similarly each of the three Υ states, thereby canceling out in the ratio. Final-state "nuclear absorption" becomes weaker with increasing energy [133] and is expected to be negligible at the LHC energies [192]. To get a estimate of cold nuclear matter effects production rates Υ states are compared in pp and pPb collisions. These measurements are described in chapter 6.

Chapter 6.

Measurement of Υ production and suppression in pPb collisions with CMS detector at the LHC.

This chapter describes measurement of production and suppression of Υ(1S), Υ(2S) and Υ(3S) in pPb and pp collisions at center of mass energies per nucleon pair of 5.02 TeV and 2.76 TeV, respectively. The datasets are collected in 2013 by the CMS experiment at the LHC. Υ production is studied as a function of two measures of event activity, namely the charged-particle multiplicity measured in mid rapidity, and the sum of transverse energy deposited at forward rapidity.

6.1. Introduction

The suppression of the Υ(1S), Υ(2S), and Υ(3S) (Υ(nS)) yields produced in heavy-ion collisions relative to proton-proton (pp) collisions was first measured by the CMS experiment, in PbPb collisions at $\sqrt{s_{NN}} = 2.76$ TeV. These measurements was described in chapter 4 and 5. The tightest bound state, Υ(1S), was observed to be less suppressed than the more loosely bound excited states, Υ(2S) and Υ(3S). Such ordering is theoretically predicted to occur in the presence of a deconfined medium in which the color fields modify the spectral properties of the $b\bar{b}$ quark pair, and prevent the formation of a bound state [4, 147]. However, other phenomena, discussed below, can affect the bottomonium yields at stages that precede or follow the formation of the $b\bar{b}$ pair and of the bound state, independently of the presence of a deconfined partonic medium. Some of these phenomena could lead to a suppression sequence that depends on the binding energy. In this context, measurements in reference systems are essential: proton-lead (pPb) collisions can probe nuclear effects, while pp collisions are essential for understanding the elementary bottomonium production mechanisms.

In heavy-ion (AA) collisions, effects that precede the formation of the $b\bar{b}$ pair (called here initial-state effects), such as the modification of the nuclear parton distribution functions (nPDFs) in the incoming nuclei [5], parton energy loss, and the Cronin effect [193, 194], are expected to affect the members of the Υ family in the same way, given their small mass difference and identical quantum numbers ($J^{\mathrm{CP}} = 1^{--}$). Consequently, any difference among the states is likely due to phenomena occurring after the $b\bar{b}$ production, during or after the Upsilon formation. Examples of final-state effects that might play a role include interactions with spectator nucleons that break up the state (nuclear absorption) [133, 195], and collisions with comoving hadrons [196] or surrounding partons [173, 191, 193, 197, 198] that can dissociate the bound states or change their kinematics. Any of these final-state processes can affect the Υ(nS) yields differently, depending on the binding energy and size of each state, and be at play in AA and/or pA collisions, possibly with different strengths and weights, depending on the properties of the environment created in each case. A measurement of the Υ(1S) and Υ(2S+3S) production cross sections in pA collisions at $\sqrt{s_{NN}} \approx 39\,\mathrm{GeV}$ using several targets, relative to proton-deuterium collisions [199], showed no difference, within uncertainties, between the ground state and the combined excited states, although a suppression was observed for both.

Understanding the production of bottomonia in elementary pp collisions is equally important for interpreting any additional effects in collisions involving heavy ions. At present, there are different proposed mechanisms to describe the evolution of a heavy-quark pair into a bound quarkonium state (a discussion about different mechanisms can be found in section 2.2 of chapter 2), but little is known of the underlying event associated with each state. For instance, the fragmentation of the soft gluons involved in some mechanisms [200, 201], or the feed-down processes [147] (decays of the higher-mass states to one of lower mass) could generate different numbers of particles associated with each of the quarkonium states. Therefore, the average contribution from each state to the global event characteristics (multiplicity, transverse energy, etc) can be different.

This Chapter describes measurements of three observables characterizing the Υ mesons produced in pp and pPb collisions within the interval $|y_{\mathrm{CM}}| < 1.93$, where y_{CM} is the meson rapidity in the center-of-mass of the nucleon-nucleon collision. First, double ratios of the yields of the excited states, $\Upsilon(2S)$ and $\Upsilon(3S)$, to that of the ground state, $\Upsilon(1S)$, are described in pPb with respect to pp collisions, $[\Upsilon(2S)/\Upsilon(1S)]_{pPb}/[\Upsilon(2S)/\Upsilon(1S)]_{pp}$, and similarly for the $\Upsilon(3S)$. Then, single yield ratios of the excited states to the ground state, $\Upsilon(nS)/\Upsilon(1S)$, are corrected for detector acceptance and reconstruction inefficiencies, and studied as a function of two event activity variables, measured in different rapidity ranges: a) the sum of the transverse energy deposited at a large rapidity gap with respect to the Υ, in the forward region ($4.0 < |\eta| < 5.2$), and b) the number of charged particles reconstructed in the central region ($|\eta| < 2.4$) that includes the rapidity range in which the Υ is measured. Lastly, $\Upsilon(nS)$ cross sections are studied as a function of the same event activity variables, with both cross sections and event activities divided by their values in all measured events. These values (denoted "activity-integrated values") are found by including all events with no selection on transverse energy or particle multiplicity.

6.2. Datasets

pPb datasets

LHC had first pPb run in Jan-Feb 2013. Total collected dataset corresponds to the integrated luminosity of $\approx$ 31 nb^{-1}. In pPb collisions the beam energies were 4 TeV for protons, and 1.58 TeV per nucleon for lead nuclei. The resulting center-of-mass energy per nucleon pair ($\sqrt{s_{NN}}$) is 5.02 TeV. The direction of the higher-energy proton beam was initially set up to be clockwise (-z direction in CMS coordinates), and was reversed after an integrated luminosity of $\approx$ 18 (nb)$^{-1}$ was recorded. This subset of data corresponds to CMS run numbers from 210498 to 211256. Another $\approx$ 12 nb^{-1} is collected with opposite settings i.e higher-energy proton beam going anti-clockwise (+z direction in CMS coordinates). This subset of data corresponds to CMS run numbers from 211313 to 211631. As a result of the energy difference of the colliding beams, the nucleon-nucleon center-of-mass in the pPb collisions is not at rest with respect to the laboratory frame. Massless particles emitted at $|\eta_{\mathrm{CM}}| = 0$ in the nucleon-nucleon center-of-mass frame are detected at $\eta = -0.465$ (clockwise proton beam) or $+0.465$ (anti-clockwise proton beam) in the laboratory frame.

The prompt reco datasets of proton lead collisions namely "/PAMuon/HIRun2013-PromptReco-v1/RECO" have been used in the analysis. The data have been reconstructed in the CMS Software version CMSSW_5_3_8_HI_patch2 with global tag GR_P_V43D::All.

pp datasets

The reference sample used for the final results is the 2013 pp at $\sqrt{s} = 2.76$ TeV. The 2013 pp sample at 2.76 TeV, run numbers 211739 to 211831, corresponds to an integrated luminosity of 5.4 $(\mathrm{pb})^{-1}$. It was reconstructed in CMSSW_5_3_8_patch2 with global tag GR_P_V43D::All.

Monte carlo samples

Officially produced pp samples of Υ at 5 and 2.76 TeV were simulated in PYTHIA 6.424 [8], decayed by EVTGEN [181] and PHOTOS [182] (for the Final State Radiation (FSR) simulation). One million events for each Υ state were generated with realistic p_T and rapidity distributions, with a rapidity boost of -0.47 and without any boost (the 2.76TeV sample). The data are reconstructed in CMSSW_5_3_8_HI_patch1 with global tag STARTHI53_V17.

6.3. Data selection

6.3.1. Event selection

In both 2013 collision setups (pPb and pp) the same trigger menu was used. For the muon analysis, all events were selected if they passed the HLT_PAL1DoubleMuOpen_v1 trigger. This trigger does not require any kinematical cut on muon candidate at HLT level and was kept unprescaled during the whole run. In addition to a muon trigger firing in the event, a coincidence with the minimum bias trigger was required. Minimum bias (MB) pPb events were triggered by requiring at least one track with $p_T > 0.4\,\mathrm{GeV/c}$ to be found in the pixel tracker for a pPb bunch crossing identified by BPTX detectors.

In the offline analysis, hadronic collisions were selected by requiring a coincidence of at least one HF calorimeter tower with more than 3 GeV of total energy in each of the HF detectors. Events were also required to contain at least one reconstructed primary vertex within 15 cm of the nominal interaction point along the beam axis and within 0.15 cm transverse to the beam trajectory. At least two reconstructed tracks were required to be associated with the primary vertex. Beam related background was suppressed by rejecting events for which less than 25% of all reconstructed tracks were of good quality.

The pPb instantaneous luminosity provided by the LHC in the 2013 run resulted in approximately 3% probability of at least one additional interaction occurring in the same bunch crossing, resulting in pileup events. A procedure for rejecting pileup events was developed to select clean, single-vertex pPb collisions. The approach was to investigate the number of tracks, $N_{\rm trk}^{\rm best}$ that is assigned to the best reconstructed vertex (e.g., the one with the greatest number of associated tracks), and $N_{\rm trk}^{\rm add}$ assigned to each of the additional vertices, as well as the distance between the two vertices in the z direction ($\Delta z_{\rm vtx}$). Based on studies using low pileup pPb data (from the 2012 pilot run), PbPb data, and MC simulations, events with $N_{\rm trk}^{\rm add}$ above a certain threshold at a given $\Delta z_{\rm vtx}$ were identified as pileup events and removed from the event sample. These criteria are tightened when applied to the pp sample, which has a higher number of simultaneous collisions per beam crossing; at maximum, at the beginning of an LHC fill, 23% of the pp events had more than one collision, compared to 3% in pPb. After the selection, the remaining integrated luminosity in the pp sample is equivalent to 4.1 pb^{-1}, with a residual pileup lower than 3%. Since pileup only biases the event activity variables, this selection is applied to the event activity dependent part of the analysis, but not for the pp integrated results. After applying all the offline cuts, the minimum bias number of events sampled are: for pp 1.770×10^{11} (which assuming $\sigma_{\rm inel}^{\rm pp} = 64\mu b$ translates in $\rm L_{int}$ = 2.8 pb^{-1}) and for pPb 6.3625×10^{10} (which assuming $\sigma_{\rm inel}^{\rm pPb} = 2.1$ b translates in $\rm L_{int}$ = 30.3 nb^{-1}).

6.3.2. Muon selection

Muon candidates are accepted if belonging to the kinematic region given by

$$-2.4 < \eta^{\mu} < 1.47 \quad \text{and} \quad p_T^{\mu} > 4.0\,\mathrm{GeV/c} \quad \text{for runs} <= 211256\,(\Delta \mathrm{y} = +0.47),$$
$$-1.47 < \eta^{\mu} < 2.4 \quad \text{and} \quad p_T^{\mu} > 4.0\,\mathrm{GeV/c} \quad \text{for runs} > 211256\,(\Delta \mathrm{y} = -0.47).$$

which corresponds in the center of mass of the collision to $|\eta_{\rm CM}| < 1.93$. The reasons for restricting ourselves only to this kinematic region is to stay in a symmetric interval in CM the only frame where the physics is expected to be symmetric. The muon candidates are further checked if reconstructed as tracker muons. (accessed via the standard method `isTracker()` in CMS software CMSSW). The complete list of all the cuts applied on muons and dimuons is the following:

- TMOneStationTight (requires one well matched segment in the muon stations for the track)
- the number of valid tracker layers > 5, indicating how good the inner track part of the track is;
- the number of pixel layers with valid hits > 1. There are 2-3% of muons with tracks with 0 pixel hits;
- the χ^2/ndf of the single-muon inner track < 1.8, which indicates the quality of the inner-track fit;
- the distance between the event vertex and the muon track in the transverse plane, $D_{xy} < 3.0$ mm, and the longitudinal plane, $D_z < 30.0$ mm, which indicates if the muon comes from a decay in flight or is a prompt muon, and removes cosmic muons;
- the probability of two tracks to belong to the same decay vertex > 1%.
- Tracker muon arbitration is done (resolves ambiguity of sharing segments; picks best based on matching based on position and pull cuts)

6.4. Yield extraction

The Υ states are identified through their dimuon decay. Muons with pseudorapidity $|\eta^{\mu}_{\rm CM}| < 1.93$ and transverse momentum $p^{\mu}_{T} > 4$ GeV/c, passing the quality requirements described in section 6.3, are selected. The same selections are used when analyzing the pPb and pp data. The p_T range of the selected dimuon candidates extends down to zero. The dimuon rapidity is limited to $|y_{\rm CM}| < 1.93$. The resulting opposite-charge dimuon invariant-mass distributions are shown in Fig. 6.1 for the pPb (left) and pp (right) datasets, in the 7–14 GeV/c^2 range.

6.4.1. Fitting procedure

Single ratios Υ(2S)/Υ(1S) and Υ(3S)/Υ(1S) are extracted from the data samples via an extended unbinned maximum likelihood fit to the dimuon invariant-mass spectra, in the range 7–14 GeV/c ^{2}. The final results are given for minimum bias, as well as in bins of energy deposited in the HF, $E_T^{|\eta|>4}/\langle E_T^{|\eta|>4}\rangle$, and in bins of reconstructed tracks, $N_{tracks}^{|\eta|<2.4}/\langle N_{tracks}^{|\eta|<2.4}\rangle$. For both the pp and the pPb sample, each of the Υ(nS) resonances

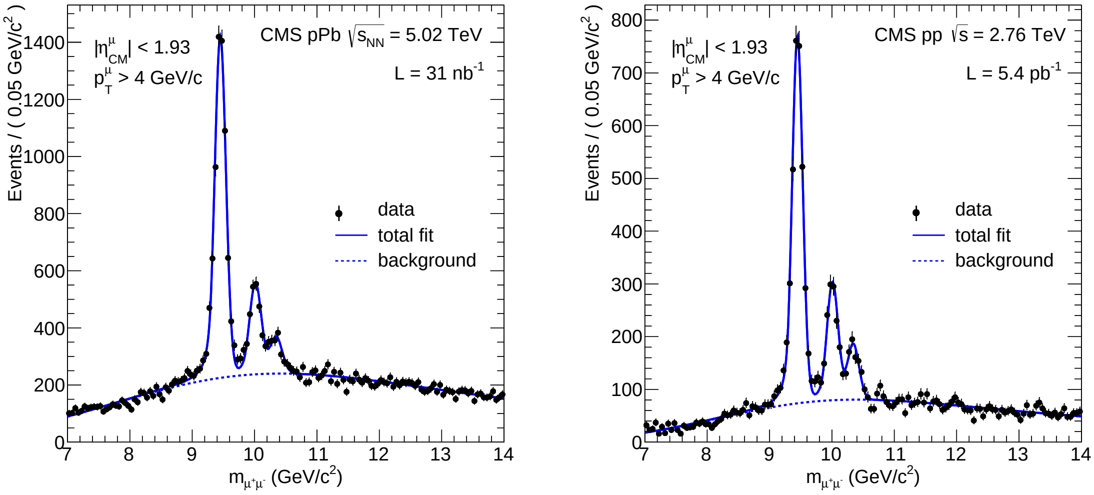

Figure 6.1.: Invariant mass spectrum in pPb (left) and pp collisions (right) of $\mu^+\,\mu^-$ pairs with single muons with $p_T^{\mu} > 4$ GeV/c and $|\eta^{\mu}_{\mathrm{CM}}| < 1.93$. The data (black circles) are overlaid with the fit (solid blue line). The background component of the fit is represented by the dashed blue line.

is modeled via a crystal-ball shape (CB), which consists of a Gaussian function with the low-side tail replaced with a power law describing final-state radiation (FSR). The crystal-ball function is given by:

$$f(x;\alpha,n,\bar{x},\sigma) = N\cdot\begin{cases}\exp(-\frac{(x-\bar{x})^2}{2\sigma^2}) & \text{for } \frac{x-\bar{x}}{\sigma} > -\alpha \\ A\cdot(B-\frac{x-\bar{x}}{\sigma})^{-n} & \text{for } \frac{x-\bar{x}}{\sigma} \leq -\alpha\,,\end{cases} \tag{6.1}$$

where

$$\begin{aligned} A &= \left(\frac{n}{|\alpha|}\right)^n\cdot\exp\left(-\frac{|\alpha|^2}{2}\right)\,, \\ B &= \frac{n}{|\alpha|}-|\alpha|\,. \end{aligned}$$

The CB function is parameterized by four parameters – the mass mean $\bar{x}$ and resolution σ, and the tail parameters α and n – which are constrained amongst the three signal peaks. The tail parameters are common; the resolution is forced to scale with the resonance mass; the ratios of the mass means are fixed to their PDG values.

The background parameterization adopted corresponds to an exponential function (exp), multiplied by an error-function (erf), The background function is given by:

$$f(x;a;x_0,W) = N \cdot \exp\left(-\frac{x}{a}\right) \cdot (\mathrm{erf}\left(\frac{x-x_0}{W}\right) + 1). \tag{6.2}$$

The background model is thus described by three parameters: the exponential decay constant (a), and the turn-on mean (x_0) and width (W). The error-function (erf) which is used to describes the kinematic shoulder, introduced by single muon p_T cut, is defined as

$$\mathrm{erf}(x) = \frac{2}{\sqrt{\pi}} \int_0^x e^{-t^2}\, dt \tag{6.3}$$

For both pp and pPb integrated (minbias) case the CB tail parameters are fixed to the values obtained from MC and σ is left free. While fitting in bins of E_{T} or $N_{tracks}^{|\eta|<2.4}$, σ and CB tail parameters are fixed to the value obtained in integrated (minbias) fit. All background parameters are left free for all fittings. The final fit results, with the nominal fit function, for the analysis kinematic range ($|\eta^{\mu}_{CM}| < 1.93$ and $p^{\mu}_{T} > 4$GeV/c), are presented in Fig. 6.2 for the 4 bins in E_{T}, and in Fig. 6.3 for the 4 bins in $N_{tracks}^{|\eta|<2.4}$.

The final fit results for pp data, with the nominal fit function, for the analysis kinematic range ($|\eta^{\mu}_{CM}| < 1.93$ and $p^{\mu}_{T} > 4$GeV/c), are presented in Fig. 6.4 for the 3 bins in E_{T}, and in Fig. 6.5 for the 3 bins in $N_{tracks}^{|\eta|<2.4}$.

6.4.2. Systematic uncertainties from fitting procedure

The following variations are considered for assessing the systematic uncertainties of the results:

Signal model variation

- all parameters fixed to MC (values are for pPb are $\alpha = 1.67$, $n = 2.2$, $\sigma = 0.089$ MeV while for pp $\alpha = 1.71$, $n = 2.2$, $\sigma = 0.086$ MeV.
- all parameters left free
- CB tail parameters fixed on MC, σ free (when binning); n fixed to MC and α and σ free (not binning)

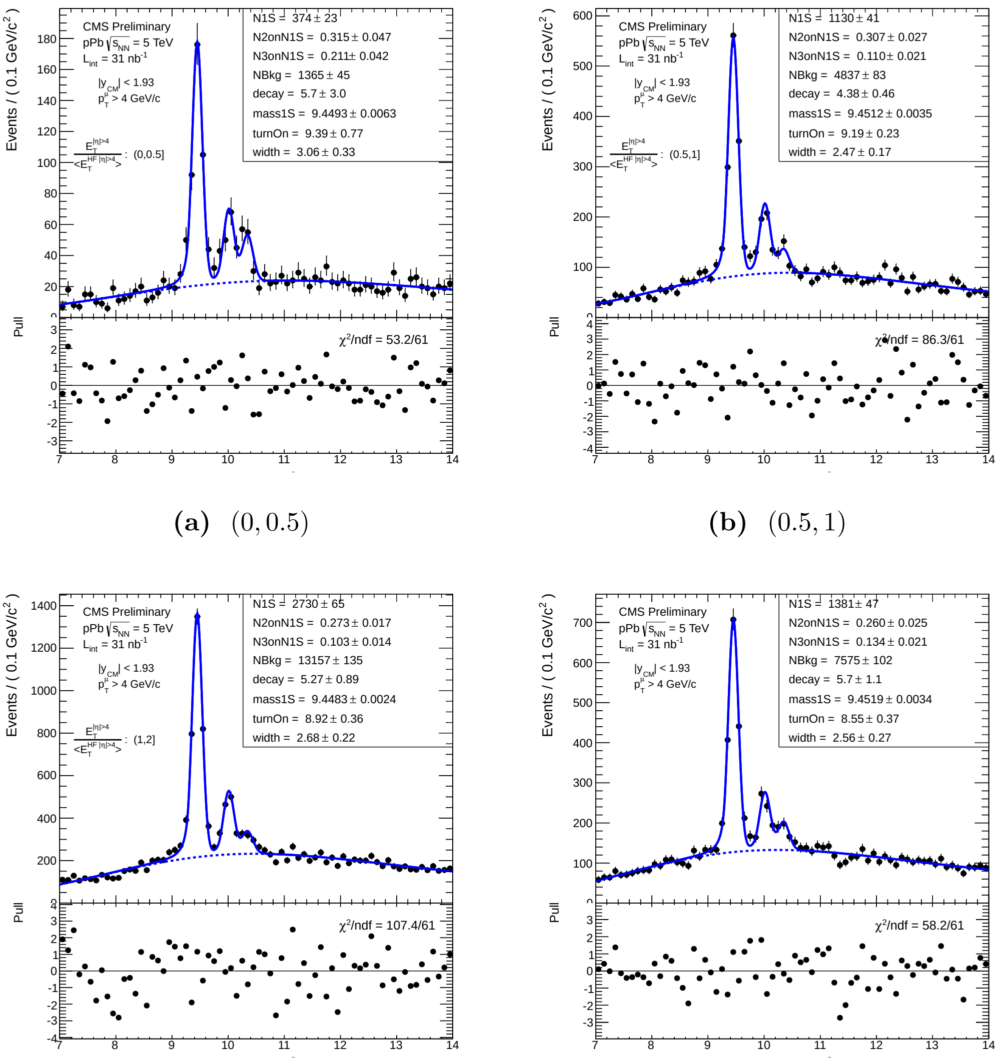

(a) $(0, 0.5)$

(b) $(0.5, 1)$

(c) $(1, 2)$

(d) > 2

Figure 6.2.: pPb mass fits in bins of $E_T^{|\eta|>4}/\langle E_T^{|\eta|>4}\rangle$, with baseline fit model, erf$*$exp with CB and σ parameters fixed on the integrated bin.

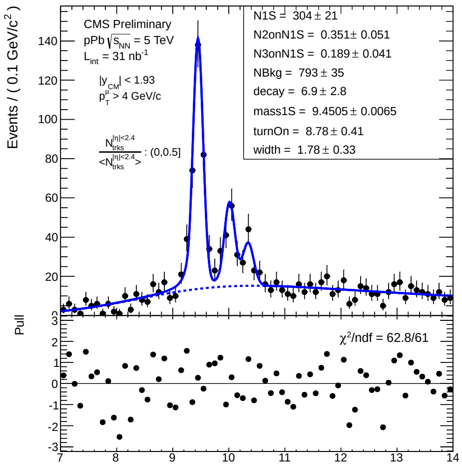

(a) $(0, 0.5)$

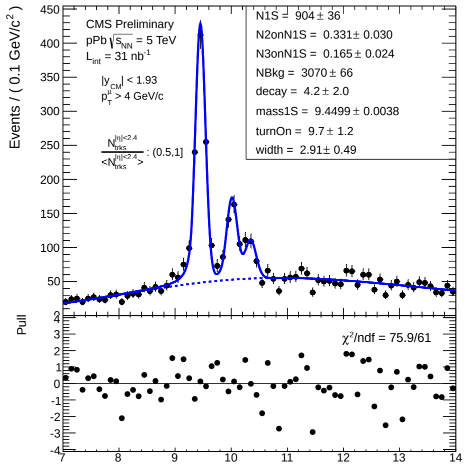

(b) $(0.5, 1)$

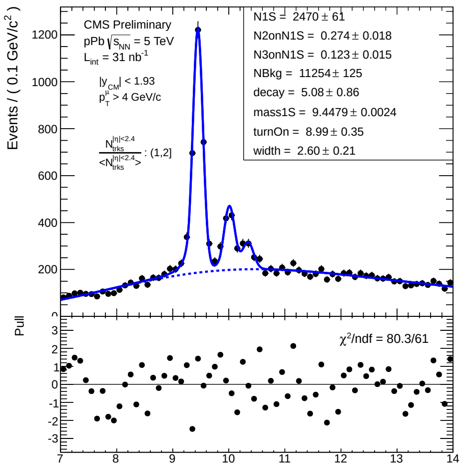

(c) $(1, 2)$

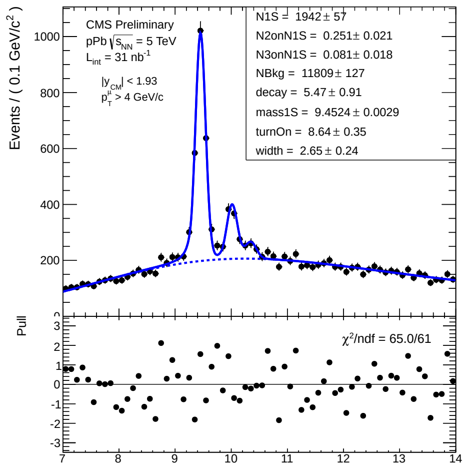

(d) > 2

Figure 6.3.: pPb mass fits in bins of $N_{tracks}^{|\eta|<2.4}/\langle N_{tracks}^{|\eta|<2.4}\rangle$, with baseline fit model: erf∗exp with CB and σ parameters fixed on the integrated bin.

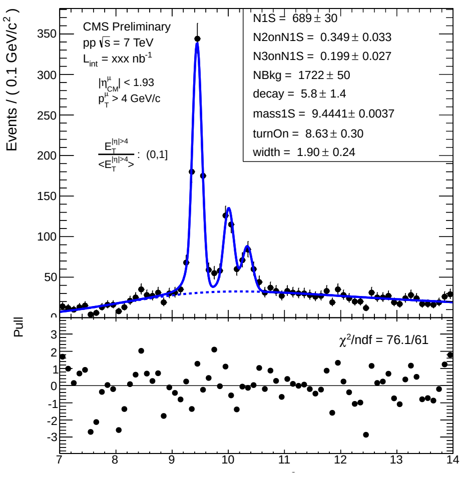

(a) $(0, 1)$

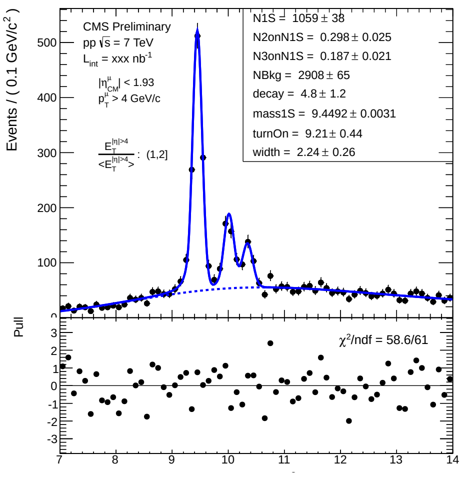

(b) $[1, 2)$

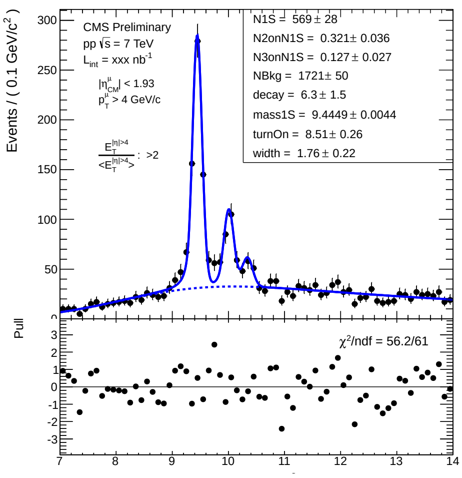

(c) $>= 2$

Figure 6.4.: pp mass fits in bins of $E_T^{|\eta|>4}/\langle E_T^{|\eta|>4}\rangle$, with baseline fit model: erf$*$exp with CB and σ parameters fixed on the integrated bin.

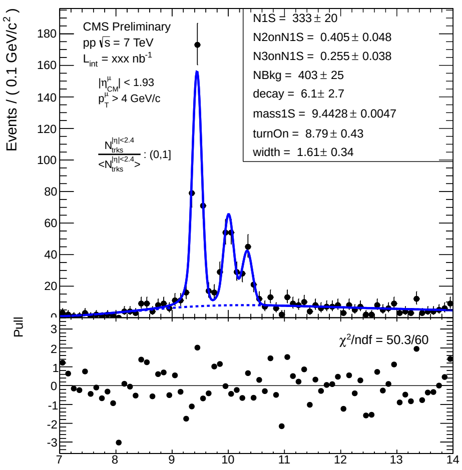

(a) $(0, 1)$

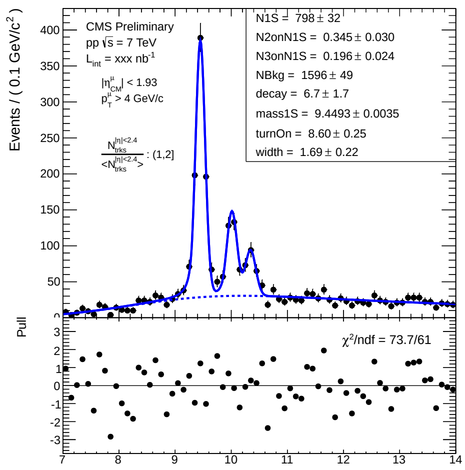

(b) $[1, 2)$

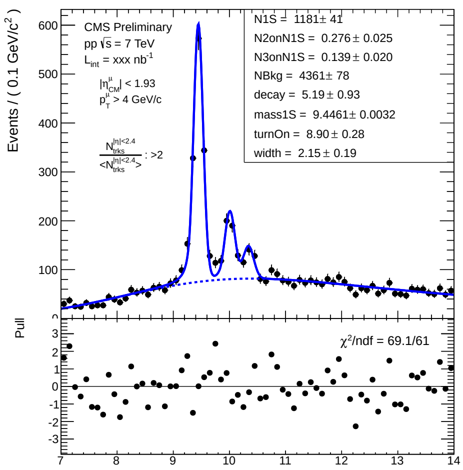

(c) $>= 2$

Figure 6.5.: pp mass fits in bins of $N_{tracks}^{|\eta|<2.4}/\langle N_{tracks}^{|\eta|<2.4}\rangle$, with baseline fit model: erf∗exp with CB and σ parameters fixed on the integrated bin.

Background model variation

- The background is constrained by second order Chebychev polynomial `pol2`.
- The background is constrained by third order Chebychev polynomial `pol3`.
- The background is constrained by second order Chebychev polynomial `pol2` combined (added) to `erf*exp` (the nominal fit).
- like-sign background modeling: the background model is formed of two components, given by the like-sign distribution and a second order polynomial (`pol2`); the PDF from the like-sign data is obtained from a fit employing the `erf*exp` model
- like-sign background modeling: the background model is formed of two components, given by the like-sign distribution and a second order polynomial (`pol2`); the PDF from the like-sign data is obtained from the `RooKeysPdf` smoothing method.

The systematic uncertainties associated to the signal and background modeling is estimated as the largest, $\mathrm{Max}_{\mathrm{variation}}$ from all background and signal shape variations. For both pp and pPb the same fit model is used for the nominal results, and the same variations to assess the systematic uncertainties.

6.5. Acceptance and efficiency corrections

Monte Carlo (MC) events are used to evaluate efficiencies and acceptances. Signal Υ(nS) events are generated, for 2.76 TeV and 5.02 TeV (boosted to have the correct rapidity distribution in the detector frame), using PYTHIA 6.424 [8]. In all samples, the Υ(nS) decay is simulated using EVTGEN [181], assuming unpolarized production [202]. No systematic uncertainties are assigned for this assumption, any possible modification due to polarization being considered as part of the physics that is studied [188]. The final-state bremsstrahlung is implemented using PHOTOS [182]. The CMS detector response is simulated with GEANT4 [10].

6.5.1. Acceptance studies

Maximum symmetric region in the collision frame (CM frame) that can be accessed in the pPb collisions, is $|y^{coll}| < 1.93$. It corresponds in the lab frame to -2.4 $< y^{lab} <$ 1.47.

The acceptance is calculated with the following formula

$$\alpha \;=\; \frac{N^{dimuon}_{-2.4<\eta^{\mu}<1.47,p_T^{\mu}>4\mathrm{GeV/c},\mathrm{M}}(p_T, y)}{N^{dimuon}_{-2.4<y^{dimuon}<1.47}(p_T, y)} \tag{6.4}$$

where $\mathrm{N}^{dimuon}_{-2.4<\eta^{\mu}<1.47,p_T^{\mu}>4\mathrm{GeV/c},\mathrm{M}}(p_T, y))$ is the number of generated events in a given (p_T, y) dimuon bin, within a mass interval M ($[9.0, 10.0]\,\mathrm{GeV}/c^2$ for Υ(1S), $[9.5, 10.5]\,\mathrm{GeV}/c^2$ for Υ(2S) and $[9.8, 10.8]\,\mathrm{GeV}/c^2$ for Υ(3S) and with single muons that pass the kinematic cuts $-2.4 < \eta^{\mu} < 1.47$ and $p_T^{\mu} > 4\,\mathrm{GeVc}$; $\mathrm{N}^{dimuon}_{-2.4<y^{dimuon}<1.47}$ represents all dimuons generated in $-2.4 < y^{dimuon} < 1.47$.

Figure 6.6 shows for the 5 TeV sample, the effect on the acceptance as a function of Υ rapidity with kinematic cuts used in the analysis. By integrating these curves, the integrated values used as corrections in the single ratios were calculated.

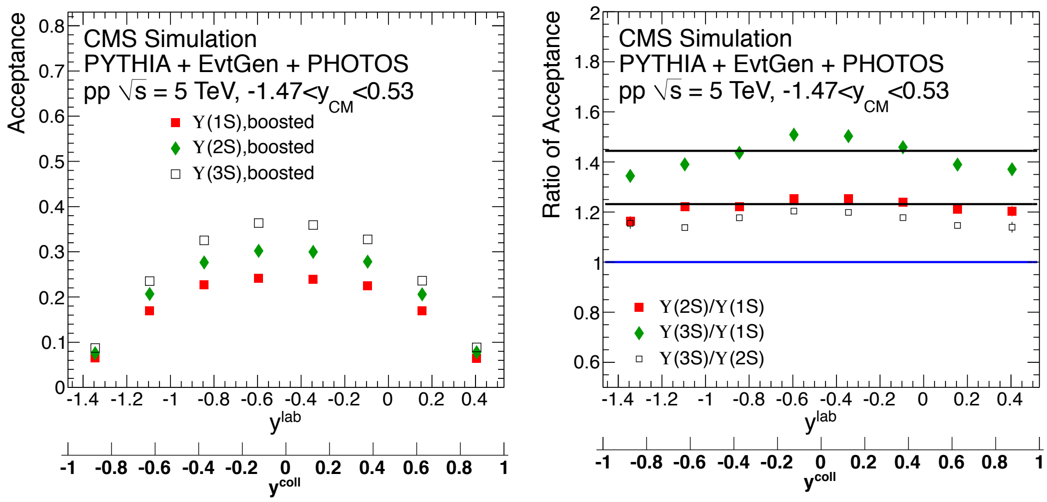

(a) **(b)**

Figure 6.6.: (a) Acceptance variation versus dimuon rapidity, for $\Upsilon(1S)$, $\Upsilon(2S)$ and $\Upsilon(3S)$, as calculated on the 5 TeV MC sample for the cuts used in the analysis. (b) Ratios of the acceptances.

Since the acceptance is a function of both p_T and y, uncertainties in the distributions for these variables can lead to a systematic uncertainty in the average acceptance over a p_T or y bin. To estimate these uncertainties, the shapes of the generated MC p_T and y distributions are varied linearly by $\pm 30\%$ over the range $|y| < 2.4$ and $0 < p_T < 30\,\mathrm{GeV/c}$. In other words, the distributions are re-weighted with a straight line that has a slope of 1.3 (and, alternatively, 0.7) in each variable range. This variation is considered to account for all possible sources of uncertainty for the upsilon states. The RMS of the resulting changes in the acceptance for each p_T and y bin are summed in quadrature to compute the overall systematic uncertainty from this source. The values of acceptance and uncertainties for $|y_{CM}| < 1.93$ (integrated over p_T), are shown in table 6.1, for the 2.76 TeV unboosted and the 5 TeV boosted MC samples.

Table 6.1.: Acceptance in $|\eta^{\mu}_{CM}| < 1.93$ for each Υ state, and two different $\sqrt{s}$.

state	5.02 TeV (boosted)					
	default	p_T up(+30%)	p_T down(-30%)	y up(+30%)	y down(-30%)	Total
Υ(1S)	0.210 ± 0.001	0.215 ± 0.001	0.207 ± 0.001	0.203 ± 0.001	0.218 ± 0.001	6%
Υ(2S)	0.262 ± 0.001	0.263 ± 0.001	0.262 ± 0.001	0.252 ± 0.001	0.271 ± 0.001	5%
Υ(3S)	0.315 ± 0.000	0.322 ± 0.000	0.309 ± 0.000	0.302 ± 0.000	0.327 ± 0.000	6%
state	2.76 TeV (unboosted)					
	default	p_T up(+30%)	p_T down(-30%)	y up(+30%)	y down(-30%)	Total
Υ(1S)	0.207 ± 0.001	0.210 ± 0.001	0.205 ± 0.001	0.200 ± 0.001	0.213 ± 0.001	5%
Υ(2S)	0.263 ± 0.001	0.263 ± 0.001	0.264 ± 0.001	0.254 ± 0.001	0.272 ± 0.001	5%
Υ(3S)	0.314 ± 0.000	0.319 ± 0.000	0.309 ± 0.000	0.301 ± 0.000	0.325 ± 0.000	6%

6.5.2. Efficiency studies

The signal reconstruction efficiencies may differ for the individual $\Upsilon(nS)$ states. These efficiencies and their residual differences are estimated, based on Monte Carlo simulation. The method consists of estimating the reconstruction efficiency making the ratio of the number of signal that is reconstructed and passes the quality cuts, and the number of signal that was generated. Efficiency is calculated with the following formula:

$$\varepsilon = \frac{N^{\text{dimuons reconstructed,M}}_{|\eta^{\mu}_{CM}|<1.93, \mu\, p_T>4.0}(p_T, y)}{N^{\text{dimuon generated}}_{|\eta^{\mu}_{CM}|<1.93, \mu\, p_T>4.0}(p_T, y)} \tag{6.5}$$

The reconstructed numbers include all efficiency corrections: trigger, identification (cuts) and tracking. Figure 6.7 shows for the 5 TeV sample, reconstruction efficiencies and their ratios as a function of Υ rapidity with kinematic cuts used in the analysis.

These values are used as corrections for single ratios calculated in the analysis. To

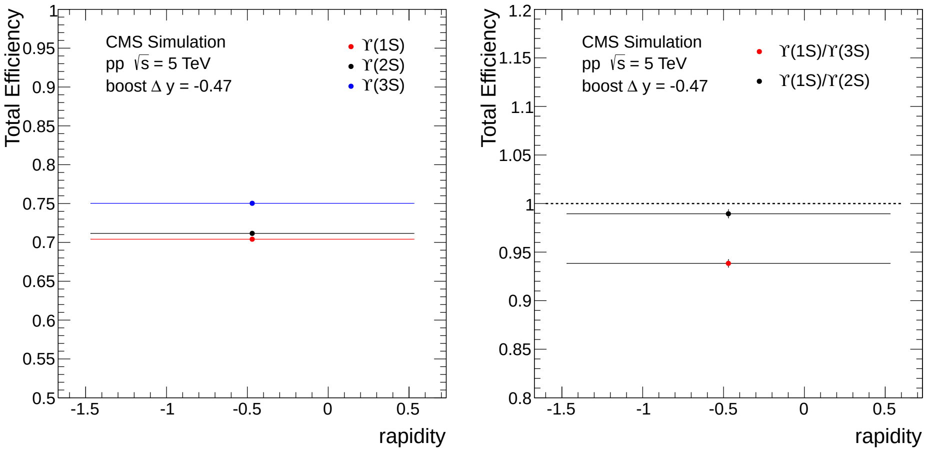

(a) (b)

Figure 6.7.: Reconstruction efficiencies for for Υ(1S), Υ(2S) and Υ(3S) (a) and their ratios (b) in the rapidity bin used in analysis.

estimate systematic uncertainty from efficiency corrections same approach was used as for acceptance systematic studies. The values of efficiencies and uncertainties for $|y_{CM}| < 1.93$ (integrated over p_T), are shown in table 6.2, for the 2.76 TeV unboosted and the 5 TeV boosted MC samples.

Table 6.2.: Efficiency variation in $|\eta^{\mu}_{CM}| < 1.93$ for each Υ state, and two different $\sqrt{s}$.

state	5.02 TeV (boosted)					
	default	p_T up(+30%)	p_T down(-30%)	y up(+30%)	y down(-30%)	Total
Υ(1S)	0.695 ± 0.002	0.700 ± 0.002	0.690 ± 0.002	0.690 ± 0.002	0.700 ± 0.002	1%
Υ(2S)	0.700 ± 0.002	0.700 ± 0.002	0.700 ± 0.002	0.700 ± 0.002	0.700 ± 0.002	0%
Υ(3S)	0.734 ± 0.002	0.740 ± 0.002	0.730 ± 0.002	0.730 ± 0.002	0.740 ± 0.002	1%
state	2.76 TeV (unboosted)					
	default	p_T up(+30%)	p_T down(-30%)	y up(+30%)	y down(-30%)	Total(%)
Υ(1S)	0.713 ± 0.002	0.720 ± 0.002	0.710 ± 0.002	0.720 ± 0.002	0.710 ± 0.002	2%
Υ(2S)	0.720 ± 0.002	0.720 ± 0.002	0.720 ± 0.002	0.720 ± 0.002	0.720 ± 0.002	0%
Υ(3S)	0.752 ± 0.001	0.760 ± 0.001	0.750 ± 0.001	0.750 ± 0.001	0.750 ± 0.001	1%

For the self-normalized ratio results (Υ(nS)/$\langle\Upsilon$(nS)$\rangle$) a correction is applied, calculated as the ratio of the efficiency in each multiplicity/Et bin, divided by the efficiency of the integrated bin. The corrections for all bins are in Tables 6.3 and 6.4 for pp and pPb respectively. We use tag and probe (T&P) method to estimate the single-muon trigger, identification, and tracking efficiencies on both data and MC. The MC sample is a prompt J/ψ sample. The purpose of this study is to check with real data the MC based efficiencies used for the final corrections. The T&P results are used then just to, eventually, assign systematic uncertainties on these efficiencies (assuming factorization of the single muon efficiencies for the dimuon).

Table 6.3.: Efficiency corrections for $\langle\Upsilon(\mathrm{nS})\rangle/\Upsilon(\mathrm{nS})$ as a function of $N_{tracks}^{|\eta|<2.4}/\langle N_{tracks}^{|\eta|<2.4}\rangle$ and $E_T^{|\eta|>4}/\langle E_T^{|\eta|>4}\rangle$ for pp multiplicities binning in $|y_{CM}| < 1.93$.

	$\langle\Upsilon(1S)\rangle/\Upsilon(1S)$		$\langle\Upsilon(2S)\rangle/\Upsilon(2S)$		$\langle\Upsilon(3S)\rangle/\Upsilon(3S)$	
Bin	$N_{tracks}^{|\eta|<2.4}$	$E_T^{|\eta|>4}$	$N_{tracks}^{|\eta|<2.4}$	$E_T^{|\eta|>4}$	$N_{tracks}^{|\eta|<2.4}$	$E_T^{|\eta|>4}$
1	1.05	1.04	1.05	1.04	1.06	1.04
2	1.00	0.98	0.99	0.98	1.00	0.98
3	0.97	0.98	0.97	0.98	0.97	0.98

Table 6.4.: Efficiency corrections for $\langle\Upsilon(\mathrm{nS})\rangle/\Upsilon(\mathrm{nS})$ as a function of $N_{tracks}^{|\eta|<2.4}/\langle N_{tracks}^{|\eta|<2.4}\rangle$ and $E_T^{|\eta|>4}/\langle E_T^{|\eta|>4}\rangle$ for pPb multiplicities binning in $|y_{CM}| < 1.93$.

	$\langle\Upsilon(1S)\rangle/\Upsilon(1S)$		$\langle\Upsilon(2S)\rangle/\Upsilon(2S)$		$\langle\Upsilon(3S)\rangle/\Upsilon(3S)$	
Bin	$N_{tracks}^{|\eta|<2.4}$	$E_T^{|\eta|>4}$	$N_{tracks}^{|\eta|<2.4}$	$E_T^{|\eta|>4}$	$N_{tracks}^{|\eta|<2.4}$	$E_T^{|\eta|>4}$
1	1.05	1.04	1.05	1.04	1.06	1.04
2	1.01	1.00	1.01	1.00	1.01	1.00
3	0.99	1.01	0.995	1.00	0.99	0.993
4	0.99	1.01	0.995	1.00	0.99	0.993

6.6. Results

6.6.1. Double ratios: $[\Upsilon(nS)/\Upsilon(1S)]_{pPb}/[\Upsilon(nS)/\Upsilon(1S)]_{pp}$

Using the raw yield ratios found by fitting separately the pPb and pp event activity integrated data samples, the double ratios are

$$\frac{\Upsilon(2S)/\Upsilon(1S)|_{pPb}}{\Upsilon(2S)/\Upsilon(1S)|_{pp}} = 0.83 \pm 0.05(\text{stat.}) \pm 0.05(\text{syst.}),$$
$$\frac{\Upsilon(3S)/\Upsilon(1S)|_{pPb}}{\Upsilon(3S)/\Upsilon(1S)|_{pp}} = 0.71 \pm 0.08(\text{stat.}) \pm 0.09(\text{syst.}).$$

The systematic uncertainties include uncertainties from the signal extraction procedure described above (6% and 13% for the Υ(2S) and Υ(3S), respectively), and from a potentially imperfect cancellation of the acceptances for individual states between the two center-of-mass energies (2% and 1%, respectively, estimated from MC). The above double ratios, in which the initial-state effects are likely to cancel, suggest the presence of final-state effects in the pPb collisions compared to pp collisions, that affect more strongly the excited states (Υ(2S) and Υ(3S)) compared to the ground state (Υ(1S)).

In Fig. 6.8 (a), the pPb double ratios are compared with the measurement in PbPb at $\sqrt{s_{NN}}$ = 2.76 TeV described in chapter 5. The pPb ratios are larger than the corresponding PbPb ones. This observation may help in understanding the final-state mechanisms of suppression of excited Υ states in the absence of a deconfined medium, and their extrapolation to the PbPb system.

6.6.2. Single cross section ratios: Υ(nS)/Υ(1S)

The single ratios used as numerator and denominator in the pPb double ratios in Fig. 6.8 (a) are further corrected for detector acceptance (to a single muon transverse momentum coverage of $p_T^\mu > 0$ GeV/c and Upsilon $|y_{\mathrm{CM}}| < 1.93$), reconstruction and trigger inefficiencies, and are given in Fig. 6.8 (b). The global uncertainties (not related to the signal extraction) are added in quadrature to the systematic uncertainties, and are estimated by following the methods described in section 6.5: by considering the effect of variations in the simulated kinematic distributions on the acceptance (7–8%) and efficiency (1–2%) corrections, and from differences in the efficiency estimations from data and MC simulation (< 1%). The PbPb values are derived from chapter 5 but, unlike the ones quoted there, they are corrected for acceptance and efficiency, similar to the double ratios, the single ratios signal the presence of different (or stronger) final state effects acting on the excited states compared to the ground state from pp to pPb to PbPb collisions.

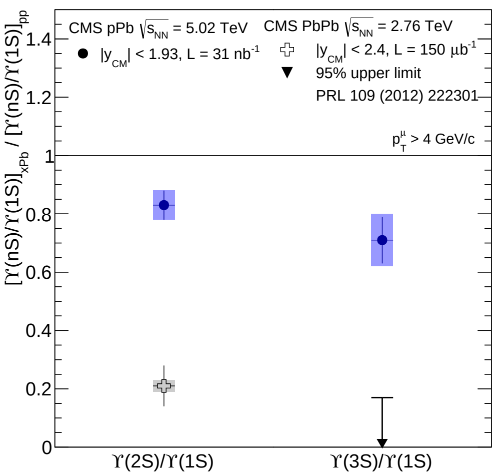

(a)

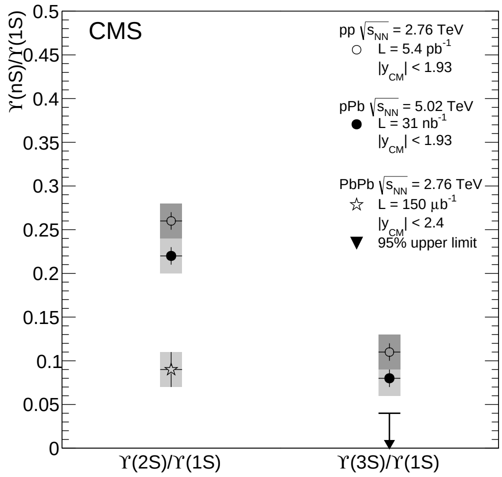

(b)

Figure 6.8.: (a) Event activity integrated double ratios of the excited states, ϒ(2S) and ϒ(3S), to the ground state,ϒ(1S), in pPb collisions at $\sqrt{s_{NN}} = 5.02$ TeV with respect to pp collisions at $\sqrt{s} = 2.76$ TeV(circles), compared to the corresponding ratios for PbPb (cross) collisions at $\sqrt{s_{NN}} = 2.76$ TeV. (b) Event activity integrated single cross section ratios of the excited ϒ(2S) and ϒ(3S) to the ground ϒ(1S) state, as measured in pp (open circles), pPb (full circles), and PbPb (open star) collisions at 2.76, 5.02, and 2.76 TeV, respectively. In both figures, the error bars indicate the statistical uncertainties, and the boxes represent the systematic uncertainties. The single ratios are shown in tabulated form in Tab. 6.5.

Table 6.5.: The excited-to-ground-state cross section ratios, $\frac{\Upsilon(\mathrm{nS})}{\Upsilon(1\mathrm{S})}$, for Upsilons with $p_T <$ 40GeV/c, in pp, pPb, and PbPb collisions at nucleon-nucleon center of mass collision energy of 2.76, 5.02, and 2.76TeV, respectively. Listed uncertainties are statistical first, systematic second, and global third.

Data	Rapidity	$\frac{\Upsilon(2S)}{\Upsilon(1S)}$	$\frac{\Upsilon(3S)}{\Upsilon(1S)}$
pp $\sqrt{s} = 2.76$ TeV	$\lvert y_{\mathrm{CM}}\rvert < 1.93$	$0.26 \pm 0.01 \pm 0.01 \pm 0.02$	$0.11 \pm 0.01 \pm 0.01 \pm 0.01$
pPb $\sqrt{s_{NN}} = 5.02$ TeV	$\lvert y_{\mathrm{CM}}\rvert < 1.93$	$0.22 \pm 0.01 \pm 0.01 \pm 0.02$	$0.08 \pm 0.01 \pm 0.01 \pm 0.01$
PbPb $\sqrt{s_{NN}} = 2.76$ TeV	$\lvert y_{\mathrm{CM}}\rvert < 2.4$	$0.09 \pm 0.02 \pm 0.02 \pm 0.01$	<0.04 (at 95% CL)

6.6.3. Excited-to-ground state cross section ratios (ϒ(nS)/ϒ(1S)) as a function of event activity

The pp and pPb data are further analyzed separately as a function of event activity variables measured in two different rapidity regions. Specifically, the single ratios,

$\Upsilon(2S)/\Upsilon(1S)$ and $\Upsilon(3S)/\Upsilon(1S)$, are measured in bins of: (1) $E_T^{|\eta|>4}$, the raw transverse energy deposited in the most forward part of the HF calorimeters at $4.0 < |\eta| < 5.2$, and (2) $N_{tracks}^{|\eta|<2.4}$, the number of charged particles, not including the two muons, with $p_T > 400$ MeV/c reconstructed in the tracker at $|\eta| < 2.4$ and originating from the same vertex as the Υ. The binning is chosen using a minimum bias event sample.The bin upper boundaries, presented in Table 6.6, are chosen for each variable so that they are half or round multiples of the uncorrected mean value in the minimum bias events, $\langle N_{\text{tracks, raw}}^{|\eta|<2.4} \rangle = 10$ and 41, $\langle E_{\text{T, raw}}^{|\eta|>4} \rangle = 3.5$ and 14.7 GeV for pp and pPb, respectively. Table 6.6 also lists, for each bin, the mean values of both variables, as computed from the dimuon sample used in the analysis, and the fraction of minimum bias events in the bin. For $N_{tracks}^{|\eta|<2.4}$, the mean is extracted after weighting each reconstructed track in one bin by a correction factor that accounts for the detector acceptance, the efficiency of the track reconstruction algorithm, and the fraction of misreconstructed tracks.The uncertainty in the total single-track correction is estimated to be 3.9% for the 2013 pp and pPb data, and 10% for the PbPb data.

The binned single ratios $\Upsilon(2S)/\Upsilon(1S)$ and $\Upsilon(3S)/\Upsilon(1S)$ are corrected for acceptance, and for trigger and reconstruction efficiencies. The bin-to-bin systematic uncertainties, represented by colored boxes in Figs. 6.9 and 6.10, come from the fitting procedure and are in the ranges 3–8% ($\Upsilon(2S)/\Upsilon(1S)$) and 4–30% ($\Upsilon(3S)/\Upsilon(1S)$) for pp, and 3–8% ($\Upsilon(2S)/\Upsilon(1S)$) and 7–17% ($\Upsilon(3S)/\Upsilon(1S)$) for pPb. The uncertainty common to all points in a given dataset, quoted in the captions, is estimated following the same procedure as for the activity-integrated results. In Fig. 6.9, for both pp and pPb, the results are shown as a function of forward transverse energy ($E_T^{|\eta|>4}$, left panel), and as a function of midrapidity track multiplicity ($N_{tracks}^{|\eta|<2.4}$, right panel). In all bins, the abscissae are given by the bin-average value listed in Table 6.6. The ratios vary weakly as a function of $E_T^{|\eta|>4}$, while they exhibit a significant decrease with increasing $N_{tracks}^{|\eta|<2.4}$.

The difference observed between the Υ states when binning in $N_{tracks}^{|\eta|<2.4}$ can arise in two opposite ways. If, on the one hand, the $\Upsilon(1S)$ is systematically produced with more particles than the excited states, it would affect the underlying distribution of charged particles and create an artificial dependence when sliced in small multiplicity bins. This dependence should be sensitive to the underlying multiplicity distribution, and would result in a larger correlation if one reduces the size of the multiplicity bins. If, on the other hand, the Υ are interacting with the surrounding environment, the $\Upsilon(1S)$ is expected, as the most tightly bound state and the one of smallest size, to be less affected than $\Upsilon(2S)$

Table 6.6.: Event activity bins in $N_{tracks}^{|\eta|<2.4}$ (left) and $E_T^{|\eta|>4}$ (right), comprising the bin edges, the mean within the bin and the corresponding mean of the other variable calculated in the dimuon sample, and the fraction of recorded minimum bias triggered events falling within the bin. The bin upper boundaries are chosen for each variable so that they are half or round multiples of the uncorrected mean value in the minimum bias events, $\langle N_{\text{tracks, raw}}^{|\eta|<2.4}\rangle = 10$ and 41, $\langle E_{\text{T, raw}}^{|\eta|>4}\rangle = 3.5$ and 14.7GeVfor pp and pPb, respectively. The quoted $\langle N_{tracks}^{|\eta|<2.4}\rangle$ values are efficiency corrected.

Bin		$N_{tracks}^{\|\eta\|<2.4}$				$E_T^{\|\eta\|>4}$			
	$[N_{tracks}^{\|\eta\|<2.4}]$ (raw)	$\langle N_{tracks}^{\|\eta\|<2.4}\rangle$	$\langle E_T^{\|\eta\|>4}\rangle$ [GeV]	Frac (%)	$[E_T^{\|\eta\|>4}]$ [GeV]	$\langle E_T^{\|\eta\|>4}\rangle$	$\langle N_{tracks}^{\|\eta\|<2.4}\rangle$	Frac (%)
pp 1	0–10	9.8 ± 0.4	3.3	64	0–3.5	2.5	9.6 ± 0.4	59
pp 2	11–20	19.4 ± 0.8	4.7	25	3.5–7.0	5.2	17.2 ± 0.7	32
pp 3	21–30	30.7 ± 1.2	5.9	8	≥7.0	9.2	25.8 ± 1.0	9
pp 4	≥31	49.9 ± 1.9	7.1	3				
pPb 1	0–21	19.1 ± 0.7	7.3	35	0–7.4	5.3	19.2 ± 0.7	30
pPb 2	22–41	40.0 ± 1.6	13.0	24	7.4–14.7	11.5	40.2 ± 1.6	27
pPb 3	42–82	75.9 ± 3.0	21.6	30	14.7–29.4	21.8	72.8 ± 2.8	33
pPb 4	≥83	137.9 ± 5.4	34.4	11	≥29.4	38.0	118.0 ± 4.6	10

and Υ(3S), leading to a decrease of the Υ(nS)/Υ(1S) ratios with increasing multiplicity. In either case, the ratios will continuously decrease from the pp to pPb to PbPb systems, as a function of event multiplicity. T he impact of additional underlying particles on the decreasing trend of the Υ(2S)/Υ(1S) and Υ(3S)/Υ(1S) versus $N_{tracks}^{|\eta|<2.4}$ in pp and pPb collisions is studied in more detail. The pp sample contains on average two extra charged tracks in the Υ(1S) events when compared to the Υ(2S) and Υ(3S) events, consistent with the pPb sample, though the average number of charged particles rises from 13 (pp) to 50 (pPb). The trend shown in the Fig. 6.9 (b) is found to weaken (or even reverse) if one artificially lowers the number of charged particles in the Υ(1S) sample by two or three tracks for every event. In contrast, the number of extra charged particles does not vary when lowering the p_T threshold down to 200 MeV/c in the $N_{tracks}^{|\eta|<2.4}$ computation, or when removing particles located in a cone of radius $\Delta R = \sqrt{(\Delta\phi)^2 + (\Delta\eta)^2} = 0.3$ or 0.5 around the Υ momentum direction.

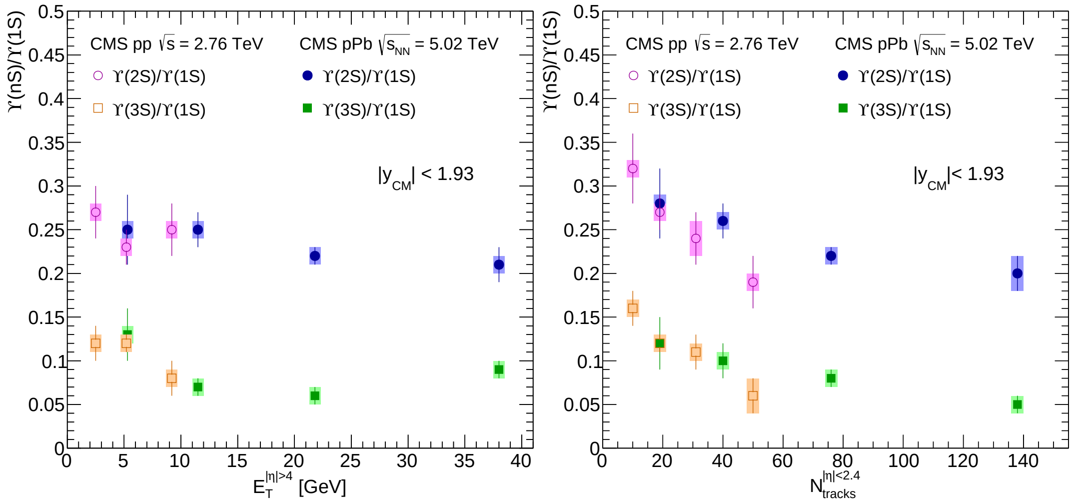

(a) **(b)**

Figure 6.9.: Single cross section ratios $\Upsilon(2S)/\Upsilon(1S)$ and $\Upsilon(3S)/\Upsilon(1S)$ for $|y_{CM}| < 1.93$ versus transverse energy measured in $4.0 < |\eta| < 5.2$ (a) and number of charged tracks measured in $|\eta| < 2.4$ (b), for pp collisions at $\sqrt{s} = 2.76$ TeV , (open symbols) and pPb collisions at $\sqrt{s_{NN}} = 5.02$ TeV , (closed symbols). In both figures, the error bars indicate the statistical uncertainties, and the boxes represent the point-to-point systematic uncertainties. The global uncertainties on the pp results are 7% and 8% for $\Upsilon(2S)/\Upsilon(1S)$ and $\Upsilon(3S)/\Upsilon(1S)$, respectively, while in the pPb results they amount to 8% and 9%, respectively. The results are available in tabulated form in Table 6.7, with binning information provided in Table 6.6.

Extra charged particles are indeed expected in the $\Upsilon(1S)$ sample because of feed-down from higher-mass states, such as $\Upsilon(2S) \to \Upsilon(1S)\pi^+\pi^-$, but decay kinematics [8], with typically assumed feed-down fractions [147], do not lead to a significant rise of the number of charged particles with $p_T > 400$ MeV/c. While most feed-down contributions should come from the decays of P-wave states, such as $\chi_b \to \Upsilon(1S)\gamma$, the probability for a photon to convert in the detector material and produce at least one electron with $p_T > 400$ MeVc, that is further reconstructed and selected, is very low (<0.2%). This makes the number of reconstructed electrons not sufficient to produce the measured trend. Therefore, it is concluded that feed-down contributions cannot solely account for the observed features in the measured ratios. It is noted also that if the three Υ states are produced from the same initial partons, the mass difference between the $\Upsilon(1S)$ and the $\Upsilon(2S)$ (>500 MeV), or the $\Upsilon(1S)$ and the $\Upsilon(3S)$ (>800 MeV), could be found not only in the momentum of the $\Upsilon(1S)$, but also in extra particles created together with the $\Upsilon(1S)$.

For comparison, similarly corrected PbPb ratios, $\Upsilon(2S)/\Upsilon(1S)$, are computed from the double ratios presented in chapter 5 versus percentiles of transverse energy deposited in the HF in the $2.9 < |\eta| < 5.2$ range, which define the centrality of the PbPb event. The point-to-point systematic uncertainties are obtained as described in chapter 5 and are in the range 13–85% across all bins, while the 8% global uncertainty is calculated as for the activity-integrated results described above. The statistical uncertainty ranges from 24% to 139%. Because there is a relatively strong correlation between the charged-particle multiplicity and the transverse energy in PbPb collisions, the results reported here are not obtained by repeating the analysis as a function of $N_{tracks}^{|\eta|<2.4}$, but by estimating, in the dimuon sample, the corresponding $N_{tracks}^{|\eta|<2.4}$ value for each of the HF energy-binned results. The estimation is done using a low-multiplicity PbPb sample reconstructed with the same reconstruction algorithm as the pp and pPb data, and the published PbPb p_T charged-track distribution [203] to account for the change in p_T shape between different PbPb event activity categories. Although the full HF acceptance is used for the centrality selection in PbPb, the plotted transverse energy is scaled to the same pseudorapidity coverage as the pp and pPb datasets ($4.0 < |\eta| < 5.2$) using the results in Ref. [37].

In Fig. 6.10, the $\Upsilon(2S)/\Upsilon(1S)$ ratios from the three collision systems are plotted versus $E_T^{|\eta|>4}$ in the left panel, and versus $N_{tracks}^{|\eta|<2.4}$ in the right panel. A logarithmic x-axis scale is chosen to allow displaying the three systems together. The relatively wide most peripheral (50–100%) PbPb bin has little overlap with the highest-multiplicity pPb bin, preventing a direct comparison of the two systems at the same event activity. It should be noted that, within (large) uncertainties, the PbPb centrality dependence is not pronounced and that all pp and pPb ratios are far above the PbPb activity-integrated ratio, shown in the Fig. 6.8 (b).

6.6.4. Self-normalized cross sections: $\Upsilon(nS)/\langle\Upsilon(nS)\rangle$

All the ratios presented so far address the relative differences between the excited states and the ground state. In addition, the individual Υ(nS) yields, self-normalized to their activity-integrated values, are computed. The results are shown in Fig. 6.11 in bins of $E_T^{|\eta|>4}/\langle E_T^{|\eta|>4}\rangle$ (top) and $N_{tracks}^{|\eta|<2.4}/\langle N_{tracks}^{|\eta|<2.4}\rangle$ (bottom), for pp and pPb collisions, where the denominator is averaged over all events. These ratios are constructed from the yields extracted from the same fit as the single ratios and are corrected for the residual activity-dependent efficiency that does not cancel in the ratio. The systematic uncertainties

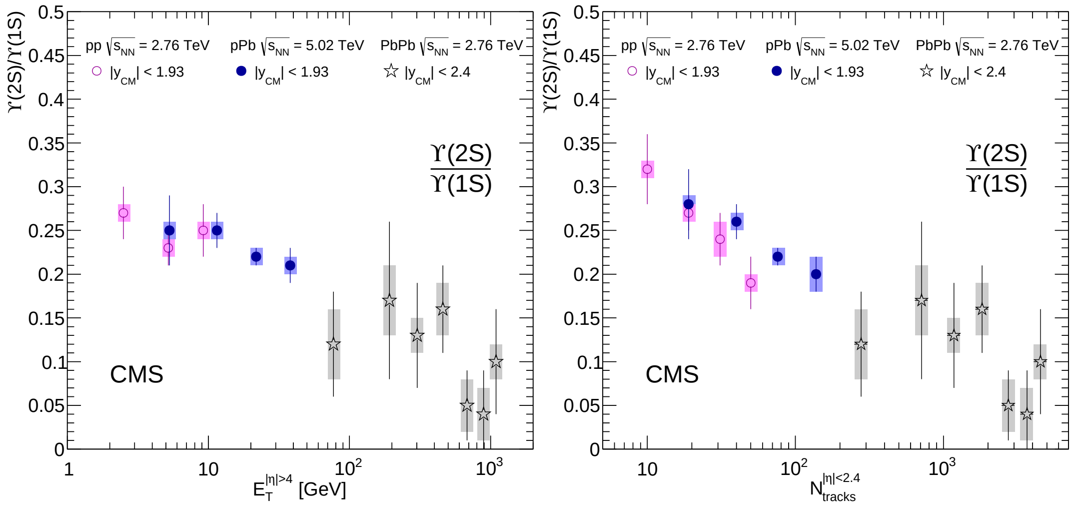

(a) **(b)**

Figure 6.10.: Single cross section ratios $\Upsilon(2S)/\Upsilon(1S)$ for $|y_{CM}| < 1.93$ versus (a) transverse energy measured at $4.0 < |\eta| < 5.2$ and (b) charged-particle multiplicity measured in $|\eta| < 2.4$, for pp collisions at $\sqrt{s} = 2.76$ TeV (open circles) and pPb collisions at $\sqrt{s_{NN}} = 5.02$ TeV (closed circles). Both figures also include the $\Upsilon(2S)/\Upsilon(1S)$ ratios for $|y_{CM}| < 2.4$ measured in PbPb collisions at $\sqrt{s_{NN}} = 2.76$ TeV (open stars). The error bars in the figures indicate the statistical uncertainties, and the boxes represent the point-to-point systematic uncertainties. The global uncertainties of the results are 7%, 8%, and 8% for the pp, pPb, and PbPb, respectively. The results are available in tabulated form in Tables 6.7 and 6.8, with binning information provided in Tables 6.6 and 6.8.

are determined following the same procedure as for the other results reported in this measurement. The bin-to-bin systematic uncertainties, represented by the colored boxes in Fig. 6.11, come from the fitting procedure and are in the ranges 3–7% (Υ(1S)), 5–14% (Υ(2S)) and 6–20% (Υ(3S)), depending on the bin. Figure 6.11 (left) also shows the corresponding ratios for the Υ(1S) state in PbPb collisions, which are derived from measurements described in in chapter 5 by dividing the nuclear modification factors (R_{AA}) binned in centrality by the centrality-integrated R_{AA} value. The Υ(2S) results are not included here because of their low precision.

All the self-normalized cross section ratios increase with increasing forward transverse energy and midrapidity particle multiplicity in the event. In the cases where Pb ions are involved, the increase observed in both variables can arise from the increase in the number of nucleon-nucleon collisions. The pp results are however unexpected and reminiscent of a similar J/ψ measurement made in pp collisions at 7 TeV [204]. A possible interpretation

Table 6.7.: Excited-to-ground state cross section ratios, in event activity bins. Listed uncertainties are statistical first, systematic second, and global scale third.

	Bin	$\frac{\Upsilon(2S)}{\Upsilon(1S)}$	$\frac{\Upsilon(3S)}{\Upsilon(1S)}$
		$E_T^{\|\eta\|>4}$	
pp	1	$0.27 \pm 0.03 \pm 0.01 \pm 0.02$	$0.12 \pm 0.02 \pm 0.01 \pm 0.01$
	2	$0.23 \pm 0.02 \pm 0.01 \pm 0.02$	$0.12 \pm 0.01 \pm 0.01 \pm 0.01$
	3	$0.25 \pm 0.03 \pm 0.01 \pm 0.02$	$0.08 \pm 0.02 \pm 0.01 \pm 0.01$
pPb	1	$0.25 \pm 0.04 \pm 0.01 \pm 0.02$	$0.13 \pm 0.03 \pm 0.01 \pm 0.01$
	2	$0.25 \pm 0.02 \pm 0.01 \pm 0.02$	$0.07 \pm 0.01 \pm 0.01 \pm 0.01$
	3	$0.22 \pm 0.01 \pm 0.01 \pm 0.02$	$0.06 \pm 0.01 \pm 0.01 \pm 0.01$
	4	$0.21 \pm 0.02 \pm 0.01 \pm 0.02$	$0.09 \pm 0.01 \pm 0.01 \pm 0.01$
		$N_{tracks}^{\|\eta\|<2.4}$	
pp	1	$0.32 \pm 0.04 \pm 0.01 \pm 0.02$	$0.16 \pm 0.02 \pm 0.01 \pm 0.01$
	2	$0.27 \pm 0.02 \pm 0.01 \pm 0.02$	$0.12 \pm 0.01 \pm 0.01 \pm 0.01$
	3	$0.24 \pm 0.03 \pm 0.02 \pm 0.02$	$0.11 \pm 0.02 \pm 0.01 \pm 0.01$
	4	$0.19 \pm 0.03 \pm 0.01 \pm 0.01$	$0.06 \pm 0.02 \pm 0.02 \pm 0.00$
pPb	1	$0.28 \pm 0.04 \pm 0.01 \pm 0.02$	$0.12 \pm 0.03 \pm 0.01 \pm 0.01$
	2	$0.26 \pm 0.02 \pm 0.01 \pm 0.02$	$0.10 \pm 0.02 \pm 0.01 \pm 0.01$
	3	$0.22 \pm 0.01 \pm 0.01 \pm 0.02$	$0.08 \pm 0.01 \pm 0.01 \pm 0.01$
	4	$0.20 \pm 0.02 \pm 0.02 \pm 0.02$	$0.05 \pm 0.01 \pm 0.01 \pm 0.00$

of the positive correlation between the Υ production yield and the underlying activity of the pp event is the occurrence of multiple parton-parton interactions in a single pp collision [206].

To compare the trends between collision systems, linear fits (not shown) are performed separately for the pp, pPb, and PbPb results. In the case of the forward transverse energy binning, the self-normalized ratios in all three collision systems are found to have a slope consistent with unity. Hence, no significant difference between pp, pPb, and PbPb results or between individual states is observed when correlating Υ production yields with forward event activity. The similarity of the three systems has to be tempered by the fact that very different mean values are used for normalizing the forward transverse energy, 3.5, 14.7, and 765 GeV, respectively, as well as by the absence of sensitivity of the $\Upsilon(\mathrm{nS})/\langle\Upsilon(\mathrm{nS})\rangle$ observable to a modification that is independent of event activity. In contrast, the case of $N_{tracks}^{|\eta|<2.4}$ binning shows differences between the three states, an

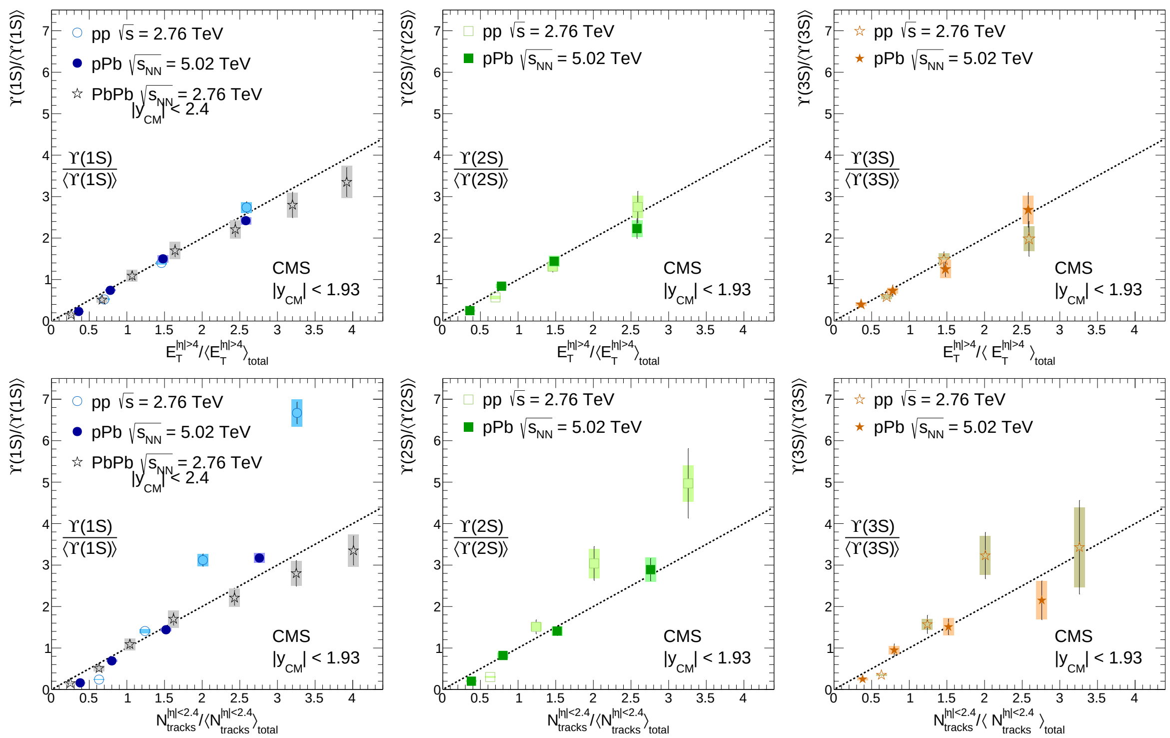

Figure 6.11.: The Υ(nS) cross section versus transverse energy measured at $4 < |\eta| < 5.2$ (top row) and versus charged-track multiplicity measured in $|\eta| < 2.4$ (bottom row), measured in $|y_{\text{CM}}| < 1.93$ in pp collisions at $\sqrt{s} = 2.76\,\text{TeV}$ and pPb collisions at $\sqrt{s_{NN}} = 5.02\,\text{TeV}$. For Υ(1S), the PbPb data at $\sqrt{s_{NN}} = 2.76\,\text{TeV}$ (open stars) are overlaid. Cross sections and x-axis variables are normalized by their corresponding activity-integrated values. For all points, the abscissae are at the mean value in each bin. The dotted line is a linear function with a slope equal to unity. The error bars indicate the statistical uncertainties, and the boxes represent the point-to-point systematic uncertainties. The results are available in tabulated form in Table 6.9.

Table 6.8.: Single cross section ratios, $\Upsilon(2S)/\Upsilon(1S)$ and $\Upsilon(1S)/\langle\Upsilon(1S)\rangle$, measured in bins of centrality (Cent.) in PbPb collisions at $\sqrt{s_{NN}} = 2.76$ TeV , derived from Ref. [205]. The quoted $\langle N^{|\eta|<2.4}_{tracks}\rangle$ values are efficiency corrected. In the second section, the denominator in the fractions is averaged over all events. Listed uncertainties are statistical first, systematic second, and global scale third.

Cent.	$\langle N^{\|\eta\|<2.4}_{tracks}\rangle$	$\langle E^{\|\eta\|>4}_{T}\rangle$ [GeV]	$\frac{\Upsilon(2S)}{\Upsilon(1S)}$
100–50%	278 ± 28	77	$0.12 \pm 0.06 \pm 0.04 \pm 0.01$
50–40%	712 ± 71	192	$0.17 \pm 0.09 \pm 0.04 \pm 0.01$
40–30%	1178 ± 118	302	$0.13 \pm 0.06 \pm 0.02 \pm 0.01$
30–20%	1825 ± 183	459	$0.16 \pm 0.05 \pm 0.03 \pm 0.01$
20–10%	2744 ± 274	681	$0.05 \pm 0.04 \pm 0.03 \pm 0.01$
10–5%	3672 ± 367	892	$0.04 \pm 0.05 \pm 0.03 \pm 0.01$
5–0%	4526 ± 453	1093	$0.10 \pm 0.06 \pm 0.02 \pm 0.01$
Cent.	$\frac{\langle N^{\|\eta\|<2.4}_{tracks}\rangle}{\langle N^{\|\eta\|<2.4}_{tracks}\rangle_{\mathrm{total}}}$	$\frac{\langle E^{\|\eta\|>4}_{T}\rangle}{\langle E^{\|\eta\|>4}_{T}\rangle_{\mathrm{total}}}$	$\frac{\Upsilon(1S)}{\langle\Upsilon(1S)\rangle}$
100–50%	0.25	0.26	$0.15 \pm 0.02 \pm 0.03$
50–40%	0.63	0.67	$0.51 \pm 0.08 \pm 0.07$
40–30%	1.04	1.07	$1.09 \pm 0.11 \pm 0.14$
30–20%	1.62	1.64	$1.70 \pm 0.15 \pm 0.21$
20–10%	2.43	2.44	$2.21 \pm 0.18 \pm 0.22$
10–5%	3.25	3.20	$2.80 \pm 0.31 \pm 0.30$
5–0%	4.01	3.92	$3.35 \pm 0.35 \pm 0.39$

observation which is related to the single-ratio variations observed in Fig. 6.9 (b). The $\Upsilon(1S)$, in particular, exhibits the fastest rise in pp collisions.

6.7. Summary

The measurement of relative production of the three Υ states in pPb and pp collisions collected in 2013 by the CMS experiment, in the $|y_{\mathrm{CM}}| < 1.93$ center-of-mass rapidity range is done. The self-normalized cross section ratios, $\Upsilon(1S)/\langle\Upsilon(1S)\rangle$, $\Upsilon(2S)/\langle\Upsilon(2S)\rangle$, $\Upsilon(3S)/\langle\Upsilon(3S)\rangle$, increase with event activity. The excited-to-ground-states cross section ratios, $\Upsilon(nS)/\Upsilon(1S)$, are found to decrease with increasing charged-particle multiplicity as measured in the $|\eta| < 2.4$ pseudorapidity interval that contains the region in

Table 6.9.: Self-normalized cross section ratios, in event activity bins. In the first column for each bin, the numerator is averaged over the bin and the denominator is averaged over all events. Listed uncertainties are statistical first and systematic second.

Bin			$\frac{\Upsilon(1S)}{\langle\Upsilon(1S)\rangle}$	$\frac{\Upsilon(2S)}{\langle\Upsilon(2S)\rangle}$	$\frac{\Upsilon(3S)}{\langle\Upsilon(3S)\rangle}$
		$\frac{\langle E_T^{\lvert\eta\rvert>4}\rangle}{\langle E_T^{\lvert\eta\rvert>4}\rangle_{\text{total}}}$		$E_T^{\lvert\eta\rvert>4}$	
pp	1	0.70	$0.52 \pm 0.02 \pm 0.02$	$0.57 \pm 0.07 \pm 0.04$	$0.59 \pm 0.08 \pm 0.06$
	2	1.46	$1.40 \pm 0.05 \pm 0.04$	$1.31 \pm 0.13 \pm 0.10$	$1.48 \pm 0.19 \pm 0.15$
	3	2.59	$2.74 \pm 0.14 \pm 0.13$	$2.75 \pm 0.38 \pm 0.27$	$1.98 \pm 0.42 \pm 0.30$
pPb	1	0.36	$0.23 \pm 0.01 \pm 0.01$	$0.25 \pm 0.04 \pm 0.02$	$0.40 \pm 0.07 \pm 0.04$
	2	0.78	$0.74 \pm 0.03 \pm 0.02$	$0.84 \pm 0.07 \pm 0.05$	$0.73 \pm 0.14 \pm 0.07$
	3	1.48	$1.50 \pm 0.04 \pm 0.09$	$1.44 \pm 0.10 \pm 0.13$	$1.25 \pm 0.18 \pm 0.22$
	4	2.58	$2.42 \pm 0.08 \pm 0.09$	$2.23 \pm 0.24 \pm 0.20$	$2.68 \pm 0.42 \pm 0.34$
		$\frac{\langle N_{tracks}^{\lvert\eta\rvert<2.4}\rangle}{\langle N_{tracks}^{\lvert\eta\rvert<2.4}\rangle_{\text{total}}}$		$N_{tracks}^{\lvert\eta\rvert<2.4}$	
pp	1	0.63	$0.24 \pm 0.01 \pm 0.01$	$0.30 \pm 0.05 \pm 0.02$	$0.35 \pm 0.05 \pm 0.02$
	2	1.24	$1.41 \pm 0.06 \pm 0.05$	$1.51 \pm 0.17 \pm 0.10$	$1.57 \pm 0.22 \pm 0.13$
	3	2.01	$3.12 \pm 0.15 \pm 0.15$	$3.04 \pm 0.41 \pm 0.35$	$3.23 \pm 0.56 \pm 0.47$
	4	3.26	$6.67 \pm 0.26 \pm 0.33$	$4.97 \pm 0.84 \pm 0.44$	$3.43 \pm 1.13 \pm 0.96$
pPb	1	0.38	$0.16 \pm 0.01 \pm 0.01$	$0.20 \pm 0.03 \pm 0.02$	$0.25 \pm 0.05 \pm 0.03$
	2	0.80	$0.69 \pm 0.03 \pm 0.03$	$0.82 \pm 0.09 \pm 0.07$	$0.95 \pm 0.15 \pm 0.10$
	3	1.52	$1.44 \pm 0.04 \pm 0.04$	$1.41 \pm 0.11 \pm 0.11$	$1.51 \pm 0.19 \pm 0.21$
	4	2.76	$3.17 \pm 0.09 \pm 0.12$	$2.89 \pm 0.27 \pm 0.29$	$2.15 \pm 0.47 \pm 0.46$

which the Υ are measured. This unexpected dependence suggests novel phenomena in quarkonium production that could arise from a larger number of charged particles being systematically produced with the ground state, or from a stronger impact of the growing number of nearby particles on the more weakly bound states. This dependence is less pronounced when the event activity is inferred from transverse energy deposited in the forward $4.0 < |\eta| < 5.2$ region. When integrated over event activity, the double ratios $[\Upsilon(\text{nS})/\Upsilon(\text{1S})]_{\text{pPb}}/[\Upsilon(\text{nS})/\Upsilon(\text{1S})]_{\text{pp}}$ are found to be equal to $0.83 \pm 0.05\,(\text{stat}) \pm 0.05\,(\text{syst})$ and $0.71 \pm 0.08\,(\text{stat}) \pm 0.09\,(\text{syst})$ for Υ(2S) and Υ(3S), respectively, which are larger than the corresponding double ratios measured for PbPb collisions. This suggests the presence of final-state suppression effects in the pPb collisions compared to pp collisions which affect more strongly the excited states (Υ(2S) and Υ(3S)) compared to the ground state (Υ(1S)). A global understanding of the effects at play in pp, pPb, and PbPb calls for more activity-related studies of the Υ yields in pp collisions, as well as for additional PbPb data allowing a more detailed investigation of the most peripheral events.

Chapter 7.

Components of dilepton continuum in PbPb collisions at $\sqrt{s_{NN}} = 2.76$ TeV

In this chapter, we calculate $c\bar{c}$ and $b\bar{b}$ production and determine their contributions to the dilepton continuum in PbPb collisions at $\sqrt{s_{NN}} = 2.76$ TeV. We also calculate the rates for Drell-Yan and thermal dilepton production. The contributions to the continuum from these dilepton sources are studied in the kinematic ranges relevant for the LHC detectors.

7.1. Introduction

Quarkonia are identified by their reconstructed mass peaks in the dilepton invariant mass distribution. Below ~ 12 GeV/c^2, the dilepton distribution includes a number of resonance peaks: ρ, ω and ϕ at low masses and the ψ and Υ states at higher masses. At 91 GeV/c^2, the $Z^0 \to l^+l^-$ peak appears. The continuum beneath these resonances is primarily composed of leptons from semileptonic decays of heavy flavor hadrons. These heavy flavor decays not only contribute to the resonance background but are important physics signals in their own right [207–209]. The continuum yields in Pb+Pb collisions compared to those in pp collisions can provide information about the medium properties. This makes it important to know the various contributions to the dilepton continuum in different kinematic regimes. In this chapter we describe calculations of $c\bar{c}$ and $b\bar{b}$ production and determine their contributions to the dilepton continuum in PbPb collisions at $\sqrt{s_{NN}} = 2.76$ TeVwith and without including heavy quark energy loss. We also calculate the rates for Drell-Yan and thermal dilepton production. The contributions to the continuum from these dilepton sources are studied in the kinematic ranges relevant for the LHC detectors.

The first measurements of the dilepton spectra at the LHC have been reported [69, 166, 210]. The CMS experiment reported the first measurements of the Z^0 mass region in Pb+Pb collisions [69] as well as measurements of the full dimuon distribution, including quarkonia [166]. ATLAS has also reported J/ψ and Z^0 measurements in the dimuon channel [210]. The second LHC Pb+Pb run, at much higher luminosity, has provided higher statistics measurements of the dilepton spectra over the full available phase space. With the measurement of dilepton spectrum in Pb+Pb collisions at the LHC, it is time to re-examine the continuum contributions to the dilepton mass spectrum. The production cross sections of $c\bar{c}$ and $b\bar{b}$ pairs at $\sqrt{s_{_{NN}}} = 2.76$ TeV are calculated to next-to-leading order (NLO) and their correlated contributions to the dilepton continuum are subsequently obtained. We also include the effect of energy loss of charm and bottom quarks in the medium consistent with measurements of the suppression factor R_{AA} on the lepton spectra from semileptonic decays of charm and bottom [211, 212]. These contributions are compared to direct dilepton production from the Drell-Yan process and from thermal production in the medium. We then evaluate the relative importance of these contributions in the LHC detector acceptances.

While there have been previous studies of Pb+Pb collisions at 5.5 TeV [213], a re-examination is appropriate at the current, lower, center of mass energy and with the final detector acceptances. In addition, updated parameterizations of the parton distribution functions as well as estimates of the effect of energy loss on single particle spectra and determinations of the initial temperature from the charged particle multiplicity are now available and should lead to improved predictions. The experimental dilepton measurements presently concentrate on resonances. However, background-subtracted dilepton continuum measurements should soon be available with good statistics at 2.76 TeV in both pp and PbPb collisions which could be used to infer propeties of the medium produced in Pb+Pb collisions.

7.2. Dilepton production by hard processes

Dilepton production from semileptonic decays of $D\overline{D}$ (charm) and $B\overline{B}$ (bottom) meson pairs has been an area of active theoretical [208, 214] and experimental [95, 215] research. The large heavy quark mass allows their production to be calculated in perturbative

QCD. We calculate the production cross sections for $c\bar{c}$ and $b\bar{b}$ pairs to NLO in pQCD using the CTEQ6M parton densities [11, 136]. The central EPS09 parameter set [12] is used to calculate the modifications of the parton densities in Pb+Pb collisions. We include the theoretical uncertainty bands on charm and bottom production following the method of Ref. [13]. We use the same set of parameters as that of Ref. [13] with the exclusive NLO calculation of Ref. [14] to obtain the exclusive $Q\overline{Q}$ pair rates as well as their decays to dileptons. We take $m_c = 1.5$ GeV/c^2, $\mu_F/m_T = \mu_R/m_T = 1$ and $m_b = 4.75$ GeV/c^2, $\mu_F/m_T = \mu_R/m_T = 1$ as the central values for charm and bottom production respectively. Here μ_F is the factorization scale, μ_R is the renormalization scale and $m_T = \sqrt{m_Q^2 + p_T^2}$. The mass and scale variations are added in quadrature to obtain the uncertainty bands [13].

Figure 7.1 shows the uncertainty bands on the p_T and rapidity distributions of charm and bottom quarks in Pb+Pb collisions at $\sqrt{s_{_{NN}}} = 2.76$ TeV with shadowing effects included. We only calculate the uncertainties in the production cross sections due to the mass and scale parameters and not those due to the EPS09 modifications or those of the parton densities. Both of these uncertainties are smaller than those due to the choice of mass and scale [216], particularly for $p_T \geq m$. The uncertainties on the heavy flavor production cross sections can be rather large, see Refs. [217, 218]. Thus the relative charm and bottom rates at 2.76 TeV may vary by a factor of two or more before dense matter effects such as energy loss are taken into account. While a recent reevaluation of the mass and scale parameters used to calculate charm production shows that the uncertainty on the charm production cross section can be reduced, it cannot be eliminated [216].

The differences in the quark p_T distributions are primarily at low p_T. For $p_T >$ 10 GeV/c, the uncertainty bands overlap almost completely with the upper limit on the bottom production band somewhat above the charm upper limit for $p_T >$ 20 GeV/c. The widths of the rapidity distributions are limited by the heavy quark mass. Thus the charm rapidity distribution is broader than that for bottom. The uncertainty bands are broader in rapidity than in p_T for charm and the bands for the two flavors are cleanly separated because the p_T-integrated rapidity distribution is dominated by low p_T where the charm cross section is clearly greater and the scale uncertainties are larger.

The production cross sections for heavy flavor and Drell-Yan dileptons at $\sqrt{s_{NN}} =$ 2.76 TeV are shown in Table 9.1. The number of $Q\overline{Q}$ pairs in a minimum bias Pb+Pb

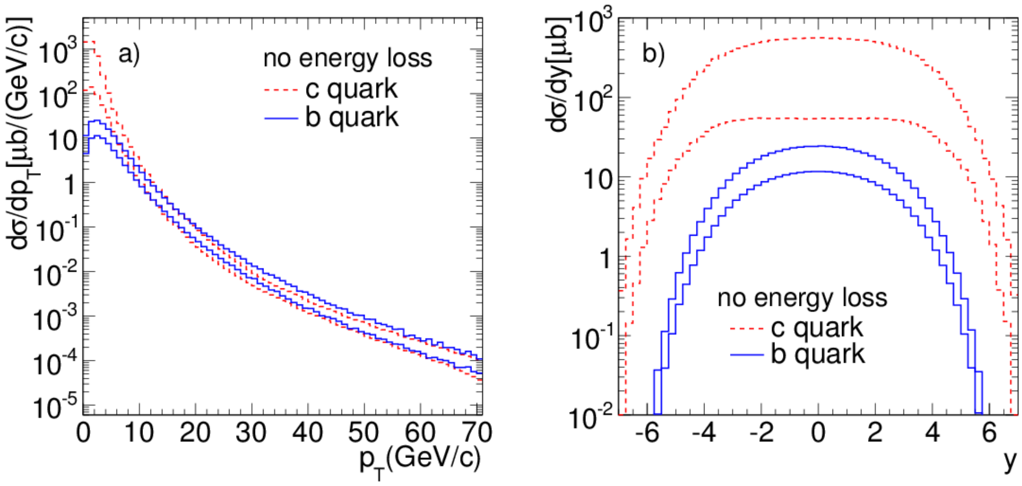

(a) **(b)**

Figure 7.1.: Theoretical uncertainty bands on inclusive single charm and bottom quark production cross sections per nucleon as functions of p_T (a) and rapidity (b) for $\sqrt{s_{NN}} = 2.76$ TeV. The uncertainties are calculated by varying the quark mass, renormalization scale μ_R and factorization scale μ_F. The calculations include modification of the initial parton distributions with the EPS09 central parameter set. No final state energy loss is included.

event is obtained from the per nucleon cross section, $\sigma_{\rm PbPb}$, by

$$N_{Q\overline{Q}} = \frac{A^2 \sigma_{\rm PbPb}^{Q\overline{Q}}}{\sigma_{\rm PbPb}^{\rm tot}} \ . \tag{7.1}$$

At 2.76 TeV, the total Pb+Pb cross section, $\sigma_{\rm PbPb}^{\rm tot}$, is 7.65 b [7].

We assume that all the observed heavy flavor production in Pb+Pb collisions occurs during the initial nucleon-nucleon collisions. Thermal production of $Q\overline{Q}$ pairs is expected to be only a fraction of this initial production unless the plasma is composed of massive quasi-particles which would lower the effective threshold for heavy flavor production in the medium [219], enhancing production in this channel. However, such production would be at lower transverse momentum and with a narrower rapidity distribution than shown in Fig. 7.3.

The heavy quarks are decayed semileptonically and lepton pairs are formed from correlated $Q\overline{Q}$ pair decays. We do not consider uncorrelated $Q\overline{Q}$ contributions to the continuum since these should be eliminated by a like-sign subtraction. We assume that

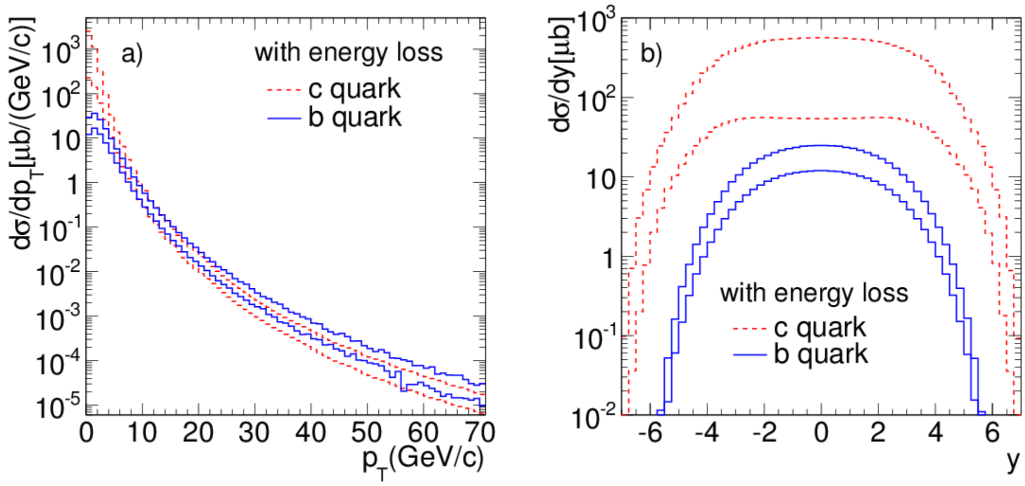

(a) **(b)**

Figure 7.2.: Theoretical uncertainty bands on inclusive single charm and bottom quark production cross sections per nucleon as functions of p_T (a) and rapidity (b) for $\sqrt{s_{NN}} = 2.76$ TeV. The uncertainties are calculated by varying the quark mass, renormalization scale μ_R and factorization scale μ_F. The calculations include modification of the initial parton distributions with the EPS09 central parameter set. Here we include final state energy loss assuming that the charm and bottom quark R_{AA} is the same, as discussed in the text.

Table 7.1.: Heavy flavor and Drell-Yan cross sections at $\sqrt{s_{NN}} = 2.76$ TeV. The cross sections are given per nucleon while $N_{Q\overline{Q}}$ and $N_{l^+l^-}$ are the number of $Q\overline{Q}$ and lepton pairs per Pb+Pb event. The uncertainties in the heavy flavor cross section are based on the Pb+Pb central values with the mass and scale uncertainties added in quadrature.

	$c\overline{c}$	$b\overline{b}$	DY $1 \leq M \leq 100$ GeV
$\sigma_{\rm PbPb}$	$1.76^{+2.32}_{-1.29}$ mb	$89.3^{+42.7}_{-27.2}$ μb	70.97 nb
$N_{Q\overline{Q}}$	$9.95^{+13.10}_{-7.30}$	$0.50^{+0.25}_{-0.15}$	-
$N_{\mu^+\mu^-}$	$0.106^{+0.238}_{-0.078}$	$0.0059^{+0.0029}_{-0.0017}$	0.0004

any uncorrelated dileptons from $c\overline{b}$ and $\overline{c}b$ decays are also removed by like-sign subtraction and that lepton pairs from a single chain decay, $B \rightarrow Dl_1X \rightarrow l_1l_2X'$, only contribute to the low mass continuum. The number of lepton pairs is obtained from the number of $Q\overline{Q}$ pairs,

$$N_{\mu^+\mu^-} = N_{Q\overline{Q}}[B(Q \rightarrow lX)]^2 \ . \tag{7.2}$$

The values of $N_{Q\overline{Q}}$ and $N_{\mu^+\mu^-}$ are given in Table 9.1, along with their uncertainties.

Dilepton production by the Drell-Yan process has also been calculated to NLO in pQCD [220]. The cross section in the mass interval $1 < M < 100$ GeV, including EPS09 shadowing in Pb+Pb collisions, is given in Table 9.1. The integrated cross section is dominated by the lowest masses. The largest potential modification due to the presence of the nucleus is on the low mass rate, in the resonance region. At larger masses, this effect becomes competitive with the effects of the relative number of protons and neutrons in the nucleus compared to a *pp* collision (isospin effects) [221]. We have used PYTHIA [8] to generate the Drell-Yan p_T distribution and to place kinematic cuts on the individual leptons of the pair. The total rate has been normalized to the calculated NLO cross section. The pQCD uncertainties on the Drell-Yan rate, particularly above the resonance region, are not large. In general, they are smaller than the uncertainties due to the shadowing parameterization [221].

Finally, we include energy loss effects on the charm and bottom quarks. Since heavy quarks do not decay until after they have traversed the medium, their contribution to the final dilepton spectra will reflect its influence. Indications from inclusive non-photonic lepton spectra (leptons excluding pair production) at RHIC[95, 215], attributed to heavy flavor decays, suggest that the effects of energy loss are strong and persist up to high p_T. They also suggest that the magnitude of the loss is similar for that of light flavors, *i.e.* independent of the quark mass so that the effects are similar for charm and bottom. The source of this loss as well as its magnitude are still under investigation, see Ref. [89] and references therein.

To estimate the effects of energy loss on the dilepton continuum, we adjust the heavy quark fragmentation functions to give a value of R_{AA} for each flavor separately that is consistent with the measured prompt lepton R_{AA} in central Pb+Pb collisions at high p_T, $R_{AA} \sim 0.25 - 0.30$ [212], for both charm and bottom quarks. We then use these modified fragmentation functions to calculate the medium-modified dilepton distributions from heavy flavor decays.

Including energy loss does not change the total cross section since it moves the quarks to lower momentum without removing them from the system. Thus the p_T-integrated rapidity distributions are also unaffected, see Fig. 7.2, which presents the single inclusive heavy flavor production uncertainty bands after energy loss. The charm and bottom quark p_T distributions still exhibit the same general behavior: the slopes are parallel to those without energy loss at high p_T but show a pile up of low p_T quarks after loss is included. After taking energy loss into account, the point where the bottom quark distribution begins to dominate is shifted to lower p_T, ~ 10 GeV/c instead of ~ 20 GeV/c when the widths of the bands are accounted for.

The relative strength of charm and bottom energy loss in medium is not yet settled. Although bottom quarks are expected to lose less energy than charm quarks, the data from RHIC and LHC exhibit important differences [167, 222]. If we assume that bottom quarks lose less energy than charm, then the bottom and charm quark uncertainty bands in Fig. 7.2 will separate at high p_T with the bottom quark band above that of the charm.

Figure 7.3 compares the central values of the uncertainty bands with and without energy loss directly. We note that the difference in the heavy flavor p_T distributions due to energy loss is larger than the uncertainty bands with and without energy loss. The rapidity distributions do not show any significant effect due to energy loss since the results are shown integrated over all p_T. Since the total cross sections are unchanged without any acceptance cuts, there is an effect only at far forward rapidity.

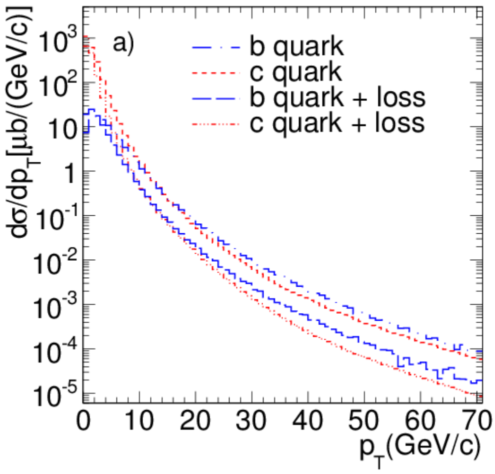

(a)

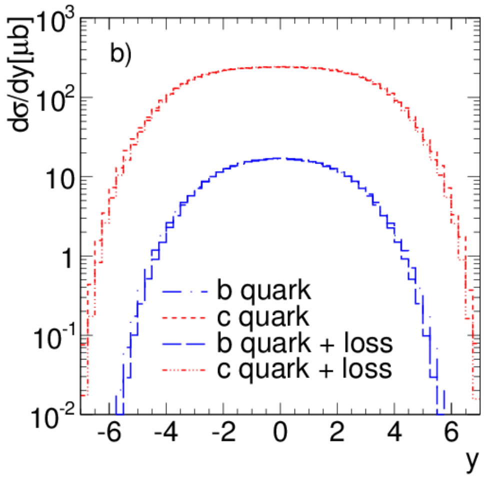

(b)

Figure 7.3.: The inclusive single charm and bottom quark per nucleon cross sections as a function of p_T (a) and rapidity (b) both with and without energy loss in Pb+Pb collisions at $\sqrt{s_{NN}} = 2.76$ TeV. The cross sections, given per nucleon, include modification of the initial parton distributions via the central EPS09 shadowing parameterization.

7.3. Thermal dilepton production

The contribution of thermal dileptons is calculated assuming that a QGP is formed in local thermal equilibrium at some initial temperature T_i and initial time τ_i which cools hydrodynamically through a 1D Bjorken expansion [36]. Assuming a first-order phase transition, when the QGP cools to the critical temperature T_c at time τ_c, the temperature of the system is held fixed until hadronization is completed at time τ_h. Afterwards, the hadron gas cools to the freeze-out temperature T_f at time τ_f [223].

The thermal dilepton emission rate due to $q\bar{q} \to l^- l^+$ is [223, 224]

$$\begin{aligned} \frac{dN}{d^4x d^2p_T dy dM^2} &= \frac{3}{(2\pi)^5} M^2 \sigma(M^2) F \exp(-E/T) \\ &= \frac{\alpha^2}{8\pi^4} F \exp(-E/T) \ . \end{aligned} \tag{7.3}$$

Here M, p_T and y are the mass, transverse momentum, and rapidity of the lepton pair while $d^4x = \tau d\tau \eta \pi R_A^2$ where η is the rapidity of the fluid with temperature T and $R_A = r_0 A^{1/3}$. The mass-dependent cross section, $\sigma(M^2) = F\ 4\pi\alpha^2/3M^2$ includes a factor F that depends on the phase of the matter. In a two-flavor QGP, $F_{\mathrm{QGP}} = \sum e_q^2 = 5/9$,

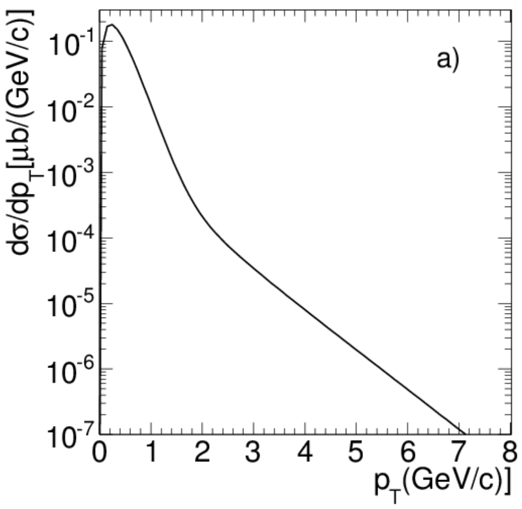

(a)

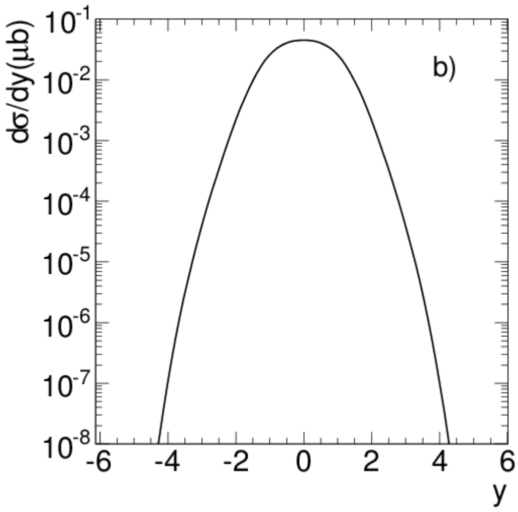

(b)

Figure 7.4.: The thermal dilepton cross section as a function of p_T (a) and rapidity (b) in Pb+Pb collisions at $\sqrt{s_{NN}} = 2.76$ TeV.

while, in the hadronic phase, form factors representing the resonance region [225] are used. We concentrate on masses above the resonance region. In the mixed phase,

$$F = (1 - h(\tau))\, F_{\text{QGP}} + h(\tau)\, F_{\text{had}} \ , \tag{7.4}$$

where $h(\tau)$ is the hadron fraction of the mixed phase.

The dilepton p_T distribution is

$$\frac{dN}{d^4x dy dM dp_T} = \frac{\alpha^2}{4\pi^4} F\, M\, p_T\, \exp\left(-\frac{\sqrt{M^2 + p_T^2}\cosh(y - \eta)}{T} \right) \tag{7.5}$$

and the dilepton invariant mass distribution, integrated over p_T, is

$$\frac{dN}{d^4x dy dM} = \frac{\alpha^2}{2\pi^3} F\, M^3 \left(\frac{1}{x^2} + \frac{1}{x} \right) \exp(-x), \tag{7.6}$$

where

$$x = \frac{M \cosh(y - \eta)}{T}. \tag{7.7}$$

The initial time is assumed to be $\tau_i = 0.1$ fm/c. The initial temperature T_i is obtained from the total multiplicity distribution,

$$\frac{dN}{dy} = \tau_i T_i^3 4 a_q \pi R_A^2 / 3.6 \ , \tag{7.8}$$

where $dN/dy = 1.5 \ dN_{\rm ch}/dy$. The charged particle multiplicity, $dN_{\rm ch}/dy = 1600$, was measured in Pb+Pb collisions at 2.76 TeV [41]. Using this value with $a_q = 37\pi^2/90$ gives $T_i = 636$ MeV. The temperature decreases in the QGP as

$$T(\tau) = T_i \left(\frac{\tau_i}{\tau}\right)^{1/3} \tag{7.9}$$

for $\tau_i \ < \ \tau \ < \ \tau_c$. The temperature in mixed phase is $T = T_c = 160$ MeV. The mixed phase ends at $\tau_h = (a_q/a_h)\tau_c$ where $a_h = 3\pi^2/90$ for a pion gas. The hadronic fraction of the mixed phase, $h(\tau)$, is

$$h(\tau) = \frac{a_q}{a_q - a_h} \left(\frac{\tau - \tau_c}{\tau}\right) \ . \tag{7.10}$$

The temperature in hadron phase between $\tau_h \ < \ \tau \ < \ \tau_f$, is

$$T(\tau) = T_c \left(\frac{\tau_h}{\tau}\right)^{1/3} \ . \tag{7.11}$$

The thermal dilepton rate given in Eqs. (7.5) and (7.6) is converted to a cross section by dividing the rate by the minimum bias nuclear overlap, $T_{\rm PbPb}$. Figure 7.4(a) and (b), shows the differential cross sections for thermal dilepton production as a function of p_T and rapidity. The p_T distribution, integrated over pair mass, shows two slopes, a steep decrease when the minimum pair transverse mass, M_T, is on the order of the temperature and a long tail when $M_T \gg T$. The rapidity distribution is significantly narrower than those resulting from the initial hard scatterings shown in Fig. 7.3.

This simple application of a one-dimensional Bjorken expansion through a first-order phase transition significantly overestimates the lifetime of the hot system. Thus, the results shown in Fig. 7.4 should be regarded as an upper limit on the thermal contribution.

To obtain the pair mass distributions including single lepton cuts, single leptons are generated by a Monte Carlo based on the pair M, p_T and y distributions using energy-momentum conservation.

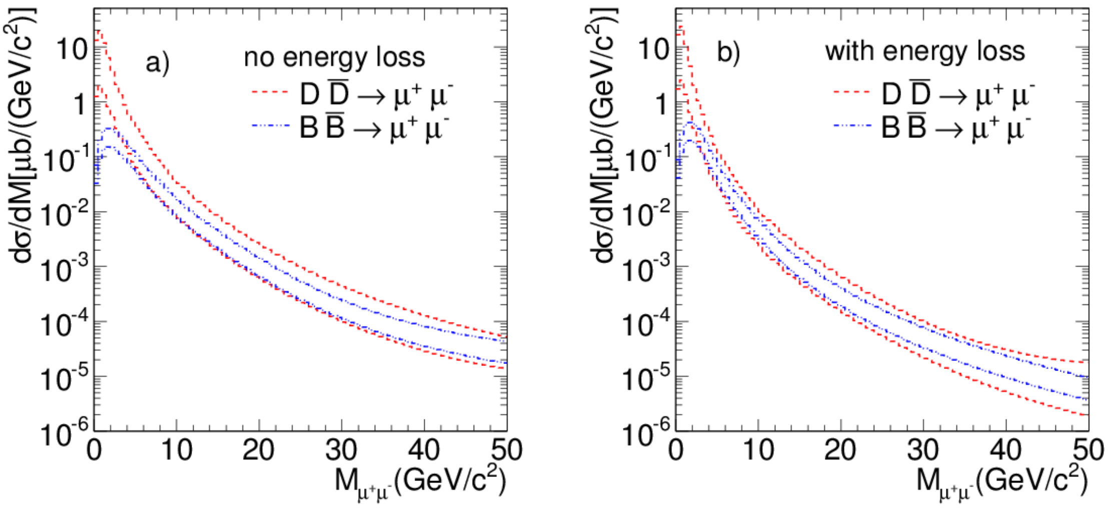

Figure 7.5.: Theoretical uncertainty bands for the dilepton invariant mass distributions from semileptonic charm (red, short-dashed) and bottom (blue, dot-dot-dashed) decays. The uncertainties are calculated the same way as in Sect. 7.2.

7.4. Results and discussion

In Fig. 7.5, we show the theoretical uncertainty bands on the dilepton invariant mass distributions from semileptonic charm and bottom decays. The uncertainty bands for the decay dileptons are calculated identically to those of the charm and bottom quark distributions shown in Sec. 7.2. The dilepton uncertainty bands are broader than those for the single inclusive heavy flavors and, here, the dilepton band from charm decays is wider than for bottom. This is the case both without, Fig. 7.5(a), and with, Fig. 7.5(b), energy loss. While we show only the central values of these distributions in the remainder of this section, it is important to keep in mind the significant mass and scale uncertainties in heavy flavor production, considerably larger than those on high mass Drell-Yan production.

Figure 7.6 shows the dimuon invariant mass distributions from each of the four sources considered: semileptonic decays of correlated $Q\overline{Q}$ pairs and direct production of Drell-Yan and thermal dileptons in Pb+Pb collisions at $\sqrt{s_{_{NN}}} = 2.76$ TeV. Figure 7.6(a) shows the heavy flavor mass distributions without any final-state energy loss while energy loss is included in the heavy flavor distributions on Fig. 7.6(b). Only the central values of the heavy flavor contributions are shown. The Drell-Yan and thermal dilepton distributions are unchanged. No kinematic cuts are included. Without cuts, dileptons from $D\overline{D}$ decays dominate over the entire mass range due to the large $c\overline{c}$ production cross section. Bottom pair decays are the next largest contribution followed by Drell-Yan production. At masses below 3 GeV/c^2, the Drell-Yan and thermal dilepton contributions are competitive. Otherwise, the thermal contribution is negligible. Including energy loss steepens the slope of the heavy flavor mass distributions and also moves the $D\overline{D}$ decay distributions closer to the $B\overline{B}$ decay distributions. In the remainder of this section, we will show only results with final-state heavy flavor energy loss included.

We now examine these distributions in the kinematic regimes appropriate for the LHC detectors. CMS [179] and ATLAS [226] have excellent muon detectors with similar coverage in the central rapidity region, $|\eta^\mu| \leq 2.4$. However, due to the large magnetic fields, only muons above a rather high minimum p_T, $p_T > 3.0$ GeV/c, make it into the muon detectors. ALICE [227] has muon acceptance on one side of the forward rapidity region, $2.5 \leq \eta^\mu \leq 4.0$. At central rapidities, $|\eta^\mu| \leq 1.0$, ALICE has an electron detector. Some previous studies of Pb+Pb collisions at 5.5 TeV, using leading order calculations of heavy quark production and assuming significantly higher initial temperatures than employed here, suggested that thermal dileptons could be extracted from the QGP [213]. Thus they reached different conclusions about the relative contributions of thermal and heavy flavor dileptons to the continuum.

Figure 7.7 shows the dimuon invariant mass distribution for single muons in the range $|\eta^\mu| \leq 2.4$, together with several muon p_T cuts. Figure 7.7(a) has no muon p_T cut, only the η cut. Comparison with Fig. 7.6 shows that the thermal dilepton contribution is almost unaffected since its rapidity distribution is sufficiently narrow to fit within the CMS rapidity acceptance. Since the Drell-Yan rapidity distribution narrows with increasing mass, only the low mass region is affected by the rather broad rapidity cut of $|\eta^\mu| \leq 2.4$. Because the charm rapidity range is broader than that of bottom production, the dileptons from charm decays are most affected by the rapidity cut. For $M_{\mu^+\mu^-} > 5$ GeV/c^2, the charm dilepton yield has dropped below that of bottom.

Adding a cut on single lepton p_T disproportionally affects the low mass part of the continuum. As the minimum lepton p_T is increased from 1 GeV/c to 10 GeV/c in Figs. 7.7(b)-7.7(d), an ever-deepening dip appears in the dilepton mass distribution for $M_{\mu^+\mu^-} < 2p_T^\mu$. Even a relatively low p_T cut essentially eliminates the thermal dilepton contribution since these leptons have a rather soft p_T distribution. Since the charm and bottom quark p_T distributions have the same slope for $p_T > 7$ GeV/c, their decays are affected the same way by the lepton p_T cut. Finally, the single lepton cut of $p_T^\mu > 10$ GeV/c, published with the CMS Z^0 measurement [69], based on approximately 50 million events, had a very low continuum background. This is in agreement with the

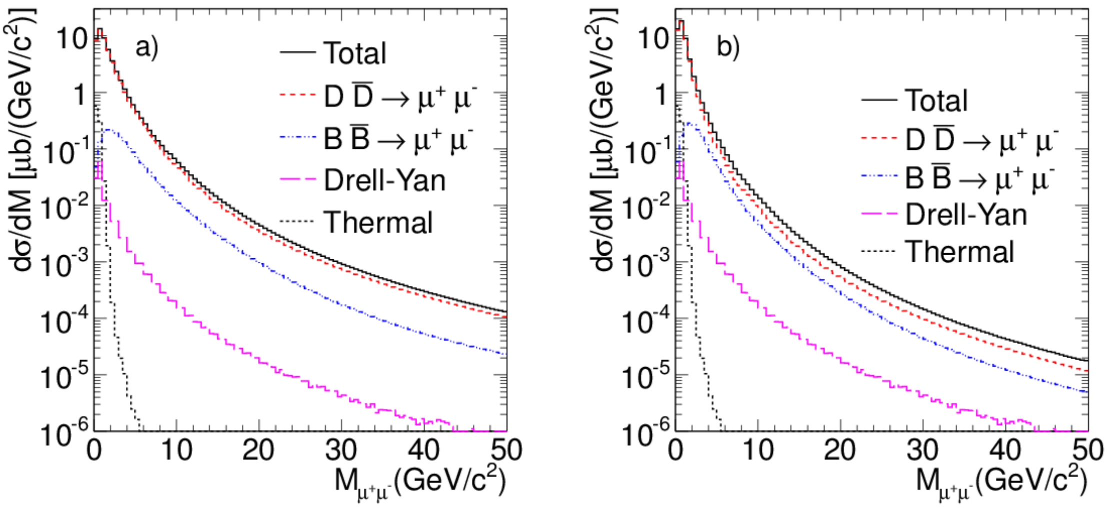

Figure 7.6.: The invariant mass distributions for the four contributions to the dilepton spectra discussed here: semileptonic charm (red, short-dashed) and bottom (blue, dot-dot-dashed) decays, Drell-Yan (magenta, long-dashed) and thermal (black, dotted) dileptons along with the sum (black, solid) in Pb+Pb collisions per nucleon pair at $\sqrt{s_{NN}} = 2.76$ TeV. Left pannel shows distributions without any final state energy loss, right pannel is after including heavy quark energy loss in the medium. The per nucleon cross sections are given. No phase space or kinematic cuts are introduced.

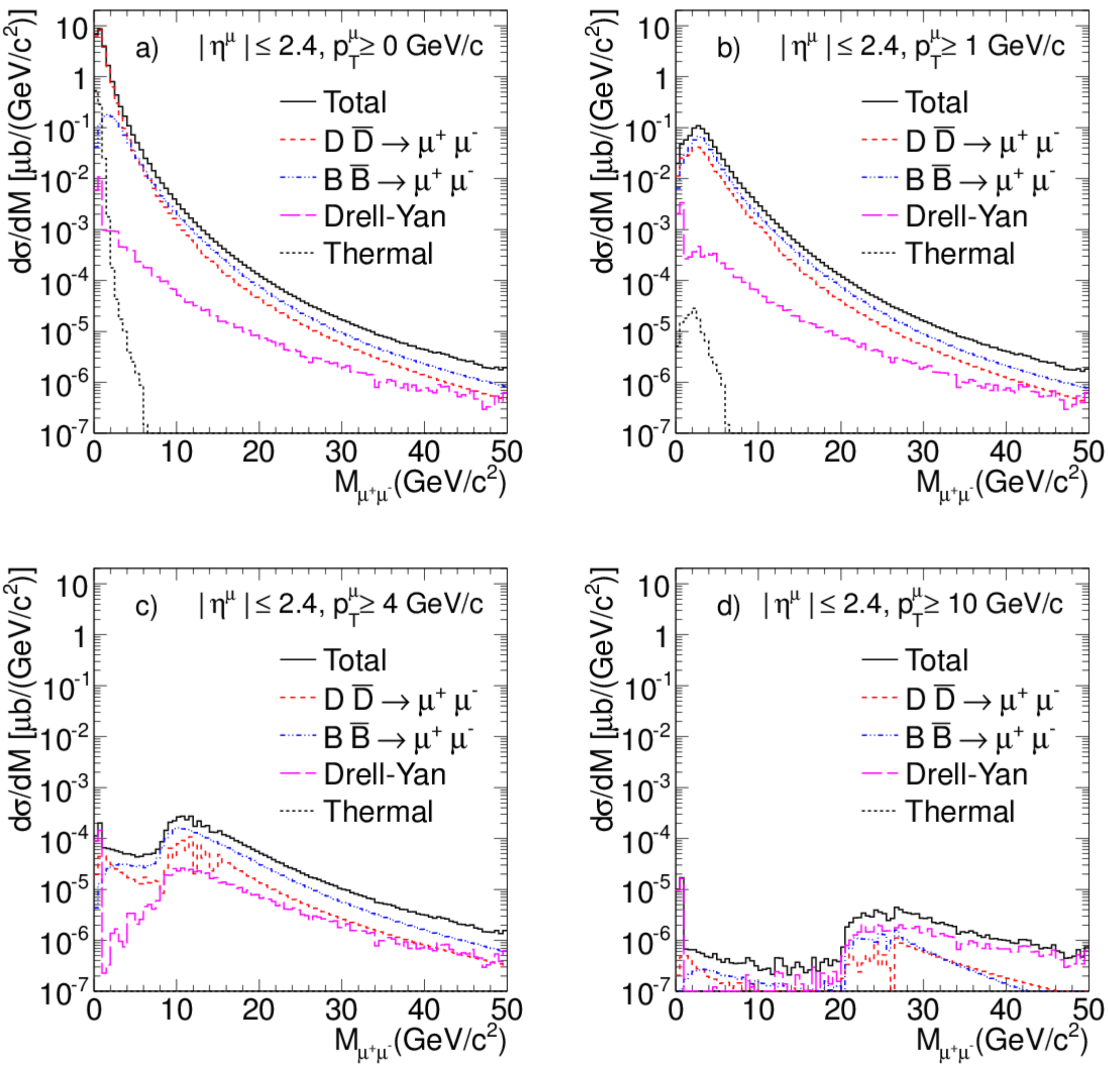

Figure 7.7.: The same as Fig. 7.6 but now with single muon rapidity cuts of $|\eta^\mu| \leq 2.4$. A minimum single lepton transverse momentum cut of $p_T^\mu \geq 0$ (a), 1 (b), 4 (c) and 10 (d) GeV/c is also shown.

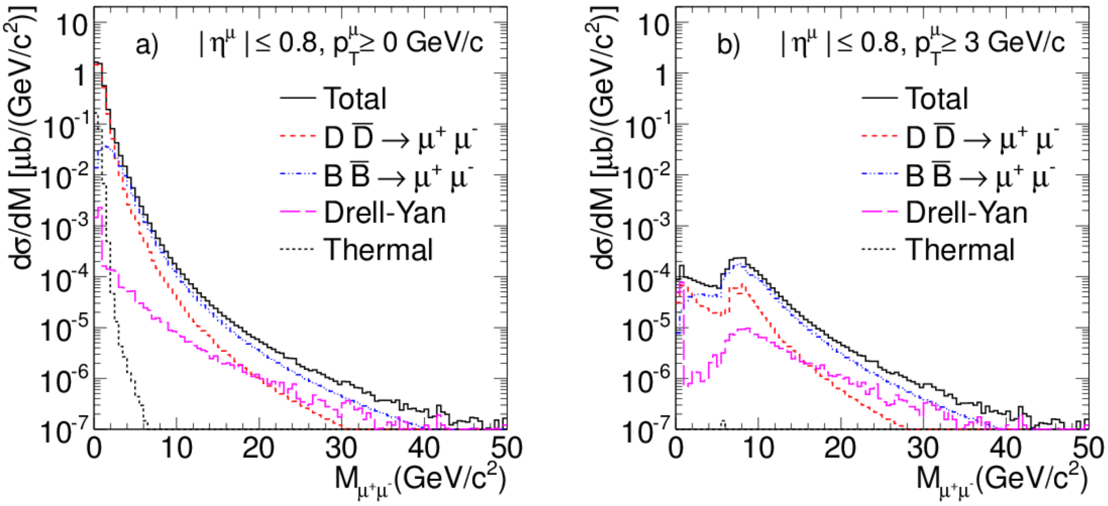

Figure 7.8.: The same as Fig. 7.6 but now with single muon rapidity cuts of $|\eta^{\mu}| \leq 0.8$. A minimum single lepton transverse momentum cut of $p_T^{\mu} \geq 0$ (a) and 3 (b) GeV/c is also shown.

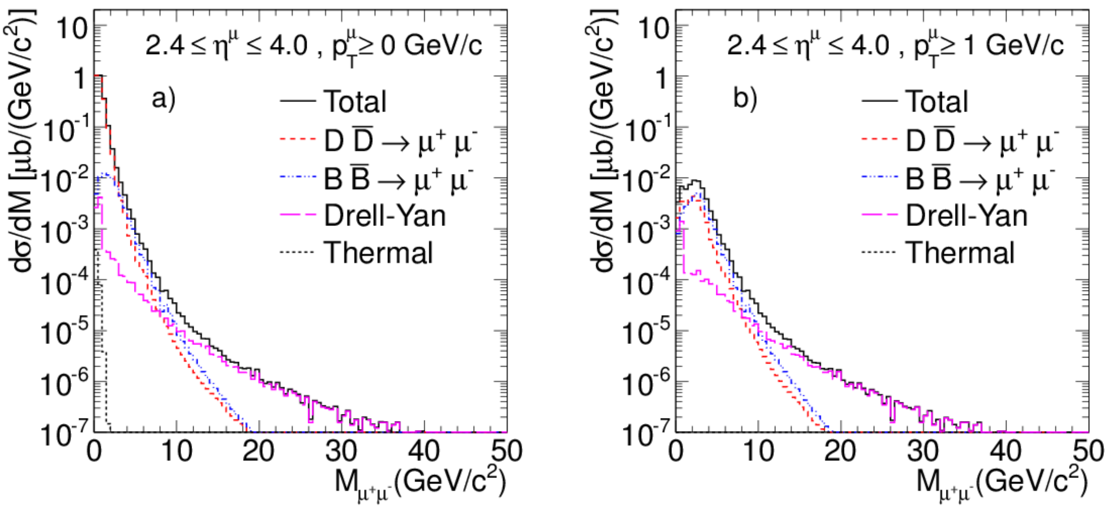

Figure 7.9.: The same as Fig. 7.6 but now with single muon rapidity cuts of $2.4 \leq |\eta^{\mu}| \leq 4$. A minimum single lepton transverse momentum cut of $p_T^{\mu} \geq 0$ (a) and 1 (b) GeV/c is also shown.

result in Fig. 7.7(d) which shows that, with energy loss included, the Drell-Yan process is now the dominant contribution to the continuum.

Figure 7.8 shows the dimuon mass distribution in the narrower central rapidity interval, $|\eta^\mu| \leq 0.8$, equivalent to the muon acceptance in the CMS barrel region and similar to the ALICE electron acceptance, $|\eta^e| \leq 1.0$. Figure 7.8(a) shows the dimuon distribution before any p_T cut. In this case, the mass distribution is more steeply falling in all cases except for thermal dilepton production because of its narrow rapidity distribution. Since the heavy flavor hadrons decay isotropically to leptons, the rapidity distribution for lepton pairs is rather broad with a width that is not strongly dependent on the pair mass. Thus the narrower rapidity acceptance reduces the high mass yields substantially relative to Fig. 7.7, even before any single lepton p_T cuts. Adding a single lepton transverse momentum cut of $p_T^\mu > 3$ GeV/c, Fig. 7.8(b), suppresses the low mass part of the distribution. However, the mass distribution is essentially unaffected by the p_T^μ cuts for $M_{\mu^+\mu^-} > 8$ GeV/c^2.

Figure 7.9 shows the dimuon mass distributions in the forward region, $2.5 \leq \eta^\mu \leq 4.0$, relevant for the ALICE muon arm. In this case, after energy loss, the Drell-Yan cross section rises above the heavy flavor decay rate for $M_{\mu^+\mu^-} > 10$ GeV/c^2. The heavy flavor production kinematics favors central production, with a rather steep decrease in the rapidity distribution as the kinematic limit is approached. There is no such constraint on the resulting lepton pairs. Because the decay of the individual heavy quark is isotropic in its rest frame, the lepton rapidity distribution has a larger plateau region, extending to more forward rapidity, than the parent quark. However, restricting the cut to one side of midrapidity eliminates many large gap pairs that might survive with a broad central rapidity acceptance such as in Fig. 7.7. Very little remains of the thermal dilepton contribution in the forward region due to its narrow rapidity distribution.

7.5. Conclusions

In summary, we calculate open charm and bottom production and determine their contributions to the dilepton continuum in Pb+Pb collisions at $\sqrt{s_{NN}} = 2.76$ TeV with and without including heavy quark energy loss. These rates are then compared with Drell-Yan and thermal dilepton production. The contributions of all these sources are obtained in kinematic regions relevant for the LHC detectors.

Since most detectors accept only high p_T single leptons, thermal dileptons would be difficult to measure. Heavy flavors are the dominant source of dileptons in most kinematic regimes, even after energy loss. At forward rapidity, the Drell-Yan contribution begins to dominate for $M > 10$ GeV/c^2. The effects of energy loss on the decay dileptons alters their acceptance, particularly for high lepton p_T cuts. In most of the kinematic regions considered, the $b\bar{b}$ decay contributions become larger than those of $c\bar{c}$ for lepton pair masses greater than 7 GeV/c^2.

From the approximately 50 M events collected by CMS in the first year of Pb+Pb collisions, we conclude that there will be few continuum contributions above 40 GeV/c^2, evident from the high mass dimuon distribution published by the CMS [69], in agreement with the result shown in Fig. 7.7(d). The second Pb+Pb run in 2011 has 20 times more events which will help quantify the heavy flavor contribution after uncorrelated pairs are eliminated by background subtraction techniques. Their yields relative to pp collisions at the same energy can be used as a high statistics probe of the medium properties in Pb+Pb collisions.

Chapter 8.

Study of different processes modifying quarkonia yields in PbPb collisions

In this chapter, we estimate the modification of quarkonia yields due to different processes. We include modifications due to shadowing, gluon dissociation, regenration and comover absorption, in the medium produced in PbPb collisions at LHC energy.

8.1. Introduction

Quarkonia state (J/ψ and Υ) have been one of the most popular signal of QGP since their suppression was proposed as a signature of deconfinement [2]. Quarkonia are produced early in the heavy ion collisions and if they evolve through deconfined medium their yields should be suppressed in comparison with those in pp. Many theoretical frameworks have been developed for the modification of quarkonia yield due to different processes. The suppression of quarkonia in QGP are understood in terms of color screening models e.g. Ref. [2, 228]and alternatively in terms of dissociation of quarkonia by gluon collision process [229, 230]. The statistical models [231, 232] offer estimates of the regeneration of quarkonia from charm quark pairs. The inverse of gluon dissociation process is also used to estimate regeneration [233].

The quarkonia yields in heavy ion collisions are also modified due to non-QGP effects such as shadowing, an effect due to change of the parton distribution functions inside the nucleus, and dissociation due to hadronic or comover interaction [5]. There have been many recent calculations to explain the LHC results on quarkonia using a combination of above theoretical frameworks and models [173, 234].

Table 8.1.: Heavy quark and quarkonia production cross sections at $\sqrt{s_{NN}} = 2.76$ TeV. The cross sections are given per nucleon pair while N^{PbPb} (including shadowing) gives the number of heavy quark pair/quarkonia per PbPb event.

	$c\bar{c}$	J/ψ	$b\bar{b}$	Υ
σ_{PbPb}	$1.76^{+2.32}_{-1.29}$ mb	31.4 μb	$89.3^{+42.7}_{-27.2}\mu$b	0.38 μb
N^{PbPb}	$9.95^{+13.10}_{-7.30}$	0.177	$0.50^{+0.25}_{-0.15}$	0.01
N^{pp}		0.177/0.93		0.01/0.95

In this chapter, we calculate the quarkonia (both J/ψ and Υ) production and suppression in a kinetic model which includes dissociation due to thermal gluons, modification of yield due to change in parton distribution functions inside nucleus and due to collisions with comover hadrons. Regeneration by thermal heavy quark pairs is also take into account. Our goal is obtain the nuclear modification factor of quarkonia as a function of transverse momentum and centrality of collision to be compared with experimental data from CMS and ALICE.

8.2. The production rates and shadowing

The production cross sections for heavy quark pairs are calculated to NLO in pQCD using the CTEQ6M parton densities [11, 235]. The central EPS09 parameter set [12] is used to calculate the modifications of the parton densities in PbPb collisions. We use the same set of parameters as that of Ref. [13] with the NLO calculation of Ref. [14] to obtain the exclusive $Q\overline{Q}$ pair rates. The production cross sections for heavy flavor and quarkonia at $\sqrt{s_{NN}} = 2.76$ TeV [236] are given in Table 9.1. The number of $Q\overline{Q}$ pairs in a minimum bias PbPb event is obtained from the per nucleon cross section, σ_{PbPb}, by

$$N_{Q\overline{Q}} = \frac{A^2 \sigma^{Q\overline{Q}}_{\mathrm{PbPb}}}{\sigma^{\mathrm{tot}}_{\mathrm{PbPb}}} \ . \tag{8.1}$$

Here A = 208, is number of nucleons inside the Pb nucleus. At 2.76 TeV, the total PbPb cross section, $\sigma^{\mathrm{tot}}_{\mathrm{PbPb}}$, is 7.65 b [7].

8.3. Modification of quarkonia in the presence of QGP

In the kinetic approach [233], the proper time (τ) evolution of the quarkonia population N_{QO} is given by the rate equation

$$\frac{dN_{QO}}{d\tau} = -\lambda_D \rho_g N_{QO} + \lambda_F \frac{N_{Q\bar{Q}}^2}{V(\tau)}, \tag{8.2}$$

where $V(\tau)$ is the volume of the deconfined spatial region and $N_{Q\bar{Q}}$ is the number of initial heavy quark pairs produced per event depending on the centrality (N_{part}). The λ_D is the dissociation rate obtained by the dissociation cross-section averaged over the momentum distribution of gluons and λ_F is the formation rate obtained by the formation cross-section averaged over the momentum distribution of Q and $\bar{Q}$. ρ_g is the density of thermal gluons. The number of quarkonia at freeze-out time τ_f is given by solution of Eq. (8.2) as

$$N_{QO}(p_T) = S(p_T)\, N_{QO}^{\mathrm{PbPb}}(p_T) + N_{QO}^F(p_T). \tag{8.3}$$

Here $N_{QO}^0(p_T)$ is the number of initially produced quarkonia (including shadowing) as a function of p_T and $S(p_T)$ is their survival probability from gluon collisions at freeze-out time τ_f and is written as

$$S(\tau_f, p_T) = \exp\left(-\int_{\tau_0}^{\tau_f} f(\tau)\lambda_{\mathrm{D}}(T, p_T)\, \rho_g(T)\, d\tau\right). \tag{8.4}$$

The temperature $T(\tau)$ and the QGP fraction $f(\tau)$ evolve from initial time τ_0 to freeze-out time τ_f due to expansion of QGP. The initial temperatures and thus the evolution is dependent on N_{part}. $N_{QO}^F(p_T)$ is the number of regenerated quarkonia per event and is given by

$$N_{QO}^F(p_T) = S(\tau_f, p_T) N_{Q\bar{Q}}^2 \int_{\tau_0}^{\tau_f} \frac{\lambda_{\mathrm{F}}(T, p_T)}{V(\tau)\, S(\tau, p_T)} d\tau \tag{8.5}$$

The nuclear modification factor (R_{AA}) can be written as

$$R_{AA}(p_T) = S(p_T)\, R(p_T) + \frac{N_{QO}^F(p_T)}{N_{QO}^{pp}(p_T)}. \tag{8.6}$$

Here $R(p_T)$ is the shadowing factor. R_{AA} as a function of collision centrality, including the regeneration will be

$$R_{AA}(N_{\rm part}) = \frac{\int_{p_{T\,\rm Cut}} N^{pp}_{QO}(p_T) S(p_T)\, R(p_T) dp_T}{\int_{p_{T\,\rm Cut}} N^{pp}_{QO}(p_T) dp_T} + \frac{\int_{p_{T\,\rm Cut}} N^{F}_{QO}(p_T) dp_T}{\int_{p_{T\,\rm Cut}} N^{pp}_{QO}(p_T) dp_T} \tag{8.7}$$

Here $p_{\rm Cut}$ defines the p_T range as per the experimental measurements. $N^{pp}_{QO}(p_T)$ is the unmodified p_T distribution of quarkonia obtained by NLO calculations which is scaled to a particular centrality of PbPb collisions.

The evolution of the system for each centrality of collision is governed by an isentropical cylindrical expansion with volume element

$$V(\tau) = \tau\, \pi\, (R + \frac{1}{2} a\, \tau^2)^2, \tag{8.8}$$

where a_T=0.1c^2 fm^{-1} is the transverse acceleration [234]. The initial transverse size, R as a function of centrality is obtained as

$$R(N_{\rm part}) = R_{0-5\%} \sqrt{\frac{N_{\rm part}}{(N_{\rm part})_{0-5\%}}}, \tag{8.9}$$

where $R_{0-5\%} = 0.92\, R_{\rm Pb}$; $R_{\rm Pb}$ being the radius of the Pb nucleus.

The evolution of entropy density for each centrality is obtained by entropy conservation condition $s(T)\, V(\tau) = s(T_0)\, V(\tau_0)$. The equation of state obtained by Lattice QCD along with hadronic resonance gas [32] is used for $s(T)$ to obtain the temperature as a function of proper time τ. The initial entropy density for each centrality is calculated using

$$s(\tau_0) = s(\tau_0)|_{0-5\%} \left(\frac{dN/d\eta}{N_{\rm part}/2}\right) / \left(\frac{dN/d\eta}{N_{\rm part}/2}\right)_{0-5\%}. \tag{8.10}$$

Measured values of $\left(\frac{dN/d\eta}{N_{\rm part}/2}\right)$ as a function of $N_{\rm part}$ [39] are used in the calculations. The initial entropy density $s(\tau_0)|_{0-5\%}$ for 0-5% centrality is obtained as

$$s(\tau_0)|_{0-5\%} = \frac{a_{\rm m}}{V(\tau_0)|_{0-5\%}} \left(\frac{dN}{d\eta}\right)_{0-5\%}. \tag{8.11}$$

Here $a_m = 5$ relating the total entropy with the multiplicity is obtained from hydrodynamic calculations [237].

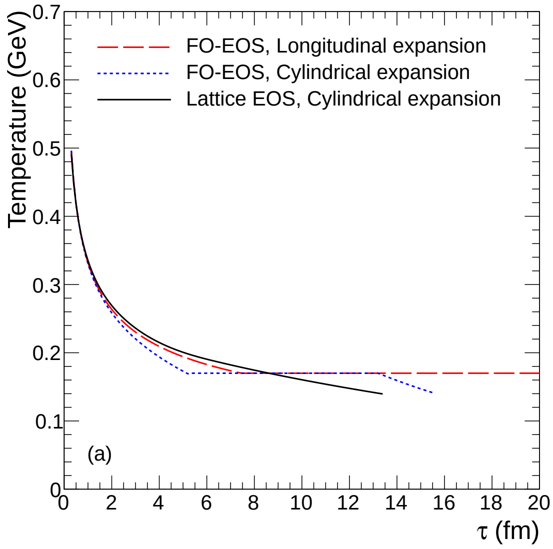

Figure 8.1.: (Color online) (a) Temperature and (b) QGP fraction in the system as a function of proper time τ in case of the most central (0-5%) collisions for longitudinal and cylindrical expansions using first order and lattice equation of state .

Using $(dN/d\eta)_{0-5\%}$=1.5 × 1600 obtained from the charge particle multiplicity measured in PbPb collisions at 2.76 TeV and with lattice equation of state we obtain the initial temperature for the most central collisions as 0.492 GeV at time $\tau_0 = 0.3$ fm/c.

The (proper)time evolution of temperature is shown in Fig. 8.1(a) and QGP fraction in Fig. 8.1(b) in case of most central (0-5%) collisions for both longitudinal and cylindrical expansions using first order and lattice Equation of state (EOS). For the first order EOS, $T_C = 0.170$ GeV and the QGP fraction goes from 1 to 0 at this temperature assuming a mixed phase of QGP and hadrons. The QGP fraction in case of lattice EOS governs number of degrees of freedom decided by entropy density. It is fixed to 1 above an entropy density corresponding to a 2-flavor QGP and fixed to zero below entropy density for a hot resonance gas. The freeze out temperature in all cases is $T_f = 0.140$ GeV.

8.3.1. Dissociation rate

In color dipole approximation the gluon dissociation cross section as function of gluon energy q^0 in the quarkonium rest frame is given by [229]

$$\sigma_D(q^0) = \frac{8\pi}{3}\frac{16^2}{3^2}\frac{a_0}{m_Q}\frac{(q^0/\epsilon_0 - 1)^{3/2}}{(q^0/\epsilon_0)^5}, \tag{8.12}$$

where ϵ_0 is the quarkonia binding energy and m_Q is the charm/bottom quark mass and $a_0 = 1/\sqrt{m_Q \epsilon_0}$. The values of ϵ_0 are taken as 0.64 and 1.10 GeV for ground states J/ψ and $\Upsilon(1S)$, respectively [238]. For excited states of bottommonia we use dissociation cross section from Ref. [239].

Figure 8.2 shows the gluon dissociation cross section of J/ψ and $\Upsilon(1S)$ as a function of gluon energy. The dissociation cross section is zero when gluon energy is less than the binding energy of the quarkonia. It increases with gluon energy and reaches maximum at 1.2 (1.5) GeV for J/ψ (Υ). At higher gluon energy, the interaction probability decreases. q^0 is related to the center of mass energy square s, of quakonium-gluon system as

$$q^0 = \frac{s - M_{QO}^2}{2\, M_{QO}}. \tag{8.13}$$

Using this relation, $\sigma_D(q^0(s))$ can be obtained which we write as $\sigma_D(s)$. The s can be obtained as $s = M_{QO}^2 + 2p_g \sqrt{M_{QO}^2 + p^2}(1 - \cos\theta)$, where M_{QO} and p are mass and momentum of quarkonium and θ is its angle with gluon.

We can calculate dissociation rate as a function of quarkonium momentum by integrating the dissociation cross-section on thermal gluon momentum distribution $f_g(p_g)$ as

$$\begin{aligned} \lambda_D \rho_g &= \langle \sigma v_{\rm rel} \rangle \, \rho_g = \frac{g_g}{(2\pi)^3} \int d^3p_g \, f_g(p_g) \, \sigma_D(s) v_{\rm rel}(s) \\ &= \frac{g_g}{(2\pi)^3} \int 2\pi p_g^2 dp_g f_g(p_g) \int \sigma_D(s) v_{\rm rel}(s) d(\cos\theta) \end{aligned} \tag{8.14}$$

The relative velocity $v_{\rm rel}$ between the quarkonium and the gluon is given by

$$v_{\rm rel} = \frac{s - M_{QO}^2}{2\, p_g \sqrt{M_{QO}^2 + p^2}} \tag{8.15}$$

The gluon dissociation rates of J/ψ as a function of temperature are shown in Fig. 8.3(a) and as a function of transverse momentum are shown in Fig. 8.3(b). The dissociation rate increases with temperature due to increase in gluon density. Dissociation rate of quarkonium is maximum when it is at rest and decreases with its (transverse) momentum.

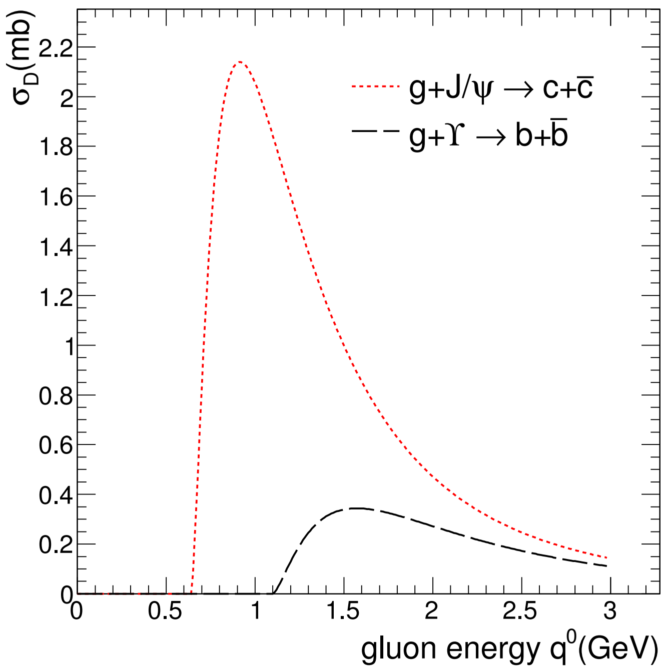

Figure 8.2.: Gluon dissociation cross-section of quarkonia as a function of gluon energy (q^0) in quarkonia rest frame.

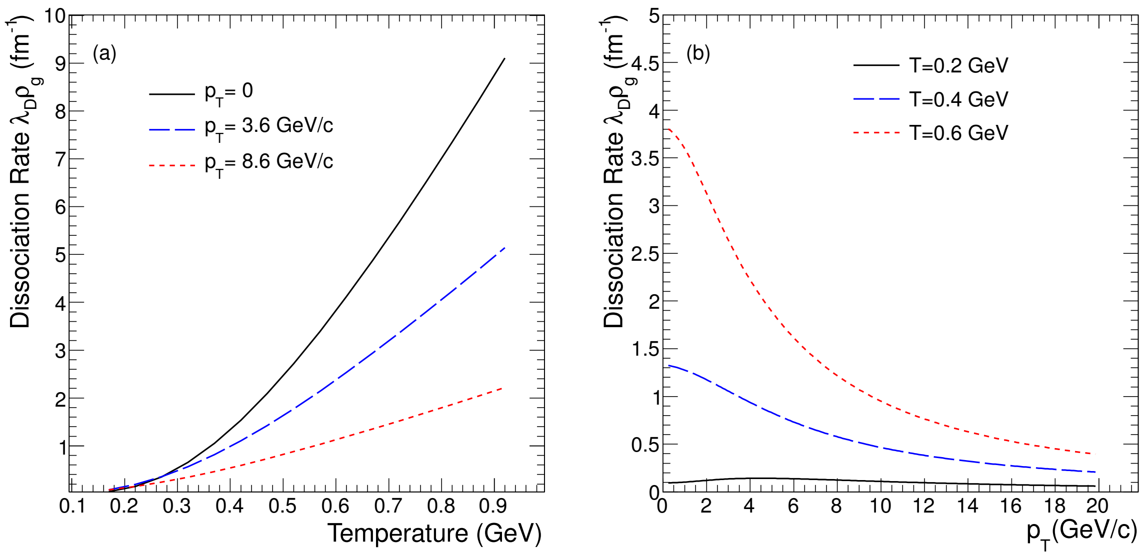

Figure 8.3.: (Color online) Gluon dissociation rate of J/ψ as a function of (a) temperature and (b) as a function of transverse momentum.

8.3.2. Formation rate

We can calculate formation cross section from dissociation cross section using detailed balance relation [233, 240] as

$$\sigma_F = \frac{48}{36}\,\sigma_D(q^0)\frac{(s - M_{QO}^2)^2}{s(s-4m_Q^2)}. \tag{8.16}$$

The formation rate of quarkonium with momentum $\mathbf{p}$ can be written as

$$d\lambda_F/d\mathbf{p} = \int \sigma_F(s)\, v_{\rm rel}(s)\, f_Q(p_1)\, f_{\bar{Q}}(p_2)\, d^3p_1\, d^3p_2\, \delta(\mathbf{p} - (\mathbf{p_1} + \mathbf{p_2})) \tag{8.17}$$

Here $f_{Q/\bar{Q}}(p)$ are taken as thermal distribution function of $Q/\bar{Q}$ which are normalized to one as per $\int f_Q(p)d^3p = 1$. $v_{\rm rel}$ is relative velocity between $Q\bar{Q}$ quark pair and is given by

$$v_{\rm rel} \;=\; \frac{\sqrt{(p_1.p_2)^2 - m_Q^4}}{E_1\, E_2} \tag{8.18}$$

Here $p_1 = (E_1, \mathbf{p_1})$, $p_2 = (E_2, \mathbf{p_2})$ are four momenta of heavy quark and anti-quarks, respectively.

Figure 8.4 (a) shows variation of formation rate of J/ψ as a function of medium temperature and Fig. 8.4 (b) shows as a function of transverse momentum of J/ψ. The J/ψ generated from recombination of uncorrelated heavy quark pairs will have softer p_T distributions than that of J/ψ coming from initial hard scattering and thus effect of recombination will be important only at low p_T.

8.4. Effect of hadronic comovers

The suppression of quarkonia by comoving pions can be calculated by folding the quarkonium-pion dissociation cross section $\sigma_{\rm I}$ over thermal pion distributions [241]. It is expected that at LHC energies cross-section of comover suppression will be very small [133]. For simplicity we take 1 mb cross-section for both J/ψ and Υ states. The

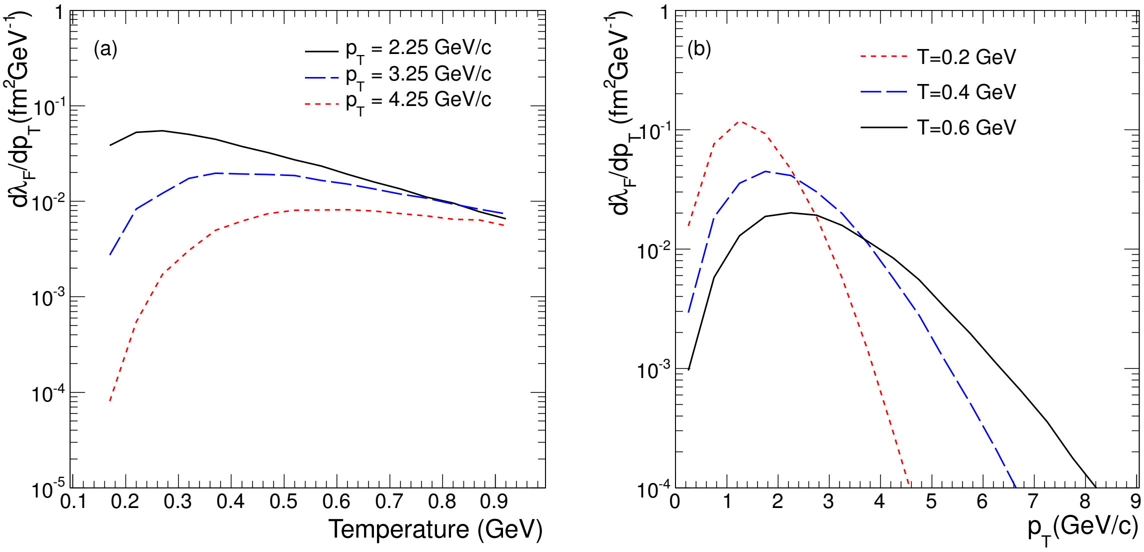

Figure 8.4.: (Color online) Formation rate of J/ψ as (a) a function of temperature and (b) as a function of transverse momentum.

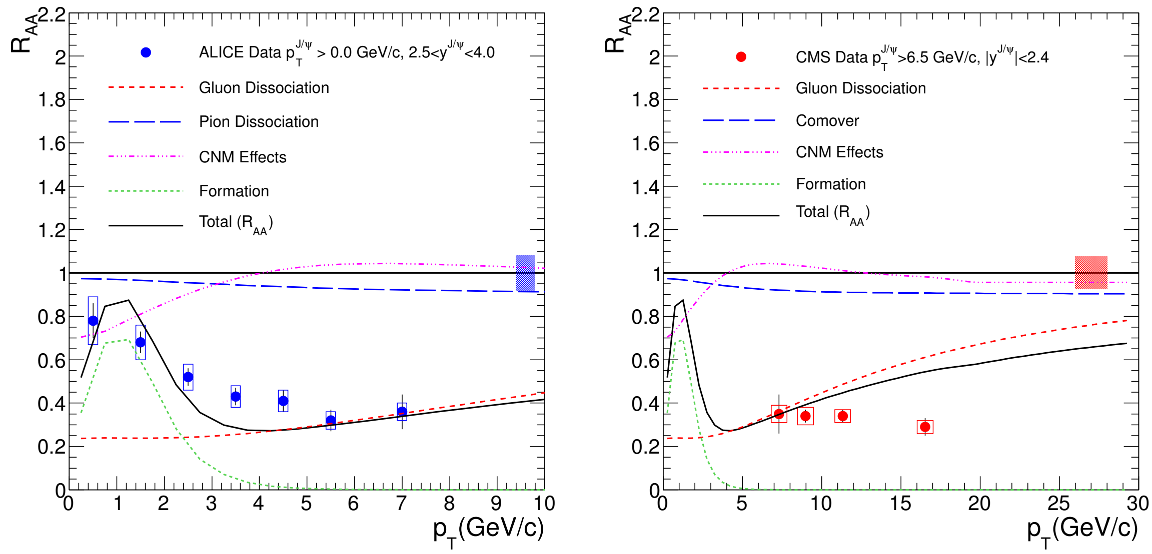

Figure 8.5.: (Color online) Calculated nuclear modification factor (R_{AA}) as a function of J/ψ transverse momentum compared with (a) ALICE and (b) CMS measurements.

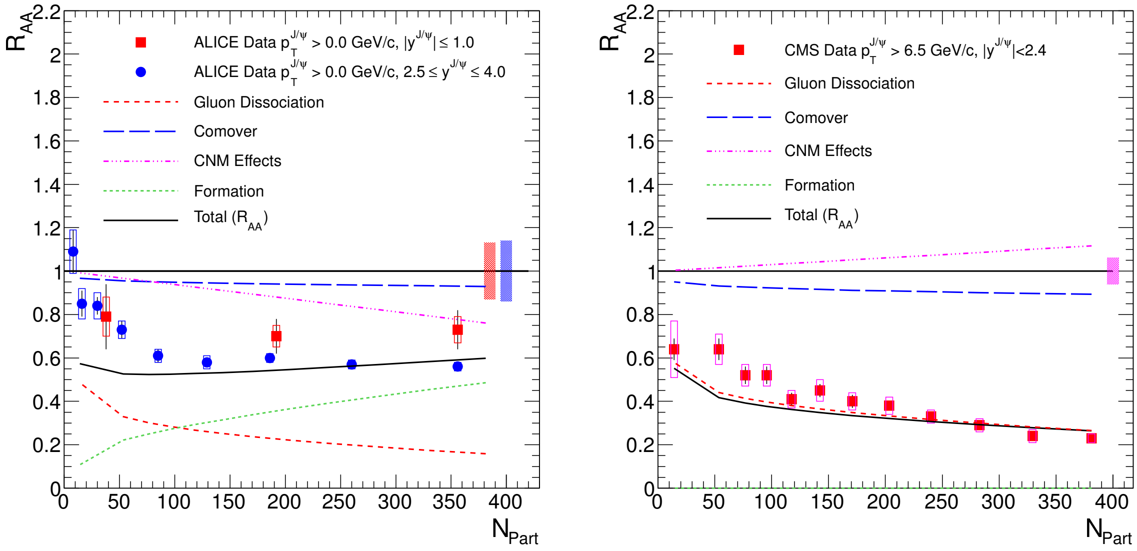

Figure 8.6.: (Color online) Calculated nuclear modification factor (R_{AA}) compared with (a) ALICE and (b) CMS measurements at LHC. The regeneration for high p_T CMS comparison is negligible. Similar cold nuclear matter effects are assumed for both ALICE and CMS rapidity ranges.

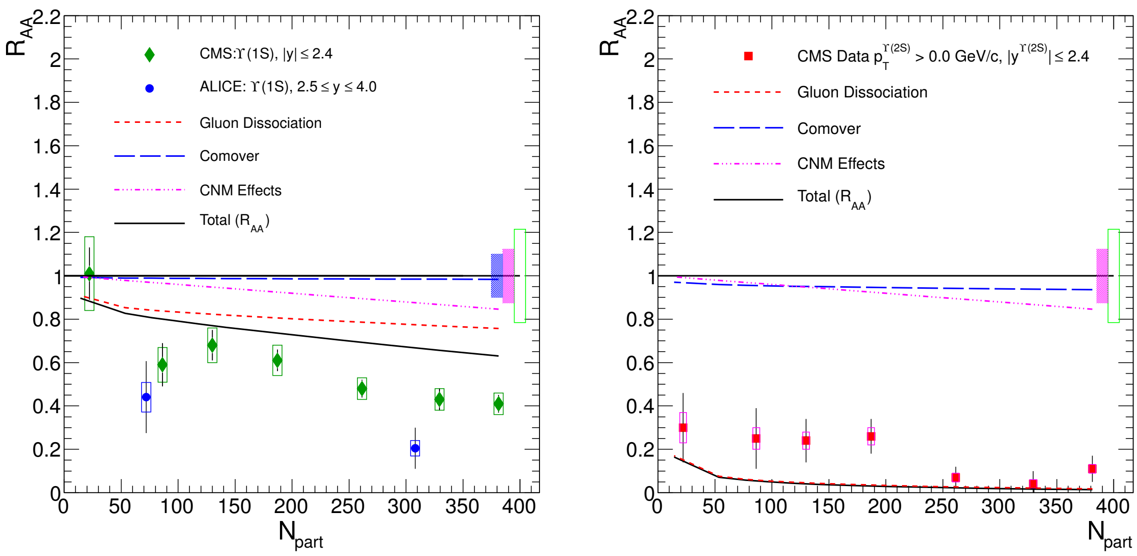

Figure 8.7.: (Color online) Calculated nuclear modification factor (R_{AA}) compared with CMS (a) $\Upsilon(1S)$ and (b) $\Upsilon(2S)$ measurements. We assume small cold nuclear matter suppression than $J\psi$ and no regeneration due to small production cross section of beauty quark as shown in Table 9.1.

dissociation rate λ_{D_π} can be written as

$$\begin{aligned}\lambda_{D_\pi}\,\rho_\pi &= \frac{g_\pi}{(2\pi)^3}\int d^3p f_\pi(p)\sigma_I v_{\rm rel} \\ &= \frac{g_\pi}{(2\pi)^3}\int 2\pi p^2 dp f_\pi(p)\int \sigma_{\rm I} v_{\rm rel}(s)\Theta(s-4m_D^2)d(cos\theta)\end{aligned} \tag{8.19}$$

where $f_\pi(p,T)$ is taken as the thermal pion distribution and the pion density ρ_π is given by

$$\rho_\pi = \frac{g_\pi}{(2\pi)^3}\int d^3p\, f_\pi(p) \tag{8.20}$$

The survival probability from pion collisions at freeze-out time τ_f is written as

$$S_\pi(p_T) = \exp\left(-\int_{\tau_0}^{\tau_f}(1-f(\tau))\lambda_{D_\pi}(T,p_T)\,\rho_\pi(T)\,d\tau\right). \tag{8.21}$$

The temperature $T(\tau)$ and the hadronic fraction (1-$f(\tau)$) evolve from phase transition time to freeze-out time. The probability $S_\pi(p_T)$ is used along with $S(p_T)$ term in Eq. (8.6).

8.5. Results and discussion

Figure 8.5(a) show different contributions in nuclear modification factor (R_{AA}) of J/ψ as a function of transverse momentum compared with ALICE measurements [169] and the Fig. 8.5(b) shows the same along with high p_T measurements of CMS experiment [167]. At low p_T, regeneration of J/ψ is the dominant process and this seems to be the process for the enhancement of J/ψ seen in the ALICE low p_T data. The gluon suppression is also more at low p_T and it reduces as we move to high p_T. Both of these processes (regeneration and dissociation) due to the presence of QGP are at play in low and intermediate p_T. The high p_T suppression (p_T > 10 GeV/c) of J/ψ measured by CMS does not seem to be originating due to dissociation by gluons in QGP.

We have also calculated R_{AA} as a function of system size. Figure 8.6 (a) shows different contributions of J/ψ nuclear modification factor as a function of system size along with the measurements by ALICE [169]. Figure 8.6 (b) shows the same for $p_T \geq$ 6.5 GeV/c, measured by CMS experiment [167]. Figure 8.6 (a) indicates that J/ψ's are increasingly suppressed when system size grows. Since the number of regenerated J/ψ's also grow the nuclear modification factor remains flat for most of the centrality regions. Our model calculations overestimate the suppression in the most peripheral data. The centrality dependence of R_{AA} of high p_T J/ψ measured by CMS is well described by the model. Most of the contribution to CMS data should come from J/ψ p_T between 6.5 and 10 GeV/c where the suppression seems to be due to gluon dissociation process.

Figure 8.7 (a) demonstrates contribution of different processes in the centrality dependence of Υ(1S) nuclear modification factor along with the data measured in mid rapidity by CMS experiment [205] and in forward rapidity by ALICE experiment [190]. The calculations underestimate the suppression but reproduce the shape of centrality dependence. Figure 8.7 (b) shows the same for Υ(2S) nuclear modification factor along with the measurements in mid rapidity by CMS experiment. The excited $\Upsilon(2S)$ states are highly suppressed. The effect of regeneration (not shown here) is negligible for Υ states.

8.6. Summary

We have carried out detailed calculations of J/ψ and Υ modifications in PbPb collisions at LHC. The quarkonia and heavy flavor cross sections calculated upto NLO are used in the study and shadowing corrections are obtained by EPS09 parameterization. A kinetic model is employed which incorporates quarkonia suppression inside QGP, suppression due to hadronic comovers and regeneration from charm pairs. Their suppression is estimated using process of gluon dissociation in medium. The rate of regeneration has been obtained using principle of detailed balance. The dissociation and formation rates have been studied as a function of medium temperature and transverse momentum of quarkonia. In addition, the modification in quakonia yields due to collisions with hadronic comovers has been estimated assuming it to be caused by pion.

The nuclear modification factor as a function of centrality and transverse momentum has been calculated and compared to J/ψ and Υ nuclear modification factors measured in PbPb collisions at $\sqrt{s_{NN}} = 2.76$ TeV. At low p_T, regeneration of J/ψ is the dominant process and this seems to be the process for the enhancement of J/ψ in the ALICE low p_T data. The gluon suppression is also more at low p_T and it reduces as we move to high p_T. Both of these processes (regeneration and dissociation) due to the presence of QGP are at play in low and intermediate p_T. The high p_T suppression ($p_T > 10$ GeV/c) of J/ψ measured by CMS does not seem to be originating due to dissociation by gluons in QGP.

The centrality dependence of nuclear modification indicates that J/ψ's are increasingly suppressed when system size grows. Since the number of regenerated J/ψ's also grow, the nuclear modification factor in case of low p_T measurements remains flat for most of the centrality regions. The centrality dependence of R_{AA} of high p_T J/ψ is also well described by the model. The centrality dependence of suppression of Υ states are reproduced by model calculations.

Chapter 9.

Summary and Outlook

The deconfinement transition and the properties of hot, strongly-interacting matter can be studied experimentally in heavy-ion collisions [38, 132]. A significant part of the extensive experimental heavy-ion program is dedicated to measuring quarkonium yields, since Matsui and Satz suggested that quarkonium suppression could be a direct signal of deconfinement [2]. However, not all of the observed quarkonium suppression in nucleus-nucleus collisions relative to scaled proton-proton collisions is due to quark gluon plasma formation. In fact, quarkonium suppression was also observed in proton-nucleus collisions, so that part of the nucleus-nucleus suppression is due to cold nuclear matter effects. Therefore it is necessary to disentangle hot and cold medium effects.

In this thesis first we reviewed present status of experimental signals for quark gluon plasma formation in chapter 1. Status of quarkonia production and suppression in SPS, RHIC and LHC energies is discussed in chapter 2. The observation of anomalous suppression of J/ψ was considered a signal of QGP formation at SPS, but later at RHIC similar amount of suppression is measured despite an order of magnitude increase in center of mass energy. Upsilons are supposed to be a better probe of QGP. Because three closely placed Υ states can provide a self calibrated measurement of temperature achieved in heavy ion collisions. At RHIC it was not possible to resolve the three Υ states.

This thesis concentrate on production and suppression of $b\bar{b}$ bound states, namely Υ(1S), Υ(2S) and Υ(3S) which are measured in pp, pPb and PbPb collisions at LHC. This is the first time we are able to measure all three Υ states separately with good statistics thanks to the large integrated luminosity and high-tech detectors available at LHC. The quarkonium states are identified through their dimuon decay. Muons are reconstructed by matching tracks in the muon detectors and silicon tracker. These measurements are explained in detail in chapter 4, 5 and 6. Here a summary of important results is presented.

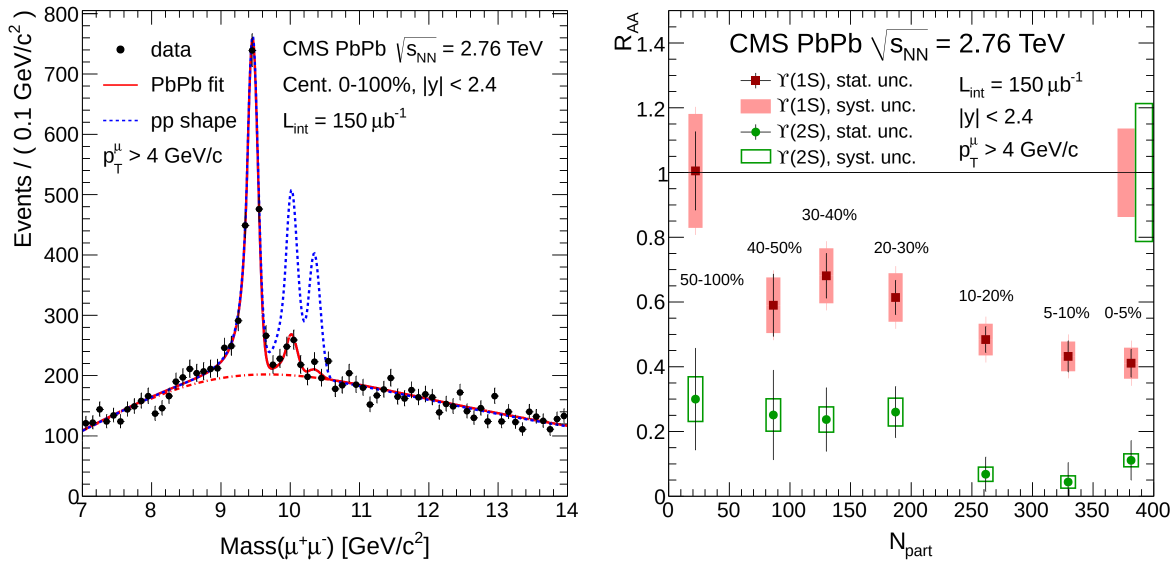

(a) **(b)**

Figure 9.1.: (a) Illustration of the excited to ground states relative ϒ suppression in PbPb compared to pp. The fit to the PbPb data, shown by the continuous line, is overlaid with the result of the pp fit, represented by the dashed line (shown on top of a common PbPb background shape, for comparison). (b) The nuclear modification factor, R_{AA}, for ϒ mesons as a function of N_{part}. The red filled squares show our results for ϒ(1S) and the green filled circles are for ϒ(2S).

Figure 9.1 (a) shows the invariant-mass distribution of three ϒ states measured in PbPb collisions. The fit to the PbPb data is overlaid with the fit to the pp data collected at same center of mass energy. This figure is a graphical representation of suppression of excited ϒ states. The excited ϒ states (ϒ(2S) and ϒ(3S)) are found to be strongly suppressed in PbPb collisions. Figure 9.1 (b) shows the absolute suppression of ϒ(1S) and ϒ(2S) in PbPb collisions. The variable shown in the figure is nuclear modification factor (R_{AA}) as a function of centrality of the collision (N_{part}). This is the first measurement of ϒ(2S) R_{AA}. In studying the data as a function of centrality, we find that the ϒ(1S) and ϒ(2S) suppression increases with N_{part}. For all the centrality bins, we observe the suppression of the ϒ(2S) state to be larger than the suppression of the ϒ(1S). In the most peripheral bin, the ϒ(1S) nuclear modification factor is consistent with unity, while that for the ϒ(2S) remains low. However, it should be noted that this bin includes a wide impact parameter range (50-100% of the total cross section), and it is expected that most of the events where an ϒ will be produced will be biased towards larger N_{coll}

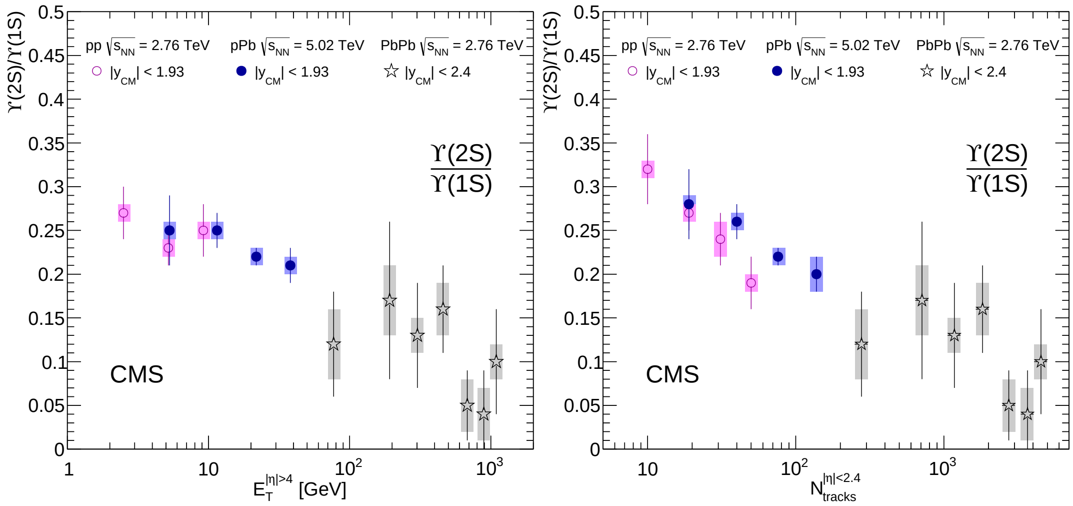

(a) **(b)**

Figure 9.2.: Single cross section ratios $\Upsilon(2S)/\Upsilon(1S)$ for $|y_{CM}| < 1.93$ versus (a) transverse energy measured at $4.0 < |\eta| < 5.2$ and (b) charged-particle multiplicity measured in $|\eta| < 2.4$, for pp collisions at $\sqrt{s} = 2.76$ TeV (open circles) and pPb collisions at $\sqrt{s_{NN}} = 5.02$ TeV (closed circles). Both figures also include the $\Upsilon(2S)/\Upsilon(1S)$ ratios for $|y_{CM}| < 2.4$ measured in PbPb collisions at $\sqrt{s_{NN}} = 2.76$ TeV (open stars). The error bars in the figures indicate the statistical uncertainties, and the boxes represent the point-to-point systematic uncertainties. The global uncertainties of the results are 7%, 8%, and 8% for the pp, pPb, and PbPb, respectively.

and hence smaller impact parameter. With the 150 μb^{-1} integrated luminosity recorded during second LHC PbPb run at $\sqrt{s_{NN}} = 2.76$ TeV, we are able to split the $\Upsilon(1S)$ and $\Upsilon(2S)$ data into seven centrality bins. But the limited pp data sample does not allow measurements of Υ R_{AA} in kinematic bins. The new pp data sample collected during Jan 2013 at $\sqrt{s} = 2.76$ TeV will allow measurements of the R_{AA} of the states as a function of p_T and rapidity.

The quarkonia yields in heavy ion collisions are also modified due to non-QGP effects such as shadowing, an effect due to the change of the parton distribution functions inside the nucleus, and dissociation due to hadronic or comover interactions [5]. To get a quantitative idea about these effects, measurements of Υ production in pPb collisions at $\sqrt{s_{NN}} = 5.02$ TeV are performed. Figure 9.2 shows the cross-section ratios $\Upsilon(2S)/\Upsilon(1S)$ and $\Upsilon(3S)/\Upsilon(1S)$ as a function of (a) transverse energy and (b) charged-particle multiplicity for pp, pPb and PbPb collisions. The ratio seems to be constantly decreasing with increasing multiplicity while trend is not very clear for transverse energy. These measurements suggest the presence of final state effects in pPb collisions

Table 9.1.: Heavy flavor and Drell-Yan cross sections at $\sqrt{s_{NN}} = 2.76$ TeV. The cross sections are given per nucleon while $N_{Q\overline{Q}}$ and $N_{l^+l^-}$ are the number of $Q\overline{Q}$ and lepton pairs per Pb+Pb event. The uncertainties in the heavy flavor cross section are based on the Pb+Pb central values with the mass and scale uncertainties added in quadrature.

	$c\overline{c}$	$b\overline{b}$	Drell-Yan $1 \leq M \leq 100$ GeV/c^2
$\sigma_{\rm PbPb}$	$1.76^{+2.32}_{-1.29}$ mb	$89.3^{+42.7}_{-27.2}$ μb	70.97 nb
$N_{Q\overline{Q}}$	$9.95^{+13.10}_{-7.30}$	$0.50^{+0.25}_{-0.15}$	-
$N_{\mu^+\mu^-}$	$0.106^{+0.238}_{-0.078}$	$0.0059^{+0.0029}_{-0.0017}$	0.0004

compared to pp collisions affecting ground state and excited states differently. A global understanding of effects at play in pp, pPb and PbPb collisions calls for more activity related study of Υ yields in pp collisions. More PbPb data are needed to investigate the dependence in three systems and their possible relation.

This thesis consist of measurements as well as theoretical results. In the first calculation we calculate open charm and bottom production and determine their contributions to the dilepton continuum in PbPb collisions at $\sqrt{s_{NN}} = 2.76$ TeV with and without heavy quark energy loss. These rates are then compared with Drell-Yan and thermal dilepton production. The contributions of all these sources are obtained in kinematic regions relevant for the LHC detectors. The production cross sections along with their uncertainties for heavy flavor and Drell-Yan dileptons at $\sqrt{s_{NN}} = 2.76$ TeV are shown in Tab. 9.1. The number of $Q\overline{Q}$ pairs in a minimum bias PbPb event is obtained from the per nucleon cross section. Figure 9.3 shows the invariant mass distributions for these four contributions to the dilepton spectra. Figure 9.3 (a) shows the heavy flavor mass distributions without any final-state energy loss while energy loss is included in the heavy flavor distributions on Fig. 9.3 (b). Dileptons from $\mathrm{D\overline{D}}$ decays dominate over the entire mass range due to the large $c\overline{c}$ production cross section. Bottom pair decays are the next largest contribution followed by Drell-Yan production. Thermal dilepton contribution is very small. It can be concluded that measurement of thermal dileptons will be very challenging for the kinematic range relevant to LHC detectors.

In the second calculation we estimate the modification of quarkonia yields due to different processes in the medium produced in PbPb collisions at LHC energy. The quarkonia and heavy flavor cross sections calculated upto NLO are used in the study and

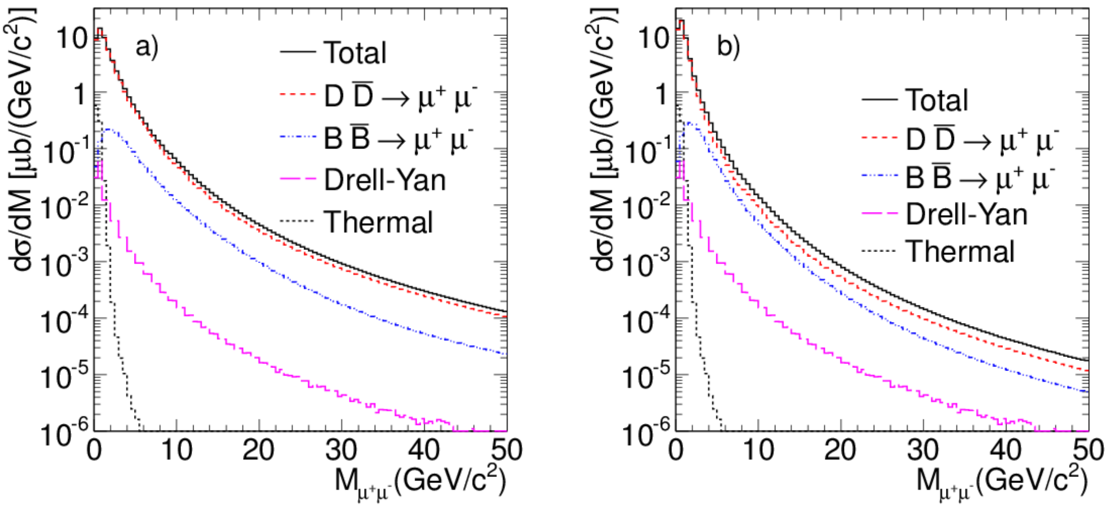

Figure 9.3.: The invariant mass distributions for the four contributions to the dilepton spectra discussed here: semileptonic charm (red, short-dashed) and bottom (blue, dot-dot-dashed) decays, Drell-Yan (magenta, long-dashed) and thermal (black, dotted) dileptons along with the sum (black, solid) in Pb+Pb collisions per nucleon pair at $\sqrt{s_{NN}}$ = 2.76 TeV. Left panel shows distributions without any final state energy loss, right panel is after including heavy quark energy loss in the medium.

shadowing corrections are obtained by EPS09 parameterization [12]. A kinetic model is employed which incorporates quarkonia suppression inside QGP, suppression due to hadronic comovers and regeneration from charm pairs. Quarkonia dissociation cross section due to gluon collisions has been considered and the regeneration rate has been obtained using the principle of detailed balance. The modification in quakonia yields due to collisions with hadronic comovers has been estimated assuming it to be caused by pion. The manifestations of these effects in different kinematic regions in the nuclear modification factors for both J/ψ and Υ has been demonstrated for PbPb collisions at $\sqrt{s_{NN}}$ = 2.76 TeV in comparison with the measurements.

Figure 9.4 shows the calculated nuclear modification factor (R_{AA}) as a function of J/ψ transverse momentum. Both the suppression and regeneration due to deconfined medium strongly affect low $p_{\rm T}$ range Fig. 9.4 (a). The large observed suppression of J/ψ at high p_T far exceeds the estimates of suppression by deconfined medium Fig. 9.4 (b).

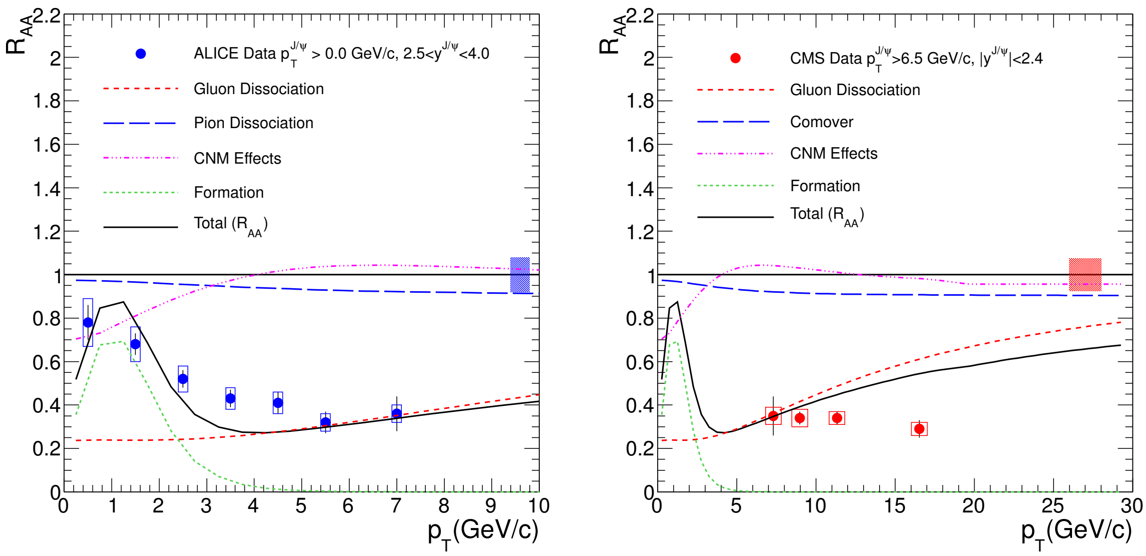

Figure 9.4.: (Color online) Calculated nuclear modification factor (R_{AA}) as a function of J/ψ transverse momentum. Calculations are compared with ALICE and CMS measurements.

Appendix A.

Tables of results from Chapter 4

Table A.1.: Yield per unit of rapidity of Υ(1S) divided by T_{AA} and nuclear modification factor R_{AA} as a function of Υ(1S) rapidity, p_T, and collision centrality. The average p_T value for each bin is given. Listed uncertainties are statistical first, systematic second, and global scale third. The latter includes the uncertainties on the pp integrated luminosity and, for centrality integrated bins, on T_{AA}.

$\lvert y \rvert$	p_T [GeV/c]	centrality	$\langle p_T \rangle$ [GeV/c]	$\frac{1}{T_{AA}} \cdot \frac{\mathrm{d}N}{\mathrm{d}y}$ [nb]	R_{AA}
0.0–2.4	0–6.5	0–100%	3.03	0.293 ± 0.057 ± 0.051 ± 0.02	0.44 ± 0.10 ± 0.06 ± 0.04
	6.5–10		8.04	0.093 ± 0.028 ± 0.017 ± 0.01	0.91 ± 0.38 ± 0.13 ± 0.08
	10–20		13.17	0.066 ± 0.016 ± 0.011 ± 0.004	1.77 ± 0.76 ± 0.24 ± 0.15
	0–20		6.79	0.485 ± 0.066 ± 0.084 ± 0.03	0.63 ± 0.11 ± 0.09 ± 0.05
0.0–1.2	0–20	0–100%	6.44	0.495 ± 0.091 ± 0.086 ± 0.03	0.54 ± 0.12 ± 0.08 ± 0.04
1.2–2.4			6.60	0.498 ± 0.097 ± 0.088 ± 0.03	0.85 ± 0.25 ± 0.12 ± 0.07
0.0–2.4	0–20	0–10%	6.65	0.347 ± 0.096 ± 0.069	0.45 ± 0.14 ± 0.08 ± 0.03
		10–20%	6.88	0.643 ± 0.144 ± 0.118	0.84 ± 0.21 ± 0.13 ± 0.05
		20–100%	6.08	0.517 ± 0.101 ± 0.101	0.68 ± 0.15 ± 0.11 ± 0.04
		0–20%	6.85	0.467 ± 0.081 ± 0.093	0.61 ± 0.13 ± 0.11 ± 0.04

Table A.2.: Cross section per unit of rapidity of Υ(1S) as a function of rapidity and p_T in pp collisions. The average p_T value for each bin is given. Listed uncertainties are statistical first, systematic second, and global scale third. The latter is the uncertainty on the pp integrated luminosity.

$\lvert y\rvert$	p_T [GeV/c]	$\langle p_T\rangle$ [GeV/c]	$\frac{d\sigma}{dy}$ [nb]
0.0–2.4	0–6.5	2.82	0.668 ± 0.091 ± 0.115 ± 0.040
	6.5–10	8.36	0.102 ± 0.031 ± 0.018 ± 0.006
	10–20	13.04	0.037 ± 0.013 ± 0.006 ± 0.002
	0–20	4.73	0.764 ± 0.089 ± 0.131 ± 0.046
0.0–1.2	0–20	5.18	0.921 ± 0.128 ± 0.157 ± 0.055
1.2–2.4		4.03	0.586 ± 0.125 ± 0.101 ± 0.035

Appendix B.

Tables of results from Chapter 5

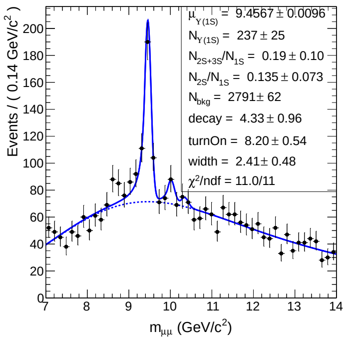

(a) 0- 5%

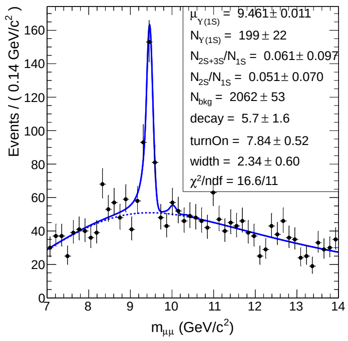

(b) 5- 10%

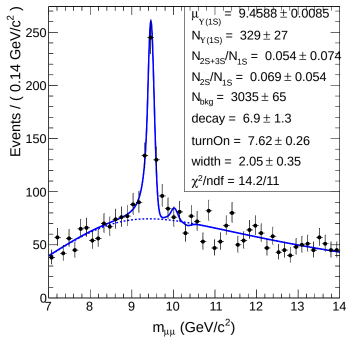

(c) 10- 20%

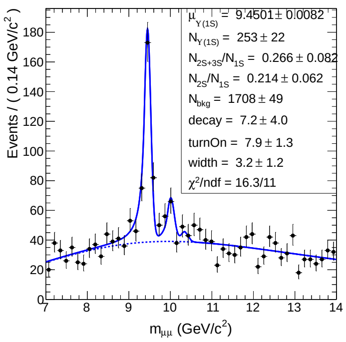

(d) 20- 30%

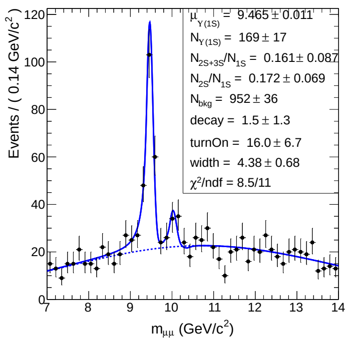

(e) 30- 40%

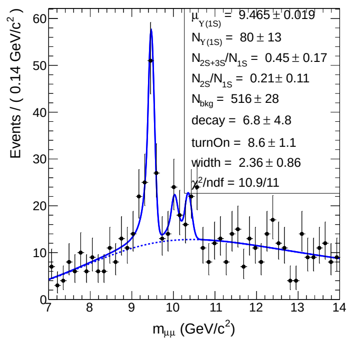

(f) 40- 50%

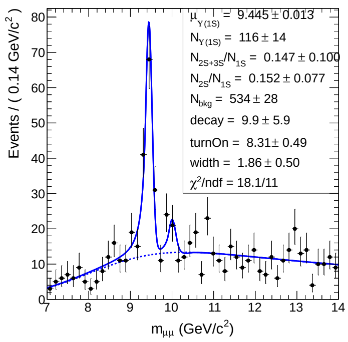

(g) 50-100%

Figure B.1.: Centrality dependence of the PbPb single ratio, for $p_T^\mu > 4.0$GeV/c. ($150\mu b^{-1}$).

	$p_T^{\mu} > 4$GeV/c, Cent. 0-100%		
	R_{23}	R_2	R_3
nominal (erf*exp)	0.155 ± 0.038	0.127 ± 0.027	0.027 ± 0.025
systematic variations:			
like-sign (LS) keyspdf + pol.2	0.159 ± 0.037	0.130 ± 0.027	0.029 ± 0.046
LS erf*exp + pol.2	0.151 ± 0.038	0.124 ± 0.027	0.027 ± 0.047
opposite-sign (OS) Track Rotation (TR) keyspdf + pol.2	0.157 ± 0.037	0.120 ± 0.027	0.037 ± 0.046
OS TR erf*exp + pol.2	0.152 ± 0.037	0.125 ± 0.027	0.025 ± 0.046
fix CB tail from MC (alpha = 1.4)	0.130 ± 0.038	0.113 ± 0.027	0.017 ± 0.047
fix resolution from MC (92 MeV/c^2)	0.159 ± 0.038	0.128 ± 0.028	0.031 ± 0.047
fix both CB and resolution from MC	0.140 ± 0.037	0.118 ± 0.027	0.022 ± 0.046
fit systematic (RMS)	0.011	0.007	0.005
fit systematic (largest variation)	0.026	0.016	0.015
other checks:			
LS Track Rotation (TR) keyspdf + pol.2	0.170 ± 0.036	0.137 ± 0.026	0.033 ± 0.044
LS TR erf*exp + pol.2	0.159 ± 0.038	0.129 ± 0.027	0.030 ± 0.047
nominal simultaneous fit (erf*exp)	0.143 ± 0.038	0.119 ± 0.027	0.024 ± 0.024

Table B.1.: Summary of single-ratio results, for the PbPb dataset.

Table B.2.: Summary of single-ratio results for the p p 2.76 TeV dataset.

	$p_T^{\mu} > 4\mathrm{GeV/c}$		
	R_{23}	R_2	R_3
nominal (pol2; signal pdf fixed from PbPb)	0.88 ± 0.17	0.50 ± 0.12	0.38 ± 0.10
systematic variations:			
fix CB tail from MC	0.85 ± 0.16	0.49 ± 0.11	0.36 ± 0.19
fix resolution from MC	0.89 ± 0.16	0.49 ± 0.12	0.40 ± 0.20
fix both CB and resolution	0.87 ± 0.16	0.49 ± 0.11	0.38 ± 0.19
erf*exp	0.86 ± 0.16	0.49 ± 0.11	0.37 ± 0.19
LS keyspdf + pol.2	0.84 ± 0.17	0.48 ± 0.12	0.36 ± 0.21
LS erf*exp + pol.2	0.87 ± 0.16	0.49 ± 0.12	0.38 ± 0.20
fit systematic (RMS)	0.023	0.012	0.015
fit systematic (largest variation)	0.051	0.024	0.035
nominal simultaneous fit (pol2)	0.97 ± 0.19	0.56 ± 0.13	0.41 ± 0.11

Table B.3.: Summary of single-ratio centrality dependent results.

	0-5%	5-10%	10-20%	20-30%	30-40%	40-50%	50-100%
R_{23} $(p_T^\mu > 4.0\mathrm{GeV/c})$							
nominal result	0.190 ± 0.100	0.061 ± 0.097	0.054 ± 0.074	0.266 ± 0.082	0.161 ± 0.087	0.450 ± 0.170	0.147 ± 0.100
systematic variations:							
LS keyspdf + pol.2	0.220 ± 0.099	0.009 ± 0.097	0.030 ± 0.075	0.246 ± 0.079	0.125 ± 0.088	0.488 ± 0.160	0.165 ± 0.095
TR keyspdf + pol.2	0.237 ± 0.097	-0.011 ± 0.093	0.109 ± 0.070	0.200 ± 0.084	0.151 ± 0.090	0.554 ± 0.169	0.164 ± 0.096
LS erf*exp + pol.2	0.189 ± 0.104	0.060 ± 0.097	0.029 ± 0.079	0.251 ± 0.082	0.125 ± 0.091	0.470 ± 0.158	0.128 ± 0.142
TR erf*exp + pol.2	0.187 ± 0.105	0.057 ± 0.100	0.078 ± 0.073	0.263 ± 0.080	0.151 ± 0.088	0.482 ± 0.156	0.055 ± 0.101
fix CB tail to MC	0.186 ± 0.109	0.039 ± 0.102	0.015 ± 0.083	0.234 ± 0.081	0.158 ± 0.087	0.512 ± 0.165	0.134 ± 0.104
fix resolution to MC	0.186 ± 0.101	0.051 ± 0.097	0.088 ± 0.076	0.287 ± 0.082	0.183 ± 0.087	0.497 ± 0.162	0.166 ± 0.100
fix both CB and resolution	0.162 ± 0.108	0.037 ± 0.099	0.039 ± 0.073	0.254 ± 0.081	0.151 ± 0.087	0.468 ± 0.169	0.126 ± 0.101
fit systematic:							
RMS	0.024	0.036	0.033	0.031	0.022	0.054	0.039
largest variation	0.047	0.072	0.055	0.066	0.036	0.104	0.092
R_2 $(p_T^\mu > 4.0\mathrm{GeV/c})$							
nominal result	0.135 ± 0.078	0.051 ± 0.070	0.069 ± 0.054	0.214 ± 0.062	0.172 ± 0.069	0.210 ± 0.110	0.152 ± 0.077
systematic variations:							
LS keyspdf + pol.2	0.154 ± 0.074	0.022 ± 0.070	0.047 ± 0.055	0.205 ± 0.062	0.150 ± 0.070	0.251 ± 0.107	0.159 ± 0.075
TR keyspdf + pol.2	0.164 ± 0.072	0.008 ± 0.068	0.102 ± 0.053	0.171 ± 0.064	0.172 ± 0.072	0.255 ± 0.112	0.160 ± 0.076
LS erf*exp + pol.2	0.134 ± 0.075	0.052 ± 0.071	0.056 ± 0.056	0.204 ± 0.063	0.152 ± 0.071	0.220 ± 0.107	0.141 ± 0.096
TR erf*exp + pol.2	0.133 ± 0.075	0.050 ± 0.071	0.080 ± 0.054	0.211 ± 0.062	0.165 ± 0.070	0.223 ± 0.107	0.103 ± 0.078
fix CB tail to MC	0.136 ± 0.077	0.039 ± 0.071	0.044 ± 0.057	0.194 ± 0.060	0.176 ± 0.069	0.204 ± 0.110	0.149 ± 0.079
fix resolution to MC	0.127 ± 0.074	0.046 ± 0.071	0.087 ± 0.056	0.224 ± 0.063	0.189 ± 0.070	0.209 ± 0.109	0.162 ± 0.078
fix both CB and resolution	0.116 ± 0.077	0.038 ± 0.070	0.057 ± 0.052	0.206 ± 0.061	0.171 ± 0.068	0.211 ± 0.110	0.144 ± 0.077
fit systematic:							
RMS	0.015	0.021	0.021	0.019	0.013	0.024	0.020
largest variation	0.029	0.043	0.033	0.043	0.022	0.045	0.049

Appendix C.

Heavy flavour production cross sections

Table C.1 shows heavy quark and quarkonia production cross sections at $\sqrt{s_{NN}} = 2.76$ TeV. Cross sections are calculated up to NLO using PQCD calcuations.

Table C.1.: Quarkonia and heavy falvour cross sections from NLO

	$J/\psi \to \mu^+\mu^-$	B$\to$ $J/\psi \to \mu^+\mu^-$	Υ	c$\bar{c}$
cross section 5.5 TeV (all y)				
cross section 4 TeV (all y)	40 μb	131.9 μb (B$\bar{B}$)	0.533 μb	4.606 mb
cross section 4 TeV $\lvert y\rvert < 2.1$	9.6 μb	86.53 μb (B$\bar{B}$)	0.165 μb	2.344 mb
shadowing factor (from 5.5 TeV)	0.62	0.84	0.80	0.65
No. of quarkonia	1.3×10^6	1.8×10^5	2.85×10^4	
No. of $\mu^+\mu^-$ pairs	76500	21640	710	
Efficiency	1 %	1 %	15 %	
Expected Number for 4 TeV	765	216	106	
cross section 2.8 TeV (all y)	31.4 μb	90.11 μb	0.38 μb	3.539 mb
cross section 2.8 TeV $\lvert y\rvert < 2.1$	8.1 μb	62.54 μb	0.124 μb	1.912 mb
Efficiency	0.8 %		15 %	
Expected Number for 2.8 TeV	338		80	

Appendix D.

Gluon-J/ψ dissociation rate

The gluon-J/ψ dissociation cross section in dipole approximation is given by

$$\sigma_D(q^0) = 4\pi \left(\frac{8}{3}\right)^3 \frac{1}{m_Q^{3/2}} \epsilon_0^3 \frac{(q^0-\epsilon_0)^{3/2}}{(q^0)^5} \tag{D.1}$$

where m_Q is the heavy quark mass, and q^0 the gluon energy in the J/ψ rest frame; its value must be larger than the J/ψ binding energy ϵ_0. We can calculate dissociation rate by folding the gluon-J/ψ dissociation cross-section on thermal gluon distribution as

$$\lambda_D = \langle \sigma v_{\rm rel} \rangle_{p_g} \;=\; \frac{\frac{1}{(2\pi)^3}\int d^3p_g f_g(p_g,T) v_{\rm rel}\sigma_D(s)}{\frac{1}{(2\pi)^3}\int d^3p_g f_g(p_g,T)} \tag{D.2}$$

if thermal gluon density is given by by ρ_g as

$$\rho_g = \frac{1}{(2\pi)^3}\int d^3p_g f_g(p_g,T) \tag{D.3}$$

then J/ψ-gluon dissociation rate can be written as

$$\begin{aligned} \lambda_D\rho_g &= \frac{1}{(2\pi)^3}\int d^3p_g f_g(p_g,T) v_{\rm rel}\sigma_D(s) \\ &= \frac{1}{(2\pi)^3}\int 2\pi p_g^2 dp_g f_g(p_g,T) \int \sigma_D(s) v_{\rm rel}(s)\Theta(s-\epsilon_0^2) d(cos\theta) \end{aligned} \tag{D.4}$$

where the thermal gluon distribution is given by

$$f_g(p_g,T) = \frac{\lambda_g(=16)}{e^{\sqrt{p_g^2+m_g^2/T}}-1} \tag{D.5}$$

The relative velocity $v_{\rm rel}$ between the J/ψ and a gluon is

$$v_{\rm rel} = \frac{s-M_{J/\psi}^2}{2E_{J/\psi}E_g} \tag{D.6}$$

and q^0 the gluon energy in the J/ψ rest frame is related to centre of mass energy of J/ψ-gluon system as

$$q^0 = \frac{s-M_{J/\psi}^2}{2\,M_{J/\psi}}, \tag{D.7}$$

'If we consider that the J/ψ moves in the transverse direction with a four-velocity $u = (M_T, \vec{P_T}, 0)/M_{J/\psi}$, where $M_T = \sqrt{p_T^2 + M_{J/\psi}^2}$ is defined as the J/ψ's transverse mass. A gluon with a four-momentum $k = (k^0, \vec{k})$ in the rest frame of the parton gas has an energy $q^0 = k \cdot u$ in the rest frame of the J/ψ given by

$$\begin{aligned} q^0 &= \frac{k^0\,m_T + \vec{k}\cdot\vec{p_T}}{M_{J/\psi}}, \\ &= \frac{s-M_{J/\psi}^2}{2\,M_{J/\psi}}, \end{aligned} \tag{D.8}$$

The dissociation rate is given by

$$\lambda_D = \langle v_{\rm rel}\sigma_D(k\cdot u)\rangle_k \;=\; \frac{\int d^3k v_{\rm rel}\sigma_D(k\cdot u) f(k^0,T)}{\int d^3k f(k^0,T)}, \tag{D.9}$$

where the gluon distribution in the rest frame of the parton gas is

$$f(k^0,T) = \frac{\lambda_g(=16)}{e^{k^0/T}-1}. \tag{D.10}$$

The relative velocity $v_{\rm rel}$ between the J/ψ and a gluon is

$$v_{\rm rel} = \frac{P_{J/\psi}\cdot k}{k^0 M_T} \;= 1 - \frac{\vec{k}\cdot\vec{P}_T}{k^0 M_T} \;= \frac{s-M_{J/\psi}}{2E_1E_2} \tag{D.11}$$

Changing the variable to the gluon momentum, $q = (q^0, \vec{q})$, in the rest frame of the J/ψ, and writing $\rho_g = \int d^3k f(k^0, T)$, the Eq. (D.9) can be rewritten as

$$\lambda_D \rho_g = \int d^3q \frac{M_{J/\psi}}{m_T} \sigma_D(q^0) f(k^0, T). \tag{D.12}$$

Using $k^0 = (q^0 M_T + \vec{q} \cdot \vec{P}_T)/M_{J/\psi}$ in Eq. D.12 and solving

$$\begin{aligned}
\lambda_D\,\rho_g &= \frac{M_{J/\psi}}{m_T} \int d^3q\,\sigma_D(q^0) \frac{\lambda_g}{e^{\frac{q^0 m_T}{M_{J/\psi}T}} e^{\frac{\vec{q}\cdot\vec{p_T}}{M_{J/\psi}T}} - 1} \\
&= \frac{\lambda_g}{2\pi^3} \frac{M_{J/\psi}}{m_T} \int d^3q\,\sigma_D(q^0) \sum_{n=1}^{\infty} e^{\frac{-n\,q^0 m_T}{M_{J/\psi}T}} e^{\frac{-n\,\vec{q}\cdot\vec{p_T}}{M_{J/\psi}T}} \\
&= \frac{\lambda_g}{2\pi^3} \frac{M_{J/\psi}}{m_T} \sum_{n=1}^{\infty} 2\pi \int (q^0)^2 dq^0\,\sigma_D(q^0)\, e^{\frac{-n\,q^0 m_T}{M_{J/\psi}T}} \int_1^{-1} e^{\frac{-n\,q^0\,p_T cos\theta}{M_{J/\psi}T}} d(cos\theta) \\
&= \frac{\lambda_g}{2\pi^3} \frac{M_{J/\psi}}{m_T} \sum_{n=1}^{\infty} 2\pi \int (q^0)^2 dq^0\,\sigma_D(q^0)\, e^{\frac{-n\,q^0 m_T}{M_{J/\psi}T}} \left[e^{-\frac{nq^0 p_T}{M_{J/\psi}T}} - e^{\frac{nq^0 p_T}{M_{J/\psi}T}} \right] \frac{M_{J/\psi}T}{nq^0 p_T} \\
&= \frac{\lambda_g}{2\pi^3} \frac{M_{J/\psi}^2}{m_T} 2\pi \sum_{n=1}^{\infty} \frac{T}{n} \int_{\epsilon_0}^{\infty} q^0 dq^0\,\sigma_D(q^0)\, e^{\frac{-n\,q^0 m_T}{M_{J/\psi}T}} \frac{1}{p_T} \left[e^{\frac{nq^0 p_T}{M_{J/\psi}T}} - e^{-\frac{nq^0 p_T}{M_{J/\psi}T}} \right]
\end{aligned} \tag{D.13}$$

The special case of Eq. (D.14) for J/$\psi\, p_T = 0$ is

$$\frac{1}{p_T} \left[e^{\frac{nq^0 p_T}{M_{J/\psi}T}} - e^{-\frac{nq^0 p_T}{M_{J/\psi}T}} \right] = \frac{2nq^0}{M_{J/\psi}T}. \tag{D.14}$$

Using this we get

$$\lambda_D\,\rho_g = 4\pi \int (q^0)^2\, dq^0\,\sigma_D(q^0) \frac{\lambda_g}{e^{\frac{q^0}{T}} - 1} \tag{D.15}$$

Appendix E.

Lattice calculatons for QCD equation of state

Equation of state of hot strongly interacting matter play important hydrodynamic description of heavy ion collisions. Attempts to calculate EoS on the lattice have been made over the last 20 years [1]. One of the difficulties in calculating EoS on the lattice is its sensitivity to high momentum modes and thus to the effects of finite lattice spacing. This problem is particularly severe in the high temperature limit. The most recent lattice calculations of EOS using improved staggered fermions are available [25]. Calculations have been done at small value of the quark masses, but still larger than the physical value, corresponding to pion mass of about $m_\pi = 200$ MeV.

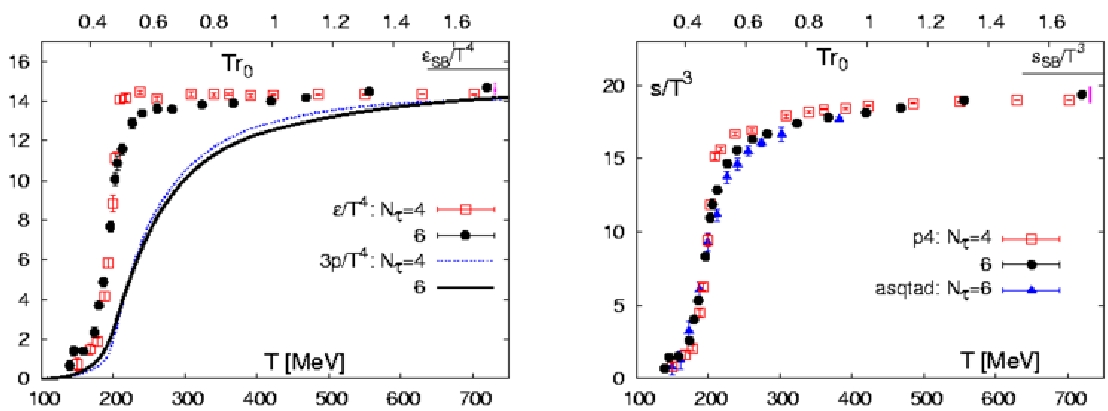

(a) (b)

Figure E.1.: (a) Energy density (ϵ) and pressure (P) (b) entropy density (s) calculated on lattice. Values for ideal gass are also shown.

Table E.1.: Parameters for different fits to lattice data.

	d_2 (GeV^2)	d_4 (GeV^4)	c_1 (GeV^{n_1})	c_2 (GeV^{n_2})	n_1	n_2	T_0
s95p-v1	0.2660	2.403×10^{-3}	-2.809×10^{-7}	6.073×10^{-23}	10	30	183.8
s95n-v1	0.2654	6.563×10^{-3}	-4.370×10^{-5}	5.774×10^{-6}	8	9	171.8
s95f-v1	0.2495	1.355×10^{-2}	-3.237×10^{-3}	1.439×10^{-14}	5	18	170.0

The trace anomaly of the lattice calculations can be can be parametrized as

$$\frac{\epsilon - 3P}{T^4} = \frac{d_2}{T^2} + \frac{d_4}{T^4} + \frac{c_1}{T^{n_1}} + \frac{c_2}{T^{n_2}} \tag{E.1}$$

and the trace anomaly of a chemically equilibrated hadron resonance gas with resonances up to 2 GeV mass can be parametrized as

$$\frac{\epsilon - 3P}{T^4} = a_1 T + a_2 T^3 + a_3 T^4 + a_4 T^{10} \tag{E.2}$$

where $a_1 = 4.654$ GeV^1, $a_2 =$ 879 GeV^3, $a_3 = 8081$ GeV^4 and $a_4 =$ 7039000 GeV^{10}, in a temperature interval $70 < T < 190$ MeV.

The fit to the lattice data can be constrained in several ways. For this parametrization it is required that the parametrized lattice trace anomaly connects smoothly to the trace anomaly of the hadron resonance gas, i.e. the trace anomaly and its first and second derivative with respect to temperature are continuous. We have made the fit to the lattice data above $T > 250$ MeV temperature, and constrained the entropy density at $T = 800$ MeV temperature to be either 90% or 95% of the Stefan-Boltzmann value (parametrizations s90 and s95, respectively). The parameter values are given in the Table E.1.

The EoS can be obtained from this parametrization by integrating over temperature

$$\frac{p(T)}{T^4} - \frac{p(T_{\text{low}})}{T_{\text{low}}^4} = \int_{T_{\text{low}}}^{T} dT' \frac{\epsilon - 3P}{T'^5} \tag{E.3}$$

where $T_{\text{low}} = 70$ MeV and $P(T_{\text{low}}/T_{\text{low}}^4 = 0.1661$.

Bibliography

[1] F. Karsch, "Lattice QCD at high temperature and density," Lect. Notes Phys. **583**, 209 (2002) [hep-lat/0106019].

[2] T. Matsui and H. Satz, "J/ψ Suppression by Quark-Gluon Plasma Formation," Phys. Lett. B **178**, 416 (1986).

[3] H. Satz, "Colour deconfinement and quarkonium binding," J. Phys. G **32**, R25 (2006), [hep-ph/0512217].

[4] Á. Mócsy and P. Petreczky, "Color Screening Melts Quarkonium," Phys. Rev. Lett. **99** 211602 (2007), [arXiv:0706.2183 [hep-ph]].

[5] R. Vogt, "Cold nuclear matter effects on J/ψ and Υ production at energies available at the CERN Large Hadron Collider (LHC)", Phys. Rev. C **81** 044903 (2010), [arXiv:1003.3497[hep-ph]].

[6] E. T. Atomssa (PHENIX Collaboration), "J/ψ production measurements by the PHENIX experiment at RHIC," Eur. Phys. J. C **61** 683 (2009), [arXiv:0805.4562 [nucl-ex]].

[7] S. Chatrchyan *et al.* [CMS Collaboration], "Observation and studies of jet quenching in PbPb collisions at nucleon-nucleon center-of-mass energy = 2.76 TeV," Phys. Rev. C **84**, 024906 (2011), [arXiv:1102.1957 [nucl-ex]].

[8] T. Sjostrand, S. Mrenna, and P. Z. Skands, "PYTHIA 6.4 physics and manual", JHEP **05** (2006) 026, [arXiv:hep-ph/0603175].

[9] I. P. Lokhtin, A. V. Belyaev, L. V. Malinina, S. V. Petrushanko, E. P. Rogochaya and A. M. Snigirev, "Hadron spectra, flow and correlations in PbPb collisions at the LHC: interplay between soft and hard physics," Eur. Phys. J. C **72**, 2045 (2012), [arXiv:1204.4820 [hep-ph]].

[10] GEANT Collaboration, "GEANT4 - A simulation toolkit", Nucl. Instrum. Meth.

A **506** (2003) 250.

[11] J. Pumplin, D. R. Stump, J. Huston, H. L. Lai, P. M. Nadolsky, and W. K. Tung, “New generation of parton distributions with uncertainties from global QCD analysis,” JHEP **0207** 12 (2002), [arXiv:hep-ph/0201195].

[12] K. J. Eskola, H. Paukkunen, and C. A. Salgado, “EPS09 - a New Generation of NLO and LO Nuclear Parton Distribution Functions,” JHEP **0904** 065 (2009), [arXiv:0902.4154 [hep-ph]].

[13] M. Cacciari, P. Nason and R. Vogt, “QCD predictions for charm and bottom production at RHIC,” Phys. Rev. Lett. **95**, 122001 (2005), [hep-ph/0502203].

[14] M. L. Mangano, P. Nason and G. Ridolfi, “Heavy quark correlations in hadron collisions at next-to-leading order,” Nucl. Phys. B **373**, 295 (1992).

[15] R. Oerter, “The theory of almost everything: The standard model, the unsung triumph of modern physics,” New York, USA: Pi Pr. (2006) 327 p

[16] D. J. Gross and F. Wilczek, “Asymptotically Free Gauge Theories. 1,” Phys. Rev. D **8**, 3633 (1973).

[17] H. D. Politzer, “Reliable Perturbative Results for Strong Interactions?,” Phys. Rev. Lett. **30**, 1346 (1973).

[18] D. J. Gross and F. Wilczek, “Ultraviolet Behavior of Nonabelian Gauge Theories,” Phys. Rev. Lett. **30**, 1343 (1973).

[19] H. D. Politzer, “Asymptotic Freedom: An Approach to Strong Interactions,” Phys. Rept. **14**, 129 (1974).

[20] R. P. Feynman, “The present status of quantum electrodynamics,” In *Brown, L.M. (ed.), Selected papers of Richard Feynman* 134-164

[21] S. S. Schweber, “QED and the men who made it: Dyson, Feynman, Schwinger, and Tomonaga,” Princeton, USA: Univ. Pr. (1994) 732 p

[22] B. Povh, C. Scholz, K. Rith and F. Zetsche, “Particles and nuclei: An introduction to the physical conceptions. (In German),” Berlin, Germany: Springer (1993) 316 p

[23] Y. Aoki, Z. Fodor, S. D. Katz, and K. K. Szabo, “The QCD transition temperature: Results with physical masses in the continuum limit,” Phys. Lett. B **643** 46 (2006), [arXiv:hep-lat/0609068].

[24] S. Borsanyi *et. al.* (Wuppertal-Budapest Collaboration), "Is there still any T_C mystery in lattice QCD? Results with physical masses in the continuum limit III," JHEP **1009**, 073 (2010), [arXiv:1005.3508 [hep-lat]].

[25] S. Borsanyi *et al.*, "The QCD equation of state with dynamical quarks," JHEP **1011** 077 (2010), [arXiv:1007.2580 [hep-lat]].

[26] K. Adcox *et al.* [PHENIX Collaboration], "Formation of dense partonic matter in relativistic nucleus-nucleus collisions at RHIC: Experimental evaluation by the PHENIX collaboration," Nucl. Phys. A **757**, 184 (2005) [nucl-ex/0410003].

[27] J. Adams *et al.* [STAR Collaboration], "Experimental and theoretical challenges in the search for the quark gluon plasma: The STAR Collaboration's critical assessment of the evidence from RHIC collisions," Nucl. Phys. A **757**, 102 (2005), [nucl-ex/0501009].

[28] M. L. Miller, K. Reygers, S. J. Sanders, and P. Steinberg, "Glauber modeling in high energy nuclear collisions," Ann. Rev. Nucl. Part. Sci. **57** (2007) 205.

[29] D. Kharzeev and M. Nardi, "Hadron production in nuclear collisions at RHIC and high density QCD," Phys. Lett. B **507** (2001) 121.

[30] I. Muller, "Zum Paradoxon der Warmeleitungstheorie," Z. Phys. **198** (1967) 329.

[31] W. Israel and J. M. Stewart, "Transient relativistic thermodynamics and kinetic theory," Annals Phys. **118** (1979) 341.

[32] P. Huovinen and P. Petreczky, "QCD Equation of State and Hadron Resonance Gas," Nucl. Phys. A **837** (2010) 26.

[33] H. Song, S. A. Bass, U. Heinz, T. Hirano, and C. Shen, "Hadron spectra and elliptic flow for 200 A GeV Au+Au collisions from viscous hydrodynamics coupled to a Boltzmann cascade," Phys. Rev. C **83** (2011) 054910 [Erratum-ibid. C **86** (2012) 059903].

[34] M. Gyulassy and L. McLerran, "New forms of QCD matter discovered at RHIC," Nucl. Phys. A **750** (2005) 30. [nucl-th/0405013].

[35] KAamodt *et al.* [ALICE Collaboration], "Charged-particle multiplicity density at mid-rapidity in central Pb-Pb collisions at $\sqrt{s_{NN}} = 2.76$ TeV," Phys. Rev. Lett. **105**, 252301 (2010), [arXiv:1011.3916 [nucl-ex]].

[36] J. D. Bjorken, "Highly Relativistic Nucleus-Nucleus Collisions: The Central Rapidity Region," Phys. Rev. D **27**, 140 (1983).

[37] S. Chatrchyan *et al.* [CMS Collaboration], "Measurement of the pseudorapidity and centrality dependence of the transverse energy density in PbPb collisions at $\sqrt{s_{NN}} = 2.76$ TeV," Phys. Rev. Lett. **109**, 152303 (2012), [arXiv:1205.2488 [nucl-ex]].

[38] B. Muller and J. L. Nagle, "Results from the relativistic heavy ion collider," Ann. Rev. Nucl. Part. Sci. **56**, 93 (2006) [nucl-th/0602029].

[39] K. Aamodt *et al.* [ALICE Collaboration], "Centrality dependence of the charged-particle multiplicity density at mid-rapidity in Pb-Pb collisions at $\sqrt{s_{NN}} = 2.76$ TeV," Phys. Rev. Lett. **106**, 032301 (2011), [arXiv:1012.1657 [nucl-ex]].

[40] G. Aad *et al.* [ATLAS Collaboration], "Measurement of the centrality dependence of the charged particle pseudorapidity distribution in lead-lead collisions at $\sqrt{s_{NN}} = 2.76$ TeV with the ATLAS detector," Phys. Lett. B **710**, 363 (2012), [arXiv:1108.6027 [hep-ex]].

[41] S. Chatrchyan *et al.* [CMS Collaboration], "Dependence on pseudorapidity and centrality of charged hadron production in PbPb collisions at a nucleon-nucleon centre-of-mass energy of 2.76 TeV," JHEP **1108**, 141 (2011), [arXiv:1107.4800 [nucl-ex]].

[42] S. S. Adler *et al.* [PHENIX Collaboration], "Systematic studies of the centrality and $\sqrt{s_{\rm NN}}$ dependence of the $\mathrm{d}E_T/\mathrm{d}\eta$ and $\mathrm{dN}_{ch}/\mathrm{d}\eta$ in heavy ion collisions at mid-rapidity," Phys. Rev. C **71**, 034908 (2005), [Erratum-ibid. C **71**, 049901 (2005)], [nucl-ex/0409015].

[43] B. I. Abelev *et al.* [STAR Collaboration], "Systematic Measurements of Identified Particle Spectra in pp, d^+ Au and Au+Au Collisions from STAR," Phys. Rev. C **79**, 034909 (2009), [arXiv:0808.2041 [nucl-ex]].

[44] B. Alver *et al.* [PHOBOS Collaboration], "Phobos results on charged particle multiplicity and pseudorapidity distributions in Au+Au, Cu+Cu, d+Au, and p+p collisions at ultra-relativistic energies," Phys. Rev. C **83**, 024913 (2011), [arXiv:1011.1940 [nucl-ex]].

[45] F. W. Bopp, R. Engel, J. Ranft and S. Roesler, "Inclusive distributions at the LHC as predicted from the DPMJET-III model with chain fusion," arXiv:0706.3875

[hep-ph].

[46] W. -T. Deng, X. -N. Wang and R. Xu, “Gluon shadowing and hadron production in heavy-ion collisions at LHC,” Phys. Lett. B **701**, 133 (2011), [arXiv:1011.5907 [nucl-th]].

[47] F. Gelis, E. Iancu, J. Jalilian-Marian and R. Venugopalan, “The Color Glass Condensate,” Ann. Rev. Nucl. Part. Sci. **60**, 463 (2010), [arXiv:1002.0333 [hep-ph]].

[48] M. A. Lisa, S. Pratt, R. Soltz and U. Wiedemann, “Femtoscopy in relativistic heavy ion collisions,” Ann. Rev. Nucl. Part. Sci. **55**, 357 (2005), [nucl-ex/0505014].

[49] K. Aamodt *et al.* [ALICE Collaboration], “Two-pion Bose-Einstein correlations in central Pb-Pb collisions at $sqrt(s_N N) = 2.76$ TeV,” Phys. Lett. B **696**, 328 (2011), [arXiv:1012.4035 [nucl-ex]].

[50] T. Schaefer and D. Teaney, “Nearly Perfect Fluidity: From Cold Atomic Gases to Hot Quark Gluon Plasmas,” Rept. Prog. Phys. **72** (2009) 126001, [arXiv:0904.3107 [hep-ph]].

[51] L. P. Csernai, J. .I. Kapusta, and L. D. McLerran, “On the Strongly-Interacting Low-Viscosity Matter Created in Relativistic Nuclear Collisions,” Phys. Rev. Lett. **97** (2006) 152303, [nucl-th/0604032].

[52] R. A. Lacey *et al.*, “Has the QCD Critical Point been Signaled by Observations at RHIC?,” Phys. Rev. Lett. **98** (2007) 092301, [nucl-ex/0609025].

[53] B. Wyslouch [CMS Collaboration], “Overview of experimental results in PbPb collisions at $\sqrt{s_{NN}} = 2.76$ TeV by the CMS Collaboration,” arXiv:1107.2895 [nucl-ex].

[54] P. Steinberg, “Recent Heavy Ion Results with the ATLAS Detector at the LHC,” J. Phys. G **38**, 124004 (2011), [arXiv:1107.2182 [nucl-ex]].

[55] F. Noferini [ALICE Collaboration], “Anisotropic flow of identified particles in Pb-Pb collisions at $\sqrt{s_{NN}} = 2.76$ TeV measured with ALICE at the LHC,” Nucl. Phys. A **904-905** (2013) 483c, [arXiv:1212.1292].

[56] B. Müller, “From Quark-Gluon Plasma to the Perfect Liquid,” Acta Phys. Polon. B **38** (2007) 3705, [arXiv:0710.3366 [nucl-th]].

[57] J. Adams *et al.* [STAR Collaboration], “Evidence from d + Au measurements for

final state suppression of high p(T) hadrons in Au+Au collisions at RHIC," Phys. Rev. Lett. **91** (2003) 072304, [nucl-ex/0306024].

[58] J. Adams *et al.* [STAR Collaboration], "Distributions of charged hadrons associated with high transverse momentum particles in pp and Au + Au collisions at $\sqrt{s_{NN}} =$ 200 GeV," Phys. Rev. Lett. **95** (2005) 152301, [nucl-ex/0501016].

[59] G. Aad *et al.* [ATLAS Collaboration], "Observation of a Centrality-Dependent Dijet Asymmetry in Lead-Lead Collisions at $\sqrt{s_{NN}} = 2.77$ TeV with the ATLAS Detector at the LHC," Phys. Rev. Lett. **105**, 252303 (2010), [arXiv:1011.6182 [hep-ex]].

[60] S. Chatrchyan *et al.* [CMS Collaboration], "Jet momentum dependence of jet quenching in PbPb collisions at $\sqrt{s_{NN}} = 2.76$ TeV," Phys. Lett. B **712**, 176 (2012), [arXiv:1202.5022 [nucl-ex]].

[61] ATLAS Collaboration, ATLAS-CONF-2011-075 (2011).

[62] T. Renk, "Energy dependence of the dijet imbalance in Pb-Pb collisions at 2.76 ATeV," Phys. Rev. C **86**, 061901 (2012), [arXiv:1204.5572 [hep-ph]].

[63] Y. He, I. Vitev and B. -W. Zhang, "$\mathcal{O}(\alpha_s^3)$ Analysis of Inclusive Jet and di-Jet Production in Heavy Ion Reactions at the Large Hadron Collider," Phys. Lett. B **713**, 224 (2012), [arXiv:1105.2566 [hep-ph]].

[64] S. S. Adler *et al.* [PHENIX Collaboration], "High transverse momentum η meson production in p^+p, d^+ Au and Au+Au collisions at $\sqrt{s_{NN}} = 200$-GeV," Phys. Rev. C **75** (2007) 024909, [nucl-ex/0611006].

[65] H. Song and U. W. Heinz, "Causal viscous hydrodynamics in 2+1 dimensions for relativistic heavy-ion collisions," Phys. Rev. C **77**, 064901 (2008), [arXiv:0712.3715 [nucl-th]].

[66] A. Dainese, "Heavy-flavour production in Pb-Pb collisions at the LHC, measured with the ALICE detector," J. Phys. G **38**, 124032 (2011), [arXiv:1106.4042 [nucl-ex]].

[67] Y. L. Dokshitzer, V. A. Khoze and S. I. Troian, "On specific QCD properties of heavy quark fragmentation ('dead cone')," J. Phys. G **17**, 1602 (1991).

[68] S. Chatrchyan *et al.* [CMS Collaboration], "Measurement of isolated photon production in *pp* and PbPb collisions at $\sqrt{s_{NN}} = 2.76$ TeV," Phys. Lett. B **710**, 256

(2012), [arXiv:1201.3093 [nucl-ex]].

[69] S. Chatrchyan *et al.* [CMS Collaboration], "Study of Z boson production in PbPb collisions at nucleon-nucleon centre of mass energy = 2.76 TeV," Phys. Rev. Lett. **106**, 212301 (2011), [arXiv:1102.5435 [nucl-ex]].

[70] I. Vitev and M. Gyulassy, "High p_T tomography of d + Au and Au+Au at SPS, RHIC and LHC," Phys. Rev. Lett. **89** (2002) 252301, [hep-ph/0209161].

[71] I. Vitev, "Jet tomography," J. Phys. G **30** (2004) S791, [hep-ph/0403089].

[72] B. Muller, J. Schukraft and B. Wyslouch, "First Results from Pb+Pb collisions at the LHC," Ann. Rev. Nucl. Part. Sci. **62**, 361 (2012), [arXiv:1202.3233 [hep-ex]].

[73] R. Sharma, I. Vitev and B. -W. Zhang, "Light-cone wave function approach to open heavy flavor dynamics in QCD matter," Phys. Rev. C **80**, 054902 (2009), [arXiv:0904.0032 [hep-ph]].

[74] T. Renk, H. Holopainen, R. Paatelainen and K. J. Eskola, "Systematics of the charged-hadron P_T spectrum and the nuclear suppression factor in heavy-ion collisions from $\sqrt{s} = 200$ GeV to $\sqrt{s} = 2.76$ TeV," Phys. Rev. C **84**, 014906 (2011), [arXiv:1103.5308 [hep-ph]].

[75] X. -F. Chen, T. Hirano, E. Wang, X. -N. Wang and H. Zhang, "Suppression of high p_T hadrons in $Pb + Pb$ Collisions at LHC," Phys. Rev. C **84**, 034902 (2011), [arXiv:1102.5614 [nucl-th]].

[76] A. Majumder and C. Shen, "Suppression of the High p_T Charged Hadron R_{AA} at the LHC," Phys. Rev. Lett. **109**, 202301 (2012), [arXiv:1103.0809 [hep-ph]].

[77] K. C. Zapp, F. Krauss and U. A. Wiedemann, "Explaining Jet Quenching with Perturbative QCD Alone," arXiv:1111.6838 [hep-ph].

[78] C. Gale, S. Jeon, and B. Schenke, "Hydrodynamic Modeling of Heavy-Ion Collisions," Int. J. Mod. Phys. A **28** (2013) 1340011., [arXiv:1301.5893 [nucl-th]].

[79] C. Gale, S. Jeon, B. Schenke, P. Tribedy and R. Venugopalan, "Event-by-event anisotropic flow in heavy-ion collisions from combined Yang-Mills and viscous fluid dynamics," Phys. Rev. Lett. **110** (2013) 012302.

[80] B. Friman, C. Hohne, J. Knoll, S. Leupold, J. Randrup, R. Rapp, and P. Senger, (eds.), *The CBM physics book: Compressed baryonic matter in laboratory*

experiments, Lect. Notes in Phys. **814** (2011) 1, (Springer, Heidelberg, 2011).

[81] V. D. Kekelidze *et al.* [NICA and MPD Collaborations], "NICA at JINR: New prospects for exploration of quark-gluon matter," Phys. Atom. Nucl. **75** (2012) 542.

[82] A. Accardi *et al.*, "Electron Ion Collider: The Next QCD Frontier - Understanding the glue that binds us all," arXiv:1212.1701 [nucl-ex].

[83] J. E. Augustin *et al.* [SLAC-SP-017 Collaboration], "Discovery of a Narrow Resonance in e^+e^- Annihilation," Phys. Rev. Lett. **33**, 1406 (1974).

[84] J. J. Aubert *et al.* [E598 Collaboration], "Experimental Observation of a Heavy Particle J," Phys. Rev. Lett. **33**, 1404 (1974).

[85] S. L. Glashow, J. Iliopoulos and L. Maiani, "Weak Interactions with Lepton-Hadron Symmetry," Phys. Rev. D **2**, 1285 (1970).

[86] W. M. Yao *et al.* [Particle Data Group Collaboration], "Review of Particle Physics," J. Phys. G **33**, 1 (2006).

[87] S. W. Herb, D. C. Hom, L. M. Lederman, J. C. Sens, H. D. Snyder, J. K. Yoh, J. A. Appel and B. C. Brown *et al.*, "Observation of a Dimuon Resonance at 9.5-GeV in 400-GeV Proton-Nucleus Collisions," Phys. Rev. Lett. **39**, 252 (1977).

[88] F. Abe *et al.* [CDF Collaboration], "Observation of top quark production in $\bar{p}p$ collisions," Phys. Rev. Lett. **74**, 2626 (1995), [hep-ex/9503002].

[89] A. D. Frawley, T. Ullrich and R. Vogt, "Heavy flavor in heavy-ion collisions at RHIC and RHIC II," Phys. Rept. **462**, 125 (2008), [arXiv:0806.1013 [nucl-ex]].

[90] P. Nason, S. Dawson and R. K. Ellis, "The Total Cross-Section For The Production Of Heavy Quarks In Hadronic Collisions," Nucl. Phys. B **303** (1988) 607;

[91] P. Nason, S. Dawson and R. K. Ellis, "The One Particle Inclusive Differential Cross-Section For Heavy Quark Production In Hadronic Collisions," Nucl. Phys. B **327** (1989) 49 [Erratum-ibid. B **335** (1990) 260].

[92] R. Vogt [Hard Probe Collaboration], "The A dependence of open charm and bottom production," Int. J. Mod. Phys. E **12**, 211 (2003), [hep-ph/0111271].

[93] R. Vogt, "Open and hidden charm production at RHIC and LHC," J. Phys. G **31**, S773 (2005), [hep-ph/0412303].

[94] J. Adams *et al.* [STAR Collaboration], "Open charm yields in d + Au collisions at $\sqrt{s_{NN}}$ = 200-GeV," Phys. Rev. Lett. **94**, 062301 (2005), [nucl-ex/0407006].

[95] A. Adare *et al.* [PHENIX Collaboration], "Measurement of high-p_T single electrons from heavy-flavor decays in p+p collisions at $\sqrt{s_{NN}}$ = 200-GeV," Phys. Rev. Lett. **97**, 252002 (2006), [hep-ex/0609010].

[96] G. T. Bodwin, E. Braaten, and G. P. Lepage, "Rigorous QCD analysis of inclusive annihilation and production of heavy quarkonium," Phys. Rev. D **51** 1125 (1995), [Erratum-ibid. D **55** 5853 (1997)], arXiv:hep-ph/9407339.

[97] N. Brambilla *et al.*, Heavy quarkonium physics, CERN-2005-005, (CERN, Geneva, 2005), arXiv:hep-ph/0412158.

[98] M. B. Einhorn and S. D. Ellis, "Hadronic Production Of The New Resonances: Probing Gluon Distributions," Phys. Rev. D **12** 2007 (1975).

[99] S. D. Ellis, M. B. Einhorn, and C. Quigg, "Comment On Hadronic Production Of Psions," Phys. Rev. Lett. **36** 1263 (1976)

[100] C. E. Carlson and R. Suaya, "Hadronic Production Of Psi/J Mesons," Phys. Rev. D **14** 3115 (1976).

[101] E. L. Berger and D. L. Jones, "Inelastic Photoproduction of J/psi and Upsilon by Gluons," Phys. Rev. D **23**, 1521 (1981).

[102] G. A. Schuler, "Quarkonium production and decays," [arXiv:hep-ph/9403387].

[103] P. Artoisenet, J. P. Lansberg, and F. Maltoni, "Hadroproduction of J/ψ and υ in association with a heavy-quark pair," Phys. Lett. B **653** 60 (2007), [arXiv:hep-ph/0703129]

[104] J. M. Campbell, F. Maltoni, and F. Tramontano, "QCD corrections to J/psi and Upsilon production at hadron colliders," Phys. Rev. Lett. **98** 252002 (2007), [arXiv:hep-ph/0703113]

[105] P. Artoisenet, J. M. Campbell, J. P. Lansberg, F. Maltoni, and F. Tramontano, "Υ Production at Fermilab Tevatron and LHC Energies," Phys. Rev. Lett. **101** 152001 (2008), [arXiv:0806.3282 [hep-ph]].

[106] H. Fritzsch, "Producing Heavy Quark Flavors in Hadronic Collisions: A Test of Quantum Chromodynamics," Phys. Lett. B **67**, 217 (1977).

[107] J. F. Amundson, O. J. P. Eboli, E. M. Gregores and F. Halzen, "Colorless states in perturbative QCD: Charmonium and rapidity gaps," Phys. Lett. B **372**, 127 (1996), [hep-ph/9512248].

[108] J. F. Amundson, O. J. P. Eboli, E. M. Gregores and F. Halzen, "Quantitative tests of color evaporation: Charmonium production," Phys. Lett. B **390**, 323 (1997), [hep-ph/9605295].

[109] G. C. Nayak, J. W. Qiu, and G. Sterman, "Fragmentation, factorization and infrared poles in heavy quarkonium production," Phys. Lett. B **613** 45 (2005), [arXiv:hep-ph/0501235].

[110] G. C. Nayak, J. W. Qiu, and G. Sterman, "Fragmentation, NRQCD and NNLO factorization analysis in heavy quarkonium production," Phys. Rev. D **72** 114012 (2005), [arXiv:hep-ph/0509021].

[111] E. Braaten, S. Fleming, and T. C. Yuan, "Production of heavy quarkonium in high-energy colliders," Ann. Rev. Nucl. Part. Sci. **46**, 197 (1996), [arXiv:hep-ph/9602374].

[112] J. C. Collins and D. E. Soper, "Parton Distribution And Decay Functions," Nucl. Phys. B **194** 445 (1982).

[113] J. P. Lansberg, "On the mechanisms of heavy-quarkonium hadroproduction," Eur. Phys. J. C **61** 693 (2009), [arXiv:0811.4005 [hep-ph]].

[114] F. Abe *et al.* [CDF Collaboration], "Production of J/ψ mesons from χ_c meson decays in $p\bar{p}$ collisions at $\sqrt{s} = 1.8$ TeV," Phys. Rev. Lett. **79**, 578 (1997).

[115] F. Abe *et al.* (CDF Collaboration), "J/ψ and $\psi(2S)$ production in $p\bar{p}$ collisions at $\sqrt{s} = 1.8$ TeV," Phys. Rev. Lett. **79** 572 (1997).

[116] T. Affolder *et al.* [CDF Collaboration], "Measurement of J/ψ and $\psi(2S)$ polarization in $p\bar{p}$ collisions at $\sqrt{s} = 1.8$ TeV," Phys. Rev. Lett. **85**, 2886 (2000), [hep-ex/0004027].

[117] D. E. Acosta *et al.* (CDF Collaboration), "Measurement of the J/ψ meson and b-hadron production cross sections in pp collisions at $\sqrt{s_{NN}} = 1960$ GeV," Phys. Rev. D **71** 032001 (2005), [arXiv:hep-ex/0412071].

[118] D. Acosta *et al.* [CDF Collaboration], "Υ production and polarization in $p\bar{p}$ collisions at $\sqrt{s} = 1.8$-TeV," Phys. Rev. Lett. **88**, 161802 (2002).

[119] A. Adare *et al.* (PHENIX Collaboration), "J/ψ production versus transverse momentum and rapidity in p^+p collisions at $\sqrt{s} = 200$-GeV," Phys. Rev. Lett. **98** 232002 (2007), [arXiv:hep-ex/0611020].

[120] S. S. Adler *et al.* (PHENIX Collaboration), "J/ψ production from proton proton collisions at $\sqrt{s} = 200$-GeV," Phys. Rev. Lett. **92** 051802 (2004), [arXiv:hep-ex/0307019].

[121] B. I. Abelev *et al.* (STAR Collaboration), "J/ψ production at high transverse momentum in p+p and Cu+Cu collisions at $\sqrt{s_{\rm NN}}$=200GeV," Phys. Rev. C **80** 041902 (2009), [arXiv:0904.0439 [nucl-ex]].

[122] C. L. da Silva (PHENIX Collaboration), "Quarkonia measurement in p+p and d+Au collisions at $\sqrt{s}$=200 GeV by PHENIX Detector," Nucl. Phys. A **830** 227C (2009), [arXiv:0907.4696 [nucl-ex]].

[123] A. Adare *et al.* (PHENIX Collaboration), "Transverse momentum dependence of J/ψ polarization at midrapidity in p+p collisions at sqrt(s)=200 GeV," Phys. Rev. D **82** 012001 (2010), [arXiv:0912.2082 [hep-ex]].

[124] V. Khachatryan *et al.* [CMS Coll.], "Measurement of the Inclusive Upsilon production cross section in pp collisions at sqrt(s)=7 TeV," Phys. Rev. D **83** 112004 (2011), [arXiv:1012.5545 [hep-ex]].

[125] R.Aaij, *et al.* [LHCb Coll.], "Measurement of Upsilon production in pp collisions at $\sqrt{s}$ = 7 TeV," Eur. Phys. J. C **72** 2025 (2012), [arXiv:1202.6579 [hep-ex]].

[126] G. Aad *et al.* [ATLAS Coll.], "Measurement of the Upsilon(1S) Production Cross-Section in pp Collisions at $\sqrt{s}$ = 7 TeV in ATLAS," Phys. Lett. B **705** 9 (2011), [arXiv:1106.5325 [hep-ex]].

[127] A. A. Affolder *et al.* (CDF Collaboration), "Production of $\Upsilon(1S)$ mesons from χ_b decays in $p\bar{p}$ collisions at $\sqrt{s} = 1.8$ TeV," Phys. Rev. Lett. **84** 2094 (2000), [arXiv:hep-ex/9910025].

[128] T. Aaltonen *et al.* (CDF Collaboration), "Production of ψ(2S) Mesons in ppbar Collisions at 1.96 TeV," Phys. Rev. D **80** 031103 (2009), [arXiv:0905.1982 [hep-ex]].

[129] P. Artoisenet, "QCD corrections to heavy quarkonium production," AIP Conf. Proc. **1038** 55 (2008).

[130] G. C. Nayak, M. X. Liu and F. Cooper, "Color octet contribution to high p_T J/ψ

production in pp collisions at $\sqrt{s}$ = 500-GeV and 200-GeV at RHIC," Phys. Rev. D **68**, 034003 (2003), [hep-ph/0302095].

[131] H. S. Chung, S. Kim, J. Lee, and C. Yu, Phys. Rev. D **81** 014020 (2010), [arXiv:0911.2113 [hep-ph]].

[132] H. Satz, "Color deconfinement in nuclear collisions," Rept. Prog. Phys. **63** 1511 (2000), [arXiv:hep-ph/0007069].

[133] C. Lourenço, R. Vogt, and H. K. Woehri, "Energy dependence of J/ψ absorption in proton-nucleus collisions," JHEP **0902** 014 (2009), [arXiv:0901.3054 [hep-ph]].

[134] K. J. Eskola, V. J. Kolhinen, and P. V. Ruuskanen, "Scale evolution of nuclear parton distributions," Nucl. Phys. B **535** 351 (1998), [arXiv:hep-ph/9802350].

[135] K. J. Eskola, V. J. Kolhinen, and C. A. Salgado, "The scale dependent nuclear effects in parton distributions for practical applications," Eur. Phys. J. C **9** 61 (1999), [arXiv:hep-ph/9807297].

[136] D. Stump, J. Huston, J. Pumplin, W. K. Tung, H. L. Lai, S. Kuhlmann , and J. F. Owens, "Inclusive jet production, parton distributions, and the search for new physics," JHEP **0310** 046 (2003), [arXiv:hep-ph/0303013].

[137] J. Badier *et al.* (NA3 Collaboration), "Experimental J/Psi Hadronic Production From 150-Gev/C To 280-Gev/C," Z. Phys. C **20** 101 (1983).

[138] B. Alessandro *et al.* (NA50 Collaboration), "J/ψ and ψ' production and their normal nuclear absorption in proton nucleus collisions at 400-GeV," Eur. Phys. J. C **48** 329 (2006), [arXiv:nucl-ex/0612012].

[139] B. Alessandro *et al.* (NA50 Collaboration), "Charmonium production and nuclear absorption in p A interactions at 450-GeV," Eur. Phys. J. C **33** 31 (2004).

[140] M. J. Leitch *et al.* (FNAL E866/NuSea Collaboration), "Measurement of J/ψ and ψ' suppression in pA collisions at 800-GeV/c," Phys. Rev. Lett. **84** 3256 (2000), [arXiv:nucl-ex/9909007].

[141] I. Abt *et al.* (HERA-B Collaboration), "Kinematic distributions and nuclear effects of J/ψ production in 920 GeV fixed-target proton-nucleus collisions," Eur. Phys. J. C **60** 525 (2009), [arXiv:0812.0734 [hep-ex]].

[142] T. Umeda, K. Nomura, and H. Matsufuru, "Charmonium at finite temperature in

quenched lattice QCD," Eur. Phys. J. C **39S1** 9 (2005), [arXiv:hep-lat/0211003]

[143] M. Asakawa and T. Hatsuda, "J/ψ and η_C in the deconfined plasma from lattice QCD," Phys. Rev. Lett. **92** 012001 (2004), [arXiv:hep-lat/0308034].

[144] S. Datta, F. Karsch, P. Petreczky, and I. Wetzorke, "Behavior of charmonium systems after deconfinement," Phys. Rev. D **69** 094507 (2004), [arXiv:hep-lat/0312037].

[145] A. Jakovác, P. Petreczky, K. Petrov, and A. Velytsky, "Quarkonium correlators and spectral functions at zero and finite temperature," Phys. Rev. D **75** 014506 (2007), [arXiv:hep-lat/0611017].

[146] C. Allton, M. B. Oktay, M. Peardon and J. I. Skullerud, "Charmonium at high temperature in two-flavor QCD," Phys. Rev. D **76** 094513 (2007), [arXiv:0705.2198 [hep-lat]].

[147] S. Digal, P. Petreczky, and H. Satz, "Quarkonium feed-down and sequential suppression," Phys. Rev. D **64** 094015 (2001), [arXiv:hep-ph/0106017].

[148] C. Y. Wong, "Heavy quarkonia in quark gluon plasma," Phys. Rev. C **72** 034906 (2005).

[149] Á. Mócsy and P. Petreczky, "Quarkonia correlators above deconfinement," Phys. Rev. D **73** 074007 (2006), [arXiv:hep-ph/0512156]

[150] A. Mocsy and P. Petreczky, "Heavy quarkonia survival in potential model," Eur. Phys. J. C **43** 77 (2005), [arXiv:hep-ph/0411262].

[151] W. M. Alberico, A. Beraudo, A. De Pace, and A. Molinari, Phys. Rev. D **75** 074009 (2007).

[152] D. Cabrera and R. Rapp, "T-matrix approach to quarkonium correlation functions in the QGP," Phys. Rev. D **76** 114506 (2007), [arXiv:hep-ph/0611134].

[153] Á. Mócsy and P. Petreczky, "Can quarkonia survive deconfinement ?," Phys. Rev. D **77** 014501 (2008), [arXiv:0705.2559 [hep-ph]].

[154] M. Laine, O. Philipsen, and M. Tassler, "Thermal imaginary part of a real-time static potential from classical lattice gauge theory simulations," JHEP **0709** 066 (2007), [arXiv:0707.2458 [hep-lat]].

[155] M. Laine, "A resummed perturbative estimate for the quarkonium spectral function in hot QCD," JHEP **0705** 028 (2007), [arXiv:0704.1720 [hep-ph]].

[156] M. Laine, "How to compute the thermal quarkonium spectral function from first principles?," Nucl. Phys. A **820** 25C (2009), [arXiv:0810.1112 [hep-ph]].

[157] N. Brambilla, J. Ghiglieri, A. Vairo, and P. Petreczky, "Static quark-antiquark pairs at finite temperature," Phys. Rev. D **78** 014017 (2008), [arXiv:0804.0993 [hep-ph]].

[158] O. Kaczmarek, F. Karsch, P. Petreczky, and F. Zantow, "Heavy Quark Anti-Quark Free Energy and the Renormalized Polyakov Loop," Phys. Lett. B **543**, 41 (2002), [arXiv:hep-lat/0207002].

[159] P. Petreczky, "Recent progress in lattice QCD at finite temperature," [arXiv:0906.0502 [nucl-th]].

[160] P. Petreczky, "Quarkonium in Hot Medium," J. Phys. G **37** 094009 (2010), [arXiv:1001.5284 [hep-ph]].

[161] B. Alessandro *et al.* (NA50 Collaboration), "A new measurement of J/ψ suppression in Pb-Pb collisions at 158 GeV per nucleon," Eur. Phys. J. C **39** 335 (2005), [arXiv:hep-ex/0412036].

[162] R. Arnaldi (NA60 Collaboration), "J/ψ production in p-A and A-A collisions at fixed target experiments," Nucl. Phys. A **830** 345c (2009), [arXiv:0907.5004 [nucl-ex]].

[163] E. Scomparin (NA60 Collaboration), "J/ψ production in p-A collisions at 158 and 400 GeV: recent results from the NA60 experiment," Nucl. Phys. A **830** 239c (2009), [arXiv:0907.3682 [nucl-ex]].

[164] A. Adare *et al.* (PHENIX Collaboration), "J/ψ production vs centrality, transverse momentum, and rapidity in Au + Au collisions at $\sqrt{s_{\rm NN}} = 200$GeV," Phys. Rev. Lett. **98** 232301 (2007), [arXiv:nucl-ex/0611020].

[165] D. de Florian and R. Sassot, "Nuclear parton distributions at next-to-leading order," Phys. Rev. D **69**, 074028 (2004) [hep-ph/0311227].

[166] S. Chatrchyan *et al.* [CMS Collaboration], "Suppression of non-prompt J/ψ, prompt J/ψ, and Y(1S) in PbPb collisions at $\sqrt{s_{NN}} = 2.76$ TeV," JHEP **1205**, 063 (2012) [arXiv:1201.5069 [nucl-ex]].

[167] C. Mironov [CMS Collaboration], "Overview of results on heavy flavour and quarkonia from the CMS Collaboration," Nucl. Phys. A **904-905**, 194c (2013).

[168] Z. Tang [STAR Collaboration], "J/ψ production and correlation in p+p and Au+Au collisions at STAR," J. Phys. G **38**, 124107 (2011) [arXiv:1107.0532 [hep-ex]].

[169] B. B. Abelev *et al.* [ALICE Collaboration], "Centrality, rapidity and transverse momentum dependence of J/ψ suppression in Pb-Pb collisions at $\sqrt{s_{NN}}$=2.76 TeV," Phys. Lett. **743**, 314 (2014) [arXiv:1311.0214 [nucl-ex]].

[170] A. Adare *et al.* [PHENIX Collaboration], "J/ψ suppression at forward rapidity in Au+Au collisions at $\sqrt{s_{NN}}$ = 200 GeV," Phys. Rev. C **84**, 054912 (2011) [arXiv:1103.6269 [nucl-ex]].

[171] L. Adamczyk *et al.* [STAR Collaboration], "Suppression of Upsilon Production in d+Au and Au+Au Collisions at $\sqrt{s_{NN}}$ = 200 GeV," Phys. Lett. B **735**, 127 (2014), [arXiv:1312.3675 [nucl-ex]].

[172] A. Adare *et al.* [PHENIX Collaboration], "Measurement of Υ(1S+2S+3S) production in p+p and Au+Au collisions at $\sqrt{s_{_{NN}}}$ = 200 GeV," arXiv:1404.2246 [nucl-ex].

[173] A. Emerick, X. Zhao, and R. Rapp, "Bottomonia in the quark-gluon plasma and their production at RHIC and LHC", Eur. Phys. J. A **48** (2012) 72, arXiv:1111.6537.

[174] H. Schopper and R.D. Heuer. LEP - The Lord of the Collider Rings at CERN 1980-2000: The Making, Operation and Legacy of the World's Largest Scientific Instrument. Springer, 2009.

[175] The CMS magnet project: Technical Design Report. Technical Design Report CMS. CERN, Geneva, 1997.

[176] The CMS Collabration. CMS TriDAS project: Technical Design Report; 1, the trigger systems. Technical Design Report CMS.

[177] Sergio Cittolin, Attila Rcz, and Paris Sphicas. CMS trigger and data-acquisition project: Technical Design Report. Technical Design Report CMS. CERN, Geneva, 2002.

[178] G.L. Bayatyan et al, CERN-LHCC-2005-023, CMS-TDR-007 (2005).

[179] S. Chatrchyan *et al.* [CMS Collaboration], "The CMS experiment at the CERN LHC," JINST **3**, S08004 (2008).

[180] M. Bargiotti and V. Vagnoni, "Heavy quarkonia sector in PYTHIA 6.324: Tuning, validation and perspectives at LHCb", LHCb Note LHCb-2007-042, (2007).

[181] D. J. Lange, "The EvtGen particle decay simulation package", Nucl. Instrum. Meth. A **462** (2001) 152.

[182] E. Barberio and Z. Was, "PHOTOS - A universal Monte Carlo for QED radiative corrections: version 2.0", Comput. Phys. Commun. **79** (1994) 291.

[183] I. P. Lokhtin and A. M. Snigirev, "A model of jet quenching in ultrarelativistic heavy ion collisions and high-p_T hadron spectra at RHIC", Eur. Phys. J. C **45** (2006) 211, [hep-ph/0506189].

[184] CMS Collaboration, "CMS physics technical design report: Addendum on high density QCD with heavy ions", J. Phys. G **34** (2007) 2307.

[185] C. Roland (on behalf of the CMS Collaboration), "Track reconstruction in heavy ion collisions with the CMS silicon tracker", Nucl. Instrum. Meth. A **566** (2006) 123.

[186] Particle Data Group Collaboration, "Review of particle physics", J. Phys. G **37** (2010) 075021.

[187] CMS Collaboration, "Prompt and non-prompt J/ψ production in pp collisions at $\sqrt{s_{NN}} = 7$ TeV", Eur. Phys. J. C **71** (2011) 1575, [arXiv:1011.4193 [hep-ex]].

[188] P. Faccioli and J. Seixas, "Observation of χ_c and χ_b nuclear suppression via dilepton polarization measurements," Phys. Rev. D **85**, 074005 (2012), [arXiv:1203.2033 [hep-ph]].

[189] G. J. Feldman and R. D. Cousins, "A Unified approach to the classical statistical analysis of small signals," Phys. Rev. D. **57**, 3873 (1998).

[190] B. B. Abelev *et al.* [ALICE Collaboration], "Suppression of Υ(1S) at forward rapidity in Pb-Pb collisions at $\sqrt{s_{\rm NN}} = 2.76$ TeV," arXiv:1405.4493 [nucl-ex].

[191] M. Strickland and D. Bazow, "Thermal bottomonium suppression at RHIC and LHC", Nucl. Phys. A **879** (2012) 25, [arXiv:1112.2761[hep-ph]].

[192] Z. -w. Lin and C. M. Ko, "Upsilon absorption in hadronic matter," Phys. Lett. B **503**, 104 (2001), [nucl-th/0007027].

[193] R. Sharma and I. Vitev, "High transverse momentum quarkonium production

and dissociation in heavy ion collisions", Phys. Rev. C **87** (2013) 044905; [arXiv:1203.0329[hep-ph]].

[194] F. Arleo and S. Peigne, "Heavy-quarkonium suppression in pA collisions from parton energy loss in cold QCD matter", JHEP **03** (2013) 122, [arXiv:1212.0434[hep-ph]].

[195] C. Gerschel and J. Hufner, "A contribution to the suppression of the J/ψ meson produced in high-energy nucleus nucleus collisions", Phys. Lett. B **207** (1988) 253.

[196] S. Gavin and R. Vogt, "J/ψ suppression from hadron-nucleus to nucleus-nucleus collisions", Nucl. Phys. B **345** (1990) 104.

[197] M. Laine, O. Philipsen, P. Romatschke, and M. Tassler, "Real-time static potential in hot QCD", JHEP **03** (2007) 054, arXiv:hep-ph/0611300.

[198] S. J. Brodsky and A. H. Mueller, "Using nuclei to probe hadronization in QCD", Phys. Lett. B **206** (1988) 685.

[199] D. M. Alde et al., "Nuclear dependence of the production of Upsilon resonances at 800-GeV", Phys. Rev. Lett. **66** (1991) 2285.

[200] M. Beneke and I. Z. Rothstein, "Hadroproduction of quarkonia in fixed target experiments", Phys. Rev. D **54** (1996) 2005, [arXiv:9603400[hep-ph]].

[201] R. Vogt, "Are the J/ψ and χ_c A dependencies the same?" Nucl. Phys. A **700** (2002) 539, [arXiv:0107045[hep-ph]].

[202] S. Chatrchyan *et al.* [CMS Collaboration], "Measurement of the Υ(1S), Υ(2S) and Υ(3S) polarizations in pp collisions at $\sqrt{s} = 7$ TeV," Phys. Rev. Lett. **110**, 081802 (2013) [arXiv:1209.2922 [hep-ex]].

[203] S. Chatrchyan *et al.* [CMS Collaboration], "Measurement of the elliptic anisotropy of charged particles produced in PbPb collisions at nucleon-nucleon center-of-mass energy = 2.76 TeV," Phys. Rev. C **87**, 014902 (2013) [arXiv:1204.1409 [nucl-ex]].

[204] B. Abelev *et al.* [ALICE Collaboration], "J/ψ Production as a Function of Charged Particle Multiplicity in pp Collisions at $\sqrt{s} = 7$ TeV," Phys. Lett. B **712**, 165 (2012) [arXiv:1202.2816 [hep-ex]].

[205] S. Chatrchyan *et al.* [CMS Collaboration], "Observation of sequential Upsilon suppression in PbPb collisions," Phys. Rev. Lett. **109**, 222301 (2012) [arXiv:1208.2826 [nucl-ex]].

[206] H. Abramowicz, P. Bartalini, M. Baehr, N. Cartiglia, R. Ciesielski, E. Dobson, F. Ferro and K. Goulianos *et al.*, "Summary of the Workshop on Multi-Parton Interactions (MPI@LHC 2012)," arXiv:1306.5413 [hep-ph].

[207] N. Armesto, N. Borghini, S. Jeon, U. A. Wiedemann, S. Abreu, V. Akkelin, J. Alam and J. L. Albacete *et al.*, "Heavy Ion Collisions at the LHC - Last Call for Predictions," J. Phys. G **35**, 054001 (2008), [arXiv:0711.0974 [hep-ph]].

[208] E. V. Shuryak, "Can dileptons be observed in heavy ion collisions at RHIC?," Phys. Rev. C **55**, 961 (1997), [nucl-th/9605011].

[209] U. Jamil and D. K. Srivastava, "Nuclear suppression of heavy quark production at forward rapidities in relativistic heavy ion collisions," J. Phys. G **37**, 085106 (2010), [arXiv:1005.1208 [nucl-th]].

[210] G. Aad *et al.* [ATLAS Collaboration], "Measurement of the centrality dependence of J/ψ yields and observation of Z production in lead-lead collisions with the ATLAS detector at the LHC," Phys. Lett. B **697**, 294 (2011), [arXiv:1012.5419 [hep-ex]].

[211] A. Adare *et al.* [PHENIX Collaboration], "Heavy Quark Production in $p+p$ and Energy Loss and Flow of Heavy Quarks in Au+Au Collisions at $\sqrt{s_N N} = 200$ GeV," Phys. Rev. C **84**, 044905 (2011), [arXiv:1005.1627 [nucl-ex]].

[212] A. Dainese [ALICE Collaboration], "First ALICE results from heavy-ion collisions at the LHC," [arXiv:1106.1341 [nucl-ex]].

[213] K. Gallmeister, B. Kampfer and O. P. Pavlenko, "Thermal dilepton signal versus dileptons from open charm and bottom decays in heavy ion collisions," Phys. Rev. C **57**, 3276 (1998), [hep-ph/9801435].

[214] M. Golam Mustafa, D. Pal and D. Kumar Srivastava, "Propagation of charm quarks in equilibrating quark - gluon plasma," Phys. Rev. C **57**, 889 (1998), [Erratum-ibid. C **57**, 3499 (1998)], [nucl-th/9706001].

[215] H. Agakishiev *et al.* [STAR Collaboration], "High p_T non-photonic electron production in $p+p$ collisions at $\sqrt{s} = 200$ GeV," Phys. Rev. D **83**, 052006 (2011), [arXiv:1102.2611 [nucl-ex]].

[216] R. Vogt, R. E. Nelson and A. D. Frawley, "Improving the J/ψ Production Baseline at RHIC and the LHC," Nucl. Phys. A **910-911**, 231 (2013), [arXiv:1207.6812

[hep-ph]].

[217] R. Vogt, “Determining the uncertainty on the total heavy-flavor cross section,” Eur. Phys. J. C **61**, 793 (2009).

[218] C. Mironov, R. Vogt and G. J. Kunde, “Dilepton-tagged Q anti-Q jet events at the LHC,” Eur. Phys. J. C **61**, 893 (2009).

[219] P. Levai and R. Vogt, “Thermal charm production by massive gluons and quarks,” Phys. Rev. C **56**, 2707 (1997), [hep-ph/9704360].

[220] R. Hamberg, W. L. van Neerven and T. Matsuura, “A Complete calculation of the order $\alpha - s^2$ correction to the Drell-Yan K factor,” Nucl. Phys. B **359**, 343 (1991), [Erratum-ibid. B **644**, 403 (2002)].

[221] A. Accardi, N. Armesto, M. Botje, S. J. Brodsky, B. Cole, K. J. Eskola, G. I. Fai and L. Frankfurt *et al.*, “Hard probes in heavy ion collisions at the lhc: pdfs, shadowing and pa collisions,” [hep-ph/0308248].

[222] T. Sakaguchi *et al.* (PHENIX Collaboration), in proceedings of Quark Matter 2012.

[223] K. Kajantie, M. Kataja, L. D. McLerran and P. V. Ruuskanen, “Transverse Flow Effects in Dilepton Emission,” Phys. Rev. D **34**, 811 (1986).

[224] R. Vogt, B. V. Jacak, P. L. McGaughey and P. V. Ruuskanen, “Rapidity distribution of dileptons form a hadronizing quark - gluon plasma,” Phys. Rev. D **49**, 3345 (1994), [hep-ph/9309213].

[225] C. Gale and P. Lichard, “Lepton pairs from thermal mesons,” Phys. Rev. D **49**, 3338 (1994), [hep-ph/9307363].

[226] G. Aad *et al.* [ATLAS Collaboration], “The ATLAS Experiment at the CERN Large Hadron Collider,” JINST **3**, S08003 (2008).

[227] K. Aamodt *et al.* [ALICE Collaboration], “The ALICE experiment at the CERN LHC,” JINST **3**, S08002 (2008).

[228] A. Abdulsalam and P. Shukla, “Suppression of bottomonia states in finite size quark gluon plasma in PbPb collisions at Large Hadron Collider,” Int. J. Mod. Phys. A **28**, 1350105 (2013) [arXiv:1210.7584 [hep-ph]].

[229] G. Bhanot and M. E. Peskin, “Short Distance Analysis for Heavy Quark Systems. 2. Applications,” Nucl. Phys. B **156**, 391 (1979).

[230] X. -M. Xu, D. Kharzeev, H. Satz and X. -N. Wang, "J/ψ suppression in an equilibrating parton plasma," Phys. Rev. C **53**, 3051 (1996) [hep-ph/9511331].

[231] A. Andronic, P. Braun-Munzinger, K. Redlich and J. Stachel, "Statistical hadronization of charm in heavy ion collisions at SPS, RHIC and LHC," Phys. Lett. B **571**, 36 (2003) [nucl-th/0303036].

[232] A. Andronic, P. Braun-Munzinger, K. Redlich and J. Stachel, "The statistical model in Pb-Pb collisions at the LHC," Nucl. Phys. A **904-905**, 535c (2013) [arXiv:1210.7724 [nucl-th]].

[233] R. L. Thews, M. Schroedter and J. Rafelski, "Enhanced J/ψ production in deconfined quark matter," Phys. Rev. C **63**, 054905 (2001) [hep-ph/0007323].

[234] X. Zhao and R. Rapp, "Medium Modifications and Production of Charmonia at LHC," Nucl. Phys. A **859**, 114 (2011) [arXiv:1102.2194 [hep-ph]].

[235] J. Pumplin, D. R. Stump and W. K. Tung, "Multivariate fitting and the error matrix in global analysis of data," Phys. Rev. D **65**, 014011 (2001) [hep-ph/0008191].

[236] V. Kumar, P. Shukla and R. Vogt, "Components of the dilepton continuum in Pb+Pb collisions at $\sqrt{s_{NN}}$ = 2.76 TeV," Phys. Rev. C **86**, 054907 (2012), [arXiv:1205.3860 [hep-ph]].

[237] E. V. Shuryak, "Two stage equilibration in high-energy heavy ion collisions," Phys. Rev. Lett. **68**, 3270 (1992).

[238] F. Karsch, M. T. Mehr and H. Satz, "Color Screening and Deconfinement for Bound States of Heavy Quarks," Z. Phys. C **37**, 617 (1988).

[239] F. Arleo, P. B. Gossiaux, T. Gousset and J. Aichelin, "Heavy quarkonium hadron cross-section in QCD at leading twist," Phys. Rev. D **65**, 014005 (2002) [hep-ph/0102095].

[240] R. L. Thews and M. L. Mangano, "Momentum spectra of charmonium produced in a quark-gluon plasma," Phys. Rev. C **73**, 014904 (2006), [nucl-th/0505055].

[241] R. Vogt, M. Prakash, P. Koch and T. H. Hansson, "J/ψ Interactions With Hot Hadronic Matter," Phys. Lett. B **207**, 263 (1988).